

**Extreme aerated water-wave impacts on floating bodies
The relevance of air content in water on ship design loads**

van der Eijk, M.

DOI

[10.4233/uuid:2c713a33-8cc6-42d3-8682-7e6872f6d422](https://doi.org/10.4233/uuid:2c713a33-8cc6-42d3-8682-7e6872f6d422)

Publication date

2023

Document Version

Final published version

Citation (APA)

van der Eijk, M. (2023). *Extreme aerated water-wave impacts on floating bodies: The relevance of air content in water on ship design loads*. [Dissertation (TU Delft), Delft University of Technology]. <https://doi.org/10.4233/uuid:2c713a33-8cc6-42d3-8682-7e6872f6d422>

Important note

To cite this publication, please use the final published version (if applicable).
Please check the document version above.

Copyright

Other than for strictly personal use, it is not permitted to download, forward or distribute the text or part of it, without the consent of the author(s) and/or copyright holder(s), unless the work is under an open content license such as Creative Commons.

Takedown policy

Please contact us and provide details if you believe this document breaches copyrights.
We will remove access to the work immediately and investigate your claim.

EXTREME AERATED WATER-WAVE IMPACTS ON FLOATING BODIES

The relevance of air content in water on ship design loads

Proefschrift

ter verkrijging van de graad van doctor aan de
Technische Universiteit Delft,
op gezag van de Rector Magnificus
prof.dr.ir. T.H.J.J. van der Hagen,
voorzitter van het College voor Promoties,
in het openbaar te verdedigen op
donderdag 26 oktober 2023 om 12:30 uur.

door

Martin VAN DER EIJK

Scheepsbouwkundig ingenieur
Technische Universiteit Delft, Nederland
geboren te Nieuwerkerk aan den IJssel, Nederland

Dit proefschrift is goedgekeurd door de promotoren en de samenstelling van de promotiecommissie is als volgt:

Rector Magnificus		(voorzitter)
prof.dr.ir. B.J. Boersma	Delft University of Technology	(promotor)
dr.ir. P.R. Wellens	Delft University of Technology	(copromotor)

Onafhankelijke leden:

Prof.Dr. D.M. Greaves	University of Plymouth	
Dr. Z. Xie	Cardiff University	
prof.dr.ir. J.A.M. Kuipers	Eindhoven University of Technology	
dr.ir. B. Hofland	Delft University of Technology	
Prof.Dr. R. Pecnik	Delft University of Technology	
prof.dr. G.D. Weymouth	Delft University of Technology	(reserve lid)

Het onderzoek dat in dit proefschrift wordt beschreven is uitgevoerd aan het departement Maritime and Transport Technology van de Technische Universiteit Delft.

EXTREME AERATED WATER-WAVE IMPACTS ON FLOATING BODIES
The relevance of air content in water on ship design loads

MARTIN VAN DER EIJK

Cover design: Martin van der Eijk
Front cover: Artistic impression of water, air, and golden bubbles
Side cover: Logo of EVA (Enhanced Volume-of-Fluid with Aeration)
Back cover: Density contours due to a wedge entry in aerated water

Printed by: Ipskamp printing
Typesetting: L^AT_EX
ISBN/EAN: 978-94-6473-260-3

An electronic version of this dissertation is available at
<http://repository.tudelft.nl>.

Martin van der Eijk: *Extreme aerated water-wave impacts on floating bodies:
The relevance of air content in water on ship design loads*, © 2023

*"Nobody trusts a computer simulation,
and everybody trusts experimental data,
except the guy who did it.
Why not combine the two and get results everybody
can mistrust a little?"*

Tony Kordyban based on a quote of Albert Einstein

To the people who like to know what I did in the past four years...
and the ones I love

PREFACE

My interests changed into a passion. Dynamic events like explosions, crashes, and impacts affecting their surroundings make the physics behind them very interesting. And, of course, the visualization of these events looks cool, leaving out the consequences. Besides my interest in coding, this was the main reason for me that I chose the presented Ph.D. topic.

Before getting into this topic, I want to point out that the presented methods are implemented from scratch, starting during my Master's. The thesis is structured such that every chapter represents a journal article to be published in the past four years. The reference to this article is given in the chapter. To keep the originality of the reviewed papers, I chose to leave the notation untouched for every chapter. I apologize for the amount of work I have done.

*Martin van der Eijk
Delft, September 2023*

CONTENTS

PREFACE	vii
1 INTRODUCTION	1
1.1 The three pillars of science	1
1.2 The presence of air in breaking waves	2
1.3 Research on aerated water-wave impacts	3
1.4 Research objective	7
1.5 A brief overview of the starting point of the presented numerical method	8
1.6 Research outline	9
I MODELING OF HIGH-DENSITY RATIO FLOWS, COMPRESSIBLE ENTRAPPED AIR-POCKET OSCILLATIONS, AND FLUID-BODY INTERACTION	
2 EXPERIMENTAL AND NUMERICAL ASSESSMENT OF VERTICAL ACCELERATIONS DURING BOW RE-ENTRY OF A RIB IN IRREGULAR WAVES	15
2.1 Introduction	16
2.2 Governing equations	18
2.2.1 One-phase flow model	18
2.2.2 Two-phase flow model	19
2.2.3 Free surface & boundary conditions	20
2.3 Numerical discretisation	20
2.3.1 Cell labeling	20
2.3.2 Discretisation of the Navier-Stokes equations	21
2.4 Simulation of wedge entry compared with experiment	22
2.4.1 Setup wedge entry	24
2.4.2 Appropriate grid resolution 2D wedge entry	24
2.4.3 Comparison one-phase & two-phase flow 2D wedge entry	26
2.4.4 Results 3D wedge entry	27
2.5 3D simulations with Fastship and ComFLOW compared with experiment	28
2.5.1 Experiment	28
2.5.2 Fastship	31
2.5.3 ComFLOW	35
2.5.4 Comparison results: Calm water simulation	38
2.5.5 Comparison results: Motion and Acceleration in irregular waves	38
2.6 Conclusions	41

3	A COMPRESSIBLE TWO-PHASE FLOW MODEL FOR PRESSURE OSCILLATIONS IN AIR ENTRAPMENTS FOLLOWING GREEN WATER IMPACT EVENTS ON SHIPS	43
3.1	Introduction	44
3.2	Mathematical model	46
3.3	Numerical discretisation	47
3.3.1	Algorithm	47
3.3.2	Viscosity	49
3.4	Free-surface displacement	50
3.4.1	Local height function	50
3.4.2	Curvature	50
3.4.3	Gravity-consistent density interpolation	51
3.4.4	Capillary forces	53
3.5	Verification and validation	54
3.5.1	2D standing viscous capillary wave	55
3.5.2	2D planar oscillating rod	56
3.5.3	2D rising bubble	59
3.5.4	1D shock tube	62
3.5.5	Dam break experiment	65
3.6	Main result	67
3.7	Conclusion	72
4	TWO-PHASE FREE-SURFACE FLOW INTERACTION WITH MOVING BODIES USING A CONSISTENT, MOMENTUM PRESERVING METHOD	75
4.1	Introduction	76
4.2	Governing equations	78
4.3	Grid and solution variables	79
4.4	Discretization and solution algorithm	84
4.4.1	Transport fluids and body	87
4.4.2	Discretization of the density	90
4.4.3	Auxiliary vector field $\tilde{\mathbf{u}}$	95
4.4.4	System of pressure Poisson equation and equation of motion	98
4.4.5	New velocity field	99
4.5	Proof of principle simulations	99
4.5.1	Moving wedge	99
4.5.2	Diagonally translating high density droplet	101
4.5.3	Momentum conservation droplet impact on fixed wall	104
4.5.4	Two-way fluid-structure interaction	107
4.5.5	Analyzing the momentum losses	108
4.5.6	Computational costs	109
4.6	Comparison benchmark & experiment	110
4.6.1	Rising bubble	110
4.6.2	Buoyant cylinder water exit & entry	114

4.7	Conclusion	120
II EXPERIMENTS AND NUMERICS WITH AERATION		
5	EXPERIMENTAL, NUMERICAL AND ANALYTICAL EVALUATION OF THE BUOYANT WEDGE ENTRY PROBLEM WITH REEMERGENCE IN 2D	127
5.1	Introduction	128
5.1.1	Introduction	128
5.1.2	Analytical	131
5.1.3	Numerical	132
5.1.4	Experimental	133
5.1.5	Article outline	134
5.2	Experiment	135
5.2.1	Setup & Tests	135
5.2.2	Results of wedge impact	138
5.2.3	Fourier analysis of system	141
5.2.4	Camera image processing	146
5.2.5	Velocity record	147
5.2.6	Natural heave period	149
5.3	Simulations with discretization in space	149
5.3.1	Numerical solver	149
5.3.2	Grid convergence	153
5.4	Simulations with an analytical approximation in space	158
5.4.1	Free surface and body	159
5.4.2	Wetted area	160
5.4.3	Velocity potential	161
5.4.4	Pressure	161
5.4.5	Forces	163
5.4.6	Equation of motion	164
5.4.7	Verification symmetric entry and fictitious body	165
5.4.8	Verification asymmetric entry	166
5.4.9	Verification slamming and jet separation stage with numerical results	167
5.4.10	Extension until closure stage: change of the FBC	170
5.4.11	Extension until closure stage: buoyancy	171
5.5	Synthesis of experimental, numerical, and analytical results	175
5.5.1	Boundary effects	175
5.5.2	Vertical deceleration after impact	176
5.5.3	Velocity after impact	178
5.5.4	Free surface configuration	182
5.6	Conclusion	186
6	AN EFFICIENT PRESSURE-BASED MULTIPHASE FINITE VOLUME METHOD FOR INTERACTION BETWEEN COMPRESSIBLE AERATED WATER AND MOVING BODIES	189

6.1	Introduction	190
6.2	Mathematical model	193
6.2.1	Interface capturing	193
6.2.2	Fluids: conservative form	194
6.2.3	Body motion	195
6.3	Closure of system of equations	196
6.3.1	Fluids: speed of sound	196
6.3.2	Fluids: equations of state	197
6.3.3	Fluids: volume fraction transport	198
6.3.4	Fluids: mixture speed of sound	200
6.3.5	Fluids: new formulation speed of sound	201
6.4	Grid structure	203
6.5	Discretization and solution algorithm	205
6.5.1	Interface transport	207
6.5.2	Auxiliary momentum field	208
6.5.3	Auxiliary density	209
6.5.4	New density & new aeration fields	209
6.5.5	Pressure equation & coupling with body	210
6.5.6	New fluid velocity field	211
6.5.7	Numerical model discretization schemes	211
6.6	Verification and validation with results from existing literature	212
6.6.1	1D Shock tube	212
6.6.2	Water or rigid body piston	217
6.6.3	2D Shock bubble	219
6.6.4	2D wedge entry in incompressible water	222
6.7	2D Wedge impact with aerated water	224
6.7.1	Brief overview of experiments with aerated water	224
6.7.2	Experimental setup	225
6.7.3	Numerical setup	228
6.7.4	Comparison simulations and experiment: maximum pressures	230
6.7.5	Comparison simulations and experiment: post-impact pressure oscillations and frequency analysis	233
6.8	Conclusion	238

III NUMERICAL IMPROVEMENTS FOR INTERFACE MODELING OF HIGH-DENSITY RATIO FLOWS

7	AN EFFICIENT 2D BILINEAR INTERFACE RECONSTRUCTION ALGORITHM AND CONSISTENT MULTIDIMENSIONAL UNSPLIT ADVECTION SCHEME FOR ACCURATE TRACKING OF HIGHLY-CURVED INTERFACIAL STRUCTURES ON UNIFORM GRIDS	243
7.1	Introduction	244
7.1.1	Motivation and Volume-of-Fluid method	244

7.1.2	Brief literature overview of geometrical interface reconstruction	245
7.1.3	Brief literature overview of fluid advection schemes	247
7.1.4	Structure of this work	250
7.2	BiLinear Interface Calculation	251
7.2.1	Identification of the interface	251
7.2.2	Initial PLIC reconstruction	252
7.2.3	Face values	253
7.2.4	Averaging method: curvature weighted	255
7.2.5	Addition of BLIC point	257
7.2.6	Evaluation & Remark	259
7.3	Static reconstruction interface	260
7.4	Unsplit edge-matched upwind flux polygon advection scheme	263
7.4.1	VOF advection	263
7.4.2	COSMIC advection scheme	264
7.4.3	Proposed Donating Quadrant Advection (DQA) scheme	265
7.5	Fundamental transport cases	272
7.5.1	Zalesak slotted disk rotation	272
7.5.2	Rider–Kothe single vortex	275
7.5.3	Computational costs	280
7.6	Consistent mass-momentum transport	281
7.6.1	Brief overview of two-phase solver	281
7.6.2	Application of an advection scheme to the solver	284
7.6.3	Inconsistency	285
7.6.4	The effect of the advection scheme on stability	290
7.7	Conclusion	296
8	CONCLUSIONS AND FUTURE WORK	299
8.1	Results and main findings	299
8.2	Outlook	302
	BIBLIOGRAPHY	305
	SUMMARY	335
	SAMENVATTING	339
	CURRICULUM VITAE	347
	PUBLICATIONS	349

INTRODUCTION

This chapter provides the background on wave impacts and objective, numerical methods, and outline of this thesis.

1.1 The three pillars of science

For centuries *theory* and *experiment* have been the foundation of science. The interaction between the two allows for verification and improvement of theories. The evolution of *computing* has led to the acceleration of mathematical calculations that resulted in new theories and explanations of natural events. Computations can fill a gap between theoretical and experimental science and become a third pillar of science.

The evolution of computing is also visible in the maritime industry. The complexity and variability of water-wave phenomena necessitate innovative approaches as the conventional (linear) techniques do not adequately represent highly non-linear wave events. The most promising direction for research in water waves is waves with large amplitudes [174]. Computational modeling can be advantageous for these waves because of their complexity involving effects of, for example, air-water interaction.

The overarching topic of this thesis is the development of an innovative computational model that can simulate complex wave events involving the contribution and effect of air on large water waves and moving structures. The focus is on the effect of air entrained in the water on the impact loading. The use of computational simulations contributes to understanding the physics and helps to design an experimental setup that can represent the desired phenomenon [244]. The following will briefly discuss the presence of air in large water waves, introduce the existing research about the effect of air on water-wave impact loading, and provide an overview of the numerical methods to deal with these events.

1.2 The presence of air in breaking waves

As large-amplitude waves become steeper, they reach a critical level, and break like plunging waves. Some large waves like this are considered "extreme". An extreme wave has a low probability of occurrence, is large with respect to the structure under consideration, and engages in complex interaction with structures that is not fully understood. Extreme waves can result in an impact loading on an offshore structure much larger than the loading in nonbreaking waves [167]. An illustration of an offshore structure acting in extreme waves is given in Fig. 1.1.



FIGURE 1.1. Shell Brent Charlie offshore structure in the North Sea experiencing loads by breaking waves [300].

Violent impacts cause damage to numerous marine structures each year and cause them to fail catastrophically even while being designed according to the regulations [22]. This does not only happen in the maritime industry but also for coastal sea defenses, geology, railway lines [135], offshore bridges [120, 286], and LNG tanks [14]. Similar failures of offshore structures resulted in the loss of people [153, 224]. A better understanding of these violent impacts is needed to prevent damage to prevent loss of life. A large number of recent studies related to large breaking waves are conducted by the aforementioned fields [14, 17, 36,

57, 79, 126, 164, 166], experimentally, numerically, and analytically.


These studies showed that air plays a role in the impact loadings, but its effect was difficult to quantify due to the complexity of the event. The interaction between water and air near the free surface often leads to air *entrapment*, enclosing a large air pocket in water, or *entrainment*, air bubbles dispersed through the water. The influence of trapped air pockets is, however, often still neglected, while recent studies showed that air does play a role in the impact process due to its high compressibility. A plunging wave can trap an air pocket between the structure and a body of water. The air pocket becomes compressed and starts to expand after the wave overturning jet has hit the wall. The entrapment of air can result in a considerable increase in impact pressure. This increase can be up to 10-100 larger than without the entrapment [28, 52, 111, 166, 171]. Specifically, ships with a blunt bottom operating in heavy seas with extreme waves can trap air beneath the hull [121] leading to pressures that can cause failure [134].

The entrainment of bubbles into the water can result from breaking water waves [56]. The closing of a plunging jet can trap an air pocket, which, after breaking up, can lead to the entrainment of air bubbles [140]. The mix of air bubbles and water is called aerated water. Other processes generating air bubbles in water are biological production, white capping, and air entrainment by capillary waves [48]. The air volume is likely to be between one to ten percent [27]. The bubbles produced by breaking waves can survive for several wave periods in salt water and tend to remain small without coalescing [237]. Standard design practices do not account for aerated water [83, 122, 249]. Without accounting for aeration, wave impact pressures can be overestimated, leading to overly conservative ship designs, but also underestimated, leading to probable catastrophic failure. Air entrainment introduces a new dimension of complexity in analyzing water-wave impacts and is the starting point of this thesis.

1.3 Research on aerated water-wave impacts

Experimental & Theoretical science

In geophysics aeration in breaking waves plays an important role in gas exchange between water and atmosphere [56]. Zooming in to the scale of a structure, the existence of bubbles in water has a notable influence on wave impact loading. Air is more compressible than water and therefore the mixture of air and water behaves differently from either water or air. One of the early studies related to water-wave impacts and air entrainment was by Peregrine and Thais [206] who developed an analytical approach that can estimate the pressure at the surface of a confined space filled with a bubbly liquid. Compared to water without air, a pressure reduction in wave impacts is found, even for a relatively small air content. This has been verified by many experiments of aerated water-waves



hitting a vertical wall [27, 28, 49, 171]. This reduction, called the *cushioning effect*, is related to the incoming wave velocity and the speed of sound in the air-water mixture [206]. Aeration is known to lower the maximum pressure but also tends to *distribute the impact pressure over a larger area* and to *increase the rise time of the pressure* during impact [27, 28]. Impacts at field scale with a high level of aeration showed these longer rise times and lower pressures, while impacts with a low level of aeration resulted in short-duration high-peaked pressures [49].

The expansion and compression of air pockets due to the impacts can cause density waves. A density wave is a sharp change of pressure that moves through the aerated water with the speed of sound of the mixture [28] and can interact with other structures. The reflection of these density waves can lead to *loading oscillations*. Fatigue analysis of ship structures may need to assess those loading oscillations [171] but investigation on the loading oscillations due to reflection is limited. Moreover, loadings below atmospheric pressure were observed in the field [48] and the laboratory [28, 167] as a result of the oscillations. Large oscillations in pressure can lead to destabilizing seaward forces on parts of a structure [28]. Cavitation, a phenomenon in which the static pressure becomes lower than the vapour pressure, may play a role in the impact loadings [167], as it did in the failure of the Mutriku Breakwater Wave plant [177].

Much research on scaling laboratory experiments to full scale has been done [12, 21, 27, 51, 55], but scaling remains a challenge. The use of traditional scaling laws significantly overestimates the forces [27, 51]. With Froude scaling, discrepancies in the level of aeration [12], in the dynamics of the fluid pressure relative to the atmospheric pressure, and in the compressible effect of aeration [21] are found, because the ratio of flow inertia and gravitational forces, only accounts for water.

Computational science

A solution for scaling could be the use of computational modeling. However, computational modeling of the breaking wave impacts is not yet at the same level as experimental modeling [137]. There is a large gap between contemporary numerical models used by industry and what is necessary for modeling impacts. The complexity lies in modeling all relevant phenomena involved in an extreme wave impact. The compressibility of air and air-water mixture, the possibility of cavitation, overturning of the wave front and the breaking process, and the coupled motion of a structure make it difficult to find a reliable solution for the impact needed for engineering purposes. The current state-of-the-art in numerical methods requires us to use expert judgement in choosing which phenomenon to represent accurately as it is not possible to model all aspects together.

There are many kinds of numerical simulation frameworks. Examples are frameworks that make use of a grid system or a particle system. This thesis will not focus on the particle methods and contribute to the numerical methods that makes use of a grid for modeling multiphase flows. A grid consists of discrete cells that cover a physical domain. The cells are used as control volumes for approximating the governing equations. Solving the governing equations simulate the motion of the fluids. The models for simulating large wave impacts are divided into different kinds of approaches. Every extension of an approach increases computational costs but also accounts for an additional process. The first class of approaches for water-wave impacts to be discussed are the single-phase incompressible potential flow models [64, 87, 225, 314, 316] and Navier-Stokes based models [97, 142]. Both classes are capable of predicting the wave before overturning and impacting. The previous section discussed that air can play a significant role in breaking waves, whereas the single-phase approach falls short in predicting this. As a result, the two-phase incompressible models based on the Navier-Stokes equations are introduced. These models can predict the entrapment of air pockets [42, 113, 164, 165, 242], but fail in the prediction of the compression and expansion of the air pocket. Including the compressibility of air with the two-phase semi-compressible models results in the ability to model compressible pocket oscillations [75, 291]. However, these models overpredict the propagation speed of density waves through the water and cannot represent aeration. The length scale between an offshore structure and entrained bubble being too large for tracking and reconstructing the bubbles on the numerical grid with sufficient accuracy [34] asks for a treatment that decreases the computational costs such that it can deal with the compressible effects of aerated water [214]. Existing models of this class are not yet ready for predicting loads on marine structures accurately.

Recently, published numerical models with aeration show promising results for wave impacts on vertical walls [22, 207, 214]. These models do not need subgrid models but make use of the assumption of a homogeneous mixture of air and water. However, these models revealed problems in resolving density waves at the air-water interface. Non-physical pressure oscillations in a one-dimensional shock tube test, a simplification of a pulsating air pocket, were experienced due to using a conservative formulation [231]. Ma et al. [168] tried to solve this problem by developing a quasi-conservative volume-fraction-based compressible two-phase flow model. The model was based on the assumption of a homogeneous mixture and could deal with dispersed-phase flows. The method shows an increased interface diffusion across several mesh cells for large flow gradient regions. The combination of the assumption of a homogeneous mixture, Woods' equation for the speed of sound [298], and interface diffusion results in non-monotonic behavior of the speed of sound and an underprediction of

the wave speed across the interface [232]. These aspects need consideration for implementing a numerical model that includes the effect of aeration.

Moving bodies

A moving body slamming the water can include similar physics as a wave hitting a wall [134]. The effects of aeration on the impact loadings can be imitated with a simplified experiment of a body hitting the water. Various numerical [81, 117, 169, 195] and experimental [27, 81, 117, 169, 170] studies have investigated drop tests in aerated water. A drop test of a 2D cross section is illustrated in Fig. 1.2. It represents the slamming event where inertia is the primary cause of the pressures.

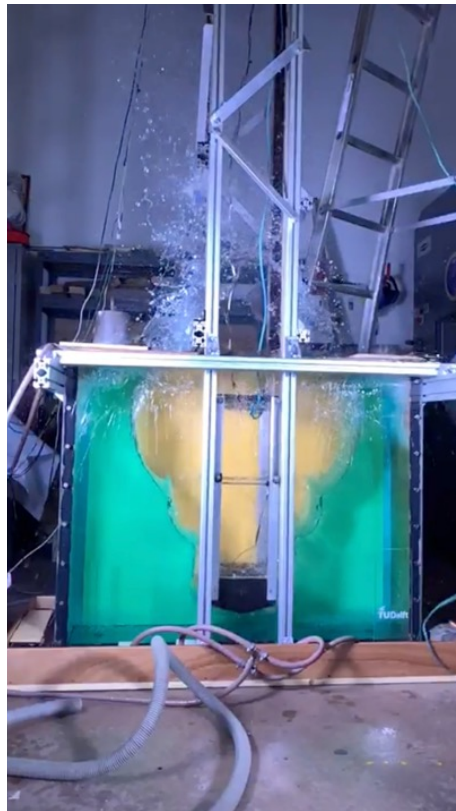


FIGURE 1.2. A drop test of a 2D wedge at Delft University of Technology [78].

The existing studies vary in dimensionality, two-dimensional and three-dimensional approaches, and in the shape of the moving body used for the drop. Similar effects of aeration on the loadings are found as for the wave impacts on vertical walls. Experimental and numerical aerated water entries of a three-dimensional flat plate revealed that the impact results in shock loading, fluid expansion loading excited by the entrapped air pocket, and secondary reloading caused by the repeated pocket pulsation. The aeration of water resulted in a significant

reduction of the impact loading by fifty percent of the pure-water loading or even more [27, 117, 169, 170]. The reduction was not only found for flat plates but also for other shapes [81, 117]. The problem of multiple rigid cone entries in aerated water showed the dependence of the slamming load and the compressible effects on the ratio of the expansion velocity of the wetted surface to the initial sonic speed in the aerated water [81]. The expansion velocity depends on the direction the fluid is forced to by the body.

1.4 Research objective

From a numerical perspective, the main objective of this thesis is to develop a novel fully compressible pressure-based numerical model for high-density ratio dispersive and separated flow problems. The model should be able to predict compressibility effects and the presence of density waves when a moving body gets hit by aerated water. Robustness and computational efficiency are main drivers in the development, together with accuracy. The challenges of the non-monotonic behavior of the speed of sound for diffusive interfaces must be overcome and large non-physical pressure oscillations must be kept in check.

From an experimental point of view, the objective is to design an experimental setup for validating the numerical method. New information and data for numerical verification about the compressibility effects of aerated water needs to be gathered. The combination of numerical and experimental results for moving bodies can provide insights regarding the compressibility effects of aerated water on the impact loads, like loading oscillations caused by reflected density waves. The description above of the numerical method indicates the steps that are needed to obtain the objectives. Each of these steps is addressed in this thesis, which is divided in three parts:

1. Develop an adequate semi-compressible pressure-based method that can model high-density ratio two-phase flows, represent the compressibility effects of an entrapped air pocket resolved by only a few grid cells, and account for the interaction between a moving body and the fluids.
2. Extend the semi-compressible model to a fully compressible multiphase flow model that can account for the presence of air in water as a homogeneous mixture and quantify the performance of this model by comparing with new experimental data.
3. Improve the model based on the experienced difficulties with representing high-density ratio interfaces and compressibility due to impacts.

1.5 A brief overview of the starting point of the presented numerical method

Core of the model

A starting point of the numerical method in this thesis is required to obtain the objectives. The presented numerical model is developed in-house from scratch, based on the one-phase flow model in the ComFLOW software package documented by Gerrits [97] and Kleefsman et al. [142]. The numerical model in the ComFLOW software package has a major application in predicting hydrodynamic wave load on offshore structures for research purposes and offshore-related companies. A description of the ComFLOW method is given below.

Numerical discretization

The equations that can describe the motion of viscous fluids, are the Navier-Stokes equations. These equations are referred to as the governing laws and express the conservation of momentum and mass for Newtonian fluids, fluids in which the viscous stresses scale linearly with strain. In the remainder, temperature effects are neglected, so that the energy equation does not have to be solved. The time discrete version of the Navier Stokes equations is obtained by integrating the pressure implicitly, and the convective and diffusive terms in the momentum equation explicitly. In ComFLOW [97, 142], the Navier-Stokes equations are solved using a pressure-based algorithm, with a one-step projection method [41].

In spatial directions, ComFLOW uses a robust finite-volume method. Robust means that the model is unlikely to break. A finite volume method is a method for approximating differential equations in the form of algebraic equations. Volume integrals are converted to surface integrals using the divergence theorem. The surface integrals are evaluated in terms of fluxes at the boundary of finite volumes. These finite volumes together form a numerical grid consisting of discrete cells covering the physical domain.

The governing equations are solved on a fixed Cartesian grid. A staggered arrangement of variables is used. In this arrangement, the velocities are defined in cell faces, and the scalar variables are defined in cell centers. Control volumes are also staggered with respect to each other. Unknown scalar variables on different locations in the grid are found by the usual averaging methods [292].

Interface tracking

A clear distinction where water is present, is made by cell labeling. The cells not filled with water are labeled empty, and cells with some water adjacent to an empty cell are labeled as surface cells. The remaining cells are labeled as fluid. The Volume-of-Fluid approach [115] is used to capture the interface between the fluids. Such an approach consists of two steps: the advection of the fluid from

and to cells, and interface reconstruction in cells labeled as surface cells.

Geometric interface reconstruction is applied to capture the moment of water-wave impacts accurately. The interface is reconstructed with piecewise (i.e. cell-by-cell) linear line segments. A local height function is used for determining the curvature. The advection of the interface. ComFLOW [142] displaces the interface using the combination of the local height function and the donor-acceptor method [115] that should prevent any mass losses and the existence of unphysical spray (separated water droplets) [142].

Multiphase modeling

The same Navier-Stokes equations apply to every fluid volume, but with different coefficients in different fluids. A jump in mass and momentum of the fluids across the interface is possible when these are separated by an interface. The application of averaging [70] for deriving the set of equations at macroscopic level is a classic technique to introduce multifluid models [212]. The averaging results in the use of volume fractions, indicating the filling rate of a fluid in a cell.

The assumptions of immiscibility, no-slip between the fluids, no mass transfer across the interface, and pressure equilibrium (a relaxed pressure to a common value) simplify the system of equations to one set of Navier-Stokes equations for the motion of a mixture where there is no need to solve the jump conditions. The model is founded on the one-fluid assumption resulting in one unique velocity and pressure field [188]. This set of equations is the start for the described method in this thesis modeling air-water phase flows.

Compressibility

The incompressible one-phase flow method of ComFLOW is extended to a semi-compressible two-phase flow model by Wemmenhove [292]. The semi-compressible flow model enforces a pressure-density relation for the air phase so that an energy equation can be omitted and the compressibility of air can be described. This thesis will improve the semi-compressible two-phase flow model and extend it to a fully compressible multiphase flow model.

1.6 Research outline

Each part in this thesis, defined in the research objective, represents a step in developing the final method. In Part I, numerical improvements for the core of the semi-compressible numerical method are discussed. The encountered numerical artifacts have been investigated and, in part, resolved. In Part II, modeling of aeration with fluid-body interaction is discussed. The final model is compared with results of self-conducted experiments. In Part III, numerical im-

1

provements for interface modeling of high-density ratio two-phase flows are discussed. Numerical schemes to increase the sharpness and accuracy of the interface are introduced. The thesis contains in total six studies described in six separate chapters.

Part I: Modeling of high-density ratio flows, compressible entrapped air-pocket oscillations, and fluid-body interaction

In Ch. 2, the suitability of the numerical model of the COMFLOW software package is tested for the global prediction of slamming loadings. For modeling a rescue boat sailing in heavy irregular seas, the numerical method does not use any assumptions or is limited in application range like a strip-theory method. The vertical accelerations computed by the first-principles numerical method are compared with a self-conducted towing tank experiment and an in-house calibrated state-of-the-art strip-theory method.

In Ch. 3, the description of the incompressible one-phase method of the COMFLOW software package is used as a starting point for developing a semi-compressible two-phase model from scratch. A semi-compressible two-phase model is tested for reproducing the oscillation effects of an entrapped air pocket represented by multiple grid cells. Important aspects of entrapped air pockets are the position of the free surface, surface tension, viscosity, and compressibility. A surface tension model that can deal with two phases improved the accuracy of representing the entrapped air pocket oscillations. Additional improvements by implementing surface tension and a higher-order free surface reconstruction are discussed.

In Ch. 4, the conservation of momentum of the two-phase model is scrutinized. The model of Ch. 3 showed unphysical free surface distortion and a reduction in momentum for incompressible cases with high-density ratios. The two-phase model is improved by using a consistent mass and momentum transfer implementation to reduce momentum losses. Furthermore, the extension of the model in Ch. 3 for two-way fluid-body interaction with a cut-cell method and a conservative transport split scheme for the interfaces is presented.

Part II: Experiments and numerics with aeration

In Ch. 5, an experimental setup for a “truly” 2D wedge entry is presented for validation. The experiment makes it possible to focus on the complicated interaction between the wedge and free surface and study both the wedge motion and the free surface deformation with a large amount of detail. The results are compared with the semi-compressible numerical model and can be used as a benchmark for violent fluid-structure interaction.

In Ch. 6, the semi-compressible numerical model in Ch. 4 is used to develop a new fully compressible pressure-based multiphase model that can account for a compressible homogeneous mixture of air and water. The numerical difficulties

discussed above give an underprediction of the propagation velocity of density waves at the material interface due to the numerical diffusivity and give numerical pressure oscillations around the material interface caused by inconsistency. Extension to fully compressible should minimize these effects. The experimental setup of Ch. 5 is reused and extended for pressure measurement on the wedge and the injection of tiny air bubbles in the water, and the experimental results are used to validate the numerical method. The combination of the experiments and numerical simulations is performed with the ambition to gain a better insight into the effect of aeration on the loadings when a wedge enters the aerated water in a closed domain.

Part III: Numerical improvements for interface modeling of high-density ratio flows

In Ch. 7, the representation of the free surface is improved and inconsistency in the transport of the free surface is prevented such to have a better distinction between air and entrained air. A new bilinear interface reconstruction scheme is introduced. This method showed to be an improvement in the representation of highly-curved interfaces, indicating an improvement in the distinction between water, air, body, and entrained air. A new consistent and conservative unsplit transport scheme is introduced to prevent instabilities near the interfaces between fluid and fluid, and between fluids and body.

The thesis closes with Ch. 8, summarizing the research findings and outlining future prospects.



Part I

MODELING OF HIGH-DENSITY RATIO FLOWS, COMPRESSIBLE ENTRAPPED AIR-POCKET OSCILLATIONS, AND FLUID-BODY INTERACTION

This part concerns the acquaintance with the core of the method based on the software package ComFLOW (Ch. 2). The method is extended to a semi-compressible two-phase model that can deal with the compressibility of entrapped air pockets (Ch. 3). The method is improved such that it can deal with high density-ratio flows, surface tension effects, and fluid-body interaction (Ch. 4). This part aims to improve the movement of the free surface and its interaction with bodies by preventing unwanted energy losses.

Photo: [132]

EXPERIMENTAL AND NUMERICAL ASSESSMENT OF VERTICAL ACCELERATIONS DURING BOW RE-ENTRY OF A RIB IN IRREGULAR WAVES

This chapter is reproduced from [79] :

M. van der Eijk and P. R. Wellens. “Experimental and numerical assessment of vertical accelerations during bow re-entry of a RIB in irregular waves.” *International Shipbuilding Progress* 67 (2020), pp. 1–26

Abstract

This work presents the comparison of a self-conducted towing tank experiment with the simulation results of a calibrated state-of-the-art strip-theory method and a first-principles numerical method. The experiment concerns a Rigid Inflatable Boat (RIB) in moderate-to-high irregular waves. These waves result in bow emersion events of the RIB. Bow re-entry induces vertical accelerations which, in reality, can lead to severe injuries and structural damage. State-of-the-art methods for predicting the vertical acceleration levels are based on assumptions, require calibration and are often limited in application range. We demonstrate how the vertical acceleration as a function of time is found from a 3D numerical method based on the Navier-Stokes equations, employing the Volume of Fluid (VoF) method for the free surface, without any further assumptions or limitations.

2D+t strip theory methods like Fastship are based on the mechanics of wedges falling in water. The 3D numerical method that is part of the software ComFLOW is compared to previous research on falling wedges in 2D to investigate the effect of air and to find suitable grid distances for the 3D simulation of the RIB. The 3D RIB simulations are compared to Fastship and the experiment. With respect to the experiment, the ComFLOW simulations show a slight underestimation of the levels of heave and pitch. The underestimation of Fastship is larger. The prediction of acceleration in ComFLOW is hardly different from the experiment and a significant improvement with respect to Fastship. ComFLOW is demonstrated to predict acceleration levels better than before, which creates opportunities for using it in seakeeping optimization and for the improvement of methods like Fastship. The properties of the RIB and the experiment are available as open data at [doi:10.4121/13078601](https://doi.org/10.4121/13078601) [288].

2.1 Introduction

After a comprehensive study of U.S. Special Operations craft crewmen, 62% of the crew reported one or more injuries that required hospitalization attributed to high-speed craft operation [209]. The demand for high speed crafts to be operational under all weather conditions without injuries leads to harsh design restrictions where bow emergence and re-entry play an important role. Bow re-entry in reality can lead to high vertical accelerations. In earlier years, reduction of the total resistance to reach the highest forward speed was the main objective. This resulted in adverse seakeeping behavior where the impacts induce severe injuries to the crew. Measurements at Fast Raiding Interception and Special forces Craft (FRISC) showed that acceleration pulses up to 15g were achieved [173]. Van Deyzen [267] concluded based on full scale trial data that the repeated occurrence of 1g vertical acceleration was acceptable for the crew. To prevent injury and structural damage following these high accelerations, the operator needs to reduce speed. Speed-adaptation results in a reduced operational profile.

To enlarge the operational profile at high speeds and reduce the vertical accelerations, the performance of the craft can be increased by improved ship design, the design subsequently evaluated by conducting experiments that test the sea keeping behavior. In support of experiments, approximating mathematical and numerical methods for predicting accelerations have been developed over the years, among which Fastship [139]. The state-of-the-art of these methods is limited in its range of application, because they depend, in part, on simplifications and calibrated empirical relations.

Here, we propose a first-principles numerical method to predict the acceleration levels of a Rigid Inflatable Boat (RIB) in moderate-to-high irregular waves. From what we were able to find in literature, the main contribution of this article is a direct deterministic comparison of vertical acceleration in time in irregular waves between 3 methods: self-conducted towing tank experiments, a calibrated state-of-the-art strip theory method called Fastship, and a 3D method based on the Navier-Stokes equations called ComFLOW [142]. The comparison is done for the entire time that a model is at constant speed in a run.

High speed craft have been widely investigated with most of the mathematical/numerical studies being based on slender body assumptions or potential theory [150, 315]. Several approaches to predict the performance of a high speed craft in calm water exist in literature. Tavakoli et al. [259] developed a mathematical model for the performance of planing hulls in forward accelerating motion. The model is extended with empirical equations of displacement ships and 2D+t theory, showing a fair agreement with experimental results. Recent numerical work of Broglia and Durante [24] focused on the challenging free

surface flow problem involving a surface vessel at high speeds in calm water using a numerical one-phase uRaNS flow solver. They mentioned that the application of a CFD based approach to study high speed craft is still rather limited. An experimental and numerical study of the total resistance and drag prediction is done by Avci and Barlas [7]. They conducted a towing tank test with a high speed hull to compare with CFD methods, resulting in a good agreement for the total resistance.

There are few accounts of validated 3D numerical approaches to predict the vertical accelerations of high speed craft in *irregular* waves in literature. Wang et al. [285] performed numerical simulations of a planing craft in regular waves using a RaNSE VoF solver where they focused on the sea keeping performance instead of the resistance. They concluded that validation with a model or full-scale measurement still remains of the essence. Mousaviraad, Wang, and Stern [187] assessed the capability of URaNS for the hydrodynamic performance and bow re-entry of a high speed craft. Simulations of a high speed craft in regular as well as irregular low-to-moderate waves were performed at a Froude number of 1.8-2.1. The results were validated with experiments for the mean and amplitudes of resistance, heave, pitch and acceleration. Similarly, Fu et al. [94] performed simulations at the same conditions finding generally good agreement in terms of expected values and standard deviations of vertical acceleration. Furthermore, they analyzed and validated the bow re-entry performance of the craft at high speed including vertical accelerations. More work where the accelerations of a RIB in irregular waves are predicted is done by Lewis et al. [157]. They used a RaNSE model in combination with non-linear strip theory through calculation of the forces occurring on a wedge impact. While the occurrence of wedge impact and the frequency of heave and pitch motions were predicted well, the magnitudes of accelerations were over-predicted compared to experimental data. Articles that deterministically compare the full time registration of the motions containing a bow re-entry event between a first-principles numerical model and an experiment have not been found.

Based on the remarks made by Wang et al. [285] and others, we conducted a towing tank experiment of a RIB in moderate-to-high irregular waves at Froude number $Fn \approx 0.25-1.0$ for validation of numerical models. During the experiment, the RIB is restricted to the heave and pitch motion while being towed through the tank at a constant speed. The heave and pitch motion, accelerations and wave height were measured for the time of a run. The experiments were controlled in such a way that in every run a bow emergence and re-entry event was experienced.

The 2D+t method Fastship is compared to the experiment at model scale for the same incoming waves as in the experiment. Fastship is a faster-than-real-time

model which makes use of 2D strips of wedges distributed over the hull length. The coefficients for the equation of motion are based on experimental results and analytical relations. The method has been extended over the years to include the effect of control systems for the forward velocity [227, 267]. Fastship has been used for the design of a RIB by Keuning et al. [138].

The proposed first-principles numerical method in this work is ComFLOW. 3D simulations of the RIB motions using ComFLOW are performed at the same scale and circumstances as the conducted experiment. Again, the incoming waves are the same as in the experiment. The numerical method ComFLOW has been under development since Fekken, Veldman, and Buchner [89]. Over the last few years, research is done to improve the description of violent flow phenomena which are both highly non-linear and highly dispersive [75, 97, 142, 292]. ComFLOW is based on the Navier-Stokes equations for the motion of an aggregated fluid with varying properties. A fixed Cartesian grid is used with a staggered configuration of variables within a cell. The free surface is displaced using the Volume-of-Fluid (VoF) method where the interface is reconstructed using piecewise-linear line segments (PLIC). Using a cut-cell method, a body can be incorporated to determine the interaction with the fluid [90]. Validation of the numerical simulation method ComFLOW with experimental data of a high speed craft in 3D has not been done before.

This article first presents the governing equations of fluid flow that Fastship and ComFLOW are based on. Then, in order to study the importance of air and to find the appropriate grid configuration for the prediction of bow re-entry, free falling wedge drop tests are simulated with ComFLOW. By conducting the wedge drop simulations, a first experience of how ComFLOW behaves for simplified bow entries is demonstrated. With the selected grids, 3D simulations with the RIB are performed. At the end, the comparison between the experiment, Fastship and ComFLOW is made and conclusions are formulated based on the results. The details of the RIB and the experiment are provided as open data by Wellens [288].

2.2 Governing equations

2.2.1 One-phase flow model

The one-phase flow model makes use of the assumption that the effect of air can be neglected. Water is considered as an incompressible and viscous liquid. Air is considered as a vacuum. The liquid motion in a 3D domain is described by the Navier-Stokes equations and a fluid displacement algorithm. For the one-phase

flow model, the governing equations are only applied in the liquid-filled part of the domain. The Navier-Stokes equations are simplified to [97]

$$\begin{aligned}\nabla \cdot \mathbf{u} &= 0, \\ \frac{\partial \mathbf{u}}{\partial t} + \mathbf{u} \cdot \nabla \mathbf{u} &= -\frac{1}{\rho} \nabla p + \frac{\mu}{\rho} \nabla^2 \mathbf{u} + \mathbf{F},\end{aligned}\quad (2.1)$$

with \mathbf{u} the velocity vector, ρ the density of the fluid, p the pressure and μ the dynamic viscosity. \mathbf{F} are the external body forces, in this case only gravity; $[0 \ 0 \ -9.81]^T$ [m/s²]. For an incompressible flow, the density does not change in a lagrangian manner and therefore the divergence of the velocity is zero.

2.2.2 Two-phase flow model

In contrast to the one-phase flow model, the two-phase flow model solves for water and air in the entire domain, making it more computationally expensive. In this model water remains an incompressible, viscous fluid. Air is chosen as a compressible viscous fluid to account for cushioning effects.

The Navier-Stokes equations are stated for a mixed fluid in which the pressure is relaxed to a single field. This results in one continuity and one momentum equation for both water and air [292]

$$\begin{aligned}\frac{\partial \rho}{\partial t} + \nabla \cdot (\rho \mathbf{u}) &= 0, \\ \frac{\partial (\rho \mathbf{u})}{\partial t} + \nabla \cdot (\rho \mathbf{u} \mathbf{u}) &= -\nabla p + \\ &\nabla \cdot \left(\mu \left(\nabla \mathbf{u} + \nabla \mathbf{u}^T - \frac{2}{3} \nabla \cdot \mathbf{u} \mathbf{I} \right) \right) \\ &+ \rho \mathbf{F}.\end{aligned}\quad (2.2)$$

The mixed fluid properties ρ and μ are defined in Eq. (2.7). To close the system of equations, an energy equation referred to as the equation of state is introduced

$$\frac{p}{p_{ref}} = \left(\frac{\rho_g}{\rho_{g,ref}} \right)^\gamma. \quad (2.3)$$

Eq. (2.3) is a polytropic relation between the pressure and density of the compressible gas. p and ρ_g are the pressure and density of the compressible air. p_{ref} is the atmospheric pressure and $\rho_{g,ref}$ is the air density at atmospheric pressure. γ is the adiabatic coefficient: $\gamma = 1.4[-]$ for air is used.

2.2.3 Free surface & boundary conditions

For both the one-phase and the two-phase model, the fluid displacement algorithm is described by a function $s(\mathbf{x}, t) = 0$, with $\mathbf{x} = (x, y, z)^T$. The equation of the displacement of the free surface is as follows [97]

$$\frac{Ds}{Dt} = \frac{\partial s}{\partial t} + \mathbf{u} \cdot \nabla s = 0. \quad (2.4)$$

The boundary conditions needed by both models are as follows. At the fixed walls of the domain or the moving objects, no penetration boundary conditions are applied, $\mathbf{u} \cdot \mathbf{n} = \mathbf{u}_b \cdot \mathbf{n}$. At domain walls also a free-slip boundary condition is imposed, $\boldsymbol{\tau} \cdot \mathbf{n} = 0$. \mathbf{u}_b is the velocity of the moving object and $\boldsymbol{\tau}$ is the shear stress tensor. When performing wave simulations, an inflow boundary is needed where the velocity profile of the incoming wave is prescribed and an outflow boundary for the absorption of waves [289]. To that end, the Generating and Absorbing Boundary Condition (GABC) of Wellens and Borsboom [289] is used in combination with the superposition of linear wave velocity components to model an irregular wave. The settings of the GABC are elaborated upon in Sec. 2.5.

In only the one-phase flow model, boundary conditions for pressure and velocity are needed at the free surface to close the system. Eqs. (2.5) and (2.6) are the result of continuity of the normal and tangential stresses [97] at the free surface

$$-p + 2\mu \frac{\partial u_n}{\partial n} = -p_0 + \sigma \kappa, \quad (2.5)$$

$$\mu \left(\frac{\partial u_n}{\partial t} + \frac{\partial u_t}{\partial n} \right) = 0, \quad (2.6)$$

where u_n and u_t denote the normal and tangential component of the velocity. p_0 is the atmospheric pressure. The two-phase flow model requires the atmospheric pressure to be set at a boundary that only connects with air, usually the ceiling of the domain.

2.3 Numerical discretisation

2.3.1 Cell labeling

The mathematical model is implemented in the pressure-based numerical solution method ComFLOW. In order to solve the Navier-Stokes equations, the computational domain is covered with a fixed and staggered Cartesian grid. In the grid, pressure and density are defined in cell centers and velocities are defined at the edges of the cell. The Navier-Stokes equations are solved in every cell (or in every cell that contains water in one-phase simulations). Structure geometries cut through the grid so that cells within the contour of the structure are partially or completely closed to flow. We call those cut cells and they are

administered by edge and volume apertures. The apertures are a measure for which part of the cell face or cell volume is open to flow.

The cells are divided into three groups to describe the fluid configuration. Cells which can be filled with water, but are filled with air (or empty in one-phase), are called E-cells. A S-cell (surface) contains fluid and is next to an E-cell. The remaining cells containing fluid are labeled with F. Cells which are fully occupied by the structure are labeled with B. An example of the labeling is illustrated in Fig. 2.1.

<i>E</i>	<i>E</i>	<i>E</i>	<i>E</i>	<i>E</i>
<i>E</i>	<i>E</i>	<i>E</i>	<i>E</i>	<i>E</i>
<i>B</i>	<i>F</i>	<i>S</i>	<i>S</i>	<i>E</i>
<i>F</i>	<i>F</i>	<i>F</i>	<i>F</i>	<i>S</i>
<i>F</i>	<i>F</i>	<i>F</i>	<i>F</i>	<i>F</i>

FIGURE 2.1. Labeling of cells.

2.3.2 Discretisation of the Navier-Stokes equations

Where for the one-phase flow model the density and viscosity do not change, with the two-phase flow model they do because of the aggregate fluid assumption and the effect of compressibility. Density values are defined in the centers of cells and found by arithmetic averaging

$$\begin{aligned}\rho &= \frac{F_s}{F_b} \rho_l + \frac{F_b - F_s}{F_b} \rho_g, \\ \mu &= \frac{F_s}{F_b} \mu_l + \frac{F_b - F_s}{F_b} \mu_g,\end{aligned}\tag{2.7}$$

where F_b and F_s are the fractions of the cells that are open for flow and occupied with liquid, respectively. The water density ρ_l remains constant and the air density is calculated using Eq. (2.3). At the cell faces the density and viscosity are calculated by cell-weighted averaging [75].

Velocities near and above the free surface are not solved for in the one-phase approach. These so-called EE and SE velocities, see Fig. 2.1, are needed to complete the discretisation of the convective term in the momentum equation. They are found by constant extrapolation from the inside of the water [142].

To solve the Navier-Stokes equations, the equations are discretised in time and space. The combination of the forward Euler method for time integration and central discretisations of the derivatives in space is used for all but the non-linear convective term. In that term, a first-order upwind discretisation is used. The forward Euler method is a first order method but accurate enough, because of small time steps and because the overall accuracy is determined by the accuracy of the free surface displacement [142]. No turbulence model is used.

The system is solved using a one-step projection method. A Poisson equation is formulated and solved for the pressure with a BiCGSTAB solver [275], with ILU(ϵ) preconditioning. This solver is compatible with both one-phase flow and two-phase flow and sufficiently robust for the large density variations from air to water near the free surface in two-phase flow simulations. The free surface is convected by the improved Volume-of-Fluid (iVOF) method in ComFLOW: the free surface is reconstructed using a Piecewise Linear Interface Calculation (PLIC [310]) and displaced with the split scheme MACHO [74] to solve Eq. (2.4). A Courant number (CFL) restriction, based on the velocity \mathbf{u} , is used for numerical stability.

In ComFLOW, we choose to keep the motion solver for the structure separate from the Poisson equation so that we can link to external libraries. That creates a difficulty: the body velocities are required at the new time step, but they depend on the pressures along the hull, and the new pressures along the hull depend on the new body velocities. The two-way coupling between structure and fluid is solved iteratively with underrelaxation applied to the update of the body velocities, that consists of body force over mass of the structure. Tangential stresses are ignored in the body force calculation.

2.4 Simulation of wedge entry compared with experiment

Water-entry of a wedge shaped section has been investigated in numerous studies, e.g. numerically in 2D and 3D by Kleefsman et al. [142] and experimentally in 3D by Zhao, Faltinsen, and Aarsnes [316]. Wedge entry is a simplification of a bow re-entry event and often used for the prediction of the forces on a cross section in a 2D strip theory approach for a ship. We use falling wedges to verify ComFLOW, to determine which physics are relevant for the 3D case, and for finding the grid resolution. The geometry of the wedge is shown in Fig. 2.2. The size of the cross section is similar to the 3D RIB. Besides 2D simulations of the wedge entry also a 3D simulation is done to compare with the 3D experimental data of Zhao, Faltinsen, and Aarsnes [316]. Muzaferija [189] determined that a gap of 0.25[m] between the back and front wall and the wedge in the 3D simulation gives results that compare well with experiments.

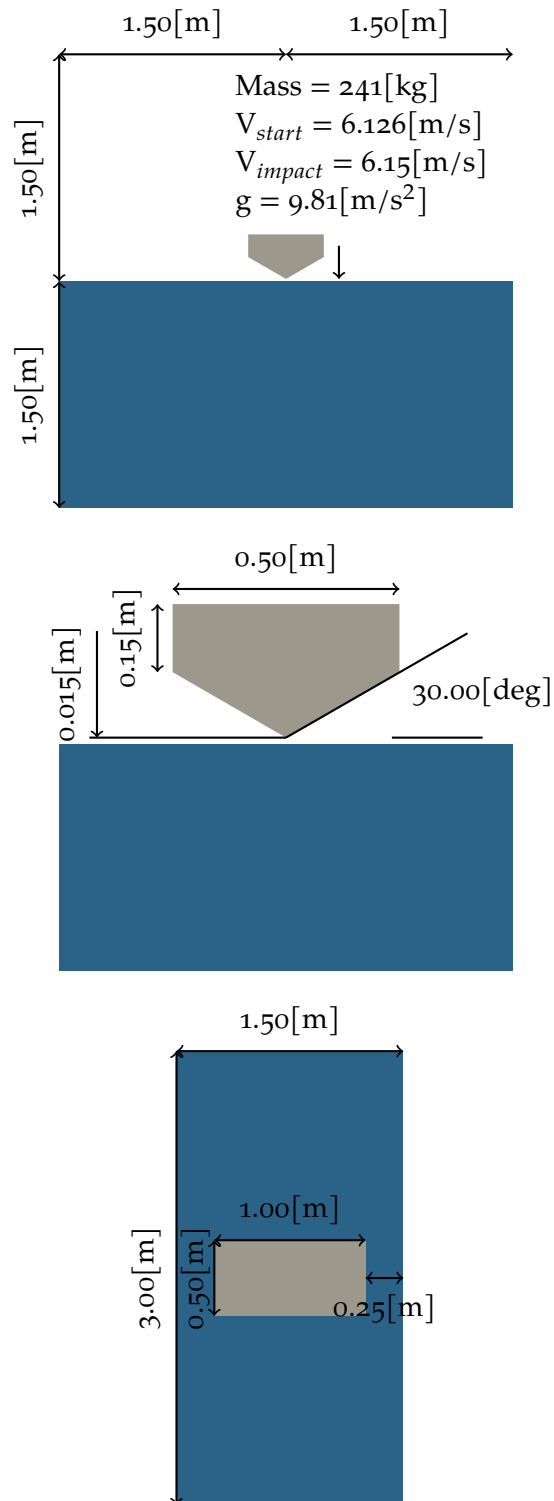


FIGURE 2.2. Domain and dimensions of the wedge in [m].

2.4.1 *Setup wedge entry*

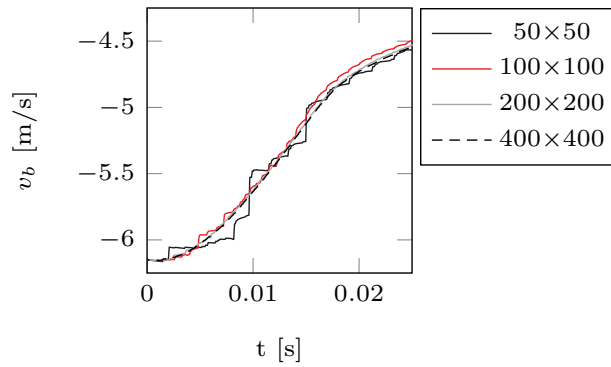
The domain, illustrated in Fig. 2.2, has the same dimensions that were used in the experiment by Zhao, Faltinsen, and Aarsnes [316]. The water depth is 1.5[m]. The free falling wedge moves in vertical direction and has an impact velocity at the water surface of 6.15[m/s]. In the one-phase simulations the wedge is simulated with an initial speed of 6.13[m/s] and a starting location 0.015[m] above the water surface. The initial speed has been calculated using conservation of energy.

For the two-phase flow simulations, the setup is largely the same as with one-phase. In order to investigate the relevance of compressible air on wedge entries, the wedge is positioned 0.1[m] above the water surface to be able to develop the air cushioning effect [27]. Again the initial velocity is calculated using conservation of energy, taking into account a margin for the air resistance. The initial speed is set at 5.99[m/s].

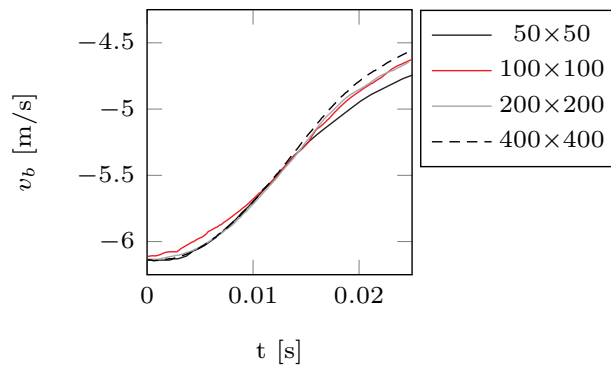
The boundary condition at the top of the domain with air defines the atmospheric pressure. For the simulation it is critical to have a small time step at the time the wedge enters the water surface so that the impact is represented accurately. For all simulations a maximum CFL restriction of 0.7 is used, enforcing smaller time steps when fluid velocities become higher. The time step is never larger than 0.001[s].

2.4.2 *Appropriate grid resolution 2D wedge entry*

In order to determine which grid size is suitable for the simulation of the RIB in the following section, a grid convergence study has been done for the one-phase flow model as well as the two-phase flow model in ComFLOW. In Figs. 2.3a and 2.3b the velocity of the wedge over time is plotted. With the grid 50x50 we capture the width of the RIB with around 8 cells.



(A) One-phase flow.



(B) Compressible two-phase flow.

FIGURE 2.3. Wedge entry: 2D grid convergence

The one-phase flow model shows jumps in the vertical speed which depend on the grid resolution. These jumps in the speed are related to label changes. The label defines whether the free surface conditions in Eqs. 2.5 and 2.6 need to be enforced. The resulting discontinuous pressure in time affects the vertical velocity of the wedge through its equation of motion. The vertical velocity is smoothed by grid refinement due to the smaller effect of local pressures on the global motion. Fig. 2.4 also shows that true grid convergence is not feasible for the discontinuity of the wedge going from dry to wet. This is in agreement with for instance the dam break simulations by Kleefsman et al. [142]. Grid refinement results in new flow features. These features affect the vertical motion, which can be observed for the two-phase 400x400 grid in Fig. 2.3b.

In Fig. 2.4 the free surface deformation due to the wedge entry is shown for different grid resolutions of the one-phase flow simulations. It shows that free surface keeps developing new flow features. For the one-phase flow simulations, however, the flow features do not affect the vertical velocities of the wedge as much as for the two-phase simulations. The computational effort of extrapolating

the finest grid resolution in Fig. 2.3 to 3D is too high to be feasible. For this reason, we choose to focus on representing the motions of the RIB well with 50x50 and 100x100 grid cells in the cross-section of the domain, and accept that the free surface near the ship is underresolved.

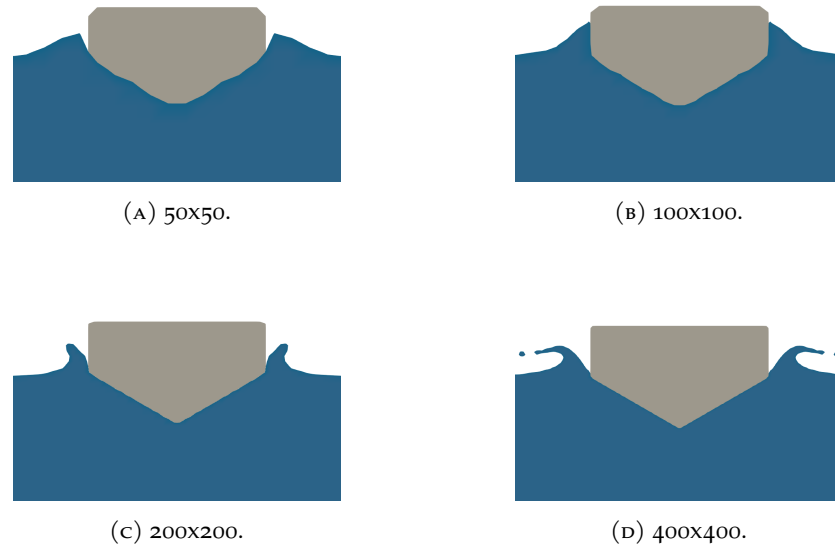


FIGURE 2.4. Wedge entry in water with one-phase model at $t=0.025[s]$.

2.4.3 Comparison one-phase & two-phase flow 2D wedge entry

Fig. 2.3a and Fig. 2.3b show that higher grid resolutions lead to lower differences between the one-phase results. The two finest two-phase results are more different than the two finest one-phase results. The comparison of a wedge entry in one-phase and two-phase for similar resolutions is shown in Fig. 2.5. Where for the one-phase model only the liquid is solved, the two-phase model using extra equations for the density is solved over the entire domain. This makes the two-phase model more computationally expensive. The difference in computational time is a factor 10 approximately. The one-phase results are so close to the two-phase results that it leads to the conclusion that the computational costs outweigh the benefit of including air effects. This conclusion was not unexpected, Faltinsen [86] concluded that the air cushion effect has an influence on the velocity for deadrise angles of only a few degrees whereas the wedge and the RIB in this study have deadrise angles of 30[deg] or larger. Two-phase is also more dissipative for wave propagation [292]. With this in mind we choose to simulate the RIB in 3D without the effect of air.

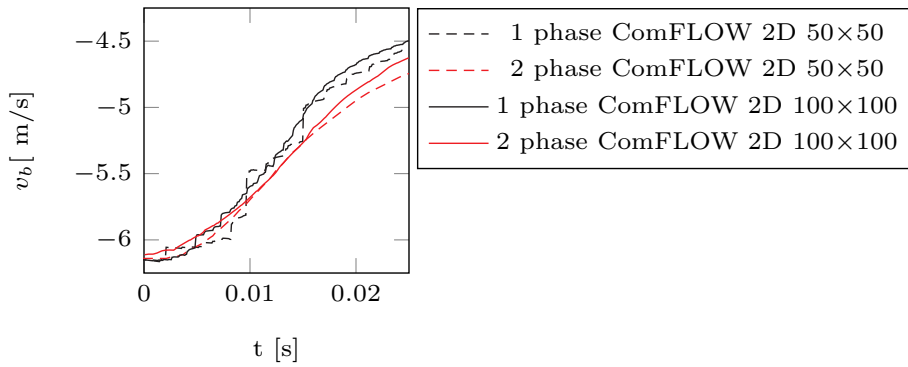


FIGURE 2.5. Wedge entry: comparison of one-phase and two-phase flow in 2D.

2.4.4 Results 3D wedge entry

The comparison of 3D wedge entry simulations on a $50 \times 50 \times 50$ and $100 \times 100 \times 100$ grid with the 3D experiment of Zhao, Faltinsen, and Aarsnes [316] is made in Fig. 2.6. The 3D one-phase flow simulation results overpredict the deceleration compared to the experimental result. However, the 2D simulations in Fig. 2.5 overpredicts the deceleration significantly more. This is a result of the restricted movement of the fluid and 3D effects. This could mean that the deceleration in 2D strip theory simulations of ships in waves is also exaggerated, which would lead to lower motions and inaccurate predictions of the vertical acceleration. Further, the velocity jumps in 3D are smoothed because the local pressure jumps have less effect on the global velocity of the wedge. Fig. 2.6 also shows the 3D one-phase simulation done by Kleefsman et al. [142] with a previous version of ComFLOW using a grid of $60 \times 60 \times 60$. The new ComFLOW results are similar to ones from the previous version.

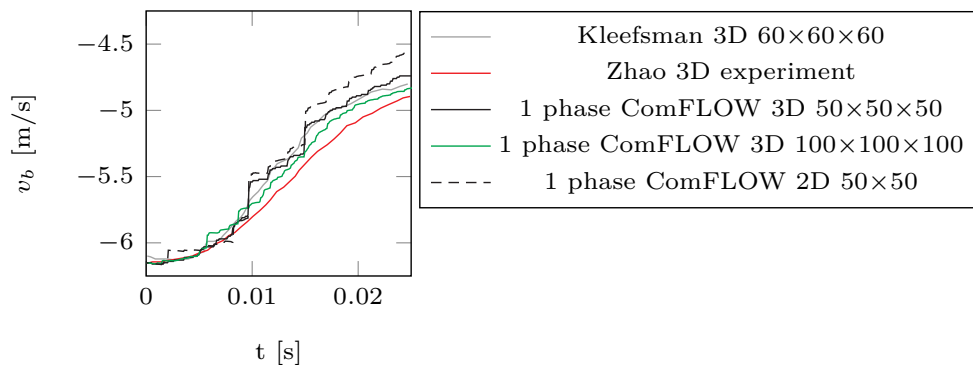


FIGURE 2.6. Wedge entry: comparison of 3D one-phase with experiment.

Based on the investigation with falling wedges, 1 phase simulations with a minimum of 8 cells along the width of the RIB are appropriate to represent its vertical motion behavior.

2.5 3D simulations with Fastship and ComFLOW compared with experiment

An experiment with a RIB was conducted specifically for the purpose of this chapter in the small towing tank of the Ship Hydromechanics Laboratory at Delft University of Technology. The main objective of the experiment was to generate a bow emergence and re-entry event in each run; to that end the highest surface elevation in a sea state defined by a JONSWAP spectrum with a set peak period and significant wave height, would be met by the RIB at the desired velocity in a specific location in the tank. That specific location was 50[m] away from the wave board, where even for the highest velocity it was certain that the boat had accelerated to meet the desired velocity. The setup is illustrated in Fig. 2.7.

2.5.1 Experiment

The RIB model was free to move in heave and pitch, while other motions were kept restrained. The mass of the RIB is 35.26[kg], with the center of gravity (CoG) at 0.57[m] from the aft perpendicular and 0.159[m] from the keel. The radius of inertia for pitch is 0.459[m]. The dimensions of the RIB and the towing tank are given in Tab. 2.1.

TABLE 2.1. Parameters RIB and towing tank.

Length towing tank	85.0	[m]
Width towing tank	2.75	[m]
Water depth	1.203	[m]
Mass model RIB	35.26	[kg]
Length model RIB	1.93	[m]
Width model RIB	0.653	[m]
Length waterline model RIB	1.837	[m]
Width waterline model RIB	0.554	[m]
Height max. model RIB	0.385	[m]
Draft model RIB	0.111	[m]
Scale factor	1:10	[-]

The velocity of the ship and towing carriage was measured using a calibrated wheel that rolls along the side of the rail of the carriage. The position of the ship with respect to the wave board is measured by a high power laser distance meter. The initial position of CoG always equals 71.439 m away from the

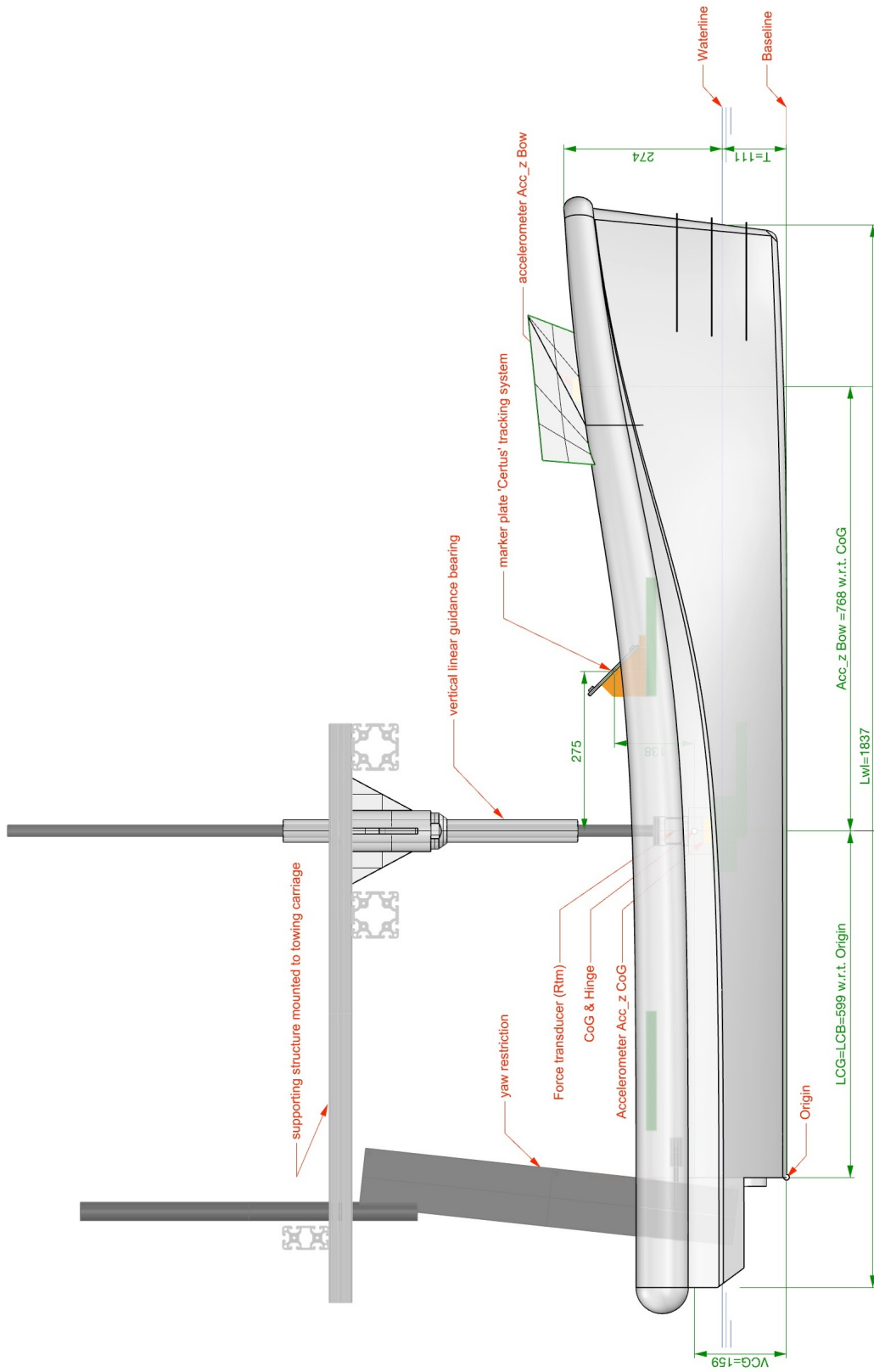


FIGURE 2.7. Experimental model setup as the midship section, dimensions are given in [mm].

wave board. The velocities v_s at which the RIB was towed were 1, 2, 3 and 4[m/s].

The position of the RIB with respect to the towing carriage was measured by means of a Certus optical motion tracking system that uses a marker plate on the model. Heave and pitch of the RIB are found from this system, with an accuracy of 0.1[mm] according to the supplier. Note that the marker plate was not at CoG, so that the heave signal from Certus needed to be transformed to CoG. Two accelerometers were placed on the RIB, one at CoG and one near the bow. The accuracy of the accelerometers was 0.01g according to the supplier.

There was a total of three wave gauges in the tank, of which two were fixed and used to confirm that the desired wave signal was generated by the wave board. They were placed at 18.632[m] and 20.840[m] from the wave board. The maximum difference between the calibration data of the wave gauges and their least square fit was 0.5[mm]. One wave gauge was towed with carriage and ship model to measure the free surface elevation as the ship encounters it. It was placed at 1.858[m] from CoG in front of the bow. The wave gauge was positioned near the side wall of the tank so that it did not disturb the incoming waves.

The width of the towing tank did not affect the results. When in waves, the term $\omega_e v_s / g$ for the lowest velocity $v_s = 1$ [m/s] indicating the significance of side wall effects is close to one. That is sufficiently high above the threshold value of 0.25 that no interference is expected [311]. Interference is only relevant for the comparison between the experiment and Fastship, because there are no side walls in Fastship. The comparison of the experiment with ComFLOW is more direct, because in ComFLOW the side walls of the domain are at the same position as the side walls of the tank. The effect that the bottom of the tank has on the waves is accounted for in both Fastship and ComFLOW.

Two peak periods of the wave spectrum were considered, 1.1[s] and 2.2[s], with the former giving the most interesting results in terms of large motions and bow emergence. The significant wave heights considered ranged from 0.03[m] to 0.14[m], of which the lower wave heights were only used to build up towards bow emergence and re-entry events. Time series of surface elevations ten thousand seconds long were generated from these peak periods and significant wave heights by converting theoretical JONSWAP spectra with peakedness factor 3.3 to the time domain. Of these signals, the largest consecutive maximum and minimum, i.e. the largest wave, was selected. Starting from the time index of the maximum elevation of that largest wave, a wave board signal was generated, making sure that the surface elevation 50[m] away from the wave board would contain all wave components in the time signal at least one peak period before the time of the largest wave, and that no reflection from the spending beach at the end of the towing tank would contaminate the results. The ship started moving at the

specific time required to arrive at the target location when the largest wave would be there too. An overview of the runs with interesting results is shown in Tab. 2.2.

TABLE 2.2. Overview experimental runs. Significant wave height is S.w.h. and Froude number is Fn..

Run #	Velocity [m/s]	Peak period [s]	S.w.h. [m]	Fn. [-]
Run 24	1	0	0	0.24
Run 38	1	1.1	0.10	0.24
Run 40	2	1.1	0.06	0.47
Run 42	2	1.1	0.09	0.47
Run 44	2	1.1	0.10	0.47
Run 46	2	0	0	0.47
Run 48	2	1.1	0.03	0.47
Run 50	3	1.1	0.09	0.71
Run 52	3	1.1	0.09	0.71
Run 54	4	1.1	0.09	0.95
Run 56	2	1.1	0.14	0.47
Run 58	1	1.1	0.10	0.24
Run 60	2	2.2	0.14	0.47

In this chapter numerical results in terms of free surface, heave, pitch and the acceleration at CoG with Fastship and ComFLOW are compared to the runs in the experiment. Heave and pitch in Run 42 as a function of time are shown in Fig. 2.12, the accelerations as a function of time for this run are in Fig. 2.13.

2.5.2 Fastship

Fastship is a strip theory 2D+t method. Runs in Fastship for the purpose of this chapter are performed at full scale with a scale factor of 1:10 between model and prototype due to the coefficients involved. The main input variables that were varied between runs were the velocity and the components of the wave signal with frequencies, amplitudes and phases. The unvarying coefficients that were input to Fastship are given in Tab. 2.3 and obtained by Keuning et al. [138], in which statistics of accelerations in Fastship were calibrated to the statistics of experiments. The geometry of the ship is defined in terms of the position of the keel, the position of the chine and the deck elevation at the perpendiculars shown in the lines plan in Fig. 2.8.

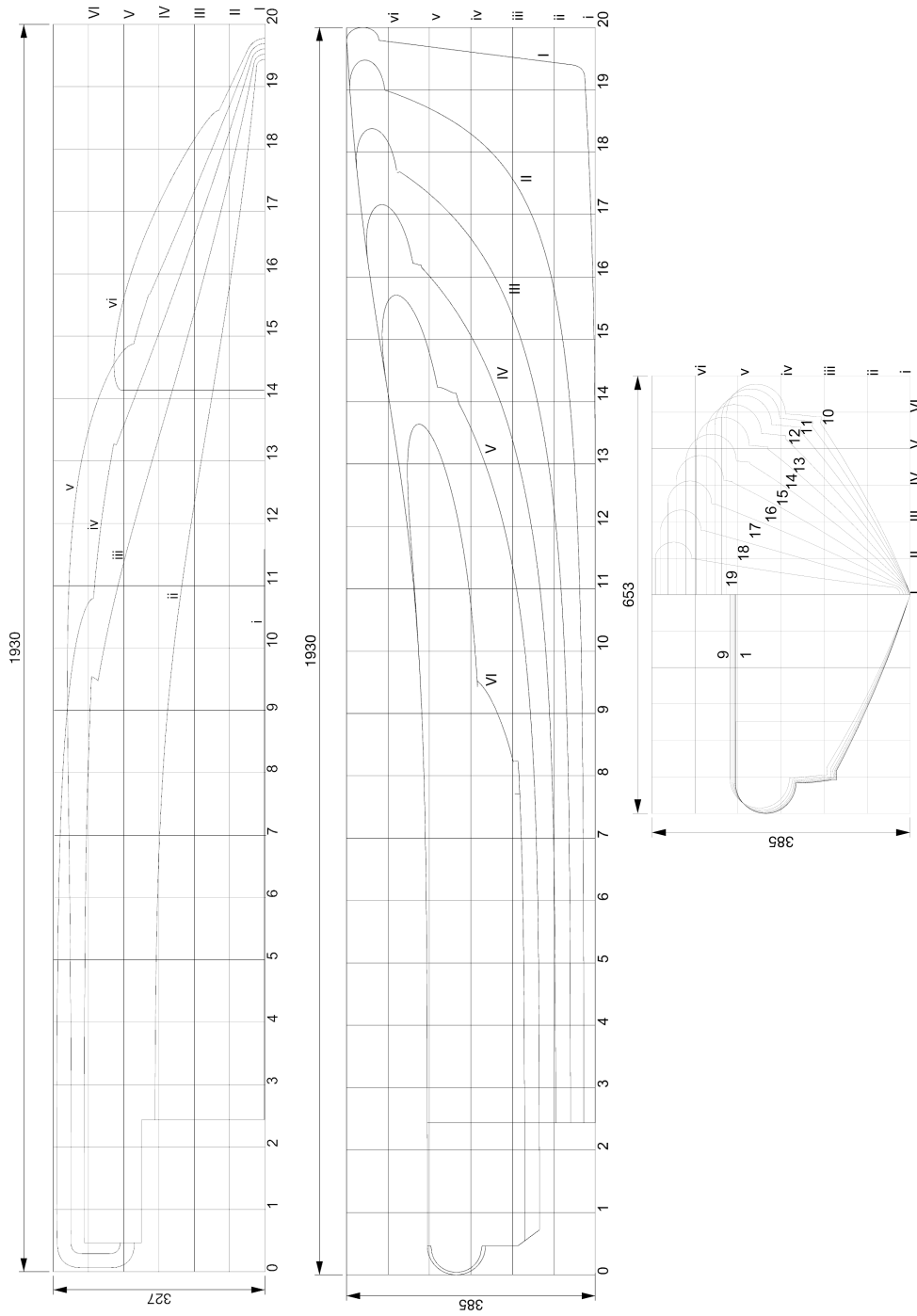


FIGURE 2.8. Lines plan RIB with dimensions in [mm].

TABLE 2.3. Coefficients Fastship.

Geometric metacentre height	3.5	[m]
Cross flow drag coefficient	1.33	[-]
Added mass coefficient	1.1	[-]
Buoyancy correction factor	0.6	[-]
Buoyancy moment factor	1.0	[-]
Critical damping coefficient	0.075	[-]
Iforce (geometry above chines)	1	[-]
Itransom (near transom pressure)	1	[-]
Ideadrise (Cm depends on deadrise)	0	[-]
Ipilup (pileup depends on deadrise)	1	[-]
Time to develop sea state	0	[s]
Total time of run (model scale)	12	[s]
Maximum time step (model scale)	0.03	[s]

Specifically for this chapter, Fastship runs were performed with the wave input from our new experiments. Internally, Fastship uses Airy wave components, together with the complete linear dispersion relation for free surface waves at any water depth.

Fastship requires wave input at CoG. At the position of CoG no waves were measured in the experiment. We used two ways to translate the signal from the signal from the wave gauge that was fixed to the towing carriage: 1. using Airy wave theory and 2. using the Airy components as input to a ComFLOW simulation dedicated to deliver the wave signal at CoG. The difference is that nonlinear interactions between wave components are included in the latter method, but not in the former.

Using only linear Airy theory, the signal of the wave gauge that was fixed to the towing carriage was transformed to its Fourier components to get frequencies, amplitudes and phases. Using the Doppler shifted dispersion relation that accounts for the forward ship speed to get the wave number, the phases were adjusted to account for the distance between the position of the wave gauge and CoG of the ship. Those same Fourier components are used in two ComFLOW simulations, with the open domain boundary at the position of the wave gauge, yielding an output wave signal at the position of CoG. The first ComFLOW simulation, Grid 1, used $\Delta x = 0.08$ [m] or 15 cells per shortest wave length. The second ComFLOW simulation, Grid 2, used twice the number of cells per shortest wave length.

The comparison between using only Airy theory and using the ComFLOW simulations with the two grid resolutions is shown in Fig. 2.9. The differences between

0 and 4[s] are due to ComFLOW ramping up the signal from 0 to the desired output. The difference in the peak at 5[s] between the two ComFLOW simulations is because the dispersion errors of especially the shortest wave components are smaller for the finer grid. The differences between linear Airy theory and the ComFLOW simulations for the time larger than 4[s] are because ComFLOW includes the nonlinear interactions between wave components.

Because the ComFLOW simulations are expected to be a better representation of what the wave signal at CoG in the experiment would have been, the output of the finer ComFLOW simulation at CoG is converted to its Fourier transform as input for Fastship.

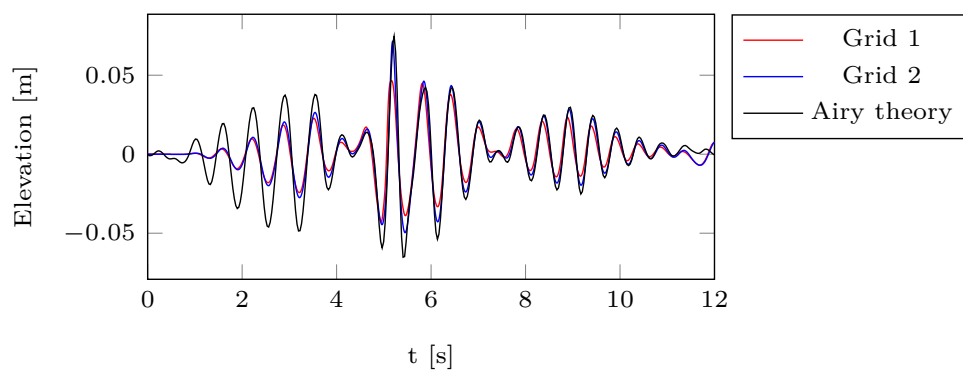


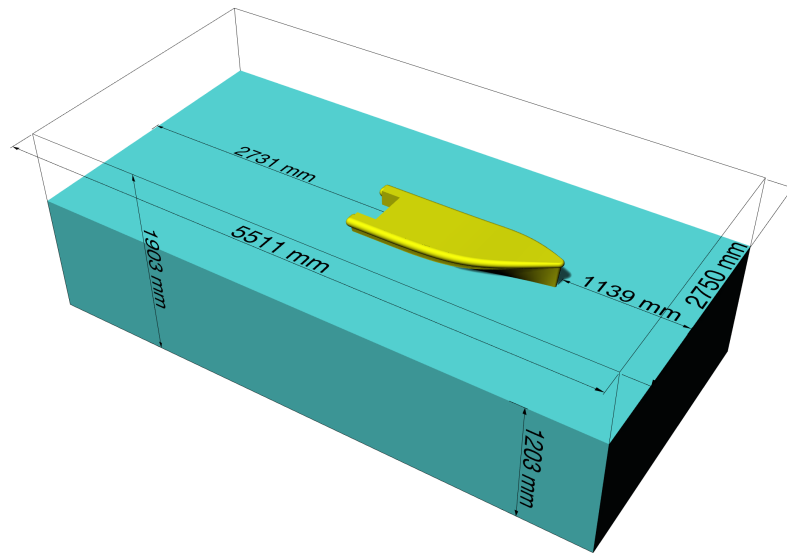
FIGURE 2.9. Free surface elevation in Fastship and 2D ComFLOW simulations at the position CoG (experiment not available).

The heave and pitch motion found with Fastship for run 42 are shown in Fig. 2.12, in which they are compared to the experiment. The axis system in Fastship, with the vertical axis downward, is different from the axis system in the experiment, with the vertical axis upward. The pitch rotation in Fastship is positive anti-clockwise, whereas it is positive in clockwise direction in the experiment. It was found after comparing Fastship output to the experiment, however, that the axis system of the ship in Fastship, positive downward, is inconsistent with the axis system of waves in Fastship, positive upward. For that reason, sinkage and trim from a Fastship run without waves were subtracted from the motion signals. The resulting signal was corrected before being recombined with sinkage and trim. The corrected signals are in Fig. 2.12. The accelerations at CoG are also corrected and visualized in Fig. 2.13, where they are compared to the experiment. It is found from comparing the Fastship motions and accelerations to the experiment, that the overall behaviour is consistent with the experiment. The magnitude of the vertical acceleration is higher around 5[s] and underpredicted in the remainder. The motions are underpredicted over the entire time span.

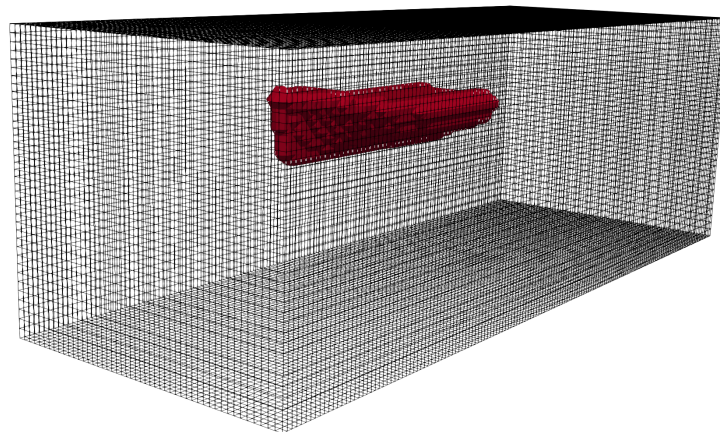
2.5.3 ComFLOW

The dimensions of the ComFLOW domain are based on the results of Wellens [290]. Along the line of wave propagation it is advised to make the domain two typical wave lengths larger than the structure in either direction, to keep the wave absorbing boundary conditions away from splashes and wave breaking near the structure and to allow nonlinear wave interaction to take place between the incoming and reflected wave systems. For this simulation, with forward speed of the RIB it was decided to shift the structure one typical wave length closer to the incoming wave boundary for two reasons. The first reason is because the reflected wave system propagating ahead of the RIB was expected to be small. The second reason is because we wanted to keep the stationary wave system behind the RIB as small as possible near the aft boundary so as not to disturb the wave absorbing boundary condition on that side too much. In x -direction, in the direction of wave propagation, the domain extends from $-2.2[\text{m}]$ to $3.3[\text{m}]$ with CoG of the RIB at $x = 0[\text{m}]$. In transverse direction, the domain is the same size as the towing tank. In vertical direction, the mean free surface coincides with $z = 0[\text{m}]$, with the bottom positioned at $z = -1.203[\text{m}]$ to match the water depth in the experiment and the top of the domain at $z = 0.7[\text{m}]$, sufficiently far away not to interfere with the motions of the ship, nor the free surface. The domain is visualized in Fig. 2.10a.

From the 2D wedge simulations, it was found that 8 and 16 cells along the width of the RIB are sufficient to capture the vertical motion behaviour. In longitudinal direction, there are two requirements to the grid spacing. The grid size cannot be too different from the transverse direction to keep the free surface reconstruction algorithm accurate, and the grid size needs to be small enough to keep numerical wave dispersion and numerical wave dissipation sufficiently small. To keep numerical errors small, there need to be approximately 15 cells in the shortest wave length in the spectrum. The minimum grid sizes in the simulations close to CoG of the vessel are $\Delta x, \Delta y, \Delta z = 0.08, 0.08$ and $0.09[\text{m}]$, with 1% of stretching in y -direction, and 2% in z -direction. This grid gives us 8 cells along the width of the RIB. We call this grid 1. For comparison, a refined grid 2 was used with cells twice as small. Grid 2, having at least 16 cells along the width, including the RIB reconstruction is visualized in Fig. 2.10b. Cut-cells are used for the object, giving a good representation for the wedge shaped ship. We are interested in the global motion and therefore not interested in representing boundary layers around the hull that would require a much higher grid resolution. The maximum CFL number allowed for all ComFLOW simulations is 0.85. The maximum time step varied with the variation of the CFL number and never exceeded $0.001[\text{s}]$.



(A) Computational domain.

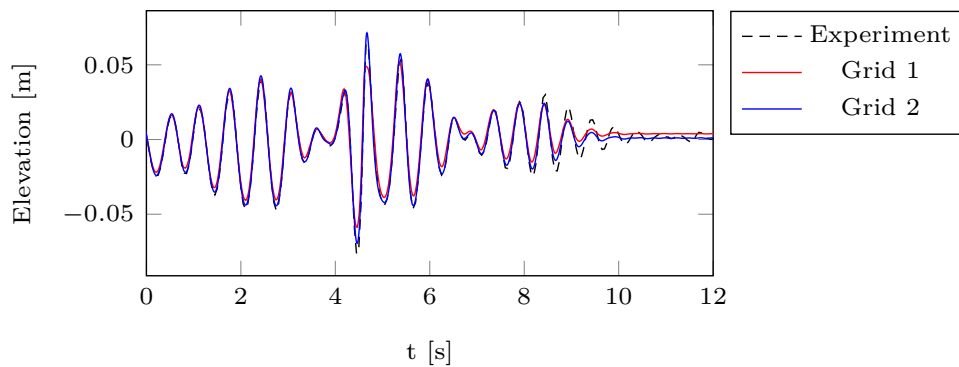


(B) Grid 2 with representation of RIB.

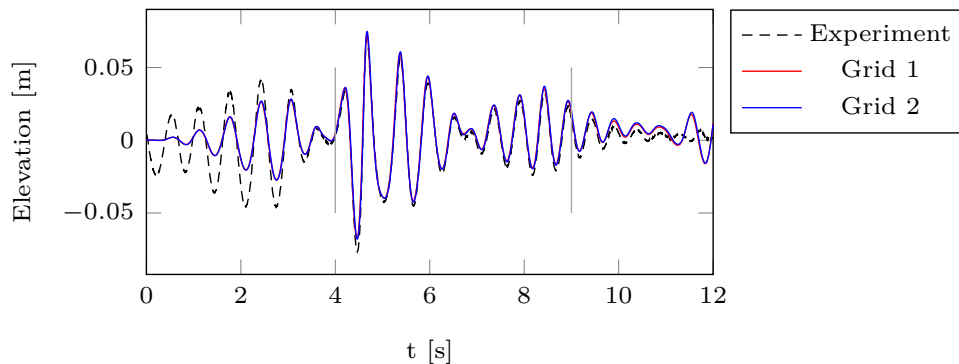
FIGURE 2.10. Snapshots of computational domain and grid.

The default boundary conditions in ComFLOW have been discussed in Sec. 2.2 above. We have performed calm water runs and runs with irregular incoming waves. In order to perform wave simulations, a Dirichlet boundary condition for the horizontal velocity is imposed at the incoming wave boundary, in combination with the Generating Absorbing Boundary Condition described by Wellens

and Borsboom [289]. One advantage of the GABC is that incoming and outgoing wave boundaries can be closer to the object in the domain. The coefficients of the absorbing boundary condition on the incoming and outgoing ends of the domain are $a_1 = 0.573$, $a_2 = 0$ and $b_1 = 0$, making them effectively Sommerfeld boundary conditions tuned to $0.573\sqrt{gh}$, with g the acceleration of gravity and h the water depth. The horizontal velocity is computed from a sum of Airy wave velocity components, which are ramped up from 0 to the obtained velocity signal over approximately 4[s]. The frequencies, amplitudes and phases for the wave components come from the Fourier transform of the signal of the wave gauge connected to the towing carriage. The phases are then corrected with the wave number for each component, multiplied by the position of the resistance type wave gauge in the simulation domain, $x = -1.858$ [m]. To demonstrate that the wave signal at the position of the wave gauge in ComFLOW is the same as in the experiment, those signals are plotted in Fig. 2.11. We will focus on the time span between 4 and 9[s], indicated by the grey markers in Fig. 2.11, because this is the time over which the velocity of the ship is constant.



(A) 2D without RIB at wave probe.



(B) 3D with RIB at wave probe, with markers at 4 and 9[s].

FIGURE 2.11. Free surface elevation comparison.

2.5.4 Comparison results: Calm water simulation

Runs in initially calm water were performed at different ship forward velocities in the experiment, in Fastship and in ComFLOW. Tab. 2.4 shows the velocities and the sinkage and trim for all methods, together with the Froude number based on the length of the RIB. Trim is in good agreement between ComFLOW and the experiment. Sinkage shows the same trend in ComFLOW and the experiment, but there is a small difference. The boundary layer underneath the ship, being dominated by numerical viscosity, is unlikely to have the correct size. This could be an explanation for the difference.

The trim and sinkage found by Fastship are quite different from the experiment. Specifically for Run 46, the sinkage is nearly three times as small as in the experiment and the trim is nearly two times as high. Here, we must make a note that Fastship was never specifically designed for the velocity range in this chapter, but for higher forward ship velocities. A specific calibration for the velocity range in this chapter will likely improve the Fastship results. However, we did not do this because we wanted to remain consistent with the settings used by Keuning et al. [138]. While the difference in sinkage is still under investigation, the difference in trim is most likely due to an incomplete representation of the boxes in the waterline at the stern in Fastship between ordinate 0 and 2 in Fig. 2.8; lack of restoring moment there can cause an overprediction of trim. Mean sinkage and trim is subtracted from the wave signals in the next section. In Fastship, the unsteady motions (heave, pitch) are treated independently from the steady position (sinkage, trim) and an error in the steady position will not lead to additional errors in the unsteady motions.

TABLE 2.4. Comparison steady values Fastship and ComFLOW with experiment (* indicates a failed run).

	Run nr.	Velocity [m/s]	Sinkage [mm]	Trim [deg]
Experiment	24	1	*	*
Fastship	24	1	2.1	0.89
ComFLOW	24	1	4.9	1.61
Experiment	46	2	22.9	2.44
Fastship	46	2	8.0	4.43
ComFLOW	46	2	19.0	2.63

2.5.5 Comparison results: Motion and Acceleration in irregular waves

Runs with waves were performed for different significant wave heights, measuring heave, pitch and the accelerations at the CoG. The runs were done for a depth Froude number of 0.6 and higher and Froude numbers based on length of the RIB as in Tab. 2.1. Mean heave and mean pitch were subtracted from the signals

and the normalized root mean square (rms) difference between the experiment on the one side, and Fastship and ComFLOW (for two grids) on the other was determined according to

$$\epsilon_{nrms} = \sqrt{\sum_{i=1}^n \frac{(\hat{y} - y)^2}{n}} \cdot \frac{1}{\bar{y}}, \quad (2.8)$$

where \bar{y} is the range between maximum and minimum of the simulation results \hat{y} . The motions in Run 42, for which the rms difference between the experiment and ComFLOW is about the mean of all rms differences, are given in Tab. 2.5, among other runs. It is found that the difference between the experiment and Fastship is consistently larger than between the experiment and ComFLOW (for both grids).

TABLE 2.5. Comparison values Fastship and ComFLOW with experiment.

Error [-]	Run nr.	Vel. [m/s]	Fastship	ComFLOW 1	ComFLOW 2
$\epsilon_{nrms,acc}$	42	2	0.146	0.067	0.107
$\epsilon_{nrms,heave}$	42	2	0.198	0.157	0.085
$\epsilon_{nrms,pitch}$	42	2	0.211	0.086	0.052
$\epsilon_{nrms,acc}$	44	2	0.157	0.071	0.097
$\epsilon_{nrms,heave}$	44	2	0.162	0.143	0.117
$\epsilon_{nrms,pitch}$	44	2	0.193	0.092	0.073
$\epsilon_{nrms,acc}$	48	2	0.167	0.068	0.112
$\epsilon_{nrms,heave}$	48	2	0.203	0.145	0.101
$\epsilon_{nrms,pitch}$	48	2	0.223	0.080	0.063

Fig. 2.12 shows heave and pitch of the RIB in the ComFLOW simulation of Run 42, where it is compared to Fastship and to the experiment. Note that mean heave and mean pitch for the Fastship and ComFLOW results have been replaced by the mean heave and pitch in the experiment. From these figures we find that heave and pitch in the simulations are of the same order of magnitude as the experiment, but the difference between Fastship and the experiment is larger than the difference between ComFLOW and the experiment. Fastship consistently underestimates the motions with respect to the experiment. In Sec. 2.4.4 it was also found that the deceleration of 2D falling wedges is larger than that of the 3D falling wedge. It needs to be investigated whether 2D versus 3D, with Fastship being based on strips of 2D wedges, could be an explanation for the lower motions. Acceleration is never truly computed in ComFLOW and therefore not part of the output. The acceleration at CoG in ComFLOW is found from numerical differentiation of the ship velocities in time in combination with a butterworth filter of order 5 with a normalized cutoff frequency of 1/250. The accelerations at CoG are shown in Fig. 2.13. From the figure we find that the vertical accelerations in experiment and simulations are of the same order of

magnitude. The agreement in acceleration between ComFLOW and the experiment is better than the agreement between Fastship and the experiment. Fastship underestimates the vertical acceleration, except for the peak at the time mark of 5[s]. The differences between the results of the different ComFLOW grids are consistent with the differences between results for the wedge, and sufficiently small to trust the results. A visual illustration of the ComFLOW simulation and the experiment for run 42 is shown in Fig. 2.14.

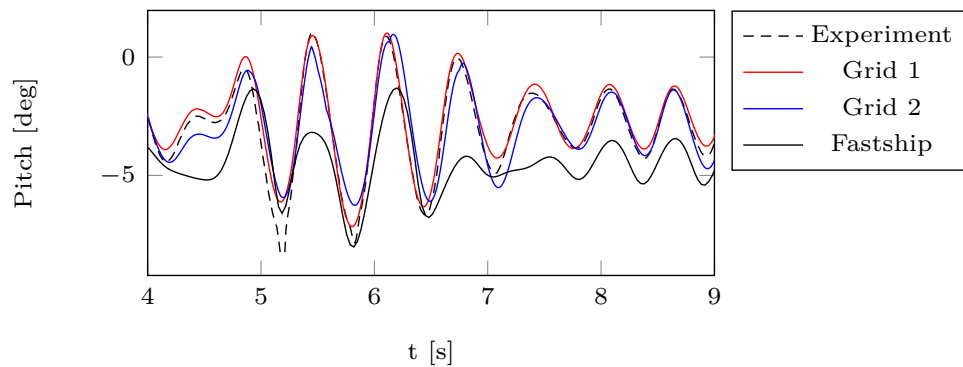
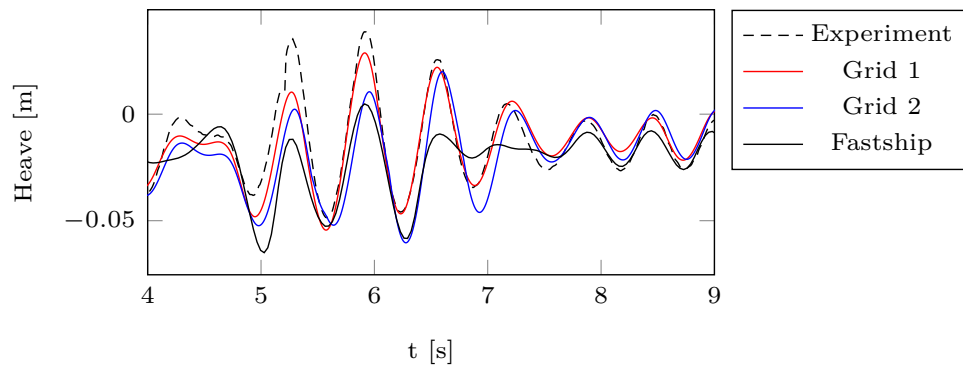


FIGURE 2.12. Numerical motion compared with experimental data.

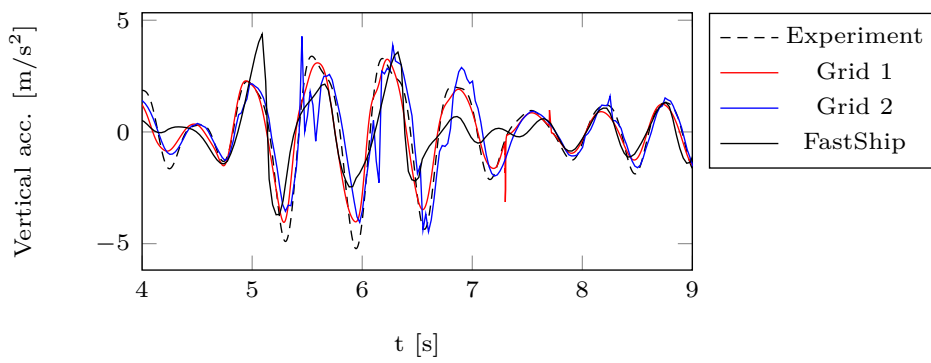
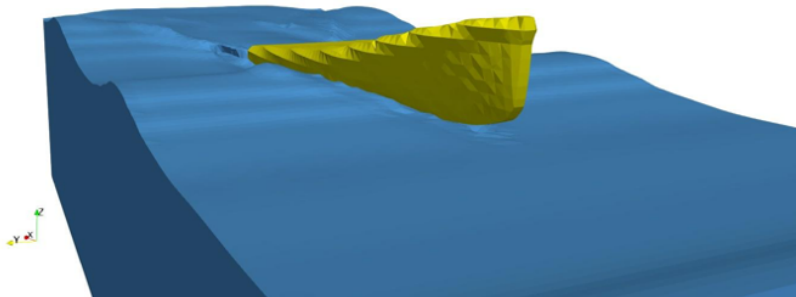


FIGURE 2.13. Comparison of acceleration with experimental data.



(A) Towing tank experiment of the RIB in irregular waves.



(B) 3D numerical simulation of the RIB in irregular waves.

FIGURE 2.14. Visual comparison of the towing tank experiment and the numerical simulation.

2.6 Conclusions

This chapter is about the vertical accelerations during a bow re-entry of a Rigid Inflatable Boat (RIB) in irregular waves. Its main contribution is the complete deterministic comparison in time of the first-principles numerical method COMFLOW with the results of a self-conducted towing tank experiment in terms

of vertical accelerations in irregular waves. The vertical accelerations are also compared with the state-of-the-art strip-theory method Fastship.

The results of the wedge drop test showed that the effect of air on the vertical motion of the wedge is marginal for a 30 degrees deadrise angle, making the one-phase model more suitable to use in terms of computational effort. A minimum of 8 cells along the width of the model is considered appropriate to represent the vertical motion of the wedge and also the RIB in waves.

Using these outcomes, the simulation results with ComFLOW showed an underestimation of the heave and pitch amplitudes with respect to the towing tank experiment. The mean of the rms differences between the experiment and ComFLOW are given in Tab. 2.5. According to Tab. 2.5, the results with Fastship are found to underestimate the motions more than ComFLOW. The simulated accelerations in ComFLOW are hardly different from the experiment. The vertical acceleration from ComFLOW is closer to the experiment than the acceleration from Fastship and showed a relative improvement of at least 20%.

In terms of computational effort, Fastship is faster. Fastship results are finished in mere seconds per run, whereas ComFLOW requires at least 2 hours on a 20-core dedicated machine to complete a run. For ComFLOW, however, no calibration with experiments is required. A model like Fastship will always remain necessary for rapid assessment, but now with ComFLOW we have an additional means to evaluate RIBs in terms of accelerations and to improve models like Fastship.



A COMPRESSIBLE TWO-PHASE FLOW MODEL FOR PRESSURE OSCILLATIONS IN AIR ENTRAPMENTS FOLLOWING GREEN WATER IMPACT EVENTS ON SHIPS

This chapter is reproduced from [75] :

M. van der Eijk and P. R. Wellens. "A compressible two-phase flow model for pressure oscillations in air entrapments following green water impact events on ships." *International Shipbuilding Progress* 66.4 (2019), pp. 315–343

Abstract

A significant part of all structural damage to conventional ships is caused by complex free-surface events like slamming, breaking waves, and green water. During these events air can be entrapped by water. The focus of this work is on the resulting air pockets affecting the evolution of the hydrodynamic impact pressure that loads the ship's structure.

COMFLOW is a computationally efficient method based on the Navier-Stokes equations with a Volume-of-Fluid approach for the free surface, designed to perform multiphase simulations of extreme free surface wave interaction with maritime structures. We have extended COMFLOW with a Continuum Surface Force (CSF) model for surface tension, thereby completing our method for representing gas-water interaction after free surface wave impacts. The implementation was verified with benchmark cases addressing all relevant aspects of the dynamics of entrapped air pockets. The implementation was validated by means of a dambreak experiment, a characteristic model for green water impact events.

The method - having been verified and validated - was applied to a dam break simulation for a different setting in which the impact on a wall leads to an entrapped air pocket. Surface tension was found not to have an influence on entrapped air pocket dynamics of air pockets with a radius larger than 0.08[m]. For wave impacts it was found that the effect of compression waves in the air pocket dominates the dynamics and leads to pressure oscillations that are of the same order of magnitude as the pressure caused by the initial impact on base of the wall. The code is available at: <https://github.com/martin-eijk/2phase.git>.

3.1 Introduction

Hydrodynamic impact loading accounts for more than 10% of structural damage to conventional ships [280]. There are multiple classes of wave impact such as those resulting from slamming, waves breaking against the structure, and green water. In rough seas, large amounts of water can flow over the ship's deck; this is called green water. Green water from the side of the ship has already been recorded to cause damage midships and further aft on several maritime vessels [25, 270]. A green water event is illustrated in Fig. 3.1.



FIGURE 3.1. Green water event after slamming [250].

During green water events involving a complex configuration of the free surface, air and water interact in a way that can lead to entrained air and entrapment of large air pockets. By entrapping an air pocket between the water and the structure, the pocket can have a cushioning effect on the peak pressure on the one hand [22, 212]. On the other hand, it can give an increase of the acting force on the structure during a wave impact [22, 196] and the pressure oscillations in the air pocket can increase pressure levels on the structure being impacted [212] as well as induce resonant fluid-structure interaction [16]. Naval architects are interested in determining these pressures for design.

The pressures on marine structures and parts of these structures can be predicted by modeling the dynamics of both water and the entrapped compressible air. To model the interaction between water and air accurately, a sharp representation of the free surface is needed. One method capable of simulating extreme free-surface flow in a computationally efficient way is ComFLOW, which has been under development for maritime applications since Fekken, Veldman, and

Buchner [89].

ComFLOW, with its most recent implementation described by Wemmenhove et al. [291], is based on the Navier-Stokes equations for the motion of an aggregated fluid with varying properties to model the combination of an incompressible liquid and a compressible gas phase. A fixed Cartesian grid is used with a staggered configuration of variables within a cell. The convective term is approximated with a second-order upwind scheme and the time integration is based on a second-order Adams-Bashforth scheme. The pressure is solved from a Poisson equation, after which the velocity is solved from the newly computed pressure gradients. To describe the free surface the Volume-of-Fluid (VoF) method is used with piecewise-linear line segments to reconstruct the position of the free surface within cells (PLIC). The treatment of the density at the free surface lead to serious errors in the form of so-called spurious velocities [230], which affected the evolution of the impact pressure. A gravity-consistent averaging method for calculating the density at the cell faces was developed to prevent these spurious velocities.

We have made an implementation based on ComFLOW to investigate the effect of surface tension on the dynamics of the pressure in entrapped air pockets during wave impacts. The important aspects to entrapped air pockets are

- the position of the free surface,
- surface tension,
- viscosity,
- compressibility.

The *additional value* of this work is to show the relevance of compressibility of air and surface tension during a wave impact in which an air pocket gets entrapped. The *novelty* of this article lies herein. With respect to Wemmenhove et al. [291] we have

- investigated the difference between piecewise-constant (SLIC) and piecewise-linear representation (PLIC) and the role of gravity-consistent density averaging,
- implemented a surface tension model based on Brackbill, Kothe, and Zemach [19],
- evaluated the effect of the term $\mu \nabla u^T$ that is often omitted in the representation of the diffusive stresses in the momentum equation

to obtain the first complete model for the representation of entrapped air pocket dynamics in wave impact events.

We have performed a verification study with a - to our knowledge - unique set of cases that test all relevant aspects of entrapped air pocket dynamics

- standing capillary waves and an oscillating initially square rod that tests the combined effect of surface tension and viscosity,
- a rising bubble to test for the combination of buoyancy (gravity) and surface tension,
- a shock tube to test for compressibility.

The verified implementation is validated with a dam-break experiment. The implementation having been verified and validated, is used for a dam-break simulation in new setting to quantify the pressure dynamics in an entrapped air pocket. The code is available at: <https://github.com/martin-eijk/2phase.git>.

3.2 Mathematical model

The flow of two phases is modeled as an aggregated fluid with variable properties representing incompressible water and compressible air. By relaxing the pressure of the two phases to a common value, the flow can be described by one continuity equation and one momentum formulation [188]. This assumption leads to a continuous velocity field. The continuity equation is given by

$$\int_V \frac{\partial \rho}{\partial t} dV + \oint_S (\rho \mathbf{u}) \cdot \mathbf{n} dS = 0, \quad (3.1)$$

where \mathbf{u} is the velocity vector $[u, v]^T$, \mathbf{n} is the normal direction to the boundary of the control volume and ρ the mixture density, defined in Eq. (3.8).

The momentum equation in integral form is given by

$$\begin{aligned} \int_V \frac{\partial(\rho \mathbf{u})}{\partial t} dV + \oint_S \rho \mathbf{u} (\mathbf{u} \cdot \mathbf{n}) dS + \oint_S p \mathbf{n} dS \\ - \oint_V \nabla \cdot (\mu (\nabla \mathbf{u} + \nabla \mathbf{u}^T)) - \frac{2}{3} \mu (\nabla \cdot \mathbf{u}) \mathbf{I} dV + \int_V \rho \mathbf{F} dV = 0, \end{aligned} \quad (3.2)$$

p is the relaxed pressure, μ is the dynamic viscosity for a mixture and \mathbf{F} are the body forces for gravity and capillary stresses, $\mathbf{F} = g - \frac{1}{\rho} (\sigma \kappa \mathbf{n} \delta_\Gamma - (\nabla \sigma) \delta_\Gamma)$. The parameter κ indicates the curvature of the free-surface interface, σ is the surface tension coefficient and δ_Γ is a delta function concentrated on the interface Γ between air and water.

The liquid is modeled as incompressible, while the density in the air is allowed to vary. This requires an additional equation with respect to solving the Navier-Stokes equations for incompressible media. Instead of solving for conservation of energy explicitly, an equation of state is used for the air density. The temperature is assumed constant, the air density is assumed barotropic, $\rho_g = \rho_g(p)$, and the polytropic energy equation

$$\frac{\rho_g}{\rho_0} = \left(\frac{p}{p_0} \right)^{\frac{1}{\gamma}}, \quad (3.3)$$

is used to close the system, where the polytropic coefficient $\gamma = 1.4$ for pure air. Instead of using $\rho_0 = \rho^n$, the initial values are used for ρ_0 and p_0 to reduce 'drift' of the pressure [292].

The free-surface indicator function is displaced as follows

$$\frac{DS}{Dt} = \frac{\partial S}{\partial t} + (\mathbf{u} \cdot \nabla)S = 0, \quad (3.4)$$

where $S(\mathbf{x}, t) = 0$ gives the position of the free surface.

All domain boundaries in this article are assumed closed, $\mathbf{u} \cdot \mathbf{n} = 0$ with \mathbf{n} the direction normal to the domain wall, and free slip, $\boldsymbol{\tau} \cdot \mathbf{n} = 0$. The top boundary is used to define a pressure reference.

3.3 Numerical discretisation

3.3.1 Algorithm

The governing equations are discretized by means of a finite volume method on a fixed Cartesian grid with staggered variables. The velocities are defined on cell faces while the density, the pressure and the curvature are defined in cell centers.

Using cell labeling, we distinguish between the liquid phase, the gas phase and representations of structures in the domain. Cell completely filled by structures are labeled B(ody) cells. The cells filled with air are labeled E(mpty) (the E-label name is a residue from when ComFLOW was one phase). Cells with some liquid, adjacent to E-cells are labeled S(urface) cells. All other cells are labeled F(luid) cells. This means that a F-cell never connects with a E-cell. Note that a F-cell is not necessarily completely filled with liquid.

Time integration of the momentum equation is implicit for the pressure, and explicit for the convective and diffusive terms of the momentum equation. The convective and diffusive terms are integrated in time with a second-order Adams-Bashforth scheme. The time discrete versions of the continuity equation is

$$\rho^{n+1} + \delta t \rho^n \nabla \cdot \mathbf{u}^{n+1} = \rho^n - \delta t u^n \cdot \nabla \rho^n, \quad (3.5)$$

and of the momentum equation after substituting the continuity equation

$$\begin{aligned}
\mathbf{u}^{n+1} + \delta t \frac{1}{\rho^n} \nabla p^{n+1} \\
= \mathbf{u}^n + \delta t \mathbf{F}^n \\
- \frac{3}{2} \frac{\delta t}{\rho^n} \left(\nabla \cdot (\rho \mathbf{u} \mathbf{u})^n - \nabla \cdot \left(\mu^n \left(\nabla \mathbf{u}^n + (\nabla \mathbf{u}^n)^T \right) \right) \right) \\
+ \frac{1}{2} \frac{\delta t}{\rho^{n-1}} \left(\nabla \cdot (\rho \mathbf{u} \mathbf{u})^{n-1} - \nabla \cdot \left(\mu^{n-1} \left(\nabla \mathbf{u}^{n-1} + (\nabla \mathbf{u}^{n-1})^T \right) \right) \right),
\end{aligned} \tag{3.6}$$

where n indicates the time level. The substitution for the momentum equation is to remove the densities, to reduce computational cost [292]. By substituting Eq. (3.6) in Eq. (3.5), a Poisson equation for the pressure is obtained

$$\begin{aligned}
\delta t \nabla \cdot \left(\frac{1}{\rho^n} \nabla p^{n+1} \right) = \frac{1 - F_s^n}{\rho^n} \left(\frac{\rho_g^{n+1} - \rho_g^n}{\delta t} + \nabla \cdot (\rho_g \mathbf{u})^n - \rho_g^n \nabla \cdot \mathbf{u}^n \right) \\
+ \nabla \cdot \tilde{\mathbf{u}}.
\end{aligned} \tag{3.7}$$

The term $\tilde{\mathbf{u}}$ is an intermediate velocity, containing contributions of the momentum terms evaluated at time level n and $n - 1$ e.g. the diffusive, convective and body force term. The first part in between parentheses on the right-hand side of Eq. (3.7) corresponds to the compressibility of the aggregated fluid. It represents the Lagrangian derivative of the density. Separately, these terms can be large due to the variety in density of the two phases at the free surface. Together, however, these terms need to be equal to zero for the liquid phase. The density in the cell center at time level n is calculated by

$$\rho^n = \rho_l F_s^n + \rho_g^n (1 - F_s^n), \tag{3.8}$$

where ρ_l and ρ_g are the constant liquid density and the variable gas density, respectively. Because of the constant liquid density within a cell, the Lagrangian derivative of the density simplifies to

$$\frac{D\rho}{Dt} = (1 - F_s) \frac{D\rho_g}{Dt}. \tag{3.9}$$

When the density of the gas is much smaller than the density of the liquid, the contribution of the Lagrangian derivative to the intermediate velocity at the free surface is relatively small. The density of the gas at the next time level is found by solving Eq. (3.3) for $\rho_g^{n+1}(p^{n+1})$. Before the highly non-linear term is transferred to the left-hand side of the pressure in Eq. (3.7), a Newton approximation is used to linearize the term $\rho_g^{n+1}(p^{n+1})$ by eliminating the power $\frac{1}{\gamma}$. The pressure at the new time level is found from the linear system of equations by solving it iteratively with Gauss-Seidel.

The liquid fraction is indicated by F_s and solved using Eq. (5.4) by reconstructing the free surface with SLIC in every cell. The flux through a cell face is calculated as the velocity times the area of the cell face times the time step [142].

3.3.2 Viscosity

Wemmenhove [292], and also Plumerault [212], neglect the term $(\nabla \mathbf{u})^T$ in the viscous term, as is common to do. Wemmenhove et al. [291] do include the term in their mathematical description, but do not evaluate its effect. The effect of neglecting this term is evaluated for the 2D rising bubble case in Sec. 3.5.3. In matrix form the stresses become as follows. For readability the compressible term is left out of Eq. (3.6). For the final simulations in the Results section, the compressible term is included.

$$\begin{bmatrix} \frac{\partial}{\partial x} \tau_{xx} + \frac{\partial}{\partial y} \tau_{xy} \\ \frac{\partial}{\partial x} \tau_{yx} + \frac{\partial}{\partial y} \tau_{yy} \end{bmatrix} = \begin{bmatrix} \frac{\partial}{\partial x} \left(\boxed{2} \mu \frac{\partial u}{\partial x} \right) + \frac{\partial}{\partial y} \left(\mu \frac{\partial u}{\partial y} + \boxed{\mu \frac{\partial v}{\partial x}} \right) \\ \frac{\partial}{\partial x} \left(\mu \frac{\partial v}{\partial x} + \boxed{\mu \frac{\partial u}{\partial y}} \right) + \frac{\partial}{\partial y} \left(\boxed{2} \mu \frac{\partial v}{\partial y} \right) \end{bmatrix}, \quad (3.10)$$

where τ indicates the shear stress. The boxed terms are added when the term $(\nabla \mathbf{u})^T$ is not neglected. As the viscosity is variable around the interface and $\nabla \cdot \mathbf{u} \neq 0$ for air, the term $\nabla \cdot (\mu(\nabla \mathbf{u} + \nabla \mathbf{u}^T))$ is not equal to $\nabla \cdot (\mu \nabla \mathbf{u})$ as assumed by others [212, 292].

The dynamic viscosities at the top and bottom of the staggered control volume in horizontal direction are needed to find the derivative, see Fig. 3.2. These are found by linear interpolation between the corner point viscosity values $\mu_{n,w}$ and $\mu_{n,e}$, $\mu_{s,w}$ and $\mu_{s,e}$ respectively. These corner point values between adjacent cell centers are found by harmonic averaging [212]. For computing the local average viscosity at a pressure point, Eq. (3.8) is used for $\mu(F_s, \mu_l, \mu_g)$, where μ_l is the dynamic viscosity of the liquid and μ_g of the gas.

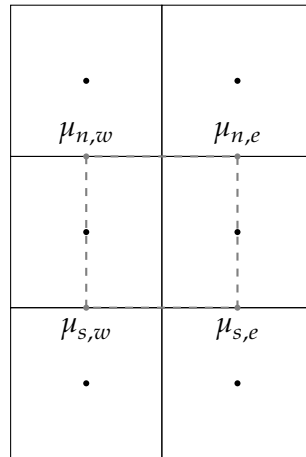


FIGURE 3.2. Corner points of μ for horizontal staggered control volume.

3.4 Free-surface displacement

The free surface is displaced with the discretization of Eq. (5.4) using F_s by calculating the fluxes at the cell faces. In Wemmenhove et al. [291] the free surface is reconstructed with piecewise-linear interface reconstruction (PLIC). For this article, we evaluate piecewise-constant interface representation (SLIC), with grid-aligned interfaces, and compare to PLIC, because of the significantly lower computational cost for almost the same accuracy in situations with highly distorted free surfaces such as wave impact simulations. This is in agreement with the results in Sec. 3.5.5.

3.4.1 Local height function

SLIC has flotsam and jetsam (small droplets disconnecting from the surface) as major drawback. As a remedy, SLIC is combined with a local height function, consisting of three cells around the S-cell in all axis directions [97]. Instead of updating the volume fraction of the S-cells separately, the height function is updated, after which the water is redistributed depending on its original surface orientation. With a local height function flotsam and jetsam are practically absent from simulations. We use the same height function to assess the local curvature for the application of surface tension.

3.4.2 Curvature

To implement surface tension, the curvature κ needs to be calculated in every center of a S-cell. To calculate the mean curvature, the local height function based on the surface orientation is used [142]. The grid-aligned free surface orientation is determined by rounding the gradient of the height function. When the free surface is oriented in x-direction (i.e. horizontally), the curvature for the free surface can be calculated from (see Fig. 3.3)

$$\kappa_c = \frac{1}{\delta x_c} \left(\frac{\frac{\partial H_{y,e}}{\partial x}}{\sqrt{1 + \left(\frac{\partial H_{y,e}}{\partial x}\right)^2}} - \frac{\frac{\partial H_{y,w}}{\partial x}}{\sqrt{1 + \left(\frac{\partial H_{y,w}}{\partial x}\right)^2}} \right), \quad (3.11)$$

where

$$\frac{\partial H_{y,e}}{\partial x} = \frac{H_{y,e} - H_{y,c}}{\frac{1}{2}(\delta x_e + \delta x_c)} \quad \text{and} \quad \frac{\partial H_{y,w}}{\partial x} = \frac{H_{y,c} - H_{y,w}}{\frac{1}{2}(\delta x_w + \delta x_c)}.$$

The curvature can be determined from the height function in a similar way when the free surface is oriented in y-direction (i.e. vertically), but then with grid distances δy and the appropriate values for the height function.

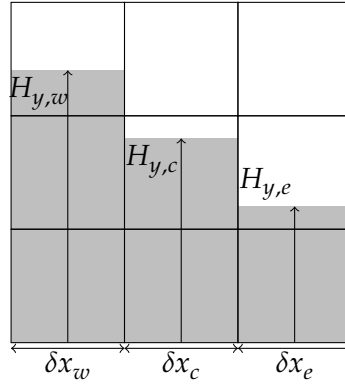


FIGURE 3.3. Notation for curvature κ .

3.4.3 Gravity-consistent density interpolation

Like the pressure, the density is defined at cell centers. In the discretization of the governing equations, the density is also needed at the cell faces. Several alternatives for calculating the density at cell faces are available. We employ a cell-weighted average of the adjacent-cell center values, see Fig. 3.4

$$\rho_f = \frac{\delta x_w \rho_w + \delta x_e \rho_e}{\delta x_w + \delta x_e}, \quad (3.12)$$

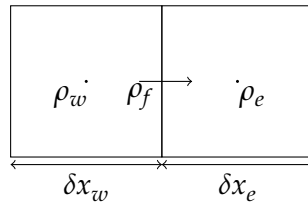


FIGURE 3.4. Notation for cell-weighted averaging.

It is demonstrated by several authors [92, 107, 230, 291] that this method leads to spurious velocities around the free surface. From the perspective of offshore applications where the gravity force dominates, spurious velocities are caused by an imbalance between gravity and the pressure gradient. To balance these forces, both terms need to be discretized in the same way. The requirement $\nabla \times (\rho \mathbf{g}) = 0$ can be found from the momentum equation. To solve in a way that meets the requirement, Wemmenhove et al. [291] came up with a gravity-consistent method (without reference to whether it is applicable for SLIC)

$$\rho_{i,j-\frac{1}{2}} = \frac{d_1 \rho_l + d_2 \rho_g}{d_1 + d_2}, \quad (3.13)$$

where d_1 and d_2 are the distances to the free surface, see Fig. 3.5.



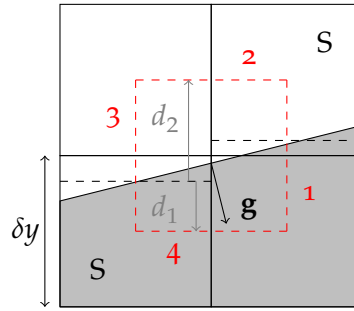


FIGURE 3.5. SLIC (dashed lines) of interface for density interpolation to cell faces.

Using Fig. 3.5, one can derive the limitations of both interpolation methods. In the case of cell-weighted averaging, the position of the interface is not taken into account. This can increase the spurious velocities following the imbalance of forces. However, residuals never become larger than 14% of $\rho\mathbf{g}$. The maximum residuals are found in between non-adjacent S-cells (a S-cell connected with an E-cell, and a S-cell below or above the E-cell).

Applying the gravity-consistent averaging method with SLIC, it prevents spurious velocities in many, but not all circumstances. Especially near cells with volume fractions of 0.5, the gravity-consistent method gives large errors in combination with SLIC. This because of the lower accuracy of the free surface reconstruction compared to PLIC. As an example, the requirement $\nabla \times (\rho\mathbf{g}) = 0$ rewritten in integral form $\int \rho\mathbf{g}dS = 0$ is calculated, assuming that both S-cells in Fig. 3.5 have a volume fraction of nearly 0.5 with the same free surface orientation. This is worked out with numbers in Tab. 3.1; it gives the sum of $\rho\mathbf{g}$ over the dashed red lines, using a gravity vector of $\mathbf{g} = [-10,-10]^T$ [m/s²] perpendicular to the free surface. The non-zero residue of the gravity-consistent method in Tab. 3.1 yields spurious velocities, whereas the cell-weighted method of density averaging does not. Note that besides the free surface configuration illustrated in Fig. 3.5, there are many other configurations that have non-zero residues, leading to spurious velocities.

TABLE 3.1. Cell-face densities multiplied by the gravity and the normal direction of the dashed line for Fig. 3.5

	Gravity-Consistent	Cell-Weighted
$(\rho g_y)_1$	-10,000	-7,500
$(\rho g_x)_2$	-10	-2,500
$(\rho g_y)_3$	10	2,500
$(\rho g_x)_4$	5,000	7,500
$\oint \rho\mathbf{g}$	-5,000	0

The effect of the residuals in Tab. 3.1 is illustrated in Fig. 3.6 for a domain size of $1[m] \times 1[m]$, 30×30 cells, and the orientation of the gravity vector and free surface mentioned above. The maximum spurious velocity reached after 3[s] using the gravity-consistent method is $0.4[m/s]$ while using cell-weighted density method a maximum velocity of $1 \cdot 10^{-9}[m/s]$ is obtained. It was found that gravity-consistent density averaging combined with SLIC produces spurious velocities, just like cell-weighted averaging. The errors for cell-weighted density averaging appear to be smaller and more similar for different free surface configurations than gravity-consistent density averaging. For this reason, combined with the fact that it requires less computational effort, we chose cell-weighted averaging together with SLIC for the remainder of this article.

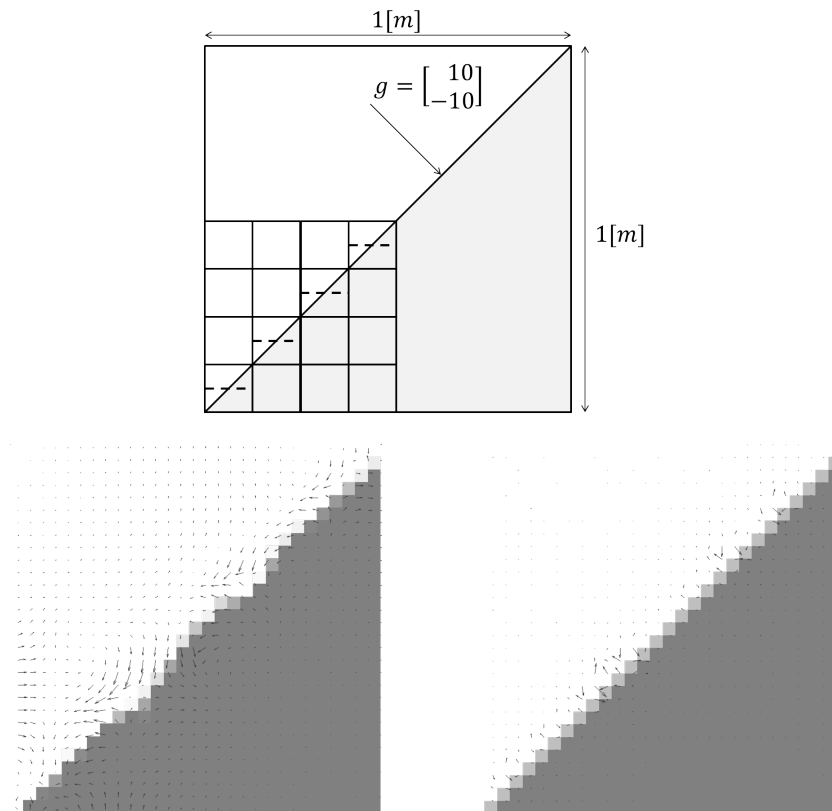


FIGURE 3.6. Liquid fraction- and velocity field: (b) gravity-consistent averaging (max. $0.4[m/s]$) versus (c) cell-weighted averaging (max. $1 \cdot 10^{-9}[m/s]$).

3.4.4 Capillary forces

Because we chose an aggregated-fluid approach to keep computational costs in check, the capillary force is added to the momentum equation as a body force. Two options considered for the implementation of the body force are Continuum Surface Force (CSF) [19] and Sharp Surface Force (SSF) [92]. Of the two, SSF is formally more accurate, but CSF is less involved and has similar practical

accuracy, because the error resulting from the imbalance between pressure and surface tension is dominated by how the curvature of the free surface is estimated [1].

The density in CSF is averaged between phases ($\tilde{\rho} = \frac{1}{2}(\rho_l + \rho_g)$) to reduce spurious velocities in high density ratio flows [19]. The delta function δ_Γ in **F** below Eq. (5.3) is equal to $|\nabla F_s|$ and the surface tension coefficient σ is assumed constant. The force is discretized over a (momentum) control volume consisting of two half (continuity) cells where either cell can have a surface orientation with a certain curvature. It was demonstrated by Francois et al. [92] that a face-centered CSF implementation performs better than a cell-centered one. Our discretization of $\int_V \frac{1}{\rho^n} \mathbf{F}_\sigma^n dV$ in horizontal direction becomes

$$-\frac{1}{\tilde{\rho}^n} \sigma \kappa_f (F_{s,e}^n - F_{s,w}^n) \delta y_c, \quad (3.14)$$

where,

$$\kappa_f = \begin{cases} (\kappa_w + \kappa_e)/2, & \text{if } \kappa_e \text{ and } \kappa_w \text{ are defined} \\ \kappa_w, & \text{if } \kappa_e \text{ is not defined} \\ \kappa_e, & \text{if } \kappa_w \text{ is not defined} \end{cases}.$$

The subscripts indicate the position of the variable in the staggered control volume. An example is shown in Fig. 3.7, where in this case $\kappa_f = \kappa_e$.

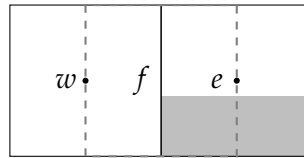


FIGURE 3.7. Cell face value of κ when using SLIC.

3.5 Verification and validation

Our implementation is verified with several cases chosen to test for all essential aspects of the dynamics of entrapped air pockets. They are: a 2D standing viscous capillary wave to compare the interaction of surface tension and viscosity near the free surface to an analytical solution; a 2D planar oscillating rod to compare the same interaction along the circumference of a circle with a benchmark; a 2D rising bubble to compare the interaction of buoyancy (gravity) and surface tension to a benchmark; and a 1D shock tube to compare the effect of compressibility after impacts to an analytical solution.

3.5.1 2D standing viscous capillary wave

Standing wave simulations can be used to assess the performance of the numerical method for free-surface waves. All important free-surface dynamics are included, while the domain is conveniently limited [290]. Standing capillary waves are driven by surface tension. We simulated them with zero gravity to verify the CSF model used for the representation of surface tension described in Sec. 3.4.4.

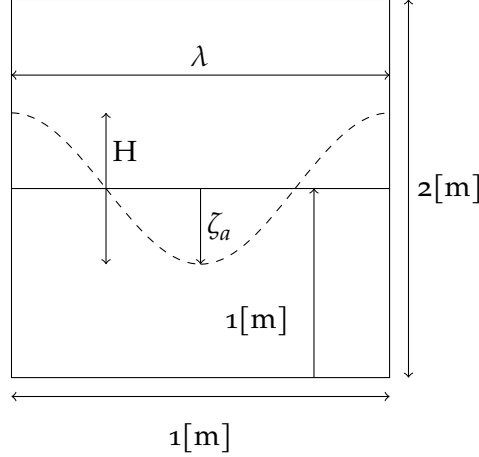


FIGURE 3.8. Setup for simulation of capillary wave.

The setup with a domain of 1[m]×2[m] is shown in Fig. 3.8. The density and the dynamic viscosity of the compressible air is $\rho_g = 1[\text{kg}/\text{m}^3]$ and $\mu_l = 0.01[\text{kg}\cdot\text{m}/\text{s}]$. The density and viscosity of the liquid are varied in three simulation. The dispersion relation for a non-viscous capillary wave at zero gravity is given by [152]

$$\omega_0^2 = \frac{\sigma}{\rho_l + \rho_g} |k^3|, \quad (3.15)$$

where the wave number k is equal to 2π over the wave length $\lambda = 1[\text{m}]$. The initial wave height H in all simulations is $0.01[\text{m}]$. The time step limit for the simulation of capillary waves is given by [19]

$$\delta t \leq \sqrt{\frac{\rho \delta x^3}{4\pi\sigma}}. \quad (3.16)$$

The analytical solution by Prosperetti [218] is used to compare the numerical results to, as done also by e.g. Dodd and Ferrante [67] and Dong and Wang [68]. Note that the solution can only be used when the kinematic viscosity is the same for both fluids. Two ratios of density and dynamic viscosity of the liquid are used, indicating the ratio of top layer over bottom layer: $\bar{\rho} = \rho_g/\rho_l$ and $\bar{\mu} = \mu_g/\mu_l$. By varying these ratios, three sets of numerical results are compared to the analytical solutions. A CFL number of 0.01 is used to keep advection errors

small [9]. The results for $\sigma = 1[\text{N/m}]$ are shown in Fig. 3.9. The numerical results are almost identical to the analytical solution of Prosperetti [218], which verifies the method for the effect of surface tension. The period is almost the same as the inviscid solution in Eq. (3.15) if one considers that viscosity makes the wave period slightly larger.

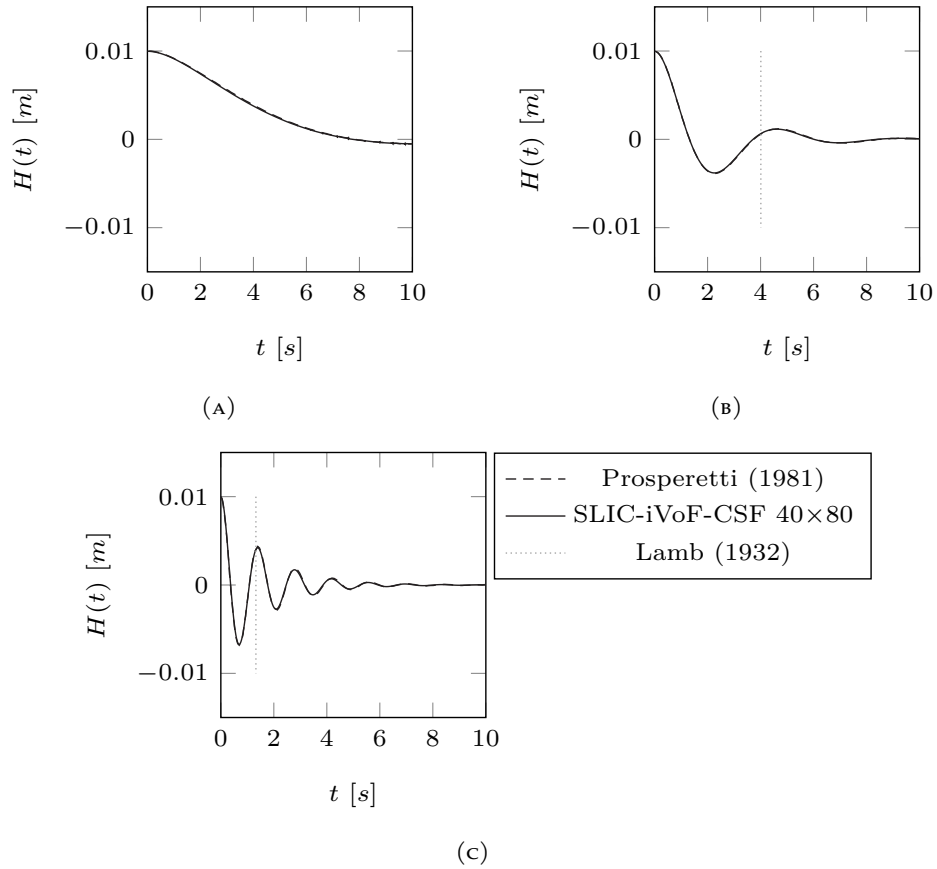


FIGURE 3.9. Capillary standing wave for different ratios compared with analytical solutions (A) $\bar{\rho}$ and $\bar{\mu} = 1,000$; (B) $\bar{\rho}$ and $\bar{\mu} = 100$; (C) $\bar{\rho}$ and $\bar{\mu} = 10$.

3.5.2 2D planar oscillating rod

Another test case for the CSF model is an initially square 2D planar rod of liquid in gas where oscillations are generated by capillary forces. This case has a direct relation to an oscillating air pocket entrapped by a wave impact. Our numerical results are compared with the results of Svihla and Xu [255] who used ANSYS Fluent.

For the simulation, a square of liquid with an area of $4 \cdot 10^{-4}[\text{m}^2]$ is used. This 2D square should become, due to the capillary forces, a 2D circle with a diameter of approximately $2.26 \cdot 10^{-2}[\text{m}]$. The surface tension coefficient in the simulations

equals $\sigma = 2.36 \cdot 10^{-2} [\text{N/m}]$. The domain size is $0.04 [\text{m}] \times 0.04 [\text{m}]$ with 40 equally spaced cells in both directions. A fixed time step of $1.0 \cdot 10^{-3} [\text{s}]$ is used. The liquid density and gas density are unvarying and equal to $\rho_l = 790 [\text{kg/m}^3]$ and $\rho_g = 1.2 [\text{kg/m}^3]$, respectively. The dynamic viscosity of the gas and liquid phase is $1.0 \cdot 10^{-3} [\text{Pa}\cdot\text{s}]$. These settings were also used by Svihla and Xu [255]. A major difference is that we used 1,600 cells, where they used 25,262 prism elements.

The simulation results are presented in terms of diameter as a function of time, shape of the rod and the pressure. The change of the rod diameter over time is compared with the results of Svihla and Xu [255] in Fig. 3.10.

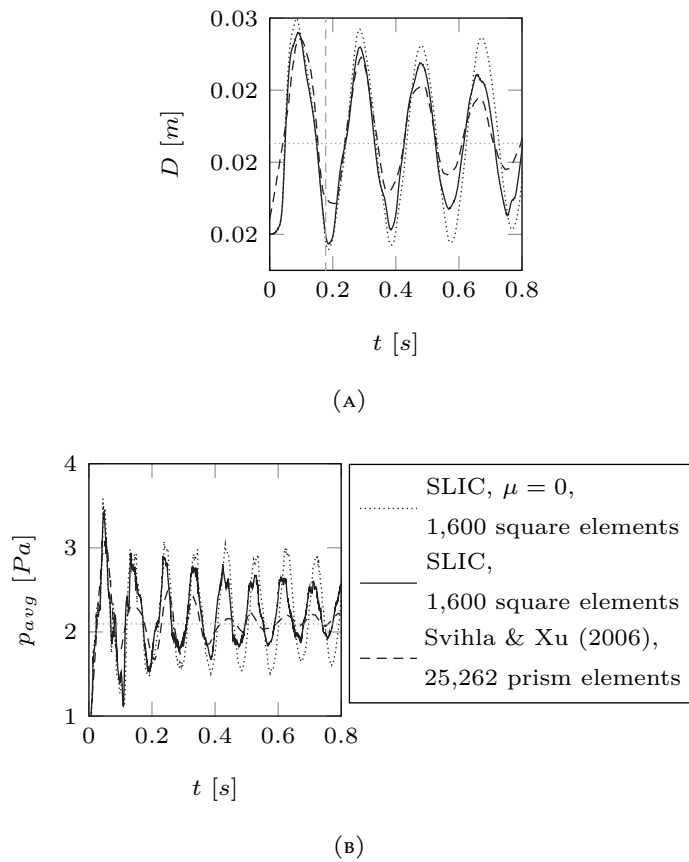


FIGURE 3.10. (A) Diameter and (B) average pressure of the bubble over time compared with Svihla and Xu [255].

The figure shows that the diameter oscillates towards the theoretical diameter and that the oscillations decrease over time as a result of both physical and numerical dissipation (the latter becoming less with grid refinement). The pressure in the bubble at equilibrium should be equal to $2\sigma/D = 2.09 [\text{Pa}]$. The pressure in Fig. 3.10 converges to a value somewhat higher than the analytical value due to

a systematic error made for the curvature [223]. Renardy and Renardy [223] showed that the integral effect of the curvature converges to a value different than the analytical value. This is also confirmed by the results of Deshpande, Anumolu, and Trujillo [59] for an initially static 2D droplet. According to Ham and Young [106], in the inviscid limit, the angular frequency of oscillation for a 2D planar rod is given by Lamb [152] as

$$\omega^2 = (n)(n^2 - 1) \frac{8\sigma}{(\rho_l + \rho_a)D^3}, \quad (3.17)$$

where n is the mode of oscillation, equal to 4 for an initial square. This results in an oscillation period of ≈ 0.178 [s]. The period in our numerical results is smaller than 2% different from the analytical value, which we attribute mostly to the presence of viscosity in our model.

In Figs. 3.11 and 3.12 the volume fraction and pressure over time are compared. Note that a different color scale is used than by Svihla and Xu [255], but these graphs are presented to demonstrate that our shape and our pressure maxima and minima match with their results, especially at the beginning. There is less of a match in Fig. 3.12(e). This is because the size of the oscillations in our method did not attenuate by the same amount as for Svihla and Xu [255] at the time of the snapshot; our method has less dissipation. The same conclusion is found from Fig. 3.10.

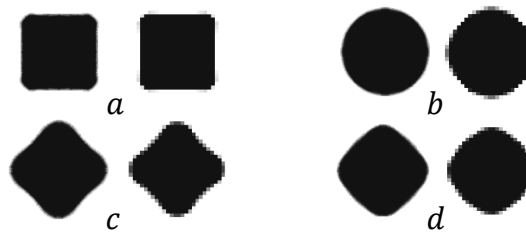


FIGURE 3.11. Volume fraction against time compared with Svihla and Xu [255] (left); (a) 0.01[s], (b) 0.05[s], (c) 0.09[s], (d) 0.13[s].

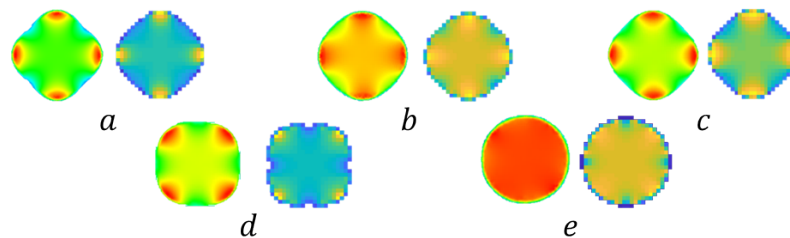


FIGURE 3.12. Pressure against time compared with Svihla and Xu [255] (left); (a) 0.49[s], (b) 0.51[s], (c) 0.67[s], (d) 0.75[s], (e) 0.79[s].

3.5.3 2D rising bubble

The following test case is for the combination of buoyancy (gravity), viscosity and surface tension. Our results are compared with the benchmark for a rising bubble [123]. This benchmark was created due the absence of analytical solutions and used for quantitative comparison of incompressible interfacial flow codes. The initial fluid configuration of the 2D rising bubble test case is shown in Fig. 3.13.

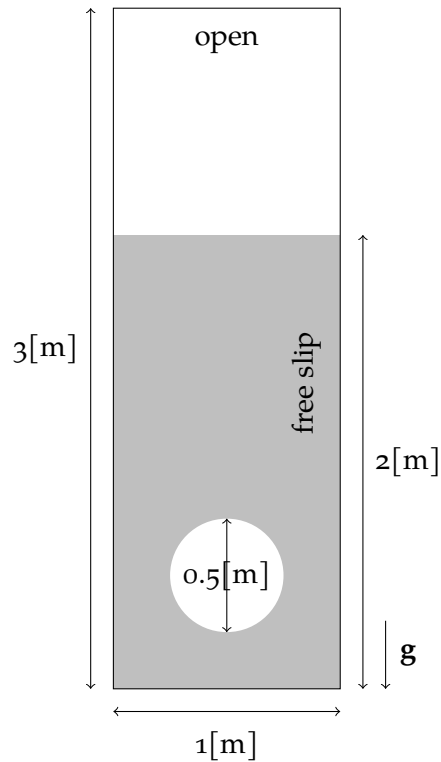


FIGURE 3.13. Flow domain for 2D rising bubble.

In the benchmark, both water and air are incompressible. The density of the water and air are $1,000[\text{kg}/\text{m}^3]$ and $100[\text{kg}/\text{m}^3]$, respectively. Further parameter values are shown in Tab. 3.2.

TABLE 3.2. 2D Rising bubble parameter variations. Simulation 3 corresponds to the benchmark values

Test	μ_w [$\frac{kg}{ms}$]	μ_a [$\frac{kg}{ms}$]	σ [$\frac{N}{m}$]	Re [-]
Benchmark	10	1	24.5	35
①	0.01	$1 \cdot 10^{-3}$	0	$35 \cdot 10^3$
②	0.01	$1 \cdot 10^{-3}$	24.5	$35 \cdot 10^3$
③	10	1	24.5	35

The spatial mean rise velocity v_c is found from the simulations and compared with the benchmark. It is calculated as

$$v_c = \frac{\int_{V_b} v dV}{\int_{V_b} dV} = \frac{\sum_b v \cdot (1 - F_s)V}{\sum_b (1 - F_s)V}, \quad (3.18)$$

where V_b is the volume of the bubble region, V the cell size, and b the number of cells which are covered by the bubble.

Before making the comparison between our implementation, the results of Wemmenhove et al. [291] and the benchmark, we investigated the setup with parameter variations. These simulations are indicated in Tab. 3.2 with numbers ranging from 1 to 3. For these simulations, a grid of 40×120 cells was used. Fig. 3.14 shows the spatial mean velocity of the rising bubble for the three simulations. Fig. 3.15 shows the different rising bubble geometries.

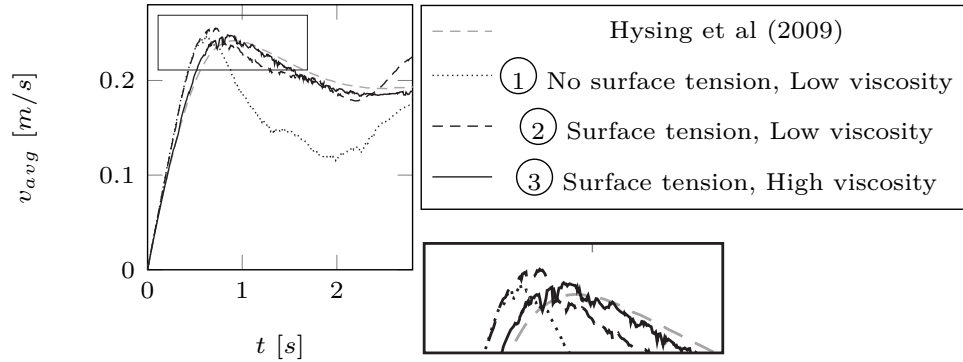


FIGURE 3.14. Spatial mean velocity for all the rising bubble cases using the original method ComFLOW with a grid size of 40×120 .

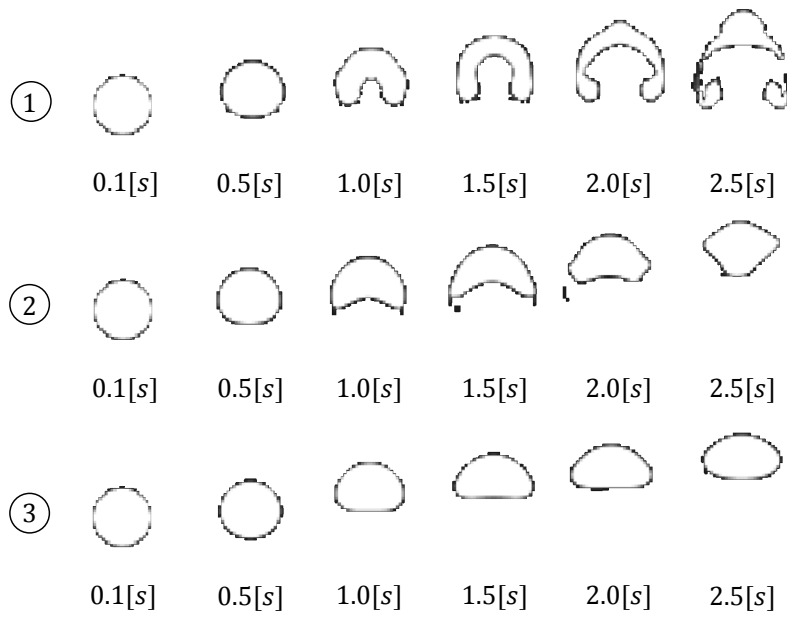


FIGURE 3.15. Snapshots of the 2D rising bubble in order of time for the three cases given in Tab. 3.2.

From the figures, we find that the evolution of the spatial mean velocity and the geometry of the bubble are highly dependent on surface tension and viscosity. Without surface tension (simulation 1), the rising velocity after the penetration of the jet is lower than with surface tension, because the bubble becomes wider as it rises. With a high surface tension for simulation 2, the bubble does not become as wide and does not slow down as much. The bubble reaches a higher maximum velocity and the bubble's acceleration (after 2.2[s]) occurs earlier in simulation 2 than in simulation 3 due to larger viscous stresses in simulation 3. Simulation 3 has the same parameters as the benchmark.

With the implementation in Wemmenhove [292], we found by varying parameters, that we were never able to capture the benchmark's spatial mean velocity when it is at maximum. After more careful consideration, it was concluded that the viscosity model was incomplete. Upon adding the boxed terms in Eq. (3.10) a better comparison with the benchmark was obtained. This is demonstrated in Fig. 3.16. With the same grid size of 80×240 and only the implementation of the missing viscous stress components, the difference in mean spatial velocity with the benchmark was reduced from 3.0% [292] to 0.3% (present implementation).

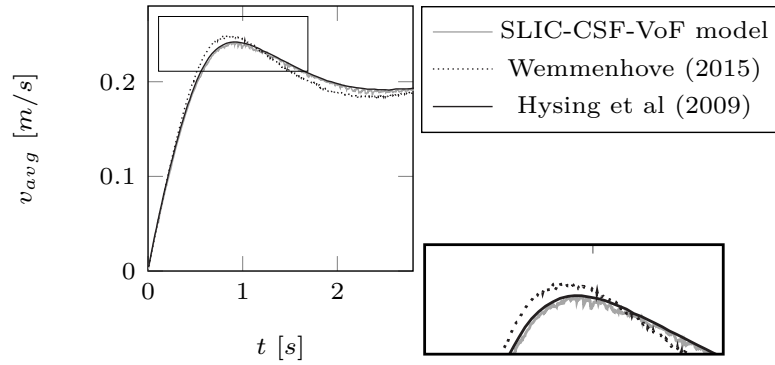


FIGURE 3.16. Spatial mean velocity compared with the benchmark of Hysing et al. [123] with a grid resolution of 80×240 .

To investigate how our method deals with two merging interfaces, the free surface and the air-water interface of the bubble, an additional simulation was performed with a similar air bubble interface configuration and a lowered free surface. It is shown in Fig. 3.17 for a numerical simulation how the rising air bubble protrudes through the free surface. Note that this event was not part of the benchmark.

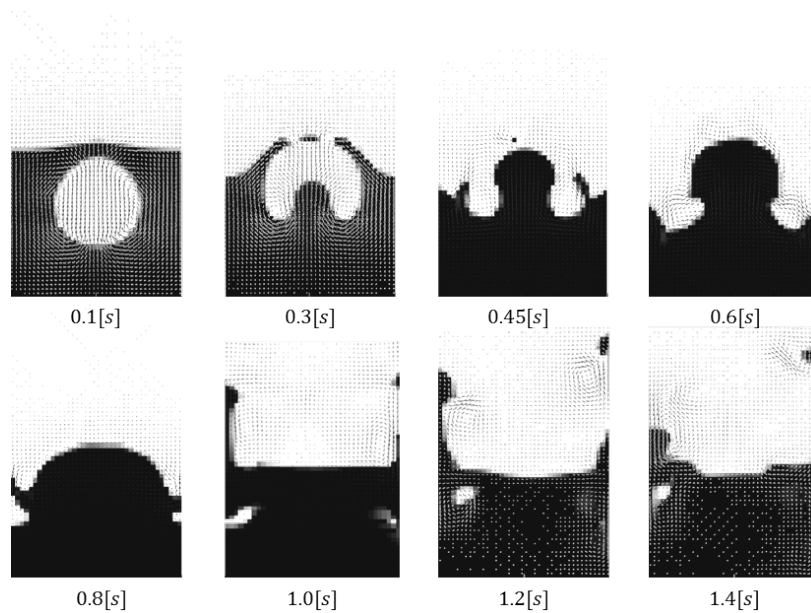


FIGURE 3.17. Snapshots of the 2D rising bubble passing through the interface in order of time.

3.5.4 1D shock tube

By entrapping an air pocket between the water and the structure, the pocket is compressed and can have a cushioning effect on the peak pressure during a wave impact [22, 212]. The modelling of the compressibility of the air is tested with the

simulation of a shock wave. Note that in our case a non-conservative momentum equation is solved which results in diffused shock waves. The interest for our slamming applications, however, is not in the exact position of the shock, but rather on the associated pressure levels.

The simulation is based on Downes, Knott, and Robinson [69], who derived an analytical solution for a 1D shock tube. The tube is simulated with unit length in two simulations. It is completely filled by gas ($F_s = 0$), using 400 cells for one simulation and 600 cells for the other. On either side, the velocity and the gradient of the pressure are set to zero. The time step is unvarying and equal to $3.33 \cdot 10^{-7}$ [s] and the specific ratio for air, $\gamma = 1.4$. The initial values in the domain are

$$p = \begin{cases} 10^6 [Pa], & x < 0.5 [m] \\ 10^5 [Pa], & x > 0.5 [m] \end{cases}, \quad u = 0 [m/s],$$

$$\rho_a = \begin{cases} 6.908 [kg/m^3], & x < 0.5 [m] \\ 1.33 [kg/m^3], & x > 0.5 [m]. \end{cases}$$

Fig. 3.18 shows the initial configuration of the shock tube, divided in a driver section with the higher pressure and a driven section with a lower pressure. The figure also shows the relevant stages of the evolution of the pressure. When released, two propagating fronts are created, moving in opposite direction, the shock front and the rarefaction. The pressure immediately upstream of the shock is called the contact surface (p_2). The Mach number associated with these two pressure levels can be found from

$$p_2 = p_1 \left(1 + \frac{2\gamma}{\gamma+1} (Ma^2 - 1) \right), \quad (3.19)$$

yielding a value of $Ma = 1.71$ [-] when $p_2 = 324$ [kPa]. The pressure downstream of the shock after reflection from the domain wall has taken place (p_3 in Fig. 3.18) can be calculated with

$$p_3 = p_2 \left(\frac{(\alpha + 2) \frac{p_2}{p_1} - 1}{\frac{p_2}{p_1} + \alpha} \right), \quad (3.20)$$

where

$$\alpha = \frac{\gamma + 1}{\gamma - 1}.$$

This results in $p_3 = 875$ [kPa].

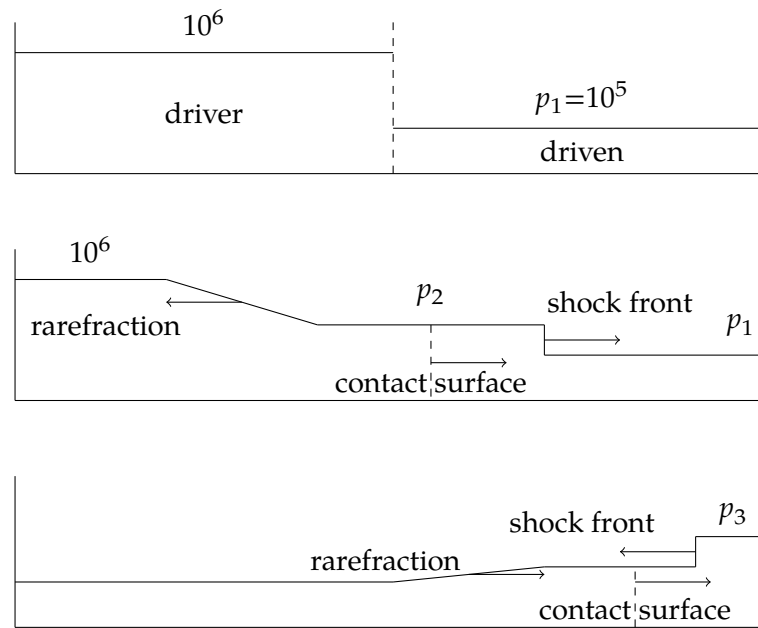


FIGURE 3.18. Initial condition and relevant stages of the pressure in a shocktube simulation.

The results of the numerical simulations are plotted in Fig. 3.19. The figure shows the pressure in the domain for different moments in time. The simulated shock front moves with an average speed of ≈ 560 [m/s] which corresponds with $Ma = 1.71$ [-]. This is in agreement with the analytical results.

When using 400 grid cells, pressure values $p_2 = 324$ [kPa] and $p_3 = 915$ [kPa] are found. When using 600 grid cells, pressure levels $p_2 = 324.5$ [kPa] and $p_3 = 908.7$ [kPa] are found. Fig. 3.19 shows wiggles near the shock front that originate from using central discretization of the pressure with an underresolved shock. As expected, the wiggles and the range in space over which they occur become smaller with increasing grid resolution.

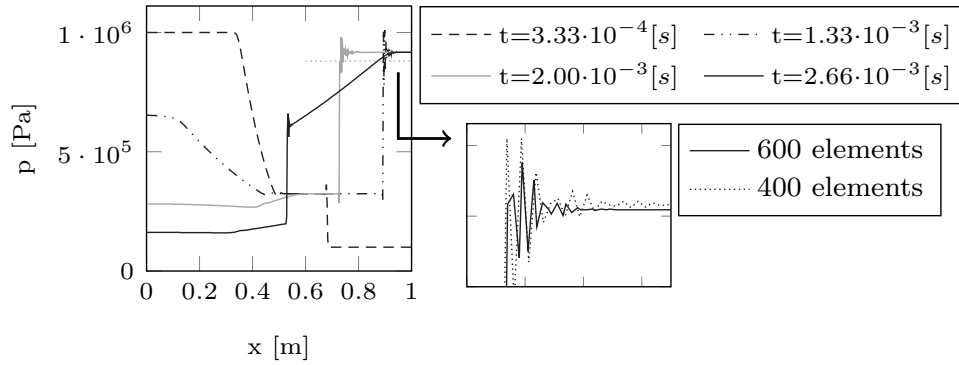


FIGURE 3.19. (Reflected) shock front in terms of the pressure at different time levels (400 grid cells and 600 grid cells in the enlargement).

It is demonstrated that the simulation results for the 1D shock tube converge for a larger number of grid cells and that they converge to the analytical values. The wiggles observed near the shock front become smaller with an increased number of grid cells. They do not grow in time and are not expected to interfere with our interpretation of the pressure levels in wave slamming events with enclosed air pockets.

3.5.5 Dam break experiment

The final comparison before moving on to our main result is for the onset of a wave impact event. The present implementation is validated against the experiments of Martin et al. [176] who focus on the evolution of the free surface in a dam break event. A dam break is a characteristic model for wave impact events.

The domain and initial condition for the experiment by [176] is shown in Fig. 3.20. The size of the domain is $a = 0.584$ [m] and $b = 0.350$ [m]. The size of the dam of water is $l_0 = 0.292$ [m] and $h_0 = 0.146$ [m]. The parameters for water and air are set to $\rho_w = 1 \cdot 10^3$ [kg/m³], $\rho_g = 1$ [kg/m³], $\mu_w = 1 \cdot 10^{-3}$ [kg/m s] and $\mu_g = 1 \cdot 10^{-4}$ [kg/m s]. The gravitational constant is set to $g = 9.81$ [m/s²] and the surface tension is equal to $\sigma = 7.2 \cdot 10^{-2}$ [N/m].

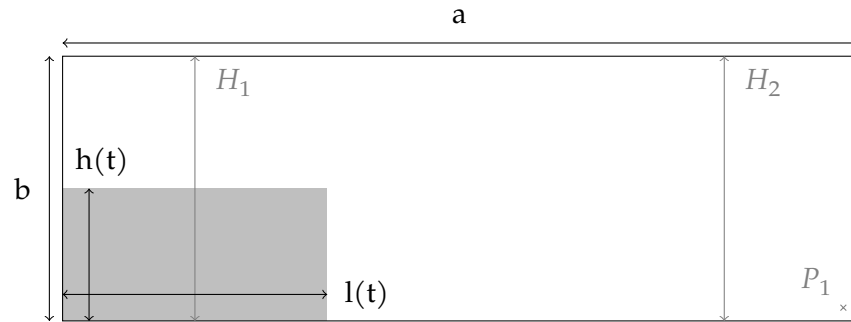
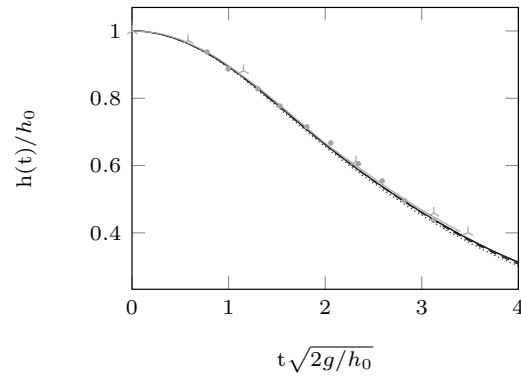
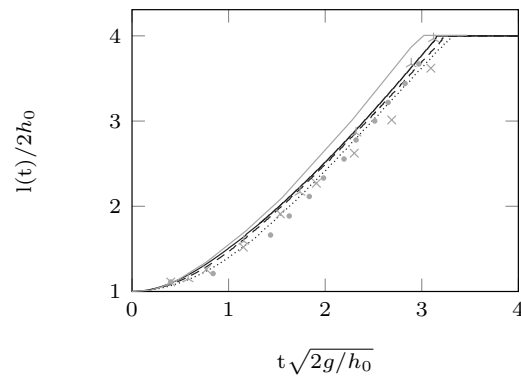


FIGURE 3.20. Setup dam break 2D case.

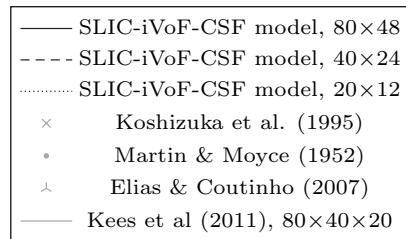
When the dam is released, the initial water level drops and a front propagates towards the opposite end of the domain. The free surface in Martin et al. [176] was measured along the left wall as an elevation $h(t)$ and as a position of the front $l(t)$ along the bottom. The simulation results are shown in Fig. 3.21, where $h(t)/h_0$ is plotted against dimensionless time. The simulation results are compared to the experiment of Martin et al. [176] as well as more recent experimental and numerical results [82, 136, 147]. Three different grid resolutions, 20×12 , 40×24 and 80×48 , were used. It is intriguing to observe that the simulation results converge away from the experimental results, i.e. the coarsest-grid simulation has the best agreement with the experiments. This is consistent with Kees et al. [136], but at present there is no explanation. The differences may be caused by not representing the friction between fluid and bottom well and by 3D effects [136, 184].



(A)



(B)

FIGURE 3.21. Change of 2D dam over time in (A) height (h) and (A) length (l).

3.6 Main result

As mentioned, a dam break is a representative case for wave impact phenomena, especially for green water. The objective is to demonstrate with dam-break simulations that oscillations in entrapped air pockets can cause pressure level variations of the order of the impact pressure. Our simulations are run in 2D, because of the increased likelihood of entrapping a pocket of air. Also, because the ratio of buoyancy force over viscous forces is lower in 2D, the rising velocity is smaller and air pockets persist longer. The simulation results are to be compared to the experiments conducted at MARIN (Maritime Research Institute Netherlands), in which the free surface and impact pressure on an obstacle in

the path of the flow were measured.

The setup of the experiment is similar to before, see Fig. 3.20. The domain is $a = 3.22[\text{m}] \times b = 1.0[\text{m}]$ and has normally a width of $1.0[\text{m}]$; the ceiling of the domain was kept open. A door was used to fill a column of water to a height of $h_0 = 0.55[\text{m}]$ and a width of $l_0 = 1.22[\text{m}]$. The water height is measured over time with vertical wave probes at positions $H_1 = 0.58[\text{m}]$ and $H_2 = 2.72[\text{m}]$ with respect to the origin. The pressure P_1 was measured at the wall at the downstream end of the domain at a height of $0.03[\text{m}]$. Experiments were conducted as follows: the door was pulled up, releasing the water. The water flows towards the opposite domain wall. There, an impact takes place with significant run-up and overturning, after which the disturbance propagates back and forth in between the domain walls.

Our main interest goes out to finding the impact pressure in the most efficient way possible. A major factor determining the efficiency of the method is how the free surface is reconstructed. In the next simulation, Young's PLIC with gravity-consistent density averaging is compared to SLIC with cell-weighted density averaging for the dam break in the MARIN experiment. The peak pressure is measured at the foot of the wall (P_1). The results are shown in Fig. 3.22. A difference in gauge pressure ($p - p_0$) of 2% is found, equal to $110[\text{Pa}]$. The time difference of meeting the wave is $2.3 \cdot 10^{-3}[\text{s}]$. This result contributes to the statement in the introduction by Wemmenhove [292] saying that SLIC with the local height function can achieve similar results as PLIC. The results with SLIC were obtained with a factor of 3 less computational effort than PLIC, making SLIC more efficient.

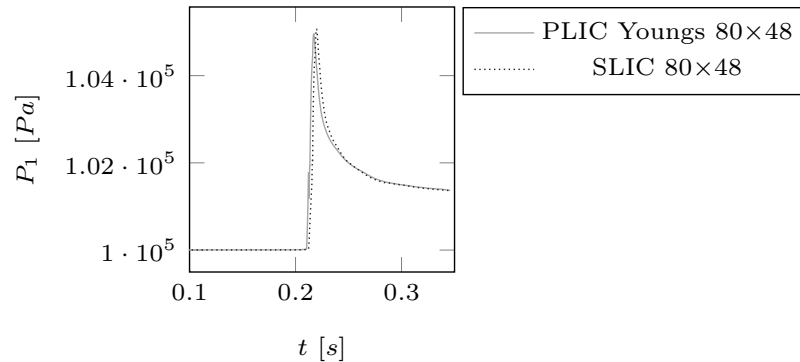


FIGURE 3.22. Difference in pressure for SLIC with height function and PLIC Youngs.

Two more simulations were run for two different grids, 48×15 and 115×36 . The parameters for water and air at a temperature of $20[\text{deg}]$ were used and the surface tension coefficient was chosen equal to $\sigma = 7.2 \cdot 10^{-2}[\text{N/m}]$. Our 2D simulation results are shown in Fig. 3.23, where they are compared to the 3D experiments

and to the 3D numerical results of Wemmenhove et al. [291]. The water heights and the pressure in Fig. 3.23 correspond reasonably well to the experiment and almost completely to Wemmenhove et al. [291], until $t = 1.54$ [s]. It is consistent with the original method that no true convergence is observed when increasing the grid resolution.

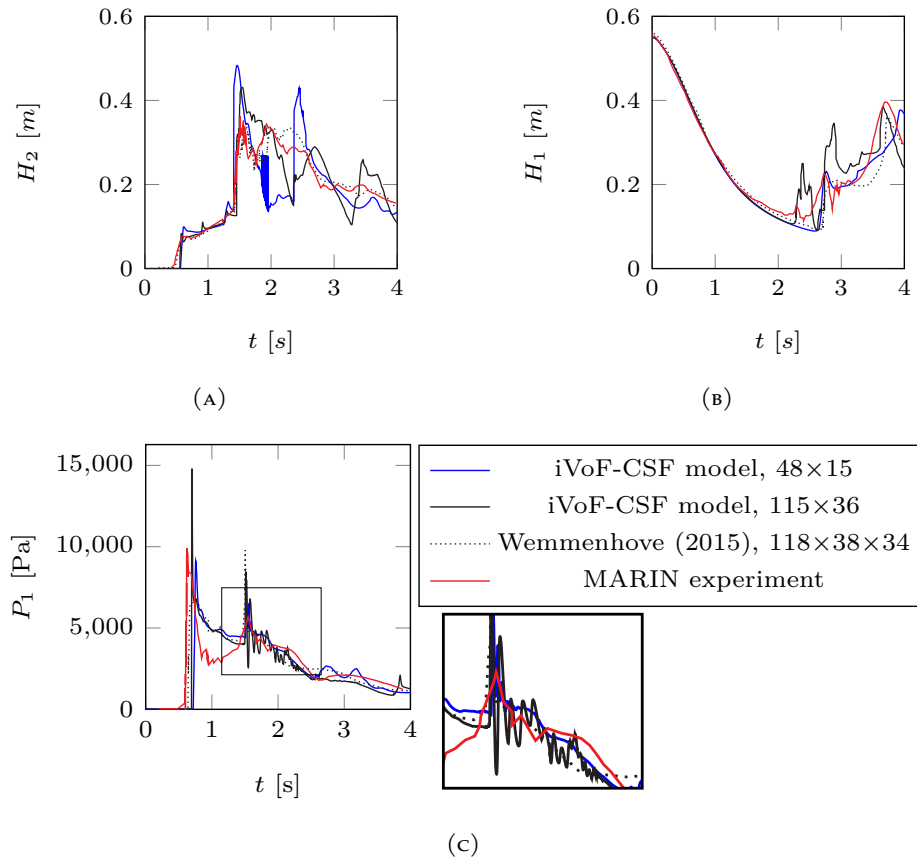


FIGURE 3.23. The results of the present model for the dam break case compared with experimental results of MARIN and numerical results of Wemmenhove et al. [291]; (A) the water height H_1 in time, (B) the water height H_2 in time, (C) the gauge pressure P_1 .

Special attention goes out to the pressure oscillations at P_1 , see the enlargement in Fig. 3.23c. These are due to the air pocket that is entrapped at around $t = 1.54$ [s] after the run-up on the domain wall has overturned. Note that the entrapped air pocket was not part of the 3D numerical results nor the experiment. The air pocket is shown in Fig. 3.25 at time instance $t = 1.54$ [s] when the pressure in the air pocket is lower than the atmospheric pressure.

When averaging the pressure in the air pocket in space, a high frequency oscillation of 14.0[Hz] is found. The same characteristic high frequency oscillation is found in the signal for pressure sensor P_1 at the wall. In P_1 , also a low frequency of around 3.0[Hz] can be found. This corresponds to the global motion of the air pocket in space. By a Fourier transform of the pressure signal after 1.2[s], the frequencies are compared. The results are illustrated in Fig. 3.24. The higher frequency peaks observed in Fig. 3.24 are due to higher harmonics and they are generated when the pocket is split in two parts [212].

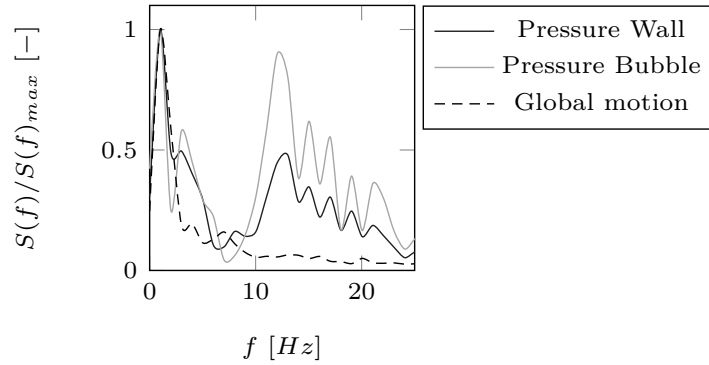
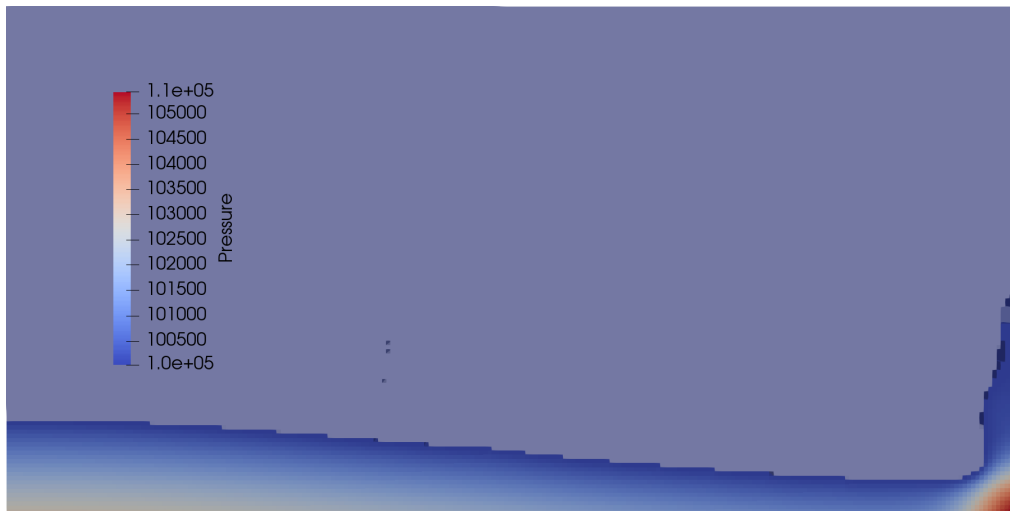


FIGURE 3.24. Normalized Fourier transform.

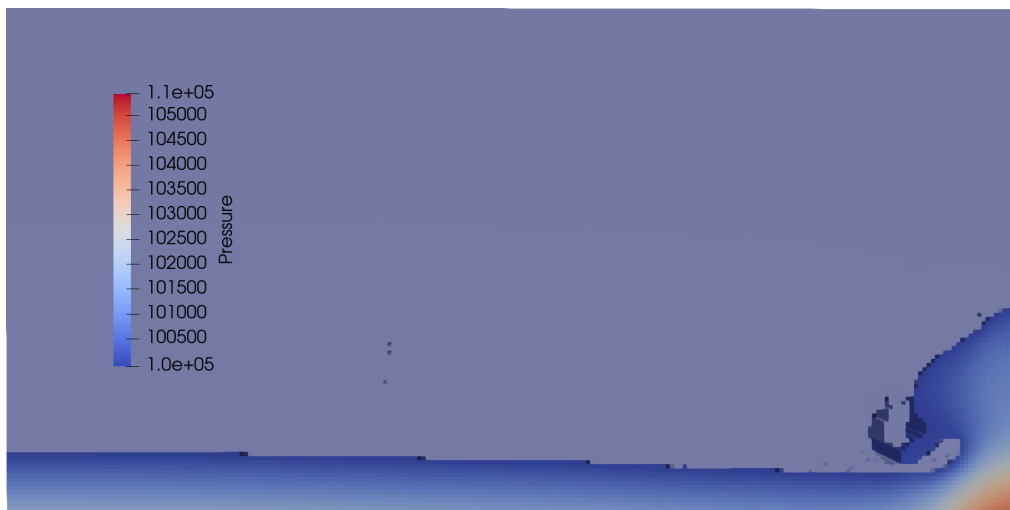
When using an equation for the natural frequency of cylindrical bubbles of this size [127]

$$R_0 f_0 = 1.10, \quad (3.21)$$

With $R_0 = 0.08$ [m] the radius of the bubble, see Fig. 3.25, we find a natural frequency of the bubble of $f_0 = 14$ [Hz]. This is of the same order of magnitude as the frequency found in the simulation. It is demonstrated that the pressure oscillations in the air pocket affect the pressure level at the wall and that the magnitude of the oscillations is of the same order as the magnitude of the impact pressure at the wall. The frequency of the oscillations is of the same order as what can be found by using simplified theory for compressible gas pockets.



(A)



(B)

FIGURE 3.25. Numerical results dam break in 2D (Fig. 3.20) using experimental setup of MARIN. Pressure contours are illustrated for the water phase. Entrapment of air pocket (diameter 0.16[m]) at 1.0[s] (A), 1.4[s] (B) and 1.6[s] (C) with pressures in [Pa].

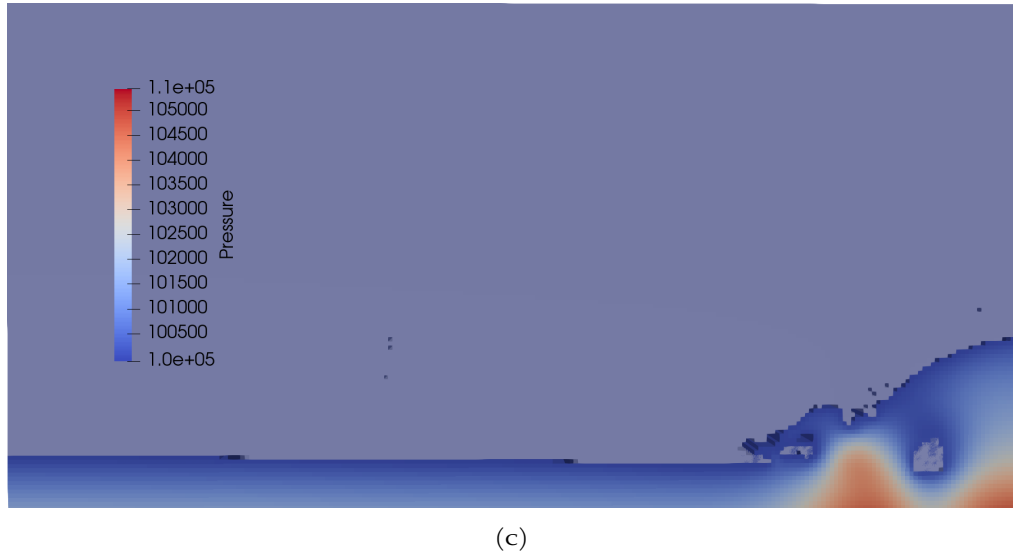


FIGURE 3.25. Numerical results dam break in 2D (Fig. 3.20) using experimental setup of MARIN. Pressure contours are illustrated for the water phase. Entrapment of air pocket (diameter 0.16[m]) at 1.0[s] (A), 1.4[s] (B) and 1.6[s] (C) with pressures in [Pa].

When the simulations were run without surface tension, the results were not any different. This means that compressibility governs the entrapped air pocket dynamics at this scale.

3.7 Conclusion

Our objective was to evaluate the effect of compressibility of air on the pressure exerted on an object during an impact with water. For this we extended the method of ComFLOW to obtain a complete model for representing the dynamics of air pockets entrapped after wave impact events. The extended implementation was verified by means of test cases relevant to the dynamics of entrapped air pockets. The extended method was validated by means of a dam-break experiment and applied to a dam break in a new setting with a wall, in which the impact leads to an entrapped air pocket. The following conclusions were found:

- PLIC does not lead to better results than SLIC for the grid resolutions used for the dam-break simulations in this article.
- Gravity-consistent density averaging as in Wemmenhove et al. [291] does not improve the results with SLIC as it does with PLIC; cell-weighted averaging gives comparable results at lower computational cost. The combination of SLIC and cell-weighted averaging reduces the computational effort with a factor of 3 with respect to PLIC and gravity-consistent density averaging.

- Our implementation compares well to test cases relevant to air pocket dynamics and compares well to dam-break experiments.
- Our extended method compares well to the 3D dam-break experiment performed by MARIN until the air pocket is enclosed.
- At the scale of the enclosed air pocket in our dam-break simulation (diameter $0.16[\text{m}]$), the effect of compression waves in the air dominates the dynamics.
- The frequency of the pressure oscillations in the air pocket is of the same order as the analytical natural frequency of an adiabatic cylindrical bubble.

Reflecting on our main objective, we found that surface tension at this scale has no effect. Furthermore, we found that compressibility of air in an enclosed air pocket during an impact with water causes compression waves and subsequent pressure oscillations with a *magnitude of the same order* as the pressure of the initial impact itself.

4

TWO-PHASE FREE-SURFACE FLOW INTERACTION WITH MOVING BODIES USING A CONSISTENT, MOMENTUM PRESERVING METHOD

This chapter is reproduced from [80] :

M. van der Eijk and P. R. Wellens. "Two-phase free-surface flow interaction with moving bodies using a consistent, momentum preserving method." *Journal of Computational Physics* 474 (2023), p. 111796

Abstract

The numerical prediction of two-phase flows with an interface is challenging, to a considerable extent because of the high density ratio at the interface. Numerical results become affected by momentum losses, diverging spurious interface velocities, free surface distortion, and even numerical instability. To prevent issues like these, consistent momentum and mass transport with an additional continuity equation were introduced.

In this work we describe how a consistent discretization was incorporated into our own method and extended for fluid-structure interaction (FSI) with moving rigid bodies. The new method was tested against benchmark simulations from literature confirming that consistent transport modeling gives a significant improvement compared to non-consistent modeling for the dynamics of two-phase flows.

Newly devised proof of principle FSI simulations with momentum transfer from fluid to body in the presence of a high density ratio between fluids are introduced that could serve as a benchmark for future studies. The simulations demonstrate that consistent modeling gives an order of magnitude improvement in terms of momentum conservation compared to non-consistent modeling.

Simulations with the new method are also compared to FSI experiments from literature. Results obtained with the consistent method are closer to the measurements than results of the non-consistent method.

The merit of consistent modeling with and without FSI becomes especially apparent for two-phase flows with a high density ratio between fluids.

4.1 Introduction

This work is about a consistent method for two-way coupled fluid-structure interaction (FSI) of two-phase flows with a high density ratio such as that between water and air, impacting with moving rigid bodies. Two-phase flows, like those surrounding floating marine structures, are difficult to predict. The structure needs to be designed for violent weather conditions to ensure crew safety [91]. Linear approaches fall short of representing highly non-linear events to an acceptable level during these weather conditions. Traditionally, experiments at scale are employed to model the events, but in specific circumstances numerical simulations are also possible. Sophisticated two-phase flow models are needed to evaluate the highly non-linear interaction between flow and structure accurately.

Our approach is based on a one-fluid formulation for incompressible flows. A unique, continuous velocity field is solved and the pressure field is relaxed to represent both fluids [188]. A finite-volume discretization of the governing equations is adopted with a staggered arrangement of variables. This type of discretization can suffer from numerical problems caused by large density ratios of the fluids near the interface.

The density is discontinuous over the interface. The interfacial discontinuities of fluid properties are often avoided or not well implemented in combination with the continuous velocity field. A lack of attention to the numerical implementation of the discontinuity in density can lead to numerical instabilities and non-physical flow features. When the density ratio between fluids increases, the flow becomes more interfacially driven, adding to the numerical error [222]. The error does not become apparent in the heavier fluid but rather in the lighter [29].

Errors can be introduced by the staggered arrangement of variables. The arrangement features different positions of the control volumes for mass conservation and momentum conservation. Errors in momentum will appear for non-matching momentum and mass fluxes. Following Rudman [230], such a method is called "non-consistent" in the remainder of this work. The momentum flux becomes dominant over the mass flux in case the density ratio increases, increasing the magnitude of the errors [222]. Numerical error accumulation near highly deformed interfaces can lead to failure of the method or can result in non-physical features [190].

Over the years, many have proposed strategies to mitigate these issues within a wide range of numerical contexts [190]; for example Li et al. [158] for a moment-of-fluid method, Vaudor et al. [268] for a staggered arrangement with a coupled level-set Volume-of-Fluid (CLSVOF) method, Le Chenadec and Pitsch [154] and Owkes and Desjardins [200] for sharp interface Volume-of-Fluid (VOF) methods, and Jemison, Sussman, and Arienti [130] and Duret et al. [73] for

compressible flow solvers. The methods referred to are similar in the way of discretization but different in the reconstruction of the interface and transport.

Earlier numerical schemes based on VOF [29, 230] were not sensitive to the numerical instabilities induced by a large density ratio. The method of Rudman [230] uses, together with a staggered arrangement of the variables, grid refinement for the transport and reconstruction of the interface. On the other hand, the method of Bussmann, Kothe, and Sicilian [29] does not need Rudman's grid refinement because of a collocated arrangement. From the authors' point of view, the last two methods mentioned use a "consistent" coupling of the momentum and mass flux together with an unsplit transport scheme. The key point made by Rudman [230] and Bussmann, Kothe, and Sicilian [29] is that in order to obtain a conservative coupling between mass and momentum fluxes, the density of the momentum flux in the convective term needs to be corrected with the mass flux obtained from the VOF transport equation. Bussmann, Kothe, and Sicilian [29] showed that the collocated arrangement results in easier enforcement of consistency between the momentum and mass transport but introduces difficulties with calculating the fluxes.

In the context of level-set methods, Raessi and Pitsch [222] introduced a consistent, stable method. The method makes use of two geometric reconstruction sweeps of the free surface at two different time levels. The disadvantage of the method is that it is limited to one- and two-dimensional problems. The methods of Ghods and Herrmann [98] for collocated unstructured grids and of Desjardins and Moureau [60] and Nangia et al. [190], adapting the method of Rudman [230] to level set methods, use an extra continuity equation. The extra continuity equation results in a auxiliary density field that is coupled with the momentum flux in the convective term in the momentum equation. Both methods [60, 98] showed that non-geometric construction of the interface from a level-set field and grid refinement can also result in consistency between momentum and mass transport. However, being based on level-set, the methods were neither mass nor momentum conserving and used first-order upwind for density and velocity transport, producing diffusive flow features.

Patel and Natarajan [203] achieved higher-order accuracy with a consistent scheme. Patel and Natarajan [204] came up with a consistent convective scheme for momentum and algebraic (non-geometric reconstruction) VOF transport. They showed that any non-consistency in the scheme leads to poor accuracy.

Recently, Zuzio et al. [320], using a staggered grid with CLSVOF for the interface between fluids, describe a consistent momentum and mass method with a temporary continuity equation. Compared to Rudman [230], they do not apply grid refinement for transporting the free surface, thereby reducing the computational effort. We will adopt the strategy of Zuzio et al. [320] into our own method [75].

Arbitrarily shaped bodies can be represented on fixed Cartesian grids by means of immersed boundary methods (IBM). An early such method is that of Peskin [208]. A distinction can be made between body forcing methods, using source terms in the governing equations to impose the boundary conditions of the body, and cut cell methods, in which the position of the boundary is reconstructed and part of the discretization. Whereas a body forcing IBM method is straightforward to implement [208, 273], the interface between body and fluids can become diffusive. Lagrange et al. [149] combined a body forcing IBM with the consistent momentum and mass method (CMOM) of Zuzio et al. [320] for non-moving bodies. Because the interface between fluids in our method [75] is also reconstructed, we choose to incorporate a cut cell method for representing the interface between body and fluids. Drawbacks of cut cell methods [38, 191, 263, 266, 269] is that work is involved in reconstructing the boundary and that special treatments of small cut cells is needed [269]. On the other hand, the reconstruction adds to the accuracy of where boundary conditions are imposed and the governing equations do not change compared to uncut cells. Cheny and Botella [38] proposed a cut cell method where small cut cells do not need any special treatment, followed by Xie, Lin, and Stoesser [306] who have recently described a cut cell method for moving bodies that is also consistent, but which does not include two-way coupled fluid-structure interaction.

Fluid-structure interaction with two-way coupled body motion appears not to have been investigated in the context of consistent momentum and mass methods, especially in terms of the momentum transfer from fluids to body when impacts take place. In this work, our former method in Eijk and Wellens [75] is extended with a cut cell method similar to Xie, Lin, and Stoesser [306] and made consistent by incorporating elements from Zuzio et al. [320] to study two-way coupled FSI.

This chapter starts with the governing equations and the discretization. The implementation of the consistent method and the coupling with the structure are discussed, highlighting the addition of the cut cell method for moving bodies. In Sec. 4.5 our method is tested by means of fundamental verification cases with a large density ratio at the interface. The verification includes newly formulated simulations for momentum conservation with FSI, that could serve as a benchmark for future studies. In Sec. 4.6 simulation results are compared with 2D experimental results with FSI. Conclusions are formulated in the final section.

4.2 Governing equations

The governing equations for two-phase flows of immiscible Newtonian fluids are given in Eq. (4.1) and Eq. (4.2). These equations are formulated in a conservative

vector form. The one-fluid formulation is used [188] with a single velocity field and a single pressure field. The continuity equation reads

$$\frac{\partial \rho}{\partial t} + \nabla \cdot (\rho \mathbf{u}) = 0, \quad (4.1)$$

in which \mathbf{u} denotes the fluid velocity vector, ρ is the mixture density. The momentum equation is given by

$$\frac{\partial(\rho \mathbf{u})}{\partial t} + (\mathbf{u} \cdot \nabla) \rho \mathbf{u} + \rho \mathbf{u} \nabla \cdot \mathbf{u} + \nabla p - \nabla \cdot (\mu(\nabla \mathbf{u} + \nabla \mathbf{u}^T)) - \frac{2}{3} \mu \nabla \cdot \mathbf{u} \mathbf{I} + \rho \mathbf{F}_f = 0, \quad (4.2)$$

where p is the relaxed pressure, μ is the dynamic viscosity for a mixture and \mathbf{F}_f represents the body forces. The body force term contains gravity and capillary stresses, so that $\mathbf{F}_f = \mathbf{F}_g + \mathbf{F}_\sigma = g - \frac{1}{\rho} (\sigma \kappa \mathbf{n} \delta_\Gamma)$.

A transport equation is solved for displacing the interface between fluids, using velocity field \mathbf{u} under the assumption of a no-slip condition between the two fluids

$$\frac{Df}{Dt} = \frac{\partial f}{\partial t} + (\mathbf{u} \cdot \nabla) f = 0, \quad (4.3)$$

where $f(\mathbf{x}, t) = 0$ gives the position of the interface. When using the Volume-of-Fluid (VOF) method, the distance function f is replaced by volume fraction C_f . The volume fraction is a measure of the ratio of fluid volumes in a cell.

The body will be assumed rigid. It is displaced with a state-space representation of Newton's second law, in which the position of the body \mathbf{x}_b is found from

$$\frac{\partial \mathbf{x}_b}{\partial t} = \mathbf{u}_b \quad (4.4)$$

and the body's acceleration is found from

$$m_b \frac{\partial \mathbf{u}_b}{\partial t} = \mathbf{F}_b, \quad (4.5)$$

with m_b the body's mass and \mathbf{F}_b the force of gravity together with the force of the fluids on the body. The fluid force on the body is equal to the integrated normal pressure along the body boundary. Viscous stresses are neglected in the determination of the force on the body, because our main interest is in representing the two-way coupled fluid-structure interaction of impacts – of the body with the fluid or vice versa. Impacts take place over time spans that are too short for viscous effects such as boundary layers to develop.

4.3 Grid and solution variables

Before presenting the numerical discretization of the governing equations and the details of including two-way coupled fluid-structure interaction in a consistent momentum and mass method, the grid structure is introduced with the

definitions and notations needed for discussing the solution method.

A fixed Cartesian grid is employed. Labeling of grid cells is used to account for the position of the interface between fluids and the interface between body and fluids, so that it is defined where surface tension needs to be applied and where reconstruction of the interface needs to take place. We have adopted the labeling system of Kleefsman et al. [142], see Fig. 4.1, that uses the label B(ody) for cells completely filled with body, the label E(mpty) for cells filled with gas only (or the lighter of two fluids), the label S(urface) for cells with some liquid (or the heavier of two fluids) directly adjacent to E-volumes. Remaining cells are labeled F(luid). By definition, F-cells are not allowed to connect with E-cells. Note that F-cells do not necessarily have to be completely filled with liquid; a cell like this is indicated in Fig. 4.1 with a black marker. A cut cell, containing both fluid and body, is indicated in Fig. 4.1 with a red marker. The blue marker in Fig. 4.1 is a “special” cut cell. It contains two interfaces, between liquid and gas and between fluids and body. The reconstruction of the interfaces needs extra attention; this is discussed in Sec. 4.4.1.

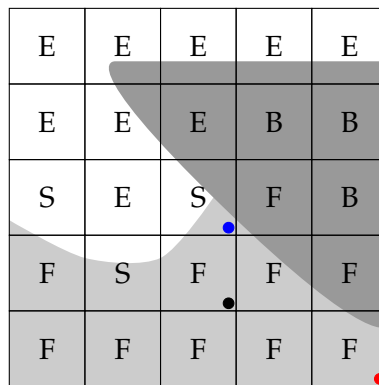


FIGURE 4.1. Labeling of cells as in Kleefsman et al. [142]; labels B, F, S, and E. Body is indicated by ■. Fluid is indicated by ■. Cut cells, always labeled with F, are necessary for representing moving bodies in the grid. A F-cell that is not completely filled (●). A cut cell is illustrated by a marker (●). A special cut cell is illustrated by another marker (●) which needs extra attention because it contains two interfaces.

In the original labeling system [142], reconstruction of the interface between fluids only takes place in S-cells and, hence, not in F-cells. In Fig. 4.2a, therefore, the interface is shown to be discontinuous and the F-cell is shown with a hatched pattern to indicate that it is not possible to distinguish between liquid and air in this cell.

In this work an additional label is introduced, called a C(orner) cell. When a F-cell diagonally connects with no more than one E-cell, it gets the C-label. The interface in a C-cell is reconstructed, resulting in a more continuous interface, as illustrated in Fig. 4.2b. Reconstructing the interface in C-cells and including it in evaluating the curvature results in a better representation of capillary effects and prevents artificial air entrainment. A disadvantage is the need for an additional calculation step during labeling. The additional computational cost is negligible compared to solving the Poisson equation. The benefits of C-labeling will become clear in Secs. 4.5 and 4.6.



FIGURE 4.2. Difference in labeling between F-cells (left) and C-cells (right). The grey area represents the geometrical reconstruction based on the fill ratio of the cells. Fluid is indicated by ■. The F-cell is not reconstructed and therefore illustrated with a hatched pattern representing a mixture of liquid and gas. New are the C-cells in which the free surface is reconstructed for a smoother interface between fluids.

The standard MAC configuration of staggered variables is adopted, where scalar variables (pressure p , density ρ , curvature κ , volume fractions C_f and C_b) are stored in the center of a grid cell, and velocities are positioned in the faces of a cell. Uncut cells are represented in Fig. 4.3 by means of continuous black lines, with open circles in cell centers. Velocities in the cell faces are represented as arrows. Continuity control volumes, used for discretizing the continuity equation, coincide with grid cells. Momentum control volumes are shifted in space with respect to continuity control volumes, horizontally for the equation describing (discrete) conservation of horizontal momentum and vertically for vertical momentum conservation, so that the velocities in the respective directions are in the centers of momentum control volumes. Variables in the centers of continuity control volumes are given indices i (horizontal) and j (vertical) to refer to their position in the grid; variables in the faces of continuity control volumes are given indices $i - \frac{1}{2}$ and $i + \frac{1}{2}$ to show that they are positioned left or right of a continuity control volume center and, similarly, $j - \frac{1}{2}$ and $j + \frac{1}{2}$ to indicate their position above or below that center.

Averaging is employed when the value of a variable is required at a different location from where it is positioned in the grid. For instance, when a velocity is required at the boundary of a horizontal momentum control volume at position (i, j) it is determined as the average of the velocities on either side. Density averaging, however, or rather the discretization of the density requires a special treatment in order to conserve momentum. It is explained in more detail in Sec. 4.4.2 when CMOM is discussed.

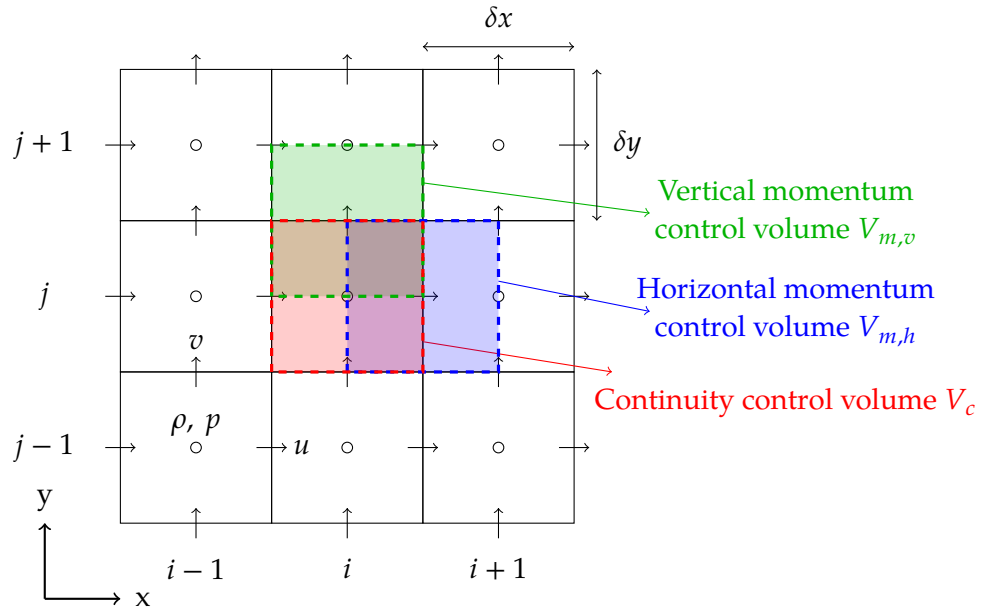
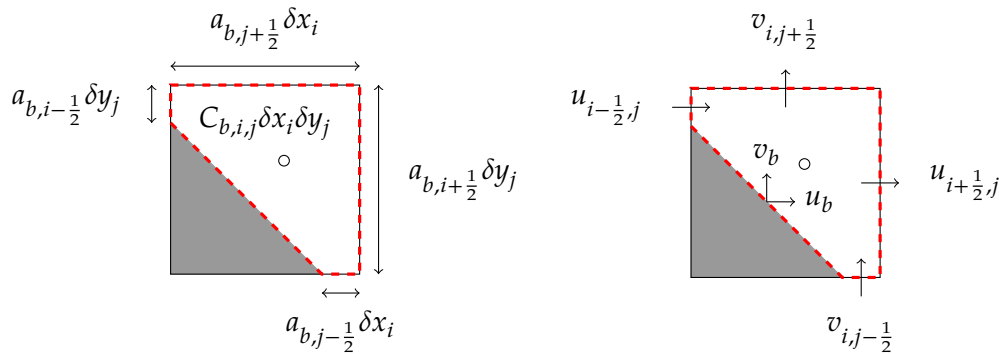


FIGURE 4.3. Standard MAC configuration (staggered); pressure p is defined in the cell center (\circ), the horizontal velocity u field is sampled on the vertical faces (\rightarrow), the vertical velocity v is sampled on the horizontal faces (\uparrow). The subscripts (i, j) for the position in the grid are defined. The overlap of the continuity control volume ($-$), with a vertical momentum control volume ($-$), and with a horizontal momentum control volume ($-$) is shown.

A cut cell method similar to Fekken [90] and Xie, Lin, and Stoesser [306] accounts for the presence of the body in the grid. Continuity control volumes that are intersected by the contour of the body are scaled by the part of the volume that is taken up by the body. That scaling factor is called volume aperture C_b and defined as the ratio of the volume open to fluid (so one minus the volume of the body) and the size of the control volume itself. It is shown in Fig. 4.4a. The faces of continuity control volumes are also scaled by face apertures a_b . They are defined as the area of the volume's face open to fluid, divided by the area of the face itself, see Fig. 4.4b. Apertures take on values between 0 and 1. For the *visualisation*, velocities represented by arrows are shown in the middle of the part of face that is open to flow, but that change in position is not actually part of

the discretization, other than through the scaling of size of the face aperture.

Fig. 4.4c gives a representation of when an amount of liquid is present in the continuity control volume V_c . The size of the control volume V_c is $C_b \delta x \delta y$. The amount of liquid is expressed, then, as the part of C_b that is taken up by liquid, i.e. C_f/C_b . This means that the amount of gas in the volume is expressed as $(C_b - C_f)/C_b$. Note that volume and face apertures change in time as the body moves through the grid.



(A) Body volume aperture open to fluid C_b .

(B) Face apertures and velocities.

(c) Liquid and gas as fractions of C_b .

FIGURE 4.4. Continuity control volume (—) (i, j) for a cut cell. Body is indicated by ■. Fluid is indicated by □. u_b and v_b are the body velocities. Center (i, j) is given by ○.

Control volumes for horizontal momentum $V_{m,h}$ are shown in Fig. 4.5 together with the lower half of a control volume for vertical momentum $V_{m,v}$. Necessarily, the size of the momentum control volume is half of the size of the continuity control volumes on either side. The volume aperture C_b of a momentum control volume in uncut cells is also determined as half of the sum of volume apertures of the continuity control volumes, and the face apertures of a momentum control volume V_m are determined as half of the sum of face apertures of the continu-

ity control volumes on either side. Applying that rigour to the visualization of volume apertures in cut cells, leads to the representation in Fig. 4.5b where the part of the horizontal momentum control volume $V_{m,h}$ that is open to fluid is precisely half of the open parts of the continuity control volumes. Note that in the discretization, again, the volume sizes and face sizes are not changed, but rather scaled by means of apertures.

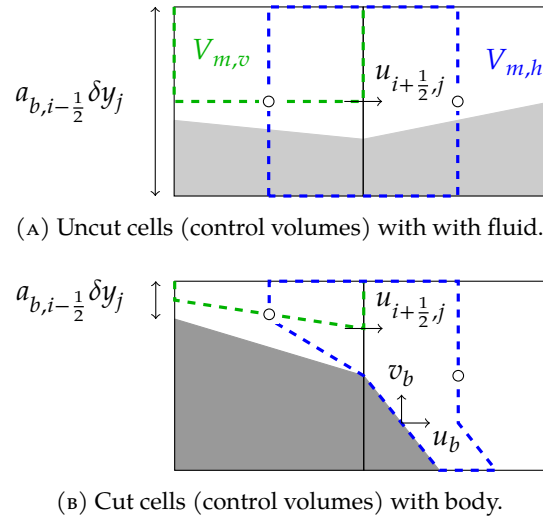


FIGURE 4.5. Horizontal momentum control volume (—) in an uncut cells and in a cut cell with indices (i, j) . The lower half of a vertical momentum control volume (—) is also shown. Body is indicated by ■. Fluid is indicated by □. The center of a continuity control volume in this representation is given by \circ .

4.4 Discretization and solution algorithm

Our main interest is in the type of violent fluid-structure interaction encountered in slamming, when a ship meets the free surface again after disconnecting from the main body of water it is sailing in. We have studied slamming with our older method for multiphase flow with gas and liquid, reported in Eijk and Wellens [75]. That method was non-conservative and non-consistent; what we mean by these terms will become clear from the discussion of the new, consistent method in this section. The first sign of trouble with the older non-consistent method was with the case of a vertical plate being impacted by a wedge shaped body of water [18], which, before impact and therefore incorrectly, started showing a large, and growing, local deformation of the interface between gas and liquid. Results of the simulation are discussed in Sec. 4.5.

Inspiration for a solution to prevent erroneous interface deformations came from the literature regarding consistent discretization of mass and momentum. Consider the time discrete version of Eqs. (4.1), (4.2), and (4.3), using Forward

Euler in time for brevity of notation, where superscript n indicates the time level. The equations are integrated over control volumes to obtain the weak form that is the basis of the discretization in space. Our method combines elements from Kleefsman et al. [142], Eijk and Wellens [75] and the consistent modeling in Zuzio et al. [320] to obtain a new algorithm that can account for two-way coupled fluid-structure interaction with moving bodies. The algorithm comprises the following within a time step. First, the fluids and the body are transported using Eq. (4.3) combined with the assumption of incompressibility of the fluids and with volume fractions C_f indicating the liquid fill ratio of volume apertures C_b

$$\begin{aligned} \int_{V_c} \frac{C_f^{n+1} - C_f^n}{\delta t} dV &= - \int_{V_c} (\mathbf{u} \cdot \nabla) C_f dV \\ &= - \int_{V_c} \nabla \cdot (\mathbf{u} C_f) dV \\ &= - \oint_{S_c} \underbrace{(\mathbf{u}^n C_f^n) \cdot \mathbf{n}}_{\text{consistent}} dS, \end{aligned} \quad (4.6)$$

in which S is the boundary of a control volume. Volume fraction C_f is equal to one when a continuity control volume is completely filled with liquid (the heavier of the fluids) and equal to zero when occupied by air (the lighter of the fluids). Because the fluids are considered to be incompressible, the continuity equation reduces to

$$\oint_{S_m} \mathbf{u}^{n+1} \cdot \mathbf{n} dS = 0. \quad (4.7)$$

The time discrete momentum equation reads

$$\int_{V_m} \frac{\rho^{n+1} \mathbf{u}^{n+1} - \rho^{n+1} \tilde{\mathbf{u}}}{\delta t} dV = - \oint_{S_m} \delta p \mathbf{n} dS, \quad (4.8)$$

in which $p^{n+1} = \delta p + p^n$ and from which auxiliary vector field $\tilde{\mathbf{u}}$ is solved from

$$\begin{aligned} \int_{V_m} \frac{\rho^{n+1} \tilde{\mathbf{u}} - \bar{\rho} \tilde{\mathbf{u}}}{\delta t} dV &= \int_{V_m} \nabla \cdot (\mu^n (\nabla \mathbf{u}^n + (\nabla \mathbf{u}^n)^T)) dV - \oint_{S_m} p^n \mathbf{n} dS \\ &\quad - \int_{V_m} \rho^{n+1} \mathbf{F}_f dV. \end{aligned} \quad (4.9)$$

A similar form to Eq. (4.8) is solved by Bussmann, Kothe, and Sicilian [29] and Raessi and Pitsch [222] with ρ^{n+1} on the left hand side to prevent unphysical velocities. Auxiliary vector field $\tilde{\mathbf{u}}$ in Eq. (4.9) is solved from

$$\int_{V_m} \frac{\bar{\rho} \tilde{\mathbf{u}} - \rho^n \mathbf{u}^n}{\delta t} dV = - \oint_{S_m} \underbrace{\rho^* \mathbf{u}^n (\mathbf{u}^n \cdot \mathbf{n})}_{\text{consistent}} dS, \quad (4.10)$$

whereas auxiliary density $\bar{\rho}$ is solved from Eq. (4.1) used as a temporary continuity equation that is integrated over momentum control volumes

$$\int_{V_m} \frac{\partial \rho}{\partial t} dV = - \oint_{S_m} \underbrace{(\rho^* \mathbf{u}^n) \cdot \mathbf{n}}_{\text{consistent}} dS. \quad (4.11)$$

Here, ρ^* is a density for which a consistent discretization in space is used. A *consistent* space discretization for momentum and mass is obtained when the fluxes along boundaries that are indicated by the word 'consistent' are treated the same with continuity control volumes and with momentum control volumes, and when the spatial discretization of ρ^n and ρ^{n+1} is the same on continuity control volumes and on momentum control volumes. Different notations from ρ^n and ρ^{n+1} are used for densities ρ^* and $\bar{\rho}$ to make clear that their spatial discretization is different.

The discrete velocity field at the new time level is solved from Eq. (4.8) and substituted into the discrete continuity equation to obtain a Poisson equation for the pressure. A system of equations that combines the Poisson equation for the pressure with the equation of motion for the moving body is solved, after which velocity field \mathbf{u}^{n+1} is reconstructed from the pressure field and a new time step commences.

The flow chart below summarizes these items. The numbers in the flow chart refer to the numbers of the subsections in which the steps are discussed, with emphasis on where the approach differs from earlier work.

Solution algorithm – in each time step:

- a) Solve transport equation fluids C_f^{n+1} and body C_b^{n+1} and reconstruct interfaces
- b) Determine the discretization of the density before establishing auxiliary vector field $\bar{\mathbf{u}}$
 - b)1. Determine ρ^n (and ρ^{n+1} and μ^n)
 - b)2. Determine ρ^*
 - b)3. Solve temporary continuity equation for $\bar{\rho}$
 - b)4. Determine auxiliary vector field $\bar{\mathbf{u}}$
- c) Determine auxiliary vector field $\tilde{\mathbf{u}}$ with p^n and $\tilde{\mathbf{u}}_b$
- d) Solve system of Poisson equation for pressure change δp and equation of motion for body velocity \mathbf{u}_b^{n+1}
- e) Solve new velocity field \mathbf{u}^{n+1} from the updated pressure differences.

4.4.1 Transport fluids and body

Eq. (4.6) is the basis for the discretization of the transport equation. A straightforward discretization of the transport equation reads

$$C_f^{n+1} = C_f^n - \frac{1}{\delta x \delta y} \sum_{face} \delta C_{f,face}, \quad (4.12)$$

in which subscript *face* refers to the sides of the continuity control volume and the flux δC_f , i.e. the amount of fluid that is transported from one continuity control volume to the next, is of the form

$$\delta C_f \sim \frac{C_f}{C_b} \mathbf{u} a_b \delta t \delta \mathbf{x}. \quad (4.13)$$

Fig. 4.6 shows the flux at the face of the continuity control volume (cut cell) with index $(i + \frac{1}{2}, j)$, with body, liquid and gas present at the same time.

Compared to Zuzio et al. [320], the flux now also depends on the face apertures a_b . The stability of the time discretization is not affected by the apertures [142]; the Courant number still needs to be smaller or equal to one.

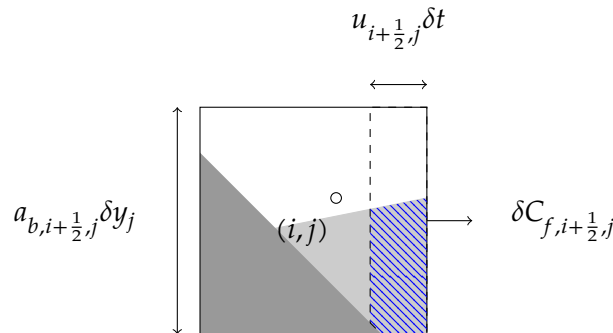


FIGURE 4.6. Flux calculated in a cut cell representation of a continuity control volume. Body is indicated by ■. Fluid (liquid) is indicated by ■. Center (i, j) is given by ○. The amount of fluid being transported (fluxed) is hatched with (-).

The discretization of the transport equation in Eq. (4.12) is subject to errors, caused to a considerable extent by the fact that the fluid is transported in the axis directions separately, instead of in the direction of the velocity vector at once. These errors are reduced when using the COSMIC transport algorithm [155] combined with the correction of Weymouth and Yue [295] to improve mass conservation.

The COSMIC split scheme we incorporate consists of multiple transport steps and reconstruction steps [155]. The COSMIC scheme, in 2D, reads as follows

$$\begin{aligned}
 C_f^{*X} &= C_f^n - \frac{1}{V_c} \left[\sum_{side=i+\frac{1}{2}, i-\frac{1}{2}} \delta C_{f,side}(a_b^n, u^n, C_f^n) \right]^1 \\
 &\quad + \frac{C_f^n}{V_c} \sum_{side=i+\frac{1}{2}, i-\frac{1}{2}} u_{side} A, \\
 C_f^{*Y} &= C_f^n - \frac{1}{V_c} \left[\sum_{side=j+\frac{1}{2}, j-\frac{1}{2}} \delta C_{f,side}(a_b^n, v^n, C_f^n) \right]^1 \\
 &\quad + \frac{C_f^n}{V_c} \sum_{side=j+\frac{1}{2}, j-\frac{1}{2}} v_{side} A,
 \end{aligned} \tag{4.14}$$

in which A is the area of the cell face open for flow. The free surface of the fraction fields C_f^{*X} and C_f^{*Y} are again reconstructed, resulting in $C_f^{X, n+1/2}$ and $C_f^{Y, n+1/2}$, respectively. The new reconstructed fraction fields are used to calculate

$$\begin{aligned}
 C_f^{n+1} &= C_f^n - \frac{1}{V_c} \left[\sum_{side=i+\frac{1}{2}, i-\frac{1}{2}} \delta C_{f,side} \left(a_b, u^n, \frac{C_f^n + C_f^{Y, n+1/2}}{2} \right) \right]^2 \\
 &\quad - \frac{1}{V_c} \left[\sum_{side=j+\frac{1}{2}, j-\frac{1}{2}} \delta C_{f,side} \left(a_b, v^n, \frac{C_f^n + C_f^{X, n+1/2}}{2} \right) \right]^2.
 \end{aligned} \tag{4.15}$$

The terms with boxes around them are the steps in which fluxes are calculated. Between these two steps, a reconstruction step takes place. The effect of these two steps on the momentum conservation is discussed in Sec. 4.5.2. Something that we have not seen discussed in literature is that we also use COSMIC for transporting the interface between fluids and body.

After transport, the interface between liquid and air in continuity control volumes is reconstructed with PLIC [202]. Reconstruction keeps the interface sharper compared to algorithms without reconstruction. Also the contour of the body is reconstructed by means of PLIC as it moves through the grid. An example of a piecewise-linear representation of the interface between fluids and the contour of the body in a continuity control volume is illustrated in Fig. 4.6. The reconstruction of the interface between structure and fluid is similar to the interface reconstruction between fluids [205].

Special attention is needed for cut cells labeled as S- or C-cell. These cells contain the interface between fluids as well as the interface between fluid and structure,

both requiring reconstruction. An iterative process is required to accomplish this. We define an initial contact angle between the free surface and the structure. The contact angle θ_1 is illustrated in Fig. 4.7a.

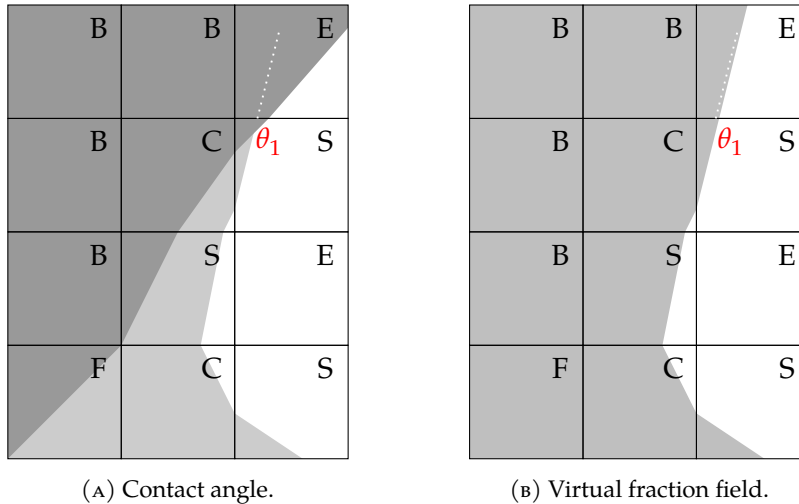


FIGURE 4.7. Reconstruction of cut cells including the labels. Body is indicated by ■. Fluid is indicated by ■.

Geometric reconstruction of the interface between fluids in a S- or C-cell withPLIC requires a stencil of 3×3 cells. The reconstruction in cut cells needs volume fractions of other cut cells or B-cells, where there are no volume fractions. The volume fraction in these cells is determined with a virtual fraction field [40]. The virtual fraction field is calculated based on the contact line represented by white dots in Fig. 4.7a, resulting in the virtual fraction field illustrated in Fig. 4.7b. The interface between fluids, then, is reconstructed based on the virtual fraction field.

In somewhat more violent two-phase flows, multiple, separate fluid bodies can be found attached to the structure. An example is shown in Fig. 4.8a. It is necessary to make the assumption that every fluid body has either two or zero cells connecting with the rigid body where θ_1 is defined. The connecting cell is found as follows: the S-labeled cut cell having the most surrounding E-cells compared to the neighboring S-labeled cut cells is defined as a contact cell, in which angle θ_1 is then imposed. The remaining S- and C-cells are assumed to be independent of θ_1 and reconstructed based on the virtual fraction field.

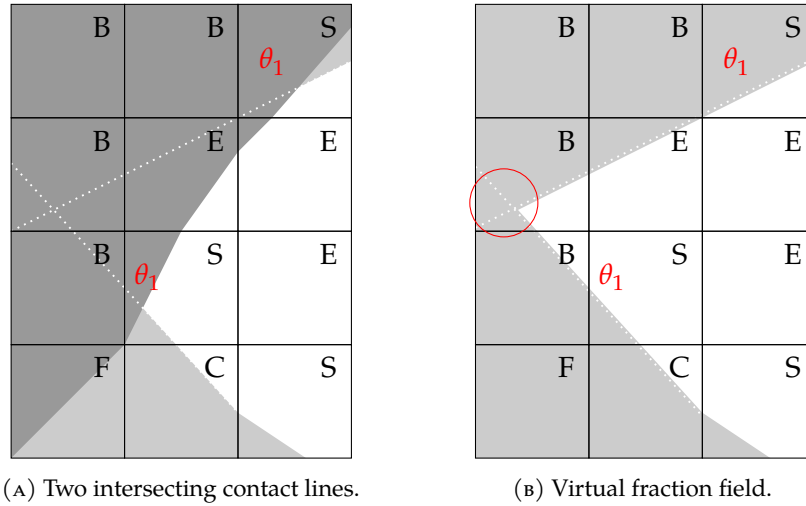


FIGURE 4.8. Reconstruction of cut cells: multiple fluid bodies with intersection at \circ . The labels are included. Body is indicated by ■. Fluid is indicated by □.

Separate bodies of fluid that are nearby can lead to intersecting contact lines and overlapping virtual fraction fields. One such overlap is indicated in Fig. 4.8b by the circle. To prevent incorrect reconstruction in surrounding S- and C-cells, the overlap needs to be considered, because otherwise fluid bodies that are separate will artificially merge. The reverse is also true. If the overlap is not considered properly, fluid bodies may artificially spawn smaller fluid bodies (droplets or bubbles). An example where fluid is kept nicely together is the buoyant cylinder in Fig. 4.27a where a thin film of liquid flows down along the boundary of the cylinder as it moves upward. In the remainder of the chapter, the angle θ_1 is chosen equal to 90 degrees.

4.4.2 Discretization of the density

A consistent discretization of mass and momentum is obtained through the discretization of the density. The density in different terms of the equations, also indicated by the different notations $\rho^n, \rho^*, \bar{\rho}$ and ρ^{n+1} , is treated differently. In general, near the interface between fluids, the density on any control volume is obtained through averaging by means of the volume fractions of the fluids

$$\rho = \rho_f \frac{C_f}{C_b} + \rho_a \frac{C_b - C_f}{C_b}, \tag{4.16}$$

in which C_f is the volume fraction of the liquid and $(1 - C_f)$ the volume fraction of the gas. C_b is the part of a cut cell that is open to flow. ρ_f is the density of the liquid, and ρ_a the density of the gas. Refer to Fig. 4.4c for the definitions of the volume fractions.

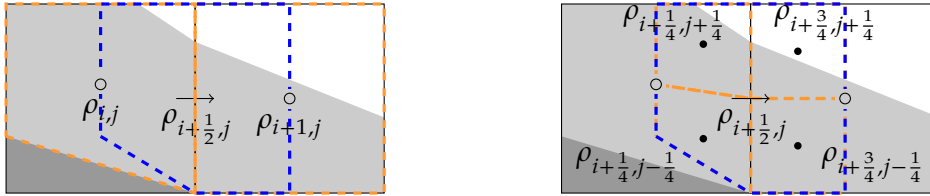
It is straightforward to use Eq. (4.16) for finding densities $\rho_{i,j}$ in the centers of continuity control volumes. The discussion below is about how to determine the aforementioned densities in momentum control volumes.

4.4.2.1 Discretization of ρ^n and ρ^{n+1}

Consider the horizontal momentum control volume indicated by the blue dashed line in Fig. 4.9a. The continuity control volumes on either side are indicated by continuous orange lines. The term $(\rho u)^n$ in the momentum equation is evaluated as $(\rho_{i+\frac{1}{2},j} u_{i+\frac{1}{2},j})^n$. In our former method [75] density $\rho_{i+\frac{1}{2},j}^n$ is obtained from weighted averaging using the volume apertures in continuity control volumes

$$\rho_{i+\frac{1}{2},j}^n = \frac{C_{b,i+1,j} \delta x_{i+1} \rho_{i+1,j}^n + C_{b,i,j} \delta x_i \rho_{i,j}^n}{C_{b,i+1,j} \delta x_{i+1} + C_{b,i,j} \delta x_i}. \quad (4.17)$$

Averaging the density like this for non-conservative formulations of the equations does not necessarily lead to the problems described in the introduction, so it does not require a consistent discretization. Our problems began when starting to work with the conservative form of the governing equations.



(A) Cell-weighted averaging using continuity control volumes (—). (B) Consistent density discretization with sub-volumes in (---).

FIGURE 4.9. Density calculation at the center of momentum control volume; the continuity control volume (—) and the horizontal momentum control volume (---), the area used by the averaging/discretization method (---), the cell center (o), the center of a quarter of a cell (•). Body is indicated by ■. Fluid is indicated by ■.

A discretization of the density consistent with the size of the momentum control volume is obtained by dividing the momentum control volume in four sub-volumes as in Zuzio et al. [320] but now taking into account the volume apertures in cut cells. By choosing four sub-volumes instead of two, one makes sure that the discretization of the density is also consistent between horizontal and vertical momentum control volumes. For each of the sub-volumes the volume apertures are determined, after which the density in a sub-volume, such as $\rho_{i+\frac{1}{4},j+\frac{1}{4}}$ in Fig. 4.9b, is determined according to Eq. (4.16).

The density for the term $(\rho u)^n$ in a horizontal momentum control volume is then found with

$$\rho_{i+\frac{1}{2},j}^n = \frac{1}{\text{bottom}} (C_{b,i+\frac{3}{4},j+\frac{1}{4}} \delta x_{i+1} \rho_{i+\frac{3}{4},j+\frac{1}{4}}^n + C_{b,i+\frac{3}{4},j-\frac{1}{4}} \delta x_{i+1} \rho_{i+\frac{3}{4},j-\frac{1}{4}}^n + C_{b,i+\frac{1}{4},j+\frac{1}{4}} \delta x_i \rho_{i+\frac{1}{4},j+\frac{1}{4}}^n + C_{b,i+\frac{1}{4},j-\frac{1}{4}} \delta x_i \rho_{i+\frac{1}{4},j-\frac{1}{4}}^n), \quad (4.18)$$

in which

$$\text{bottom} = C_{b,i+\frac{3}{4},j+\frac{1}{4}} \delta x_{i+1} + C_{b,i+\frac{3}{4},j-\frac{1}{4}} \delta x_{i+1} + C_{b,i+\frac{1}{4},j+\frac{1}{4}} \delta x_i + C_{b,i+\frac{1}{4},j-\frac{1}{4}} \delta x_i.$$

The term ρ^{n+1} in Eq. (4.9) is discretized in the same way as in Eq. (4.18). Something that we have not seen being discussed in literature is the discretization of the viscosity μ^n near the interface between fluids. As the viscosity in liquids can be quite different from the viscosity in gases, it seemed ‘consistent’ to also apply the discretization in Eq. (4.18) to the viscosity μ^n . The evaluation of this decision has been made explicit for the case of the 2D rising bubble in Sec. 4.6.

4.4.2.2 Convective term with ρ^*

The convective term $\oint_{S_m} \rho^* \mathbf{u} (\mathbf{u} \cdot \mathbf{n}) dS$ in the momentum equation requires discretization of ρ^* on momentum control volumes. Our older method [75] used weighted averaging based on the volume apertures in continuity control volumes for ρ^* , see Eq. (4.17). The new, consistent discretization is similar to [320], but now with apertures. The objective of the discretization of ρ^* is to keep the fluxes $\rho \mathbf{u} dS$ in the transport equation, discretized on continuity control volumes, consistent with the momentum fluxes $\rho^* \mathbf{u} dS$ in the convective term of the momentum equation. For this reason, the term $\rho^* \mathbf{u}$ in the momentum flux is discretized by means of mass fluxes through the faces of the momentum control volume as

$$\rho^* \mathbf{u} = \rho_f \frac{1}{\delta t A} \delta C_f + \rho_a \frac{1}{\delta t A} (\mathbf{u} \delta t A - \delta C_f), \quad (4.19)$$

in which A is the area of the face open for flow depending on a_b and the size of the face. Note that the mass flux δC_f needs to be determined in a similar way to what is shown in Fig. 4.6, but then through the boundary of a momentum control volume instead of a continuity control volume. The parameters required for determining ρ^* along the faces of a horizontal momentum control volume – velocities, apertures and mass fluxes – are shown in Figs. 4.10a through 4.10c.

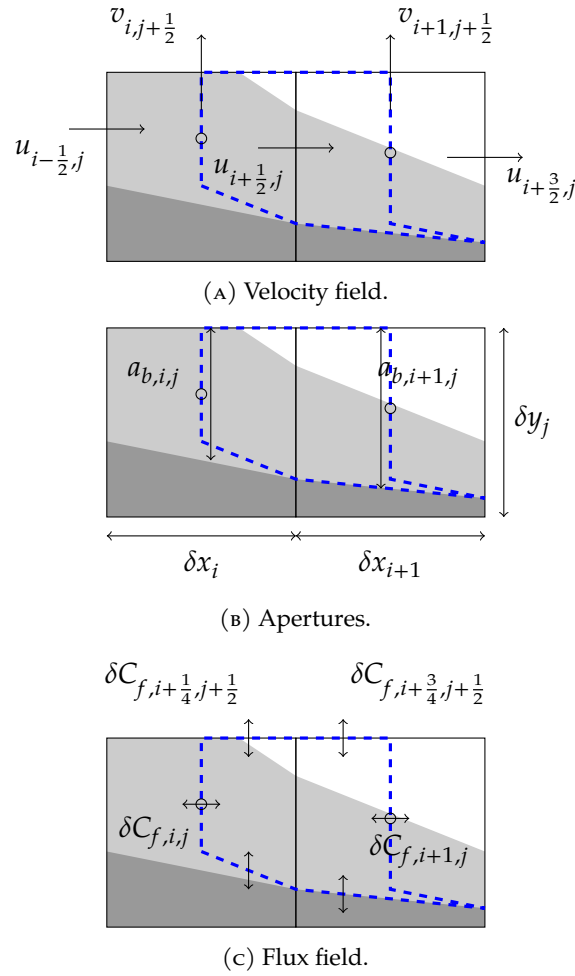


FIGURE 4.10. Horizontal momentum control volume with velocities (a), face apertures (b) and mass fluxes (c) along the faces of the control volume necessary for the consistent discretization of the density ρ^* .

The density ρ^* in Eq. (4.19) in the left face of the horizontal momentum control volume shown in Fig. 4.10 can then be rewritten as

$$\rho_{i,j}^* = \frac{|\delta C_{f,i,j}| \rho_f + |a_{b,i,j} u_{i,j} \delta t \delta y_j - \delta C_{f,i,j}| \rho_a}{|a_{b,i,j} u_{i,j} \delta t \delta y_j|}, \quad (4.20)$$

with the face aperture of the momentum control volume at that location found from

$$a_{b,i,j} u_{i,j} = \frac{1}{2} \left(a_{b,i+\frac{1}{2},j} u_{i+\frac{1}{2},j} + a_{b,i-\frac{1}{2},j} u_{i-\frac{1}{2},j} \right). \quad (4.21)$$

4.4.2.3 Determine $\bar{\rho}$ through temporary continuity equation

The left-hand side of Eq. (4.10) features the term $\bar{\rho}\bar{\mathbf{u}}$. In order to prevent instability, the auxiliary density $\bar{\rho}$ requires a consistent discretization. Such a discretization can be obtained when Eq. (4.11) is used as a temporary continuity equation, see Zuzio et al. [320]. Similar discretizations can be found in Bussmann, Kothe, and Sicilian [29], Raessi and Pitsch [222] and Nangia et al. [190].

For a horizontal momentum control volume, discretization of the temporary continuity equation with apertures to account for cut cells yields

$$\begin{aligned} \bar{\rho}_{i+\frac{1}{2},j} = & \rho_{i+\frac{1}{2},j}^n - \frac{\delta t}{V_{m,h}} (G_{i+1,j}^n - G_{i,j}^n) \delta y_j \\ & - \frac{\delta t}{V_{m,h}} \left(G_{i+\frac{1}{2},j+\frac{1}{2}}^n - G_{i+\frac{1}{2},j-\frac{1}{2}}^n \right) \frac{1}{2} (\delta x_i + \delta x_{i+1}), \end{aligned} \quad (4.22)$$

in which $V_{m,h}$ is the size of the horizontal momentum control volume and

$$G_{i,j}^n = \rho_{i,j}^* \left(a_{b,i,j} u_{i,j}^n + \frac{1}{2} (a_{b,i-\frac{1}{2},j} - a_{b,i+\frac{1}{2},j}) u_b^n \right), \quad (4.23)$$

and

$$G_{i+\frac{1}{2},j+\frac{1}{2}}^n = \frac{1}{2} \left(G_{i+\frac{3}{4},j+\frac{1}{2}}^n + G_{i+\frac{1}{2},j+\frac{1}{2}}^n \right). \quad (4.24)$$

Note the use of the horizontal body velocity u_b in Eq. (4.23). This is different with respect to Zuzio et al. [320].

4.4.2.4 Determine temporary velocity $\bar{\mathbf{u}}$

Apart from density ρ^* , the spatial discretization of the convective term is comparable to Kleefsman et al. [142] and therefore referred to as $C(\rho^*\{\mathbf{u}^n, \mathbf{u}_b^n\})\mathbf{u}^n$. An auxiliary vector field $\bar{\mathbf{u}}$ is solved from the discrete form of Eq. (4.10) that reads

$$\bar{\rho}\bar{\mathbf{u}} = \rho^n \mathbf{u}^n - \delta t (\Omega_m^{n+1})^{-1} C^n(\rho^*\{\mathbf{u}^n, \mathbf{u}_b^n\})\mathbf{u}^n. \quad (4.25)$$

The operators, like the convective operator C and momentum control volume operator Ω_m , include the cell face apertures a_b and body apertures C_b . The operators are explained in more detail by Kleefsman et al. [142].

For the sake of the discussion, Forward Euler time integration of the momentum equation was used in the notation up to here. When using a second-order upwind discretization in the convective term of the momentum equation combined with Forward Euler time integration, it comes with a Courant stability limit that is too low for practical simulation. Using a one-step Adams-Bashforth time integration

of the momentum equation instead yields a larger stability region when using a second-order upwind discretization [292], leading to the criterion that the Courant number should remain smaller or equal to 0.25. The convective term $C^n(\rho^*\{\mathbf{u}^n, \mathbf{u}_b^n\})\mathbf{u}^n$ in Eq. (4.25) then becomes $\frac{3}{2}R^n - \frac{1}{2}R^{n-1}$ with

$$\begin{aligned} R^n &= -C^n((\rho^*)^n\{\mathbf{u}^n, \mathbf{u}_b^n\})\mathbf{u}^n \text{ and} \\ R^{n-1} &= -C^{n-1}((\rho^*)^{n-1}\{\mathbf{u}^{n-1}, \mathbf{u}_b^{n-1}\})\mathbf{u}^{n-1}. \end{aligned} \quad (4.26)$$

The use of Adams-Bashforth scheme for the convective term implies that this scheme also needs to be used for the advective term of the auxiliary density field. When doing so, spurious velocities are introduced around the interface. Because the Adams-Bashforth uses two different time levels in one step, it is expected that we need the same for the densities ρ^* . However, the densities at the old time level $n - 1$ are based on an older volume fraction field. This means that they do not match the VOF mass fluxes at time level n and can lead to density values in control volumes without an interface at time level n . Time integration as in Eq. (4.26) is not consistent and can lead to interface distortions. To prevent interface distortions, Eq. (4.26) needs to be solved as follows

$$R^n = -C^n((\rho^*)^n\{\mathbf{u}^n, \mathbf{u}_b^n\})\mathbf{u}^n \text{ and } R^{n-1} = -C^n((\rho^*)^n\{\mathbf{u}^{n-1}, \mathbf{u}_b^{n-1}\})\mathbf{u}^{n-1}, \quad (4.27)$$

where $(\rho^*)^n$ is based on the volume fluxes to find C_f^{n+1} . The same is true for the operators accounting for the body.

An example of the effect of using Eq. (4.26) instead of Eq. (4.27) is shown for a high-density horizontal translating bubble in vacuum. The results in Fig. 4.11 are shown after 0.04[s] where the bubble have an initial speed of 10[m/s].



FIGURE 4.11. Comparison of the effect of using Eq. (4.26) and Eq. (4.27) on the free surface deformation. Black indicates volume fraction C_f equal to one. White indicates volume fraction C_f equal to zero.

4.4.3 Auxiliary vector field $\tilde{\mathbf{u}}$

The spatial discretization of gravity in the external force term \mathbf{F}_f is the same as Kleefsman et al. [142], and therefore not specifically discussed. \mathbf{F}_f also contains

the capillary force at the interface between fluids.

A continuum surface force (CSF) model is used for modeling the capillary force. The CSF-model imposes surface tension as a body force [9, 19], for which interface curvature is an input. The curvature κ is calculated in every S-cell and C-cell, using a local height function and is defined for every continuity control volume. The direction in which "height" is defined depends on the largest component of the interface's normal vector found from the PLIC reconstruction. The combination of the CSF-model and the height function ensures that the curvature calculation is not the governing error resulting from the imbalance between pressure and surface tension [1]. A height value H consists of the sum of the volume fractions in three cells in height direction as illustrated in Fig. 4.12. The curvature of the continuity control volume with indices (i, j) in Fig. 4.12 is found from

$$\kappa_{i,j} = \frac{1}{\delta x_i} \left(\frac{\frac{\partial H_{y,i+1}}{\partial x}}{\left(1 + \left(\frac{\partial H_{y,i+1}}{\partial x}\right)^2\right)^{3/2}} - \frac{\frac{\partial H_{y,i-1}}{\partial x}}{\left(1 + \left(\frac{\partial H_{y,i-1}}{\partial x}\right)^2\right)^{3/2}} \right), \quad (4.28)$$

where

$$\kappa = \frac{H''}{(1 + H'^2)^{3/2}} \quad \text{and} \quad H_{y,i} = \sum_{k=-1}^1 C_{f,i,j+k} \delta y_{j+k}$$

and

$$\frac{\partial H_{y,i+1}}{\partial x} = \frac{H_{y,i+1} - H_{y,i}}{\frac{1}{2}(\delta x_{i+1} + \delta x_i)} \quad \text{and} \quad \frac{\partial H_{y,i-1}}{\partial x} = \frac{H_{y,i} - H_{y,i-1}}{\frac{1}{2}(\delta x_{i-1} + \delta x_i)}$$

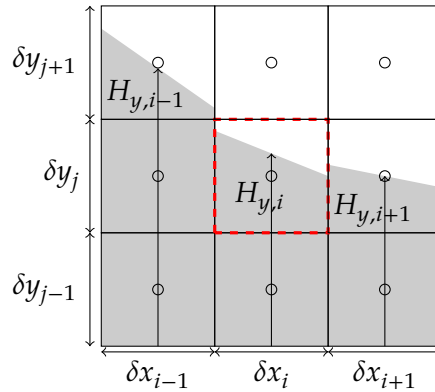


FIGURE 4.12. Stencil for curvature κ in case of a horizontally oriented interface using continuity control volumes. Fluid is indicated by \blacksquare . The considered continuity control volume is given by $(-)$.

For the horizontal momentum cell in Fig. 4.13 the discretization of the capillary force becomes

$$\mathbf{F}_{\sigma, i+\frac{1}{2}, j} = \frac{1}{\rho_{i+\frac{1}{2}, j}^{n+1}} \sigma \kappa_{i+\frac{1}{2}, j} (C_{f, i+1, j} - C_{f, i, j}) \delta y_j, \quad (4.29)$$

in which

$$\kappa_{i+\frac{1}{2}, j} = \begin{cases} (\kappa_{i, j} + \kappa_{i+1, j})/2, & \text{if } \kappa_{i, j} \text{ and } \kappa_{i+1, j} \text{ are defined and labeled as S} \\ \kappa_{i, j}, & \text{if } \kappa_{i+1, j} \text{ is not defined and labeled as E} \\ \kappa_{i+1, j}, & \text{if } \kappa_{i, j} \text{ is not defined and labeled as E} \\ 0, & \text{if } \kappa_{i, j} \text{ and } \kappa_{i+1, j} \text{ are not defined and labeled as E} \end{cases}.$$

The subscripts indicate the position relative to continuity control volume with indices (i, j) , where $i + \frac{1}{2}, j$ indicates the center of the horizontal momentum control volume shown in Fig. 4.13. The density $\rho_{i+\frac{1}{2}, j}^{n+1}$ in Eq. (4.29) is determined as in Eq. (4.18).

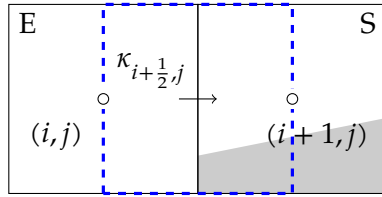


FIGURE 4.13. Cell face value of κ when using PLIC. The cells are labeled as E-cell and S-cell. Fluid is indicated by ■. Horizontal momentum control volume is illustrated by (—).

The discussion of the capillary force completes the discretization of the external force term \mathbf{F}_f . The spatial discretization of the viscous term is comparable to Wemmenhove et al. [291] and referred to as $\mathcal{D}^n \mathbf{u}^n$, keeping in mind that here the kinematic viscosity μ^n near the interface is discretized 'consistently' as in Eq. (4.18). Using these,

$$\rho^{n+1} \tilde{\mathbf{u}} = \bar{\rho} \bar{\mathbf{u}} - \delta t \left(\mathbf{F}_f - \nabla \cdot (\mu^n (\nabla \mathbf{u}^n + (\nabla \mathbf{u}^n)^T)) + \nabla p^n \right), \quad (4.30)$$

where

$$\tilde{\mathbf{u}} = \bar{\mathbf{u}} - \delta t \left(\Omega_m^{n+1} \right)^{-1} \left(\mathbf{F}_f - \frac{1}{\rho^{n+1}} \mathcal{D}^n \mathbf{u}^n + \frac{1}{\rho^{n+1}} (M_0^T)^{n+1} p^n \right), \quad (4.31)$$

and the term $\bar{\mathbf{u}}$ is an auxiliary vector field with the contributions of the convective term, see Eq. (4.25) (or Eq. (4.27) when using Adams-Bashforth).

4.4.4 System of pressure Poisson equation and equation of motion

The continuity equation is solved for the continuity control volumes. When the densities away from the interface are not allowed to vary, the discrete representation of the continuity equation can be written as

$$M_0^{n+1} \mathbf{u}^{n+1} = -M_b^{n+1} \mathbf{u}_b^{n+1}, \quad (4.32)$$

with \mathbf{u} the vector of fluid velocities, M_0 the discrete divergence operator working on the fluid velocities, \mathbf{u}_b the velocity of the body imposing a boundary condition on the flow and M_b the discrete divergence operator working on those boundary velocities.

When \mathbf{u}^{n+1} is solved from Eq. (4.8), it is substituted into Eq. (4.32), which results in a Poisson equation for the pressure

$$\delta t M_0^{n+1} (\Omega_m^{n+1})^{-1} \frac{1}{\rho^{n+1}} (M_0^T)^{n+1} \delta p - M_b^{n+1} \mathbf{u}_b^{n+1} = M_0^{n+1} \tilde{\mathbf{u}}. \quad (4.33)$$

The operators Ω_m^{n+1} , M_0^{n+1} and M_b^{n+1} depend on the time-varying volume apertures C_b^{n+1} and face apertures a_b^{n+1} . The operators are explained in more detail by Kleefsman et al. [142] and Fekken [90].

The motion of the body is solved from

$$\mathbf{u}_b^{n+1} = \mathbf{u}_b^n + \delta t m_b^{-1} \left(m_b \mathbf{g} + \frac{1}{2} A_f^{n+1} (p^n + \delta p) + \frac{1}{2} A_f^n p^n \right), \quad (4.34)$$

using Crank-Nicolson time integration. Here, m_b represents the body's mass and A_f^{n+1} the operator that integrates the pressure over the surface of the body. The operator A_f^{n+1} makes use of the cell face apertures a_b^{n+1} to determine the area of the body that the pressure acts on. Multiplying the operator with the pressure field results in a force vector.

Using an auxiliary body velocity

$$\tilde{\mathbf{u}}_b = \mathbf{u}_b^n + \delta t m_b^{-1} \left(m_b \mathbf{g} + \frac{1}{2} (A_f^{n+1} + A_f^n) p^n \right), \quad (4.35)$$

and the Poisson equation in Eq. (4.33), the coupled system of fluid and body can be written in compact form as

$$\begin{bmatrix} A & -M_b^{n+1} \\ \frac{\delta t}{2m_b} A_f^{n+1} & \mathbf{I} \end{bmatrix} \cdot \begin{bmatrix} \delta p \\ \mathbf{u}_b^{n+1} \end{bmatrix} = \begin{bmatrix} M_0^{n+1} \tilde{\mathbf{u}} \\ \tilde{\mathbf{u}}_b \end{bmatrix}, \quad (4.36)$$

where A represents the combination of the operators on the left-hand side of Eq. (4.33) associated with δp . Solving the system will find the pressure change δp and the body velocities \mathbf{u}_b .

4.4.5 New velocity field

The new fluid velocity field is solved from the pressure change δp as

$$\mathbf{u}^{n+1} = \tilde{\mathbf{u}} - \delta t (\Omega_m^{n+1})^{-1} \frac{1}{\rho^{n+1}} (M_0^T)^{n+1} \delta p. \quad (4.37)$$

4.5 Proof of principle simulations

Our method is verified by means of several proof of principle simulations that were specifically designed for this work. These simulations show the properties of the method with regard to preserving mass, momentum and the shape of the interface. The implementation of the method that is called "consistent", abbreviated with "C", is compared with the non-consistent implementation ("NC") of Eijk and Wellens [75]. The non-consistent method makes use of weighted averaging to determine densities at control volume boundaries. Compared with the consistent implementation described above, the former non-consistent method uses no auxiliary density field, no density discretization based on the mass fluxes through the boundaries of a momentum control volume, and the non-conservative momentum equation is solved.

4.5.1 Moving wedge

The first moment "problems" were encountered because of using a non-consistent method was for the case of a moving wedge [18]. The case represents a liquid wave impact against a wall in a LNG container undergoing motion. The wave is represented as a wedge, because the objective in the original article was to study the effect of rise time on the dynamic deformation of the container wall. The fluid configuration is illustrated in Fig. 4.14a. The domain is 1 [m] by 1 [m] with 80 grid cells in each direction. That means that the height of the wedge is captured by 16 cells. The density of the liquid is 10^3 [kg/m³]. The air density is set equal to 10^{-9} [kg/m³] to exclude effects that air may have on the wave impact. Typically we find that the bigger the density ratio between liquids, the larger the issues associated with non-consistent modeling. The wedge shape should be preserved before the impact takes place.

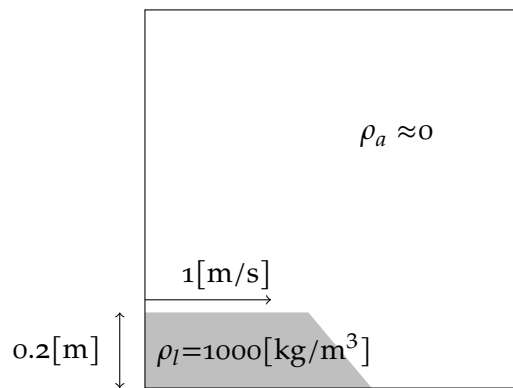
The simulation result with NC, however, shows a distorted interface between fluids. It is shown in Fig. 4.14c for time instance 0.04[s]. Furthermore, it is expected that the momentum in vertical direction remains zero before impact. The total vertical momentum I_{vert} is calculated at each time step as

$$I_{vert} = \sum_{i,j+\frac{1}{2}} (\rho^n v^n dV_{m,v})_{i,j+\frac{1}{2}}, \quad (4.38)$$

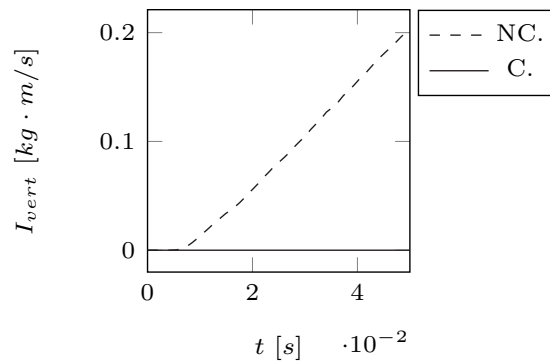
where $dV_{m,v,i,j+\frac{1}{2}}$ is the size of the vertical momentum control volume. The evolution of I_{vert} over time is shown in Fig. 4.14b. It is clear that the vertical momentum

for the non-consistent method shows a spurious increase over time. From Zuzio et al. [320] came the inspiration that the shape deformation could be due to the non-consistent discretization. Where the spurious momentum for a low density ratio scales with the flow velocity, for a high density ratio the spurious momentum change due to non-consistent modeling becomes dominant over the changes that scale with the velocity.

With the former method (NC.), momentum transport and mass transport are not consistent; they are decoupled. The non-consistency results in spurious velocities around the interface. Fig. 4.14d shows the result of applying the new method (C.). No strange interface distortion is visible anymore.



(A) Flow domain.

(B) Change in vertical momentum I_{vert} .



(c) Non-consistent with C-labeling. (d) Consistent with C-labeling.

FIGURE 4.14. Moving wedge at $0.04[s]$ for a wedge height represented by 16 grid cells.

4.5.2 *Diagonally translating high density droplet*

After the wedge case with grid-aligned translation, the next case considers diagonal translation and the effect of a split scheme. A diagonally translating droplet with a high density compared to the surrounding gas is modeled. The case was proposed by Bussmann, Kothe, and Sicilian [29] and also used in Zuzio et al. [320]. This case is designed to be a good indicator for non-consistency between mass and momentum transport, as the high density ratio quickly leads to momentum losses and interface deformation.

The density ratio, 10^6 over $1[\text{kg}/\text{m}^3]$, is the same as used by others [98, 222, 320]. The large ratio will mainly affect the convective term in Eq. (4.25). The effect of surface tension and viscosity is neglected. The gravity constant is zero. A square domain with sides of length $1[\text{m}]$ is used with an initial velocity field of $10[\text{m}/\text{s}]$ in x and y directions throughout both high and low density fluid. The simulated time is $0.05[s]$. The radius of the droplet is $0.15[\text{m}]$. A Courant restriction of 0.2 is used. The setup is illustrated in Fig. 4.15.

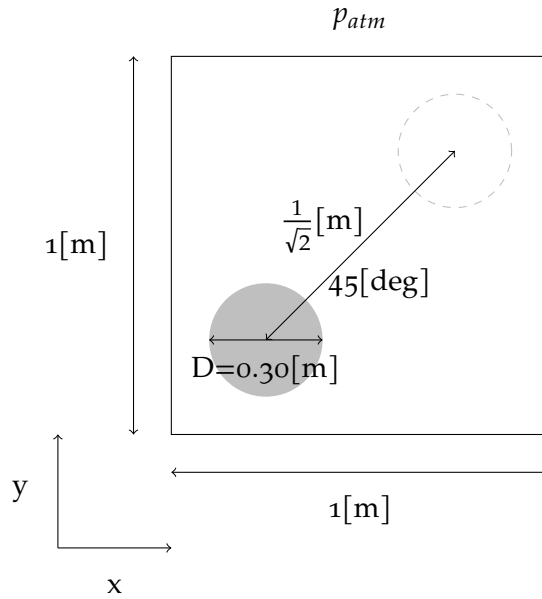


FIGURE 4.15. Diagonally translating droplet: setup of simulation domain.

With the large density ratio at the interface, we expect that the interaction between fluids is small and that the shape of the droplet is preserved. The kinetic energy should be conserved during the simulation. It is calculated using the following equation

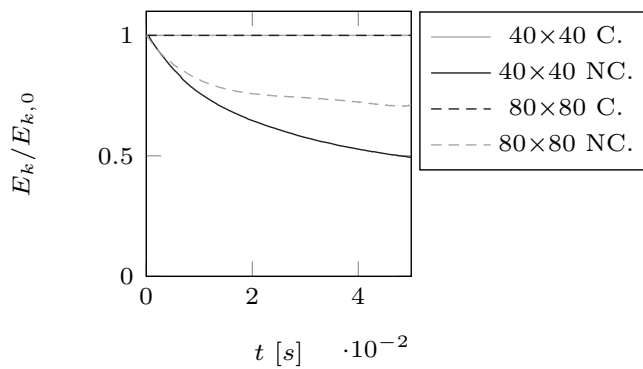
$$E_k = \frac{1}{2} \sum_{i,j} \rho_{i,j} \left(\left(\frac{1}{2} (u_{i+\frac{1}{2},j} + u_{i-\frac{1}{2},j}) \right)^2 + \left(\frac{1}{2} (v_{i,j+\frac{1}{2}} + v_{i,j-\frac{1}{2}}) \right)^2 \right) dV_{c,i,j}, \quad (4.39)$$

where u and v are the horizontal and vertical velocity, respectively. The subscripts indicate the position of the velocity in the staggered arrangement of variables within a cell. The energy losses over time are depicted in Fig. 4.16a for the non-consistent and consistent method. The new consistent method is better at preserving kinetic energy in comparison with the original non-consistent method. Even coarse meshes demonstrate good energy preserving behavior with the consistent method. Fig. 4.16b shows an enlargement of the graph of energy over time for the consistent method to investigate grid convergence. The energy loss becomes smaller for higher grid resolutions. The (small) spikes in energy are related to the droplet propagating through cells.

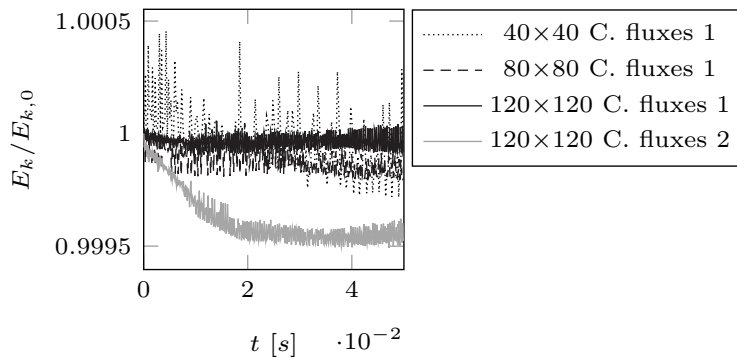
All results in this work were obtained with the COSMIC interface advection method. The densities ρ^* and $\bar{\rho}$, see Eqs.(4.21) and (4.22), are based on the mass 'fluxes 1' calculated in the first step of the COSMIC scheme, see the box with number 1 in Eq. (4.14). One of the results, called 'fluxes 2', was obtained with densities ρ^* and $\bar{\rho}$ based on the mass fluxes indicated by the box with number 2

in Eq. (4.15) to evaluate the differences.

The simulation with these densities based on the fluxes indicated by 2 had the same setup as described above, and a grid resolution of 120x120. Its result in terms of the kinetic energy is shown in Fig. 4.16b. Result 'fluxes 2' is accompanied by higher velocities near the interface, with, hence, smaller time steps to satisfy the Courant criterion. The increased computational effort involved in using mass fluxes 2 does not lead to improved kinetic energy preservation. On the contrary, Fig. 4.16b shows that the non-consistency in using mass fluxes 2 leads to more kinetic energy loss than even the coarsest-grid simulation that is based on mass fluxes 1. In the remainder, the densities ρ^* and $\bar{\rho}$ are based on fluxes 1 in Eq. (4.14).



(A) Comparison between consistent discretization method (C.) and the non-consistent method (NC.).



(B) Comparison between grid resolutions for consistent method (C.) with discrete densities based on the fluxes '1' in Eq. (4.14). One result with densities based on '2' in Eq. (4.15). Note that it leads to more energy loss.

FIGURE 4.16. Diagonally translating droplet: kinetic energy as a function of time.

The droplet's interface deformation is illustrated in Fig. 4.17. These figures show that the consistent method with a grid of 80x80 preserves the shape of the droplet



while the non-consistent does not. The C-labeling that was discussed improves the results. Without the extra label, the shape of the droplet is preserved less well and fluids with different densities are kept separate less well. The kinetic energy losses also increase when no C-labels are used from 0.017% to 0.090% with a grid resolution of 40×40 .

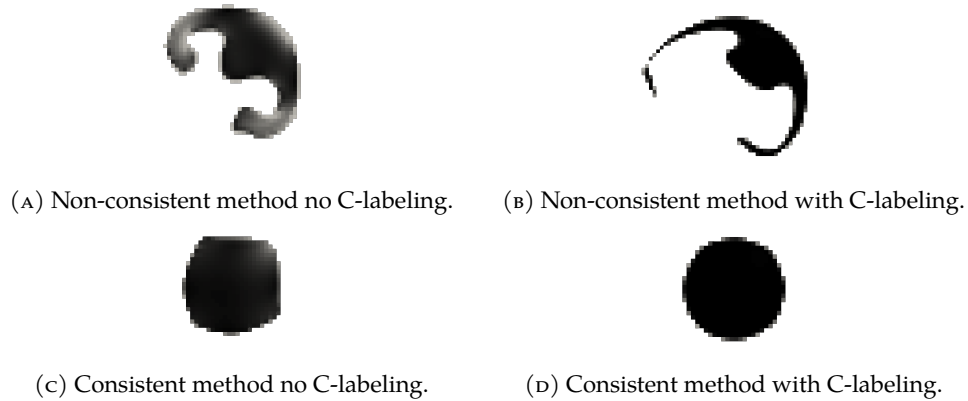


FIGURE 4.17. Diagonally translating droplet (grid 80×80): difference in shape of the interface after $0.05[s]$. Black: $F_s=1.0$ and white: $F_s=0.0$, with grey values in between.

4.5.3 Momentum conservation droplet impact on fixed wall

The next step is to look at momentum conservation after an impact. In this case, one-way interaction is tested between a solid wall and a droplet of fluid. The setup is similar to the case with the droplet translating diagonally through the domain, but, now apertures (C_b, a_b) that represent the solid are involved.

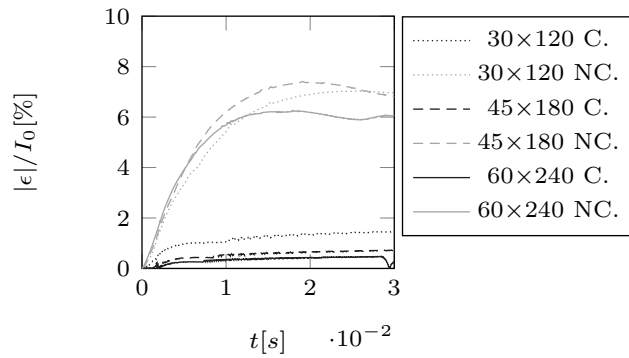
The setup is illustrated in Fig. 4.18 where the dashed line indicates the expected deformation of the fluid droplet, which because of the 2D nature of the setup is actually a fluid cylinder. During the impact of the droplet with the wall, all horizontal momentum is converted to vertical momentum as the droplet exerts a force on the wall. The initial speed of the fluid droplet is $10[m/s]$ and it has a density of $1000[kg/m^3]$. The density of the gas surrounding the fluid is kept low at $10^{-9}[kg/m^3]$, for the same reasons as before. The radius of the cylindrical droplet measures $0.15[m]$ initially. Gravity is equal to zero. The effect of viscosity and surface tension is neglected. After $0.03[s]$, the impact finishes when the fluid jets reach the bottom and top of the domain. The droplet is positioned such that the loss of momentum takes place during the impact and not because of translation. The edge of the wall being impacted is positioned along the center of a cell.

The initial horizontal momentum I^0 is equal to 706.9[kgm/s]. After the impact, loss of horizontal momentum of the fluid should be equal to the integrated force in time acting on the wall. The following equation is used for the horizontal momentum transfer at any time

$$\int_{t^0}^{t^n} F_{b,x}^n dt + \epsilon = \sum_{i+\frac{1}{2},j} (\rho^n u^n dV_{m,h})_{i+\frac{1}{2},j} - I^0, \quad (4.40)$$

where $F_{b,x}$ is the force acting on the wall as a function of time t^n , $V_{m,h}$ is the volume of the corresponding momentum control volume with indices $(i + \frac{1}{2}, j)$, n the time level, and I^0 the initial momentum. The value ϵ indicates the fluid-structure interaction error during the transfer. The case is simulated with the consistent (C.) and the non-consistent (NC.) method for three different grid resolutions. The integral in (4.40) is solved using the midpoint rule.

The value ϵ as a function of time is plotted in Fig. 4.19a for different grid resolutions and both the non-consistent and the consistent method. The results show convergence. The error for the non-consistent method is an order higher than for the consistent method. The error of the non-consistent method first goes up, but then, unexpectedly, it goes down. It was found that the error goes down because the free surface started to form protrusions similar to those in Fig. 4.14c with a velocity in opposite direction. Negative velocities reduce the error as it is defined in Eq. (4.40). The maximum errors are given in Tab. 4.19b.



(A) Value of the error ϵ over time.

Grid	30x120	45x180	60x240
C. [$I_0\%$]	1.46	0.72	0.48
NC. [$I_0\%$]	7.03	7.40	6.26

(B) Maximum value of the error ϵ .

FIGURE 4.19. Droplet impact with fixed wall: fluid-structure interaction error ϵ .



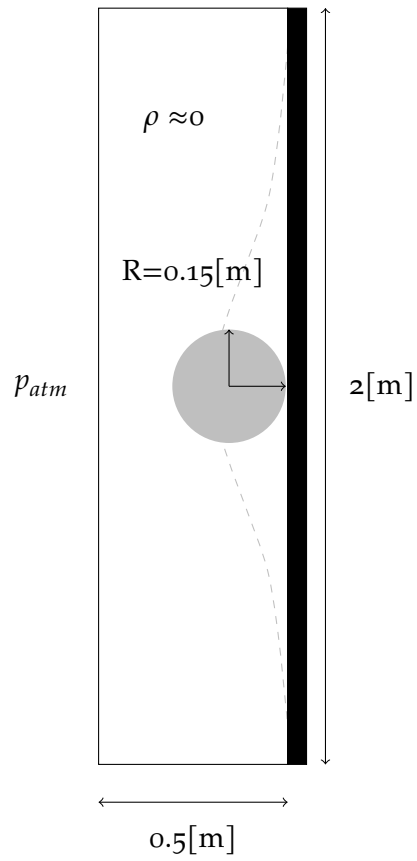


FIGURE 4.18. Droplet impact with fixed wall: setup of simulation domain.

4.5.4 Two-way fluid-structure interaction

Two-way fluid-structure interaction is evaluated next. A droplet of fluid with a horizontal velocity will impact with a wall that is initially at rest but free to move. Special about this case is that the apertures are not only included, but that their size now also depends on time. A similar configuration is used as in the previous section, but now the change in horizontal momentum of the fluid should be equal to the gain of (horizontal) momentum of the structure after impact.

The setup is illustrated in Fig. 4.20. The speed of the droplet is 10[m/s] initially, while the rectangular wall is at rest. The droplet has a smaller initial radius than the previous case with the fixed wall to make sure the wall has reached its limit velocity before the fluid jets hit the top and bottom of the domain. The droplet, with a radius of 0.10[m] is positioned 0.06[m] in front of the rectangular wall at the start of the simulation. The rectangular wall has a height of 0.9[m] and a width of 0.19[m] , centered at 0.655[m] . The impact takes place after around 0.006[s] . The gravity constant is set to zero. The density of the fluid and the structure both are $1000\text{[kg/m}^3\text{]}$. The density of the gas around the droplet and the wall is equal to $10^{-9}\text{[kg/m}^3\text{]}$. The Courant restriction equals 0.2 .

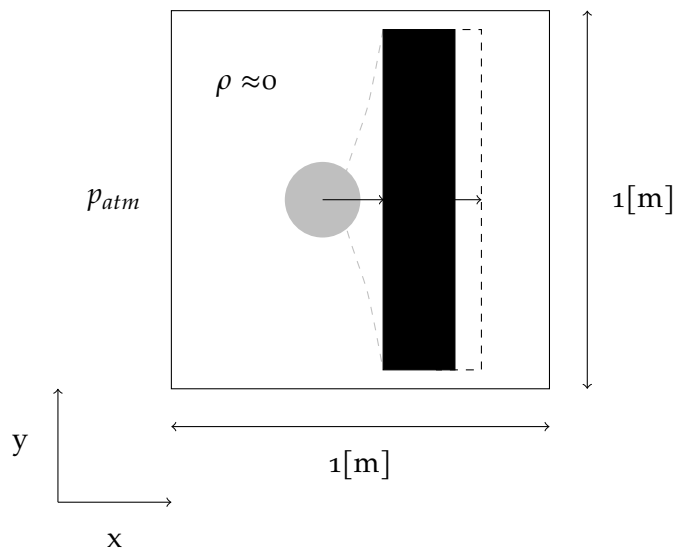


FIGURE 4.20. Two-way fluid-structure interaction: setup of simulation domain with fluid droplet impacting a wall that is free to move.

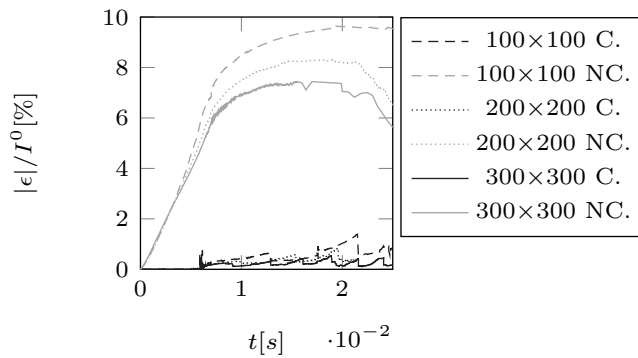
We expect that all the horizontal momentum of the fluid is converted into horizontal momentum of the structure. The data required for the comparison is straightforward to obtain from the simulation results until the jets created by the

interaction with the structure hit the bottom and top of the domain. Horizontal momentum conservation is calculated using

$$m_b u_b^n + \epsilon = \sum_{i+\frac{1}{2},j} (\rho^n u^n dV_{m,h})_{i+\frac{1}{2},j} - I^0, \quad (4.41)$$

where I^0 is $314.16[\text{kgm/s}]$.

The case is simulated with three different grid resolutions. The results for ϵ are illustrated in Fig. 4.21. Similar results are obtained as for the case discussed in the previous section with the solid wall; the errors are of the same order. Note that also here, the errors of the NC. simulations goes down because of the protrusions in the interface with negative horizontal velocities.



(A) Value of the error ϵ over time.

Grid	100x100	200x200	300x300
C. [$I_0\%$]	1.39	0.83	0.56
NC. [$I_0\%$]	9.70	8.30	7.46

(B) Maximum value of the error ϵ .

FIGURE 4.21. Fluid cylinder: fluid-structure interaction error ϵ due moving wall impact for consistent method (C.) and non-consistent method (NC.).

4.5.5 Analyzing the momentum losses

The governing error appears to be related to an inconsistency between the auxiliary density field $\bar{\rho}$ and the new density field ρ^{n+1} . The discretization of $\bar{\rho}$, see Eq. (4.22), is based on fluxes through the boundary of a momentum control volume, while the discretization of ρ^{n+1} , see Eq. (4.18), is based on volumes in the four sub-volumes of the momentum control volume. The difference between these two density fields is caused by reconstruction of the interface that changes the distribution of the fluids in the four sub-volumes of a momentum cell to become different from what one would expect based on the fluxes of the momentum control volume alone. Therefore, the source of the error is located near

the interface.

This is investigated by varying the radius R of the droplet in the two-way interaction case with a grid resolution of 200×200 . For the circular shape of the droplet, the number of internal cells varies with the radius squared, while the number of interface cells, which is related to the circumference, varies linearly with the radius. The results of the investigation are in Tab. 4.1. It shows that the momentum errors reduce with increasing radius of the droplet and, hence, with an increase of the number of F-cells over the number of S-cells. In smaller droplets, therefore, the ratio of cells that contribute to the error versus cells that contribute to the total momentum is less favourable. Note that the errors of the consistent simulations in Tab. 4.1 are approximately two orders of magnitude smaller than those in the non-consistent simulations. This is an argument that using the consistent method becomes more relevant for keeping errors in check in even more violent interfacial flows with larger curvature than in the test cases with a droplet impacting the moving and fixed walls.

Potential solutions to decrease these errors further could be omitting the reconstruction of the interface and take the diffusion of the interface for granted, using a collocated arrangement of solution variables, or using the method of Rudman [230] with interface transport and reconstruction on a grid that is twice as fine as the base grid at the expense of computational effort.

R [m]	0.05	0.10	0.15	0.20
Ratio S/F-cells [-]	0.243	0.122	0.079	0.056
Max. ϵ/I_0 trans. [%]	(C.) 0.012 (NC.) 9.45	(C.) 0.009 (NC.) 5.27	(C.) 0.005 (NC.) 3.85	(C.) 0.002 (NC.) 3.06
Max. ϵ/I_0 impact [%]	(C.) 1.20 (NC.) 3.98	(C.) 0.82 (NC.) 3.03	(C.) 0.53 (NC.) 2.51	(C.) 0.45 (NC.) 2.04

TABLE 4.1. Effect of the size of the droplet radius in the case of the two-way interaction with the moving wall for a grid of 200×200 . The radius is a measure of the number of interface cells (S, C) over internal cells (F). The maximum momentum loss during translation (trans.) and after impact are given for consistent (C.) and non-consistent (NC.) simulations.

4.5.6 Computational costs

The difference in computational cost between the consistent method and the non-consistent method is not straightforward. Considering the droplet impact on a fixed wall with grid 60×240 , the consistent method needed 14% more time steps than the non-consistent method. The increase of computational costs is caused by the discontinuous handling of the density, resulting in a better prediction of the moment of impact with higher flow velocities immediately after impact and,

hence, smaller time steps because of the Courant restriction. Similarly, for the two-way fluid-structure interaction with the moving wall and grid 300x300, the consistent method needed 16% more time steps. However, for the diagonally translating high density droplet the number of computational time steps with grid 80x80 is almost 50% higher for the non-consistent scheme with respect to the consistent scheme. The increase is due to spurious velocities at the distorted interface.

4.6 Comparison benchmark & experiment

Results of the consistent method (this work) and of the older non-consistent method [75] are compared with two benchmarks and with experimental results.

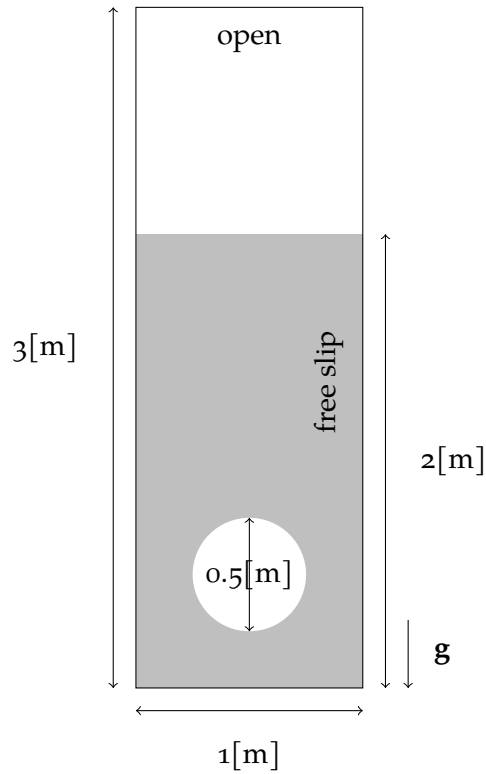
4.6.1 Rising bubble

The first case is a 2D rising bubble benchmark. Our results, with the consistent method (C., this work) and the non-consistent (NC.) method [75], are compared with the results of Hysing et al. [123]. Literature has shown that non-consistent methods with CLSVOF for the interface [252, 254] give good results for rising bubble simulations. Therefore, when referring to 'non-consistent' we are only referring to Eijk and Wellens [75]. The proof of principle simulations in the previous section mainly evaluated the convective term in the momentum equation. Simulating the rising bubble also requires accurate modeling of capillary, diffusive, and buoyancy effects. New in this work is the 'consistent' discretization of the viscosity near the interface, where other methods typically make use of harmonic averaging for the viscosity [75, 222]. The focus for the rising bubble case is to evaluate the discretization of the viscosity and the curvature.

The benchmark of Hysing et al. [123] with the 2D rising bubble was created due to the absence of analytical solutions and is based on the average of the results of high grid resolution simulations with several methods. The initial fluid configuration of the 2D rising bubble case is illustrated in Fig. 4.22a. The fluid variables per specific instance of the case are given in the ta in Fig. 4.22b. Results of different simulations are compared in terms of the velocity of the bubble over time, which is calculated as the mean of the vertical velocities in the cells contained within the contour of the bubble

$$v_c = \frac{\int_{V_b} v dV}{\int_{V_b} dV} = \frac{\sum_{E,C,S} \frac{1}{2}(v_n + v_s) \cdot (1 - C_f)V}{\sum_{E,C,S} (1 - C_f)V}, \quad (4.42)$$

in which V_b and v_c are the volume of the bubble and the terminal velocity, respectively. The bubble is tracked based on the labels. Only cells with labels C, S and E contribute to the average velocity. The subscripts of the velocities v_n and v_s indicate the northern and southern velocity in the staggered arrangement.



(A) Setup of flow domain.

Benchmark	ρ_l [$\frac{kg}{m^3}$]	ρ_g [$\frac{kg}{m^3}$]	μ_l [$\frac{kg}{ms}$]	μ_g [$\frac{kg}{ms}$]	σ [$\frac{N}{m}$]	Re [-]
1	1000	100	10	1	24.5	35
2	1000	1	10	0.1	1.96	35

(B) Fluid properties of the two instances of the benchmark.

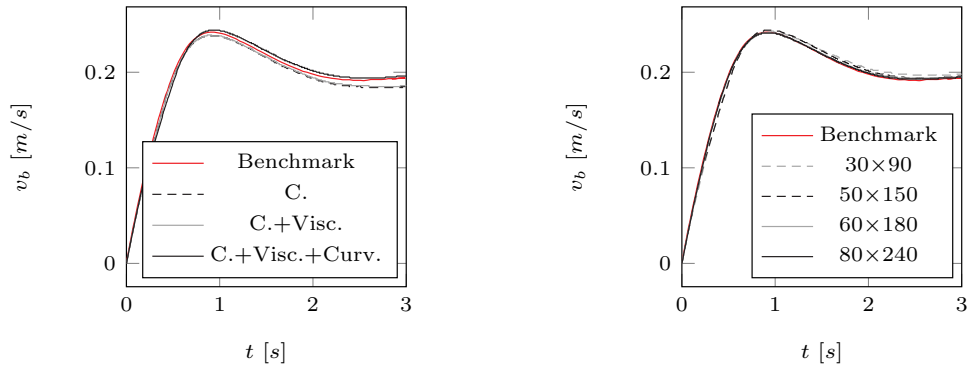
FIGURE 4.22. 2D Rising bubble benchmark.

The first instance in the table in Fig. 4.22b does not have large fluid property ratios. The viscosity and density of the liquid are both only one order of magnitude higher than for the gas bubble. As discussed in earlier sections, a low ratio between fluid densities is expected to lead to small differences between the consistent (C., this work) approach and the non-consistent (NC.) approach [75]. The NC. results are therefore omitted from this part of the benchmark.

The base case for simulating the first benchmark is the consistent method for the density (this work), harmonic averaging of the viscosity near the interface, and computation of the curvature with a stencil of 3×3 cells. One by one, the improvements discussed in this work are evaluated, the consistent discretization of the viscosity (Visc.), as described in Sec. 4.4.2.1, and a larger stencil of 5×5

cells for the curvature (Curv.). The simulation results in terms of the velocity of the bubble as a function of time are shown in Fig. 4.23a.

The maximum velocity reached by the bubble is considered a good error measure for the quantification of the difference between our results and the benchmark. The maximum velocity of the consistent simulation is 1.6% smaller than the benchmark. When using the flux-based viscosity the difference with the benchmark reduces to 1.2%. Changing the stencil for the curvature from 3×3 to 5×5 cells yield a difference with the benchmark of 0.8%. And when everything is combined, the difference with the benchmark in maximum bubble velocity at a grid resolution of 50×150 drops to 0.6%. The convergence of our newest consistent implementation for different grid resolutions is shown in Fig. 4.23b. Even at coarse grid resolutions, the difference with the benchmark can be considered small. The difference with the benchmark in maximum velocity of the bubble at the highest resolution of 80×240 is 0.02%.



(A) Differences with the benchmark of results with different combinations of methods at grid resolution 50×150 .

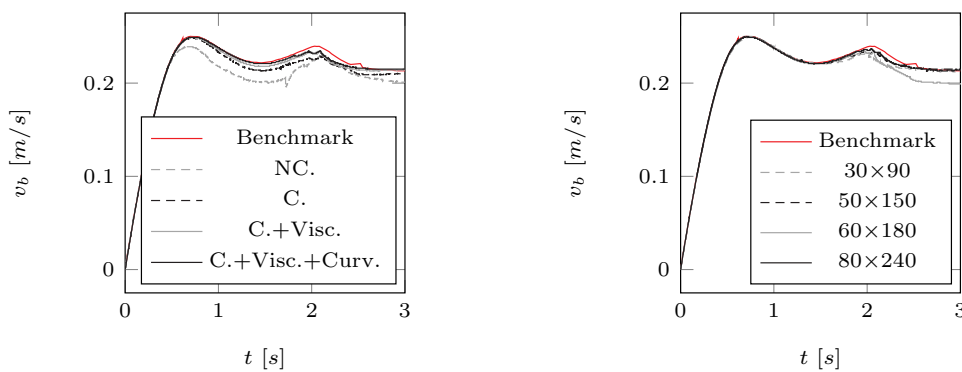
(B) Grid convergence of consistent method (C.+Visc.+Curv.).

FIGURE 4.23. 2D Rising bubble: results of the first instance of the benchmark with low fluid property ratios.

The second instance of the benchmark in Fig. 4.22b has larger fluid property ratios than the first instance. We now expect that the effect of using the consistent approach for the density near the interface is larger. The results of the consistent method (C., this work) and the older non-consistent (NC.) method [75] are compared with the benchmark and with each other to show the difference between the two methods.

Fig. 4.24a compares the velocity of the bubble with large ratios in fluid properties over time between simulations. The maximum velocity of the bubble in the NC. simulation has a difference of 4.45% with the benchmark. When the non-

consistent method for determining the density near the interface is replaced by the consistent method, the difference in maximum velocity with the benchmark reduces to 0.45%. Both the consistent discretization of the viscosity (instead of harmonic averaging) and increasing the stencil for the curvature from 3×3 to 5×5 cells each have a marginal influence on the results and bring the difference in maximum velocity with the benchmark down to 0.44%, which is also the difference with the benchmark when all improvements are combined. The grid convergence study is shown in Fig. 4.24b. The consistent method with improvements is in good agreement with the benchmark, already at low grid resolutions. At the highest resolution of 80×240 , the difference in maximum bubble velocity with the benchmark is as low as 0.03%.



(A) Differences with the benchmark of results with different combinations of methods at grid resolution 50×150 .

(B) Grid convergence of consistent method (C.+Diff.+Curv.).

FIGURE 4.24. 2D Rising bubble: results of the second instance of the benchmark with high fluid property ratios.

The use of C-labels has not been discussed for the comparison with the rising bubble benchmark. C-labels did not significantly affect the velocity of the rising bubble, but they did affect its shape. That becomes most apparent for the rising bubble when C-labels are combined with the older non-consistent method [75]. In Fig. 4.25 the bubble shapes are shown when C-labels are combined with the older method [75] at grid resolution 50×150 . Half of the rising bubble shape is extracted from the non-consistent simulation results by filtering for fluid fractions above 0.05. It is shown to the left. The half of the bubble to the right shows the results when the non-consistent method is combined with C-labels. The C-labels have made sure that a lot less distortion of the shape of the bubble has occurred and that the simulation result is closer to the shape presented in Hysing et al. [123].

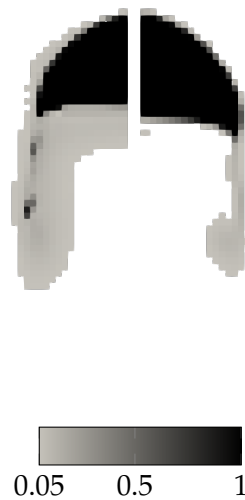


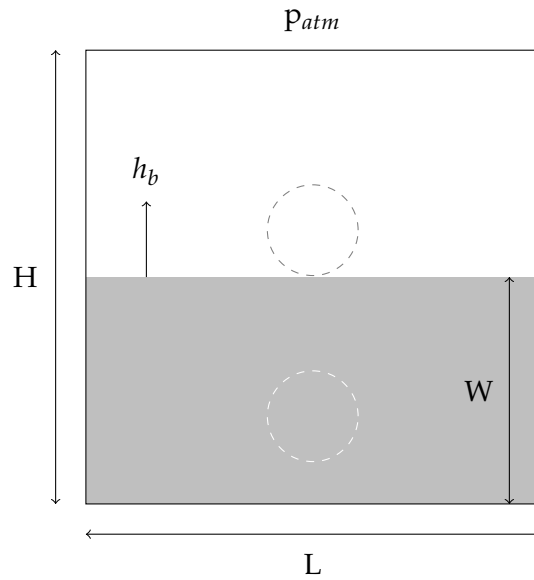
FIGURE 4.25. Simulation NC. without C-label (left) and NC. with C-label (right). Difference in shape with grid resolution 150×50 , filter $F_s < 0.95$.

4.6.2 Buoyant cylinder water exit & entry

Like in Eijk and Wellens [79], our ultimate interest is in modeling the fluid-structure interaction involved in the motions (accelerations) of high-speed craft in heavy seas that frequently disconnect from the main water body when moving vertically upward before falling downward with an impact. An experiment that captures fundamental aspects of these phenomena was conducted by Colicchio et al. [46]. The experiment consists of two parts. The first is a buoyant cylinder that moves vertically upward before exiting the water, the other is that same cylinder moving vertically downward before impacting with the water. The experiment was designed to be as 2D as possible. The tests were conducted in a prismatic tank with a length of 3000[mm], a water depth of 1400[mm] and a width of 400[mm] in the direction that is assumed not to be relevant to the dynamics of the cylinder. The cylinder itself has a radius of 0.15[m] and an effective density of 620[kg/m³]. During testing, the cylinder's position and velocity was measured, together with pressures at discrete locations along the contour of the cylinder. In their article, the measured quantities were also compared to results of a numerical method with a level-set free surface displacement algorithm. Details of the numerical simulations, such as grid size and time step were not reported.

The initial fluid configuration for our simulations is illustrated in Fig. 4.26, with specifics provided in the table in Fig. 4.26b. The value h_b indicates the center position of the structure, and $h_{b,0}$ the initial position. The following fluid

properties are used: densities $\rho_a=1[\text{kg/m}^3]$ and $\rho_l=1000[\text{kg/m}^3]$, viscosities $\mu_a=1.48\cdot 10^{-5}[\text{kg/ms}]$ and $\mu_l=10^{-6}[\text{kg/ms}]$, gravitational constant $g=9.81[\text{m/s}^2]$ and surface tension coefficient $\sigma=0.072[\text{N/m}]$. The simulations are run until 1.5[s] with a maximum Courant number of 0.2. The initial speed for the cylinder exiting the water is 0[m/s]; for the cylinder falling downward before entering the water, it is 2.55[m/s].



(A) Domain.

	Exit	Entry
H [m]	2.5	2.5
L [m]	3.0	3.0
W [m]	1.4	1.4
$h_{b,0}$ [m]	0.15	-0.46

(B) Size domain.

FIGURE 4.26. Setup cylinder exit & entry.

Comparing numerical simulations to measurements from experiments is challenging, because you need to make sure that the differences between the two are sufficiently small not to have an effect on the comparison. Two, what we think are, cardinal moments during the experiments are shown in Fig. 4.27. These are the moments when, for the water exit case, a free surface jet impinges on the main body of the fluid, and when, for the water entry case, the fluid from either side starts flowing over the cylinder and meets in the middle. These are events that can be compared to long-crested wave breaking, that are inherently 3D and sensitive to small perturbations [179], even when the setup of the experiment is



otherwise flawless. This will be discussed in more detail.

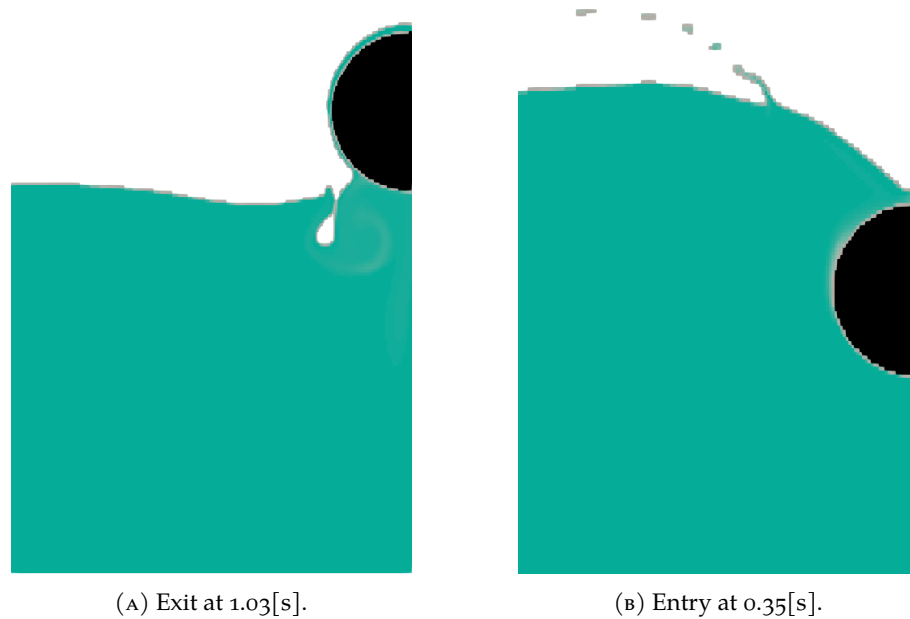


FIGURE 4.27. Snapshots of cylinder exit & entry.

4.6.2.1 *Cylinder exit*

We will first discuss the case with the buoyant cylinder rising upward and exiting the water. Much of the dynamics of the cylinder takes place away from the interface between water and air. For this reason, the difference between results of the non-consistent and the consistent method should remain small.

The cylinder's velocity and position during exit are shown in Fig. 4.28. The measurements (Exp.) are compared with level-set method (Num.) of Colicchio et al. [46], our older non-consistent method (NC.), and the consistent method (C.) discussed in this work with all improvements at different grid resolutions. Those are for $N = 75, 125$, or 175 cells in both directions. A dashed line is plotted around $1[s]$. From that moment, according to our interpretations, 3D effects will start to play a role, see Fig. 4.27a, and the results in the simulations will start to diverge from the measurements. The simulation results in Fig. 4.28, for NC. and C. alike, match well with the experimental results before $t=1[s]$, and grid refinement with the consistent method (C.) leads to convergence.

The pressures from a simulation with the consistent method at a resolution of 125 cells in both directions at discrete locations along the cylinder contour are compared with the measurements (Exp.) and the numerical results (Num.) of

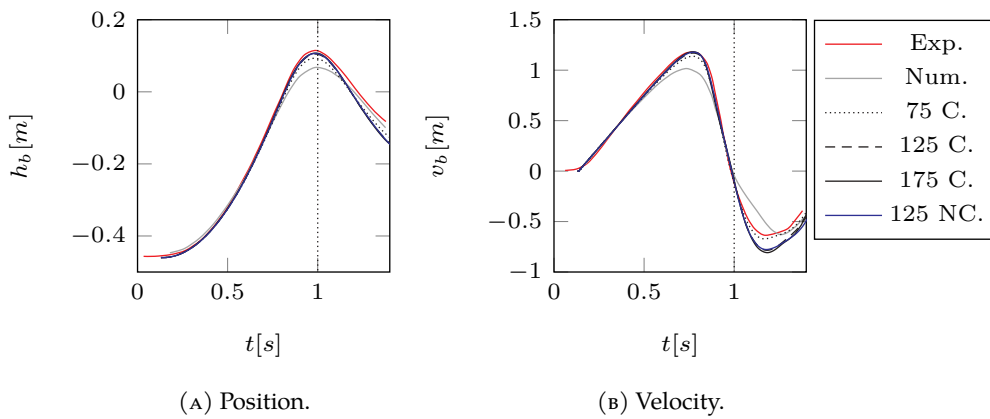
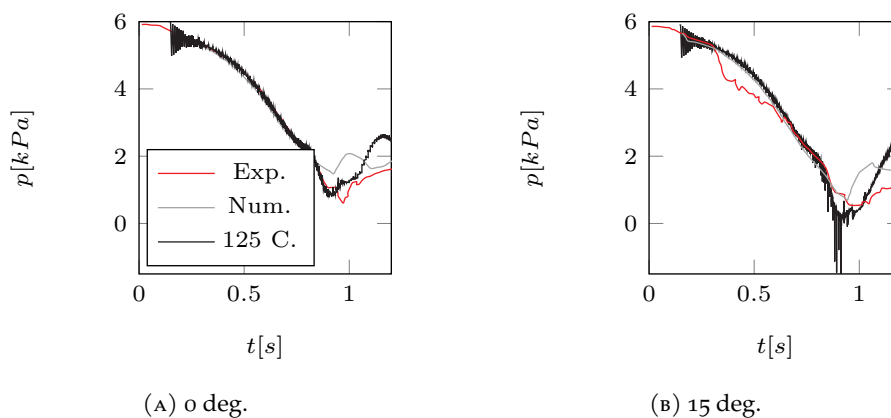


FIGURE 4.28. Results for buoyant cylinder exiting the water with NC., and C. at resolutions of $N = 75, 125, 175$ cells in each direction (Exp. and Num. results taken from Colicchio et al. [46]).

Colicchio et al. [46] in Fig. 4.29. The pressures were measured at angles of 0, 15, 45, 105, and 145 degrees, where 0 degrees indicates the bottom of the cylinder. During the cylinder exiting the water, the low-pressure wake formed behind it during its upward movement interacts with the air phase and entrains air bubbles. The first moment of entrainment is illustrated in Fig. 4.27a. In the experiment, the entrainment caused noisy pressure records, which were filtered out before being presented [46]. The results of our simulations are not filtered. The smaller spikes are due to the cylinder moving from cell to cell, the larger spikes are due to the object moving from cell to cell near the interface between water and air. The pressures in the simulation show a fair agreement with the experiment. The probe at 105 degrees becomes dry after 0.82[s] while 0, 15, and 45 degrees remain wetted by a mixture of water and air. It is our interpretation that the simulations overestimate the pressure in the water-air mixture later in the simulation, because the breaking-up of air bubbles is not part of the formulation of the method.



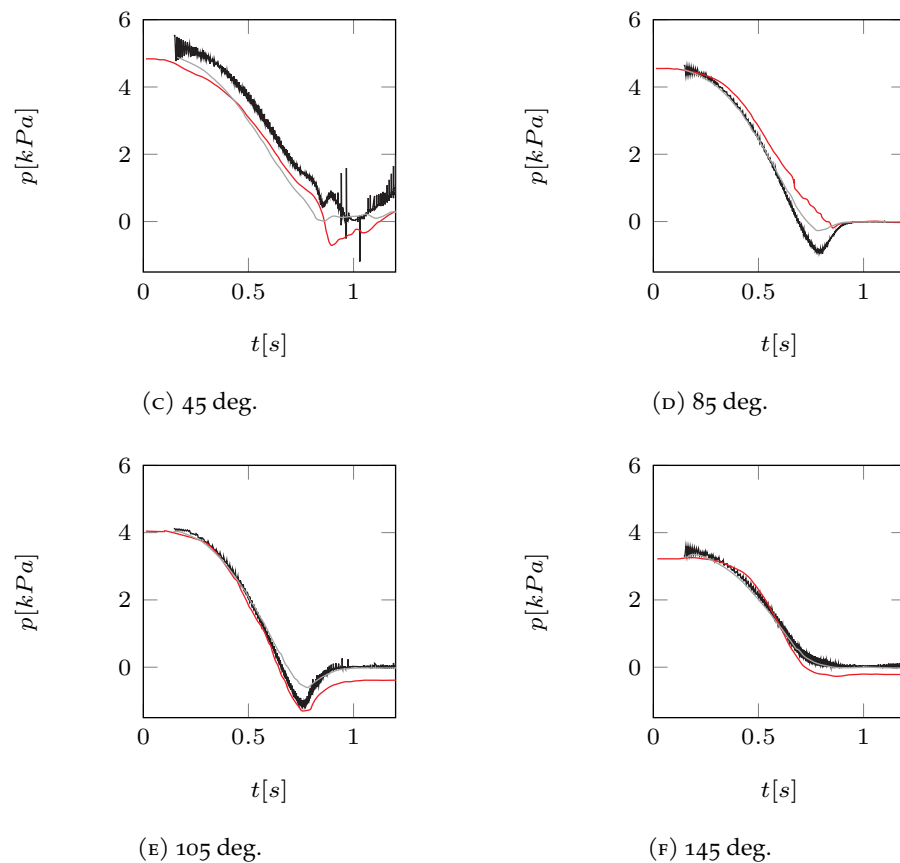


FIGURE 4.29. Pressure for buoyant cylinder exiting the water with $N = 125$ cells in each direction (Exp. and Num. results taken from Colicchio et al. [46]). 0 degrees indicates the bottom of the cylinder.

4.6.2.2 Cylinder entry

Next, the case with the cylinder entering the water with an impact is discussed. Moments after the cylinder has penetrated the interface, two fluid jets are formed that develop in the direction opposite to the downward motion of the cylinder. The difference between results of using the non-consistent or the consistent method are expected to be larger than for the cylinder exiting the water, because of the higher fluid velocities and the larger contour of interface along the jets.

In the wake above the cylinder as it is falling down through the interface, an air cavity is generated. At some moment, the air cavity becomes unstable and collapses. The collapse results in the mixing of air and water. After the collapse, the free surfaces at both sides of the top of the cylinder move towards each other and make contact (approximately) in the middle. In the experiment, it is around $0.35[s]$ when the cylinder gets fully surrounded with water. This moment is shown in Fig. 4.27b. Our interpretation again is that the experiment is 2D until

the free surfaces merge above the cylinder. Just like wave breaking the merge is not expected to occur uniformly in the third dimension, causing 3D effects from that moment on.

The velocity and position are plotted in Fig. 4.30. The position data extracted from Colicchio et al. [46] is shifted along the vertical axis so that at time instance 0[s] the position h_b is 0. In both directions, $N = 75, 100,$ or 125 cells were used. The results obtained with the consistent method (C.) converge, and there is a clear difference with the results of the non-consistent method (NC.). Until $0.35[s]$, the position h_b with the consistent method matches well with the experiment. With the non-consistent method the penetration depth is somewhat smaller than in the experiment. After $0.35[s]$, the simulation results start to deviate from the experiment. Especially the velocity with the consistent method undergoes a sudden change when the cylinders becomes completely enclosed in water. We think that the water above the cylinder in the experiment is actually a mixture of water and air with a lower density than water alone, affecting the velocity of the cylinder to a lesser extent. This interpretation is in agreement with the difference between the consistent method and non-consistent method, because in the latter the density near the interface is also more diffuse, comparable to Fig. 4.17.

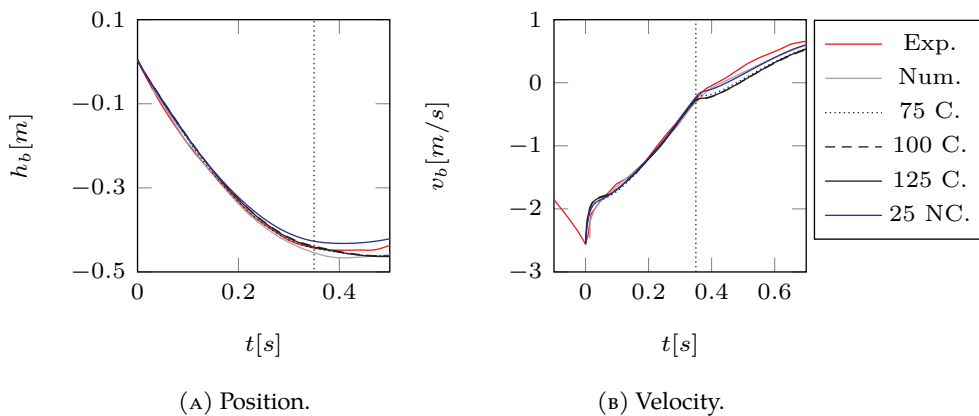


FIGURE 4.30. Results for cylinder entering the water with $N = 75, 100, 125$ cells in each direction (Exp. and Num. taken from Colicchio et al. [46]).

The pressures from the simulations with 125 cells in both direction, both with the consistent method (C.) and the non-consistent method (NC.), are compared to the pressures from the experiment of Colicchio et al. [46] in Fig. 4.31. For reference, their numerical results are also added to the plots. The pressure sensors were placed at 40 or 45 [deg] intervals along the contour of the cylinder where 0 [deg] coincides with the bottom of the cylinder. The agreement in pressures from the simulation and those in the experiment is fair, good perhaps when the pressure from the sensor at 145 [deg] would have been disregarded.

This sensor is placed in what can be called the wake of the cylinder and experiences the most complicated combination of water and air. The sensor at 0° in Fig. 4.31a registers the impact pressure when the cylinder hits the free surface. Note that the time axis for the graph of this sensor is different from the time axes of the other sensors in Fig. 4.31. The pressure peak at 0° in the simulation with the consistent method reaches to approximately $2/3$ of the peak in the experiment. From the pressure in the experiment one can tell that more is going on: the pressure oscillations following the impact are likely due to vibration of the container in which the cylinder is dropped or density waves at the speed of sound in water. Those oscillations are absent from the simulations.

The comparison between consistent simulation results and non-consistent simulation results in terms of the pressure does not allow interpretation, except for the pressure sensor at 0° . Oddly, the simulation with the non-consistent method does not register a peak in the pressure at all, and produces an elevated pressure level some time before the impact takes place in the experiment. For this sensor it is clear that the non-consistent method does not represent the expected physical behaviour, and that the consistent method does.

4.7 Conclusion

In this work the method of Eijk and Wellens [75] is combined with the consistent mass-momentum transport (CMOM) scheme of Zuzio et al. [320] and extended with two-way coupled fluid-structure interaction (FSI). With the new method, we found similar results in terms of kinetic energy conservation as Zuzio et al. [320] for the diagonally translating high-density bubble.

In addition to the translating bubble, results of our method are compared with the rising bubble benchmark of Hysing et al. [123], which is highly relevant for this type of two-phase flow. The difference in maximum velocity of the bubble between the consistent implementation and the benchmark was 1.6% when the density ratio was 10, and 0.45% when the density ratio was 1000 with a grid of 50×150 cells in horizontal and vertical direction, respectively. That needs to be compared with a 1.6% (density ratio 10) and 4.5% (density ratio 1000) difference between the older, non-consistent implementation at the same resolution and the benchmark. Several other improvements contributed to further reducing the difference in velocity: the viscosity discretized using VOF fluxes had a small, but measurable influence, and the combination of a larger stencil for the curvature of the interface and C-labels near the free surface made sure that also the shape of the bubble was in agreement with the benchmark and that fluids were kept separate better. With these improvements the consistent method converges to a 0.03% difference in maximum velocity with the benchmark at a grid of 80×240 .

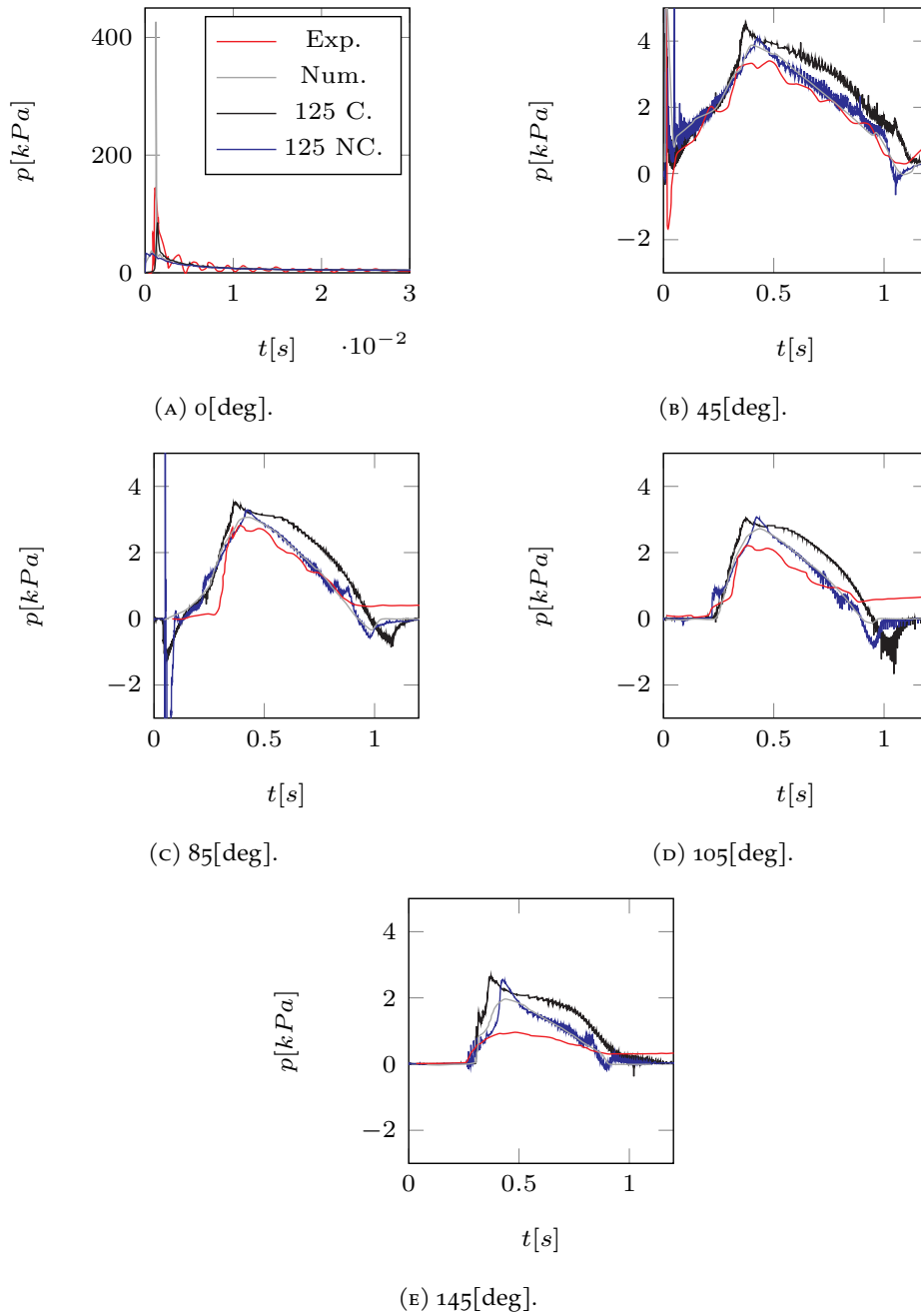


FIGURE 4.31. Pressure for cylinder entering the water with $N = 125$ cells in each direction (Exp. and Num. taken from Colicchio et al. [46]; note that the time axis is different in Fig. 4.31a).

It was demonstrated that using a consistent method in a setting with FSI is advantageous for momentum conservation. Newly devised proof of principle simulations involving a droplet of water impacting a moving solid wall showed



an order of magnitude improvement in momentum conservation between the consistent method and the older, non-consistent method.

Simulations with both the consistent and the non-consistent method compared well with the cylinder exit experiment of Colicchio et al. [46] until, in our opinion, the experiment cannot be considered 2D anymore. The comparison with a similar experiment of the same authors, involving a cylinder falling on an free surface that is initially at rest, demonstrates that the non-consistent method gives an elevated pressure before the time the impact takes place in the experiment, but does not reproduce a peak impact pressure. In contrast, the consistent method captures the moment of impact well and produces a peak impact pressure that is approximately two thirds of the impact pressure in the experiment.

The benefits of consistent transport modeling become especially apparent for two-phase flows with a high density ratio between fluids. This was observed both for the simulations with FSI and without. Consistent modeling improves momentum conservation and yields a more realistic shape of the interface.



Part II

EXPERIMENTS AND NUMERICS WITH AERATION

This part concerns the extension of the numerical method to a fully compressible multiphase model that can deal with the compressible effects of air entrainment during a water-wave impact (Ch. 6). An experimental setup for a wedge entry is presented (Ch. 5) that is evolved into a setup that can deal with air entrainment and provide data for validation of the numerical model (Ch. 6).

Photo: [245]

5

EXPERIMENTAL, NUMERICAL AND ANALYTICAL EVALUATION OF THE BUOYANT WEDGE ENTRY PROBLEM WITH REEMERGENCE IN 2D

This chapter is reproduced from [78] :

M. van der Eijk and P. R. Wellens. “Experimental, numerical and analytical evaluation of the buoyant wedge entry problem with reemergence in 2D.” *Journal of Fluid Mechanics* (nd)

Abstract

Maritime structures are designed to endure impact events such as the fall back onto the free surface after clearing the water or getting hit by a large water wave. In studying these events, the structure’s cross-section is often simplified to a wedge. Methods of modelling the wedge entry and emergence problem broadly divide into experimental, numerical and analytical. We argue that all three methods are required for reliable results when buoyant wedges are concerned.

An experiment with falling buoyant, symmetric wedges was designed to be as 2D as possible so that it may serve as a benchmark. The wedges undergo stages of fluid-structure interaction ranging from slamming upon first contact with water on the way down, to periodic oscillation in the free surface after having risen back up. Simulations with a numerical two-phase flow method were performed to design the experiment and to determine the forces on the wedge. The simulations were also used to extend an analytical method for the accurate representation of the interaction between wedge and water until the closure stage to study uncertainties in the experiment with respect to the wedge’s velocity and inclination angle upon impact. The models of buoyancy force and fictitious body continuation have properties not described before.

The methods show good agreement until the end of the closure stage, when a new type of cavity closure in the experiment is shown to have intrinsically 3D characteristics not captured by the 2D simulations. Details of the experimental setup, the data, and the post-processing routines have been made available at <https://doi.org/10.4121/a698656f-2648-4bc7-99ae-4f9a27fd869c>.

5.1 Introduction

5.1.1 Introduction

Modeling the interaction between (high-speed) marine structures and waves is crucial for a safe and economical design [22, 120, 135, 153, 224, 286]. Every so many waves the interaction leads to an impact between structure and water. Impacts are observed for the maritime application of high-speed vessels undergoing slamming [79], free-fall lifeboats experiencing large deceleration when entering the water [13], sloshing in liquid cargo containments [63], and green water on deck hitting a superstructure [15]. Impacts are also relevant in the fields of aerospace engineering for water landings and spacecraft returning to earth [238], biology for diving birds [228], the transfer of disease from leaf to leaf as result of impacts with rain drops [99], and many more.

The typical cross-section of a (high-speed) vessel is wedge-shaped, undergoing impact on its way down back into the water after having cleared the water before. The bottom plates of the wedge are inclined with a deadrise angle. The transition from bottom plates to vertical side walls are called chines. The side walls stop at the top end of the wedge at the level of the horizontal deck of the cross-section. The so-called 2D wedge entry problem has become a benchmark to obtain a better understanding of the physics involved in impact with water. The wedge experiences different stages during impact, described for instance by Wang, Lugni, and Faltinsen [282]. Here, we will make an attempt at an unambiguous definition of the stages that are illustrated in Fig. 5.1. The first is the slamming stage (I), that starts when the tip of the wedge first touches the water. During this stage the force rapidly increases and free-surface jets are formed along the inclined bottom of the wedge. The added mass increases quadratically with the wetted length between contact points of the free surface with the wedge. The slamming stage is described extensively by Dias and Ghidaglia [63] and Korobkin and Pukhnachov [146], among others. The second stage is called transition stage [282], although we prefer to call it separation stage (II). Here, the jets formed in the stage before detach from the chine of the wedge leading to a strong drop in acting force and a decrease in added mass. The separation stage has been investigated in Tassin, Korobkin, and Cooker [257], Hascoët et al. [110], Iafrati and Battistin [124] and Wen et al. [293], among others. Also during the separation stage, a cavity of air is formed above the wedge when its top end falls beyond the level of the initial free surface (before impact). A number of studies is dedicated to the generation of the cavity, see Duclaux et al. [72] and Vincent et al. [272] for example. The buoyancy force on the wedge is insignificant in the slamming stage (I), but develops during the separation stage (II) and becomes the dominant force contribution. The closure stage (III) starts when the side walls of the wedge become wet above the chine, indicated in Fig. 5.1 by crosses in the dashed contour of the wedge at that moment. During the closure stage the air cavity above the wedge starts

to become more narrow [281, 282]. The closure stage ends when the separate free water surfaces on either side of the wedge meet to form a continuous free surface water surface above the wedge. That moment of contact between free water surfaces left and right of the wedge therefore defines the start of enclosed stage (IV). For wedges with a constant vertical velocity that is sufficiently high, an air-pocket can be entrapped between wedge and water above. That air-pocket is not visualized, because in our case, when the vertical velocity of the wedge is nearly zero at the end of the closure stage, the free surfaces on either side roll over the top of the wedge until they meet impulsively in the middle, creating the additional vertical jet shown in Fig. 5.1IV. This type of transition from the closure stage (III) to the enclosed stage (IV) is specific to this article and has not been described yet by others. The enclosed stage is called “post-closure” by Wang, Lugni, and Faltinsen [282], but that term seems to imply that it is the final stage. Based on the research for this article, we would like to propose an additional and, in our view, final stage of the wedge entry problem: the Archimedal stage (V). The Archimedal stage starts when the buoyancy force on the wedge has converged to the value of the weight of the displaced volume, that becomes a function of time again when the wedge on its way up breaks through the free surface.

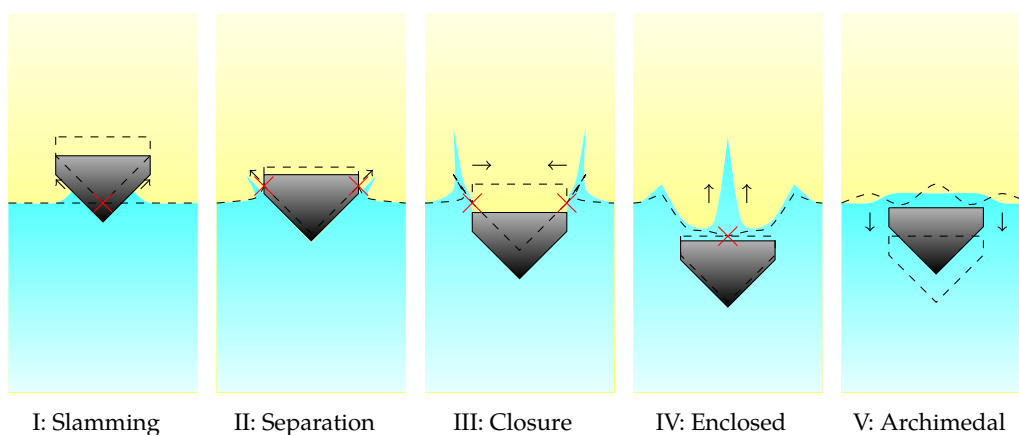


FIGURE 5.1. The five stages of wedge entry in water in chronological order. The enclosed stage shows the free surface configuration after a type of closure that is specific to this article. The dashed lines indicate the start of the stage, with the red crosses the intersection between wedge and water at that moment.

Because of our interest in maritime applications we chose to investigate free-falling wedges with different masses, expressed as the ratio μ of mass over mass of the displaced wedge volume. When the ratio is lower than one, the wedge is buoyant and the dynamics of the wedge are more representative of the cross-section of a ship or falling life boat. Despite the extent of literature on wedge entry, studies with buoyant wedges are fairly rare, with – to our knowledge –

only Yettou, Desrochers, and Champoux [309] showing results of a 3D structure that floats back to the free surface without analysis of the closure and enclosed stage. We felt it was necessary to study free-falling wedge entry by means of experiments, numerical simulations and analysis, because experiments validate the numerical and analytical methods for the application, the simulations provide information that is difficult to obtain from the experiment such as the force and the fluid velocity field, and the analytical method is used to break down the force on the wedge in the different components that are relevant in the different stages of wedge entry. The analytical method is also used to investigate uncertainties in the measurements from the experiment. The interdependencies of the three methods are illustrated schematically in Fig. 5.2.

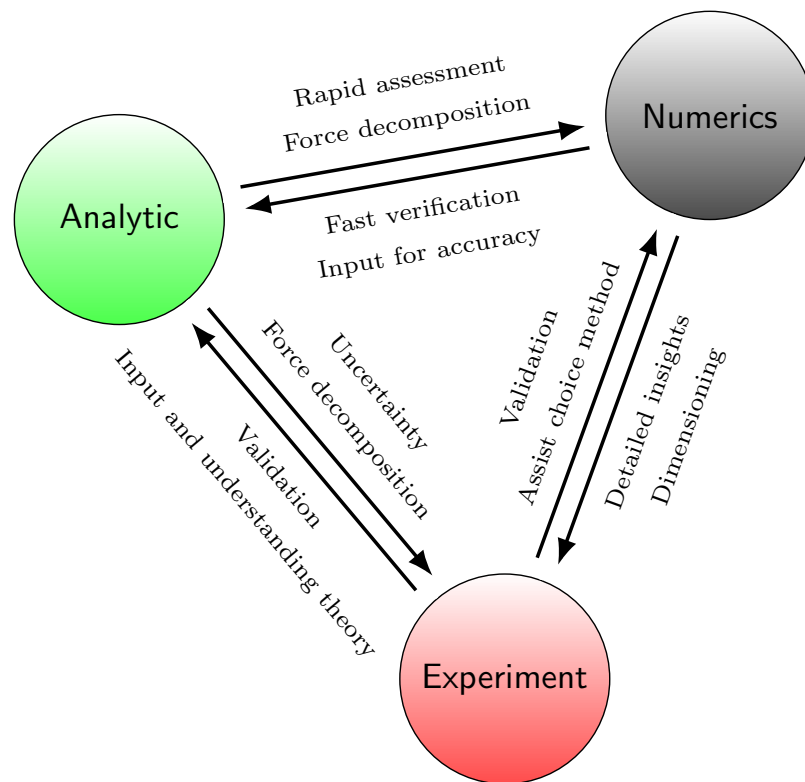


FIGURE 5.2. The interaction between analytical, numerical and experimental modeling. A combination of the three methods gives more reliable results than any of them used by itself.

The existing literature for wedge entry is discussed with analytical methods first, then numerical methods, followed by studies with an emphasis on experiments. It is stated after each subsection what the contribution of this article will be.

5.1.2 Analytical

An early report of modeling the slamming stage during 2D wedge entry was given in Von Karman [274] for analyzing the interaction between seaplanes and water during landing. The slamming force was estimated based on conservation of momentum and the added mass effect by means of potential flow theory. The model was extended in Wagner [278] to account for the increased wetted area due to the water piling up along the inclined bottom of the wedge. This led to an improvement in determining the load, with the difficulty, however, of a singularity in pressure at the position where the wedge surface and the free water surface meet. The singularity needs to be resolved because it could lead to an incorrect contribution to the load [144].

Zhao, Faltinsen, and Aarsnes [316] proposed a nonlinear method for the determination of the slamming force during wedge entry. Analytical theories for entry in water of arbitrary shapes in different stages, including the separation stage, are provided in series by Korobkin [144] and others together with Korobkin [143, 145, 146, 185, 251]. In Korobkin [144], the singularity is addressed by replacing the value of the pressure by zero where it becomes negative, to good effect but without a mathematical explanation. His overview further showed that a number of analytical methods [162, 178, 294] are based on Wagner, together with different extensions. The extensions apply higher order terms in approximating either the level of the root of the deflected jet or the shape of the body in the velocity potential. The reported type of analytical method is representative of the physics of wedge entry up to deadrise angles of 30 degrees – deadrise angle being the inclination of the bottom plane of the wedge with respect to the horizontal – without accounting for the specific shape of the body [162]. For sharper bodies, the body shape needs to be accounted for [144].

The above-mentioned analytical methods can be used up to and including the separation stage by the assumption of zero pressure at the flow separation point, at the chine between inclined bottom and vertical side wall. Tassin, Korobkin, and Cooker [257] showed that these methods overestimate the force reduction after separation, and introduced a correction based on the Fictitious Body Continuation (FBC) concept. When the orientation of the free surface after flow separation from the chine is known, using a linear FBC with that orientation improves the estimation of loads compared to above mentioned during initial cavity formation in the separation stage. Wen et al. [294] proposed a curved FBC, instead of linear, providing better force predictions at the start of the separation stage compared to Tassin, Korobkin, and Cooker [257].

It is necessary to include asymmetry in our analytical method in order to investigate an uncertainty in the experiment with respect to the wedge's inclination

angle. A different form of the Wagner conditions is needed than the usual ones for symmetric entries. The Wagner conditions were derived under the assumption that the free surface remains unchanged. Existing accounts of included asymmetry are given in Korobkin and Malenica [145], Hascoët et al. [110], Qin, Zhao, and Shen [220], and Tassin et al. [258].

Theoretical analysis of the dynamics of a cavity up to the moment of closure is provided in several studies [72, 261, 262], mostly for cavities after 3D entry of objects with a round or flat bottom. Where Greenhow [103] recognized cavities after wedge entries, Wang and Soares [284] evaluated the effect of the shape of the falling object on the cavity, Wang, Lugni, and Faltinsen [282] and Wang, Lugni, and Faltinsen [281] investigated the airflow before and after closure of the cavity in 2D, Gekle et al. [96] analyzed the cavity closure in 3D for axisymmetric objects, and Vincent et al. [272] reported on modeling the shape of the free-surface deformation, which generally curves outward and downward away from the object [103].

We adopt an analytical approach for arbitrarily shaped objects using a curved FBC, which we have extended to account for the asymmetry of the object and for the cavity formation. The approach is combined with an equation of motion for the wedge. The results are compared with the numerical and experimental results in this article, and those of other literature for verification. The analytical method is also used for force decomposition. Hydrostatic forces are incorporated and used to analyze when the closure stage starts. The method, when verified by means of experimental and numerical results, can be used in 2D strip theory methods which are often used for rapid assessment of high-speed vessels in water [79].

5.1.3 Numerical

Numerical simulations of wedge entries have routinely been compared with experimental data as a means of validation [129, 240, 272, 282]; it is considered standard procedure. Analytical methods, on the other hand, are often compared with numerical simulation results as a means of verification [144, 257]. Different types of numerical method have been adopted to simulate wedge entries: explicit finite element methods [248, 283], finite volume methods [142, 211], boundary element methods [124], particle methods [201], and hybrid methods [58] are examples.

The numerical modeling of jets generated by the entry is seen as difficult. Jets are sometimes limited by means of additional restrictions such as 'jet cut' [124] or not considered [162]. Smoothed particle methods [101], level-set immersed boundary methods [30], finite volume methods [142, 211], or boundary element

methods with potential flow theory [8] have been presented which do model the free jet.

Our numerical method, described in Eijk and Wellens [80], is used in support of the experiments. It is based on the Navier-Stokes equations with a finite volume discretization of the spatial derivatives. A geometric Volume-of-Fluid (VOF) method is used to track the interface between two fluids, with a cut-cell method for the representation of the wedge. Reconstruction is applied to the interface between fluids and the interface between fluids and wedge. Mass and momentum transport are matched consistently to reduce momentum losses in the fluid-structure interaction between wedge and fluids. The method is validated for a cylinder entry [80].

The numerical method was used to design the experimental setup. It is also used to determine the forces on the wedge, jet formation, and the free surface deformation altogether. The simulation results are the main reference for identifying which parts of the acceleration signal are inherent to buoyant wedge entry and which parts are model errors originating from the structure of the wedge's guiding mechanism or the box with water it lands in. The numerical method is considered indispensable in verifying the main assumption regarding the 2D nature of the experiment.

5.1.4 *Experimental*

Vertical drop experiments with simplified shapes of the falling object, including wedges and ship-like sections, have been reported on in several studies. Examples of the shapes that were used are: a cylinder [46], a spheroid [193], a flat plate [43], a bow-flare section [23, 304, 305], a hydro-elastic wedge [201, 260], and others [37]. In some instances the object in the experiment is asymmetric [10, 241]. The fact that some of the studies above are very recent demonstrates that the water entry problem still warrants study.

Chuang [44], besides studying flat plate entry, also considered wedge entry with a specific deadrise angle. The experiments conducted by Takemoto [256] were a validation of the pressure distribution along the wetted area of the wedge according to Wagner. Yamamoto, Ohtsubo, and Kohno [308] looked at the position of the maximum peak pressures and how it is affected by the deadrise angle of the wedge and the impact velocity. Greenhow [103] also looked at the pressure distribution on a wedge and compared the measurements with an exact solution [66], while, in addition, noticing the formation of a cavity above the wedge. 2D wedge entry experiments for the main purpose of validating a numerical method have been conducted a number of times [240, 301, 316]. Zhao, Faltinsen, and Aarsnes [316] described the differences between 3D and 2D wedge entry, like

others described the differences between axisymmetric object entry (cones) and wedge entry [45, 129]. Yettou, Desrochers, and Champoux [309] looked into the pressure distribution variation along the wedge surface and the wedge's dynamics as it decelerates. Tveitnes, Fairlie-Clarke, and Varyani [264] conducted, in their account, the first experiment of a wedge entry with constant velocity, until an immersion depth of the wedge where its added mass in water does not change anymore. Those results were found to be consistent with analytical methods. Tveitnes, Fairlie-Clarke, and Varyani [264] also considered a wedge emerging from the water. Lewis et al. [156] provide a rather complete account of jet formation, its evolution, and ultimate breakdown for a free-falling wedge on the basis of experiments, supported by means of numerical simulations.

Wang, Lugni, and Faltinsen [282] conducted experiments with more attention to the stages after slamming and separation. They showed that airflow plays an important role in the cavity pressure during the closure stage. The pressure could even attain negative values with respect to atmospheric pressure. The airflow hardly affects the object velocity and the configuration of the free surface due to the short duration of the closure stage. After closure, compressibility of air might play a role and can generate force oscillations on the wedge. Vincent et al. [272] looked at the drag force on the wedge after jet separation from the sides and found a smaller drag than for fully immersed wedges with the same velocity. They showed that the shape of the separated jet upon impingement with the free surface depends on the Venturi-suction force and on surface tension. Jain et al. [129] also provided experimental data of the slamming pressures for a constant velocity and compared it with analytical results, focusing on the role of air below the wedge just before impact.

Few experiments with free-falling wedges are 2D, an observation also mentioned by Jain et al. [129] and Vincent et al. [272]. Our experimental setup aims to be as 2D as possible, and we investigate when the assumption of the flow being 2D does not hold any more. The other account of an experiment with having a buoyant object is in Yettou, Desrochers, and Champoux [309], but it is not "truly" 2D and is without analysis of the final three stages in Fig. 5.1 when the buoyancy force starts to play a role. Our results will show that the closure stage and enclosed stage take place differently for buoyant wedges than for wedges in the setup of Wang, Lugni, and Faltinsen [282] and Jain et al. [129].

5.1.5 *Article outline*

Whereas the discussion of existing literature for historical reasons followed the order analytical methods, numerical methods and experiments for wedge entry problems, the article is composed with that order in reverse. A description of the setup and the results of the 2D (buoyant) wedge entry experiments

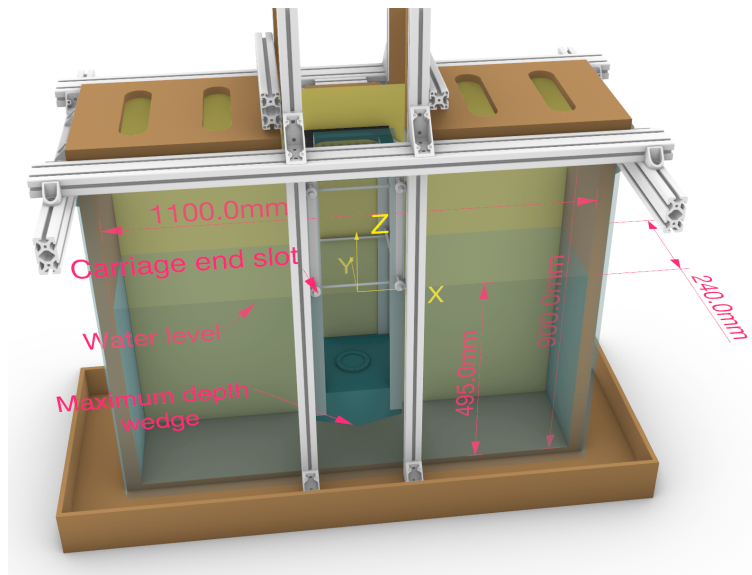
are described in Sec. 5.2. Sec. 5.3 features an account of the numerical method and the simulations that were performed to find the force on the wedge and to investigate the 2D nature of the experiment. The analytical method is documented in Sec. 5.4, together with the way its results were used to analyze the contributions to the force on the wedge and uncertainties in the experiment. Conclusions from the results are summarized in the final Sec. 5.6. The experimental data and additional resources are provided at <https://doi.org/10.4121/a698656f-2648-4bc7-99ae-4f9a27fd869c> [287].

5.2 Experiment

5.2.1 Setup & Tests

An experiment was conducted for detailed observations of violent immersion events of a 2D wedge and its subsequent path back to the free surface under the influence of buoyancy. Similar data for especially that re-emergence have not been found in the existing literature. The setup can be representative of slamming of high-speed ships, but for wave interaction events with the lining of a liquid cargo container [18] or the deck structure of a ship in the case of green water [15]. The experiment is conducted in the Ship Hydromechanics Laboratory at Delft University of Technology. The setup of the experiment is shown in Fig. 5.3. A fall tower is used to allow the wedges to accelerate to a high velocity upon impact. The maximum height of the fall tower was limited by the 4[m] height of the ceiling, bringing the impact velocity into a range that is fairly unique - high for slamming or free-fall life boats but not uncommon when breaking waves hit the deck of a ship [26, 95]. Below, details of the experiment and the experimental results are discussed, starting with the measurement of the impact speed, followed by a Fourier analysis of the accelerometer signal and filters, free surface deformation due to the wedge impact, the velocity signal, and ending with a frequency analysis of the wedge's heave motion after re-emergence.

The experimental setup is composed of three parts: a fall tower, a box filled with water, and the wedge. The box was chosen to be small enough to ensure structural rigidity, but large enough to prevent the side walls of the box to influence the slamming stage of the wedge on the free surface. The optimal domain size, e.g. the distance between the side walls, was found by performing numerical simulations with the in-house numerical method [80] described in Sec. 5.3. The structure of the fall tower adds to the rigidity (stiffness) of the box. At the top of the box, 40 by 80[mm] aluminium profiles of the brand ITEM® reinforce the front and back walls of the box. The side and back walls are made of 36[mm] and 18[mm] thick plywood, respectively. The front is made of perspex with a thickness of 30[mm]. The thickness of the perspex is such to maintain stiffness as it is not fixed to the tower. The perspex plate is mounted to the plywood with around 40 screws equally distributed. As the box is made for a vertical



(A) Domain box.



(B) Wedge with stiffeners and bearings.

(C) Stiffened fall tower.

FIGURE 5.3. Experimental setup.

5

2D case, stability is needed in the third dimension, the y -direction. The size of the box in that y -direction is 0.24[m] on the inside. The box is mounted to a plywood plate, on which lead weights are placed to prevent movement of the box. The water level is set to 0.495[m] to prevent the bottom from influencing the force on the wedge during the slamming stage. That water level was found using numerical simulations. The box was made waterproof with several coats of epoxy. For visualization purposes, the contrast is increased by painting the wall yellow and by adding blue dye to the water.

The fall tower is made of 40 by 40[mm] stainless steel profiles. The tower legs are supported with brackets. To every tower leg resin-coated plywood is attached, guiding the bearings of the wedge's falling mechanism. The top of the tower is fixed against the ceiling to prevent swinging and to keep it level. After carefully adjusting and readjusting the legs of the tower, the distance of a leg with respect to vertical was nowhere larger than 0.5[mm] and the distance between legs did not vary more than 0.5[mm]. Uncertainty of the position of the legs can lead to an uncertainty of inclination angle of the wedge. The sensitivity of the force on the wedge to a small deviation in its inclination angle is investigated later by means of the analytical method we describe. At the top of the tower, a wooden plate was installed, supporting a magnet so that the data acquisition system could release the wedge and start the measurement at the same time. The wedge is dropped from a height (z) of 2.760[m] above the waterline. Theoretically, without friction, the drop height would have resulted in a maximum impact velocity of 7.35[m/s] ($\sqrt{2gh}$ where g is the gravitational constant of 9.81[m/s²]). Two light gates are fixed to the legs of the tower at different elevations. The gates provide accurate position measurements to reduce integration errors of the measured acceleration.

The wedge is painted black and waterproofed with several coats of epoxy. The wedge was given a deadrise angle, the angle between a horizontal plane through the tip of the wedge and its bottom plane(s), of 15 degrees to match it with the cross-section at the stern of a high-speed vessel [79]. The deadrise angle was not varied. The outside of the wedge is made of 12.0[mm] plywood with two bottom plate stiffeners. The wedge was given three different weights to study the wedge's dynamics in water after impact. The weight is changed by adding lead blocks on the inside, kept restrained to the wedge by means of a stainless steel threaded rod positioned in the middle of the wedge. A guiding mechanism is connected to the wedge featuring 16 wheels with ball bearings to fit between the resin coated plywood of the tower. The vertical accelerations are measured with two accelerometers connected to the top plate on the inside of the wedge. A carriage end slot prevents the tip of the wedge from going deeper than 0.4[m] below the initial free surface.

TABLE 5.1. Measurement equipment used in falling wedge experiment.

Quantity	Device	Type
Acceleration	Accelerometer 100g	ME systeme AS28E
Acceleration	Accelerometer 200g	Analog Devices ADXL377
Free surface	Camera	GoPro Hero 4
Position	Lightbarriers	RS PRO Retroreflective
Release	Electro Magnet	Binder 10-320-06b00
Data collection	DAQ	Native instruments USB 6211

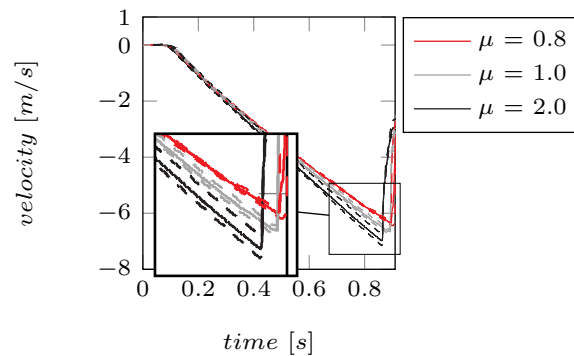
The measurement equipment is summarized in Tab. 5.1. The aforementioned light gates are installed 0.431[m] apart, the lowest positioned 0.570[m] above the water level at rest. The two accelerometers are rated at 100g and at 200g to investigate the different accuracy levels. The sampling rate of the data acquisition system is set at 1[kHz]. The camera measures 720 times 480 pixels at 240 frames per second. The camera images were used for extracting the contours of the air-water interface, but also for tracking the position of the wedge with CSRT [88].

The three different weights of the wedge in the tests were 4[kg], 5[kg] and 10[kg]. In the analysis the weights are scaled with the weight of the displaced volume so that in the remainder of this article the weights are referred to as $\mu = 0.8$ (buoyant), $\mu = 1.0$ (neutrally buoyant), and $\mu = 2.0$ (not buoyant). A value for μ below one means that the wedge is buoyant and will float when at rest. Each test is repeated five times to investigate the variability of the dynamics. The water temperature in the box was kept at 16.3 degrees [C].

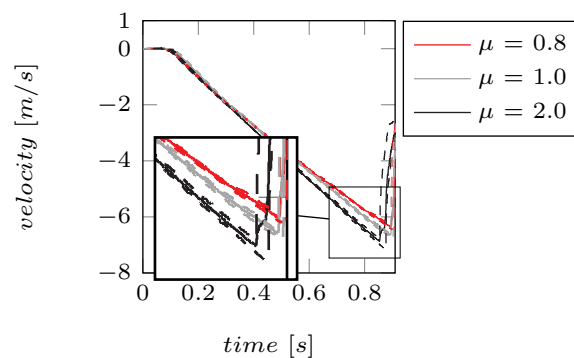
5.2.2 Results of wedge impact

Before focusing on the impact itself, it is discussed how the measurements of acceleration are processed to determine velocity and position of the wedge at any time. From this approach the impact velocity is determined, i.e. the vertical velocity of the wedge when it first touches the free water surface. The measurements start when the magnet releases the wedge. The wedge passes two light gates, an upper and a lower one, before impacting with the free surface. The wedge penetrates the water column and floats back up when buoyant and oscillates to rest. When not buoyant, the wedge's final position is the carriage end stop. The measurements finish when the wedge has come to rest. Tests are repeated five times. The velocity and position along the wedge's fall trajectory are determined in two main ways. The first approach is integration of a least-square fit of the measured accelerations under the requirement that its position coincides with the position of the light gates at a least-square fit of the time the light gates lose signal. For this approach, we have first looked at the 100g and 200g accelerome-

ters separately, and then at the combined data of the two accelerometers. The second approach was to fit a theoretical parabola of position to the positions of the light gates for a least-square fit of the times the light gates lose signal. A value of $9.81 \text{ [m/s}^2\text{]}$ for the acceleration of gravity g and an initial velocity at the position of the upper light gate was used, based on the measurements of the light gates only. This approach provides an overestimation of the impact velocity, because the vertical acceleration of the wedge was lower than g due to friction. The overestimation was necessary because it allowed us to exclude data from the 100g accelerometer, that we think was damaged during the course of the experiment. Camera results are used in a later stage for comparison. The velocity over time, determined from integrating the accelerations measured with the 200g sensor is illustrated in Fig. 5.4 with the min/max confidence intervals before and after correction using the positions of the light gates. The correction improves the estimate of the impact velocity by 3% and reduces the uncertainty (size of the min/max confidence intervals).



(A) Integrated 200g sensor data.



(B) Integrated 200g sensor data, corrected with positions of light gates.

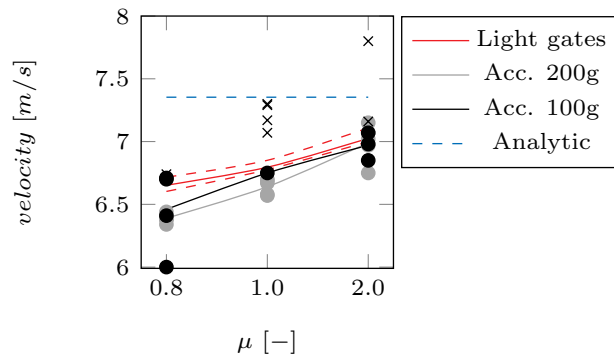
FIGURE 5.4. Velocity over time using data from the 200g accelerometer and from light gates. Correcting the accelerometer data with the light gate data reduces the uncertainty in impact velocity.

The impact velocity is defined as the velocity when the tip of the wedge reaches the position of the initial free water surface. It is shown in Fig. 5.5 for the different wedges with $\mu = 0.8, 1.0,$ and 2.0 . Fig. 5.5a compares velocity upon impact between the different repetitions of the test. The dashed blue line in this graph represents the naive estimate of the impact velocity, based on g and the distance between initial position and initial free water surface. It is the same for all weights of the wedge. In reality, friction prevents the wedge from falling with the acceleration of gravity. The ratio of friction to weight of the wedge makes that the impact velocity is higher for wedges with higher weight. When the five runs are compared, the velocity upon impact reconstructed from the light gates has a maximum deviation of around 1% in Fig. 5.5a with respect to the mean value. The deviation with respect to the mean of the impact velocity based on the 200g accelerometer (together with the light gates) is larger, especially for the wedge with $\mu = 2.0$. The main reason for the variation in impact velocity is noise in the acceleration signal. Some noise is caused by the magnet at the start of the measurements, some by transitions along the length of the guides, some by the transition from tower to container, and a final cause of noise is the instrument itself and its connection to the data acquisition system. Recall that the red line of the light gates was considered an upper limit for the impact velocity, because it did not account for friction (it is still lower than the dashed blue line, because it uses a measured estimate of the initial velocity of the wedge at the position of the upper light gate). Yet some estimates of the impact velocity of the wedge $\mu = 1.0$ using the 100g accelerometer are higher than the upper limit. This was the first reason for distrusting the measurements of the 100g sensor; other reasons are described below. In our estimates of the impact velocity, The data points above the upper limit of the light gates were excluded from the estimate of the impact velocity; excluded data points are indicated with crosses (\times) in Fig. 5.5a.

In Tab. 5.5b the vertical acceleration measured at the start and at the end of the fall trajectory is compared between wedges of different weights. It is found that the vertical acceleration decreases almost linearly in time. Air drag was expected to increase with increasing velocity, but turns out to constitute only a small part of the total friction force. The friction also increases somewhat with increasing velocity.

Tab. 5.5c gives the mean impact velocities for the different instruments and for the different weights of the wedge, together with the minima and maxima of velocity from the five repetitions. The entries for the 100g sensor were determined without excluded data points; the values for the impact velocity when those data points would have been included are given in between parentheses. From the table, using the 200g sensor with the light gate corrections, we find that the impact velocity is $6.39[\text{m/s}]$ for $\mu = 0.8$, $6.64[\text{m/s}]$ for $\mu = 1.0$ and $6.99[\text{m/s}]$ for

$\mu = 2.0$. In the remainder, time $t = 0$ [s] represents the moment when deceleration starts.



(A) Variation in impact velocity compared with analytic value. Solid line is the mean, dashed lines is the max./min.. Accelero data is given.

μ	Acc. 200g		Acc. 100g	
	Start	End	Start	End
0.8	0.96g	0.55g	1.00g	0.59g
1.0	0.97g	0.67g	0.98g	0.78g
2.0	1.00g	0.80g	1.00g	0.82g

(B) Accelerations measured during fall (normalized with g). 'Start' the moment the wedge is released. 'End' the moment of impact.

μ	0.8		1.0		2.0	
	Mean	Max/Min	Mean	Max/Min	Mean	Max/Min
Acc. 100g	6.46	6.71/6.06 (6.74/6.06)	6.75	6.75/6.75 (6.75/7.30)	6.97	7.07/6.85 (7.80/6.85)
Acc. 200g	6.39	6.44/6.34	6.64	6.70/6.57	6.99	7.15/6.75
Light gates	6.65	6.72/6.62	6.80	6.85/6.78	7.03	7.11/7.00

(C) Mean values, minima and maxima of the impact velocity, in [m/s]. In between parentheses are the impact velocities when the data points of the 100g sensor are not removed.

FIGURE 5.5. Impact velocity and variation of acceleration of the wedges.

5.2.3 Fourier analysis of system

The frequencies in the acceleration signals are investigated in order to determine which are caused by the structures of the wedge and its guidance system, and of the box. By filtering out these frequencies, the results of the experiment can be compared with the numerical and the analytical results, in which the structural vibrations are not taken into account.

A hammer test was performed by hitting the guiding mechanism of the wedges with a hammer in vertical direction. The wedges with $\mu = 0.8$ and $\mu = 1.0$ were

a float during the hammer test; the wedge with $\mu = 2.0$ was also in the water, but rested on a length of rope that spanned the top of the box. For each weight, the hammer test was repeated three times. The spectrum of accelerations with the mean of the amplitudes of the five repetitions is shown in Fig. 5.6. Eigenmodes of the structure appear to be near 100[Hz], 240[Hz] and 380[Hz] for all weights. The wedge with $\mu = 1.0$ also appears to have a mode at 460[Hz].

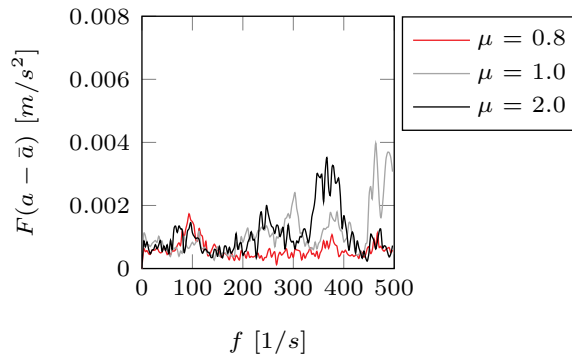


FIGURE 5.6. Amplitude spectra of accelerations following hammer tests with vertical impact on the guiding mechanism of the wedges in water. The amplitudes are the mean of three tests.

The frequencies of all acceleration signals with wedge entries were analyzed. The evaluated signals start at $-0.003[s]$, with $t = 0$ the moment of maximum deceleration, and ends at $0.15[s]$ in the separation stage. The time between -0.003 and the moment of maximum deceleration is the rise time of the force, as will be demonstrated below. Fig. 5.7 gives the amplitude spectra of acceleration for the three different wedge weights. The amplitudes are the mean of five repetitions. A spectrum of accelerations based on numerical results, obtained with the method in Sec. 5.3, is added for comparison, because we can be sure that this signal is without structural modes. The eigenmode near 380[Hz] is apparent for the wedges with $\mu = 0.8$ and $\mu = 1.0$, but not for $\mu = 2.0$. That latter wedge shows amplified acceleration amplitudes near 240[Hz]. The eigenmode near 100[Hz] found from the hammer test does not appear to be excited during impact. A jump in amplitude is found near 20[Hz] for all wedge weights. We believe that 20[Hz] could be an eigenfrequency of the box, because it so consistently becomes apparent for all wedge weights. In Fig. 5.7c for the wedge with the weight $\mu = 2.0$, the 100g sensor is showing much larger acceleration amplitudes than the 200g sensor for nearly all frequencies. The acceleration amplitudes are also higher than the amplitudes from the numerical simulation. This is the second reason to distrust the measurements of the 100g accelerometer.

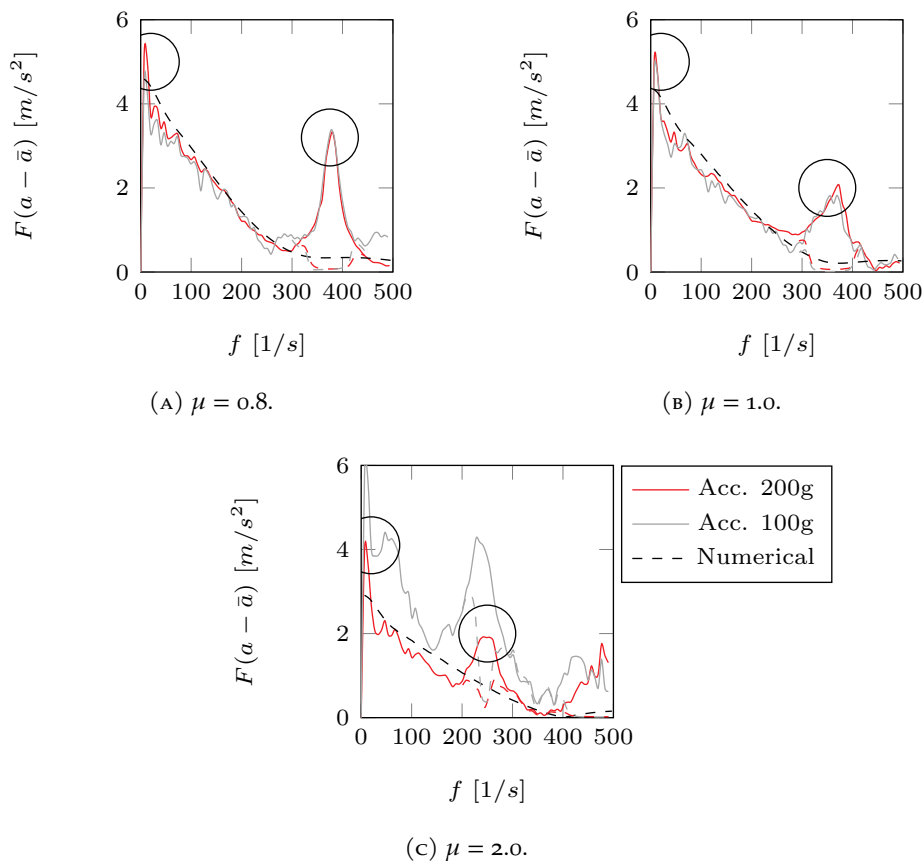
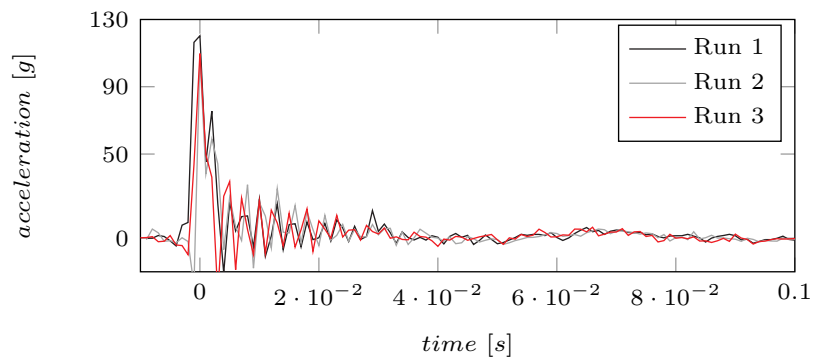


FIGURE 5.7. Amplitude spectra of acceleration for wedge entry signals between $-0.003[s]$ to $0.15[s]$. The dashed lines indicate the filtered spectra. The black dashed line represents the spectrum obtained from simulations with the numerical method described in the next section that excludes structural modes.

Based on hammer test and spectral analysis of the acceleration signals it was decided to filter out the amplitudes at the frequencies of the structural modes as follows: between $330\text{-}420[\text{Hz}]$ for $\mu = 0.8$, and between $310\text{-}400[\text{Hz}]$ for $\mu = 1.0$. The filtered amplitudes are given by the dashed lines in Fig. 5.7. The procedure for the acceleration spectrum of the wedge with $\mu = 2.0$ requires extra explanation. The amplitudes for the structural mode at $250[\text{Hz}]$ could not be completely removed because the amplitude spectrum from the numerical simulations showed that part of that information originates from the interaction with water. A first-order Butterworth filter was employed to smoothen the amplitude spectrum around $250[\text{Hz}]$. Amplitudes at frequencies of $400[\text{Hz}]$ and higher were completely removed. Now the structural modes are no longer part of the comparison that will be made below between experiment on the one side, and the numerical method and analytical method on the other, because the latter two only model the rigid body dynamics of the wedge.

Fig. 5.8 shows the acceleration signals as a function of time before and after filtering for the first three of the five runs with wedge $\mu = 0.8$. The graphs show the acceleration signal of the 100g and the 200g accelerometers before and after filtering. Filtering removes the oscillations of acceleration after impact, but hardly affects the maximum acceleration. For the wedge with weight $\mu = 0.8$ the signals from the 100g and the 200g accelerometers are in good agreement.

The maximum accelerations of all five runs, for all three wedge weights, are shown in Fig. 5.8e, together with the mean value of the five runs. The variation of the maximum acceleration is about 20% of the mean value. As expected, the maximum acceleration goes down for increasing wedge weight, if we only consider the 200g sensor (the ratio of impact force to weight is lower for higher weights). The values of the 100g sensor for the runs with the $\mu = 2.0$ wedge do not follow this trend and are so clearly off that this is now the third reason to distrust the 100g sensor. We believe the 100g accelerometer started to fail during the tests for wedge $\mu = 1.0$. Although the sensor specifications stated that 25% overloading was allowed, perhaps consistently overloading the accelerometer during the tests for $\mu = 0.8$ initiated failure, see Fig. 5.8. The results for the tests with $\mu = 1.0$ showed that the sensor was not reliable. It really malfunctioned for the tests with $\mu = 2.0$. Therefore, the 100g sensor results are not considered in further analysis and when accelerations are discussed in the remainder, only the 200g sensor is considered. The results of the 100g sensor are still presented to show that experimental results do not always reflect reality.



(A) $\mu = 0.8$ acc. 100g non-filtered.

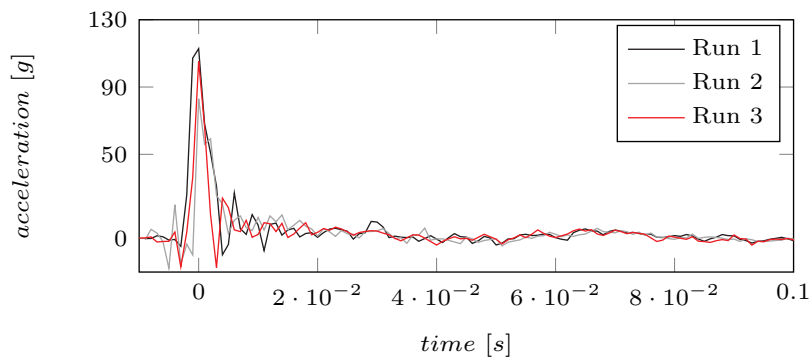
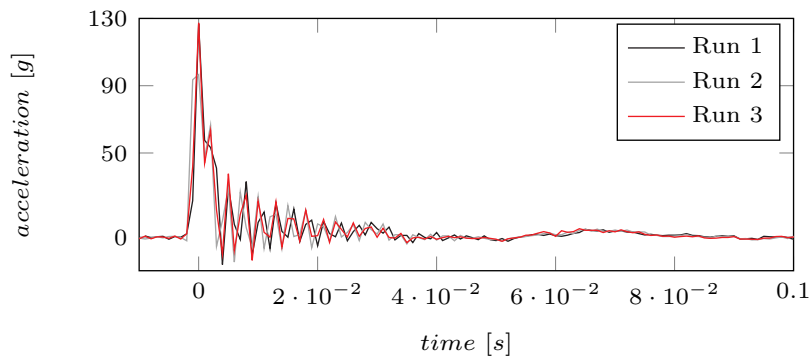
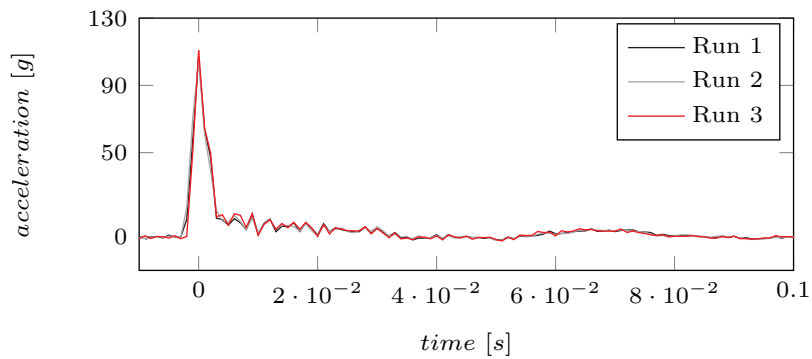
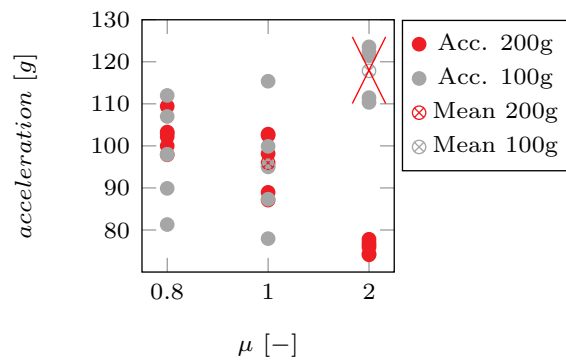
(b) $\mu = 0.8$ acc. 100g filtered.(c) $\mu = 0.8$ acc. 200g non-filtered.(d) $\mu = 0.8$ acc. 200g filtered.

FIGURE 5.8. Deceleration due to the impact of the wedge on the free water surface before and after filtering.



(E) Variation of max. deceleration after filtering. Red cross indicates which data should be omitted.

FIGURE 5.8. Deceleration due to the impact of the wedge on the free water surface before and after filtering.

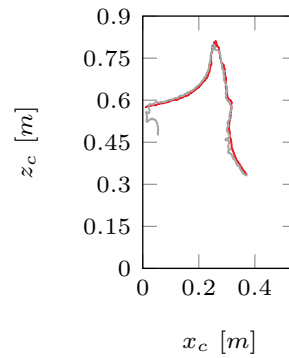
5.2.4 Camera image processing

The free surface extraction to compare with the numerical results and to help to understand the physics is done in multiple steps using Python. The perspective of the recordings of the impact is undistorted using a checkerboard behind the perspex. This ensures that straight lines that should be straight in reality are also straight in the video frames, unaffected by the camera. The undistorted frames are cropped to only account for the box. Where already contrast between the interfaces is created by painting the back wall yellow, the wedge black, and blue-dyeing the water, extra contrast is added by using CLAHE filtering [319]. The extra contrast helps with identifying the wedge and free surface. We applied CLAHE on the A channel of the LAB color model. Subsequently, the A channel is switched with the L channel that showed an increase in contrast. The new color model is changed back to the BGR color model. On the provided frames, a bilateral filter is used to reduce the noise in a frame. Hereafter, an adaptive binary threshold is used to segment the video frames in two colors. By doing so, the free surface becomes noticeable. Static saliency algorithms are able to identify the free surface and results in contours. The Otsu binary threshold with dilation increases the contour thickness. The increased thickness makes it easier for OpenCV [20] in Python to extract the contours.

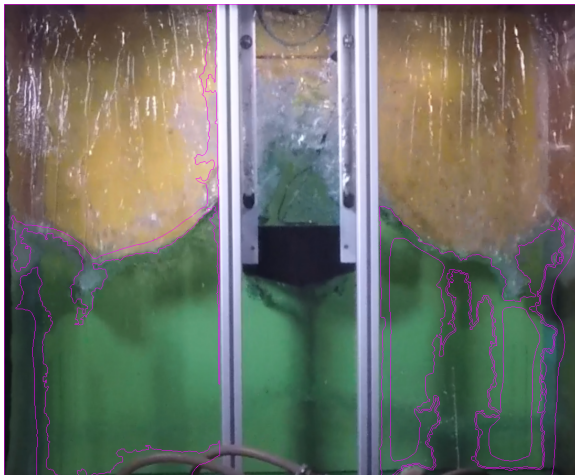
Two examples of video frames from which the free surface is extracted are shown in Fig. 5.9. An impression of how symmetric the experiment is, can be made by mirroring the free surface along a vertical line through the middle of the wedge. The free surfaces on either side are in fair agreement with each other. From the moment the wedge is in an upward motion and a new jet is generated above the wedge, the symmetry is lost and - what we call - 3D flow features start appearing. These 3D effects are found above the wedge and are discussed below when the comparison with the numerical and analytical results is made.



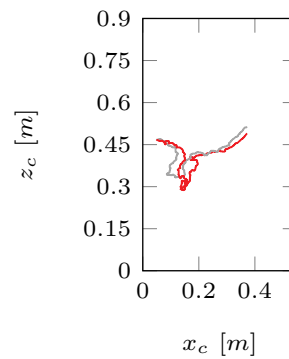
(A) Contour of the free surface in test with wedge $\mu = 2.0$ at $0.08[s]$ in closure stage.



(B) Comparison free surface left and right of wedge $\mu = 2.0$ at $0.08[s]$.



(C) Contour of the free surface in test with wedge $\mu = 0.8$ at $0.58[s]$ in Archimedal stage.



(D) Comparison free surface left and right of wedge $\mu = 0.8$ at $0.58[s]$.

FIGURE 5.9. Extraction of free surface from camera recordings. Symmetry is compared by mirroring the free surface from right to left; (—) experiment left, (—) experiment right.

5.2.5 Velocity record

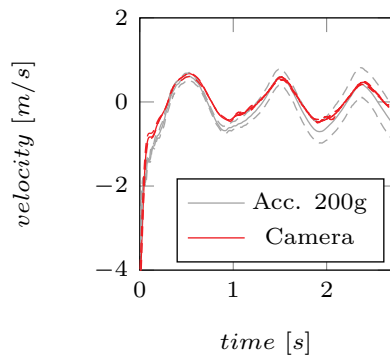
After the impact, the buoyant wedge starts to decelerate due to an increase in added mass and hydrostatic forces. A remaining step is extracting the motion of the wedge from the camera recordings. The actual size of the camera recorded frames is determined by the size of the experimental configuration. The position of the wedge is tracked with CSRT [88]. The effect of perspex on the angle of view is neglected. A Fourier analysis is done to remove the noise caused by the

pixels (720x480) and frame rate (240 per second). A low-pass filter of 8[Hz] is used. The velocity signals found with the recordings are averaged in time and illustrated in Fig. 5.10 for the three different cases.

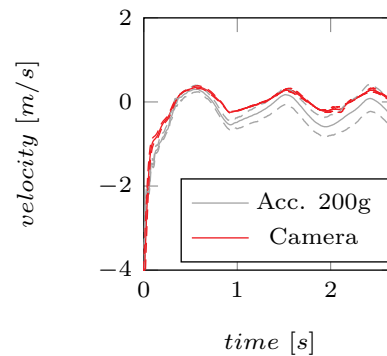
It is important to mention that the camera recordings are used for the global motion. The initial entry with a high deceleration is high frequency related and therefore not well captured because of the filter. The same is true for the instantaneous break of the 2x buoyant case reaching the maximum depth. The 2x buoyant case is finished around 0.18[s].

The unfiltered accelerometer signal is calibrated based on the position of the light gates, discussed in the previous section. The velocity signal is obtained by integrating this signal, resulting in Fig. 5.10. The signals are calibrated on the average impact velocity in Tab. 5.5c to show the variation found after impact and not before the impact. In Fig. 5.10b, the mean oscillatory motion of the velocity signal is vertically shifting over time compared with the camera recordings. The standard deviation is, however, smaller than for the impact velocity in Tab. 5.5c and increase in time.

To reduce the vertical shift, the velocity records of the accelerometers are calibrated on the camera recordings when the velocity is for the first time zero.



(A) $\mu = 0.8$.



(B) $\mu = 1.0$.

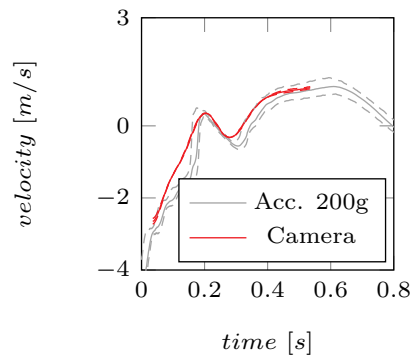
(c) $\mu = 2.0$.

FIGURE 5.10. Accuracy velocity during impact: the solid line is the mean, dashed lines is the max./min..

5.2.6 Natural heave period

After the impact, the wedge ends up in an oscillatory heave motion for which the theoretical period can be compared with the period found from the experiment. The heave period is related to the restoring spring coefficient, the mass, and the added mass. When the motion of the wedge has become small (after time 4.0[s]), the heave period of the wedge is determined from the average of six oscillations within the same test. Then the period is averaged over the 5 tests. For the 0.8x buoyant wedge, a period of 0.88[s] is found, averaged over five runs.

The restoring spring coefficient is determined by means of the waterline area. The chines are fully wetted for the wedge with $\mu = 0.8$ during heave, resulting in a waterplane area of around 0.05[m²]. The added mass is approximated using

$$(1 + m_a)m = \frac{\rho g A_w}{\left(\frac{2\pi}{T}\right)^2}, \quad (5.1)$$

where m_a is the added mass factor, m the mass of the wedge, A_w the waterplane area, and T the period. This resulted in an added mass factor of around 0.48 for the wedge with $\mu = 0.8$, which is the same as found from Vugts [277] for this kind of cross-section.

5.3 Simulations with discretization in space

5.3.1 Numerical solver

The numerical method of Eijk and Wellens [80] is used to determine the forces on the wedge. It is also used to analyze the physics of the experiment in more detail, in particular when 3D free surface phenomena in the experiment start to play a role. Understanding the 3D nature of these phenomena is important

for 2D strip theory methods used for rapid assessment of ship motions [79]. The numerical method is an incompressible two-phase flow model based on the Navier-Stokes equations. Compressible effects of water and air are small enough to ignore as the deadrise angle of the wedge (15[deg]) is sufficiently large [79, 86, 129].

The numerical method was inspired by the tradition of consistent methods following Rudman [230] and has been developed for predicting wave impact forces on structures [18, 75, 77, 80]. Monolithic two-way coupling of the equations of motion for fluid and structure is used to prevent the instabilities due to added mass when it is in the same order as the mass of the wedge [18, 90]. A key feature of the method is that momentum losses during the interaction between fluid and structure are negligible [80]. A significant reduction of interface diffusivity was made [76] so that an accurate prediction of the wedge's moment of impact can be made. A brief overview of the solver is given below with an account of the governing equations and the grid structure.

The governing equations for two-phase flows of immiscible Newtonian fluids are given in Eq. (5.2) and Eq. (5.3). The equations are formulated in conservative form, using vector notation. A one-fluid formulation is used with a single velocity field and a single pressure field [188], assuming that the two phases behave like a mixture separated by an interface. The continuity equation reads

$$\int_V \frac{\partial \rho}{\partial t} dV + \oint_S (\rho \mathbf{u}) \cdot \mathbf{n} dS = 0, \quad (5.2)$$

in which \mathbf{u} denotes the fluid velocity vector, ρ is the mixture density, V the control volume and S the boundary of V . The momentum equation is

$$\begin{aligned} \int_V \frac{\partial(\rho \mathbf{u})}{\partial t} dV + \oint_S \rho \mathbf{u} (\mathbf{u} \cdot \mathbf{n}) dS + \oint_S p \mathbf{n} dS + \int_V \rho \mathbf{F}_f dV \\ - \int_V \nabla \cdot (\mu (\nabla \mathbf{u} + \nabla \mathbf{u}^T) - \frac{2}{3} \mu \nabla \cdot \mathbf{u} \mathbf{I}) dV = 0, \end{aligned} \quad (5.3)$$

where p is the mixture pressure, μ the dynamic viscosity for a mixture and \mathbf{F}_f the body forces. The body force term accounts for gravity and capillary stresses and equals $\mathbf{F}_f = \mathbf{F}_g + \mathbf{F}_\sigma = g - \frac{1}{\rho} (\sigma \kappa \mathbf{n} \delta_\Gamma)$, with g the constant of gravity ($[0, -9.81]^T [\text{m/s}^2]$), σ the surface tension coefficient ($0.072 [\text{N/m}]$) between fluids, and κ the curvature of the interface.

The free surface is captured with

$$\frac{Df}{Dt} = \frac{\partial f}{\partial t} + (\mathbf{u} \cdot \nabla) f = 0, \quad (5.4)$$

where $f(\mathbf{x}, t) = 0$ gives the position of the free surface.

The structure, or body, is assumed rigid and displaced with a state-space representation of Newton’s second law. The force acting on the body is equal to integrated pressure along the body boundary S_b .

$$\mathbf{F}_b = \oint_{S_b} p \mathbf{n}_b dS. \tag{5.5}$$

The governing equations are solved on a computational grid of cells. A Cartesian grid is adopted with a staggered MAC (Marker-and-Cell) arrangement of variables. Velocities ($\mathbf{u} = [u, v]^T$) are defined in cell faces. Scalar variables, pressures (p), volume fractions (C_f), and densities (ρ), are defined in cell centers. The control volumes for the continuity equation coincide with the grid cells. The control volumes for the momentum equations are shifted in space with respect to continuity control volumes as shown in Fig. 5.11, together with the positions of variables in the grid. The control volumes partially overlap.

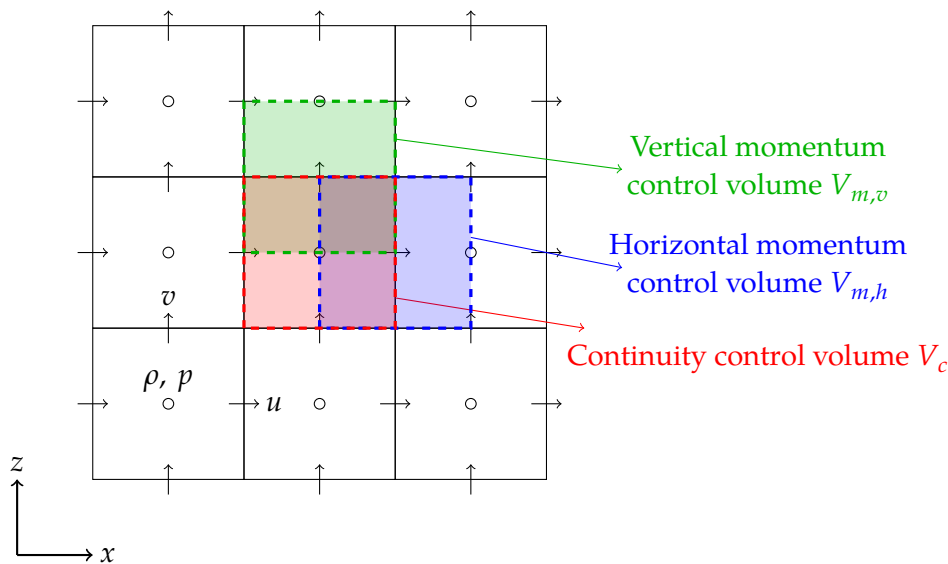


FIGURE 5.11. Standard MAC configuration of variables (staggered); pressure p is defined in the cell center (\circ), the horizontal velocity u field is sampled on the vertical faces (\rightarrow), the vertical velocity v is sampled on the horizontal faces (\uparrow). A continuity control volume is shown as $(-)$, a vertical momentum control volume as $(-)$, and a horizontal momentum control volume is $(-)$. Note that there is partial overlap between control volumes.

A Volume-of-Fluid (VOF) method is adopted for the geometrical reconstruction and transport of the interface. The distance function f in (5.4) is replaced by a discrete volume fraction C_f having a value between 0 and 1. The volume fraction indicates the filling ratio of one of the fluids in the cell. The interface between the two phases is identified by labeling the grid cells [80]. The choice of label depends on the volume fraction. In Fig. 5.12, the labeling of cells for a

2D Cartesian grid is illustrated: label E(mpty) for cells completely filled with the lighter of the two fluids ($C_f = 0$), label S(urface) for cells with some of the heavier of the two fluids in them and adjacent to E cells in directions aligned with the axis system, and label C(orner) for cells neighboring E cells in a diagonal direction. The remaining cells are labeled F(luid). S-labeled cells and C-labeled cells contain the interface. In these cells, reconstruction of the interface between the two fluids takes place. Geometrical reconstruction is performed by means of what we call bilinear interface calculation (BLIC) [76]. Transport of the interface is achieved by solving Eq. (5.4) in combination with the unsplit, multidimensional donating quadrant advection (DQA) scheme [76]. The advantage of this scheme with respect to similar methods [163] is that it is consistent with the discretization of the Navier-Stokes equations, i.e. complies with the tradition of consistent methods.

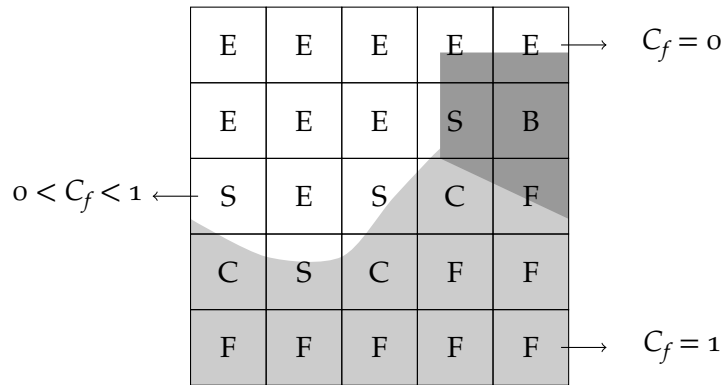


FIGURE 5.12. Labeling of cells [80]; labels F, B, S, C, and E. Fluid is indicated by ■ ($C_f > 0$). Body is indicated by ■.

The word 'consistent' is used for methods in which the spatial discretization of the terms for momentum advection in Eq. (5.3) and mass advection in Eqs. (5.2) and (5.4) is treated the same with continuity control volumes (V_c) and with momentum control volumes (V_m). The word 'flux' is used to refer to the amounts of mass and momentum that are transported between cells within a time step. In order to achieve a consistent discretization, the density is discretized using volume fraction fluxes such that the same combination of variables in the momentum flux has the same value as that combination of variables in the mass flux. Without consistency, spurious velocities are generated near the interface and conservation errors occur, but also – according to our investigations for this article – interface diffusivity and smearing of the impact force over time.

A cut-cell method is used to represent the wedge [80, 90]. This method has the advantage that, when adopted, the spatial discretization of the governing equation remains the same. The control volumes are scaled by means of coefficients

(volume apertures and edge apertures) to account for the parts of the volume and its boundary that are open to flow (i.e. the parts not occupied by the wedge). The interface between wedge and fluids is reconstructed and transported in the same way as the interface between fluids, using Eq. (5.4) with f replaced by the discrete volume fraction C_b that accounts for the volume of wedge in a cell, in combination with BLIC and DQA. Special treatment for small cut cells, like virtual cell merging [239], was found not to be necessary.

The velocity updates of fluid and structure are found with a pressure-based solver. Implicit Crank-Nicolson time integration is used for the equation of motion of the structure, so that it combines well with the implicit discretization of pressure in the momentum equation. Explicit time integration of the convective and diffusive terms in the momentum is adopted using an Adams-Bashforth method. The convective term is discretized in space with a second-order upwind scheme. The time step is chosen dynamically during a simulation by means of the Courant restriction that applies to our specific combination of discretizations in time and space ($CFL < 0.25$). The Courant restriction needs to be based on the uncut cell size, as shown by Dröge [71].

The fluid properties used for the numerical simulations are based on the input of the experiment. Fluid properties for a water temperature of 16.3 degrees [C] are used. The numerical domain has the same size as the inside of the box used in the experiment: a height of 0.9[m], a width of 1.1[m], and a water depth of 0.495[m]. The top boundary is closed and at that boundary the atmospheric pressure is defined (1032.2[hPa] not measured in experiments, but taken from a meteorological report covering the days the experiment took place). As the numerical simulations are in 2D, the masses of the wedge per unit width for the three cases are 16.95, 21.19, and 42.37[kg/m] for the wedge with $\mu = 0.8, 1.0$ and 2.0, respectively. A maximum Courant restriction of 0.2 to stay on the safe side of the stability limit. The numerical wedge is released at 0.005[m] above the waterline with the initial velocity that the wedge in the experiment would also have at that elevation.

5.3.2 Grid convergence

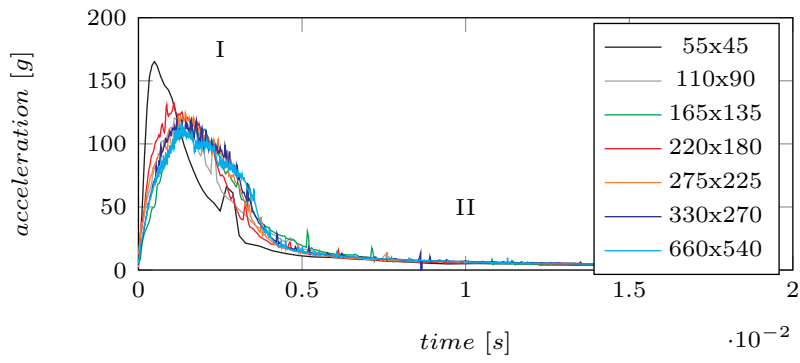
A grid convergence study is performed to find a grid resolution that can represent the four stages of impact. The domain is divided in cells of a uniform cell size. The simulations are named for their number of cells in horizontal direction and vertical direction. For the wedge with $\mu = 0.8$ the convergence of the following parameters is assessed: the maximum vertical acceleration experienced upon impact in the slamming stage, the velocity of the wedge after impact in the enclosed stage, and the free surface configuration at different times in the separation stage.

An impact speed of $6.4[\text{m/s}]$ is used in this section, representative of all wedges but not specific to any one of them. The formal comparison with the experiment is described later in Sec. 5.5.

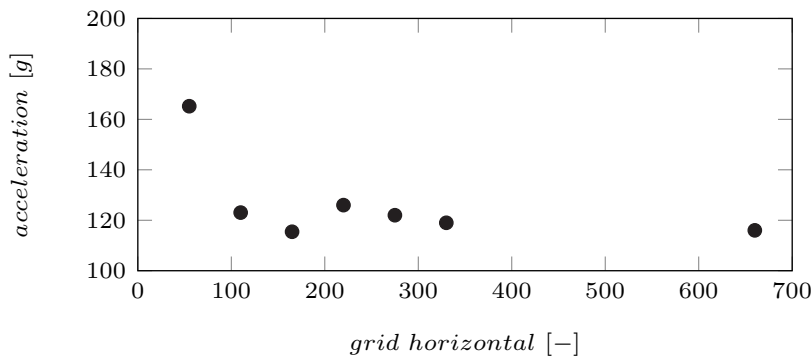
The wedge's vertical acceleration during the impact is plotted in Fig. 5.13a for different grid resolutions. The spikes in acceleration are caused by numerical artifacts. The size of the spikes decreases with increasing grid resolution, because the ratio of number of cut cells with a near-zero volume to total number of cut cells becomes smaller. The maximum vertical acceleration from the simulations with seven different grid resolutions is shown in Fig. 5.13b. The maximum acceleration is demonstrated to converge to approximately $116[\text{m/s}^2]$. A grid of 330×270 cells is sufficiently accurate for this parameter as its results are within 2.5% of the maximum acceleration on the finest grid.

The free surface configuration on the left side of the wedge is shown for six grid resolutions in Figs. 5.13c and 5.13d at two different times in the separation stage. Formal convergence of the shape of the jet is not achieved. A higher resolution is associated with a thinner jet that reaches a higher vertical position. Although convergence of the shape of the jet was not obtained, this does not imply that the force on the wedge is affected, because Eijk and Wellens [79] showed that the shape of the jet does not influence the force during the slamming and separation stage of the wedge.

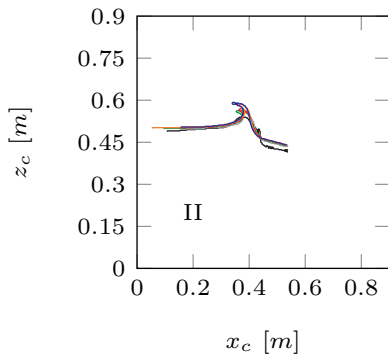
Fig. 5.13e shows the velocity of the wedge over time, with emphasis on the velocity during the enclosed stage. The closure stage (see Fig. 5.1) ends at around $0.32[\text{s}]$ when the fronts of the water that is propagating over the deck of the wedge meet in the middle and generate a jet in upward direction. When the wedge emerges through the free surface again, it starts oscillating vertically. The velocity signals for six grid resolutions are compared. The velocity maximum of the first oscillation is taken from the time signals and plotted in Fig. 5.13f. Those velocity maxima are shown to converge to around $0.45[\text{m/s}]$ for increasing grid resolution. The wedge's vertical velocity signals for the different grid resolution start to deviate more further in time, with the results of the two highest resolutions close, but not on top of each other. Several free surface breaking events occur during that time; free surface breaking, just like jet formation, is different for all grid resolutions, and formal convergence of the wedge's vertical velocity, when it depends on the specifics of free surface waves after breaking, is therefore hard to achieve.



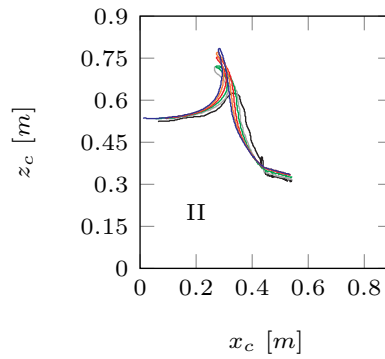
(A) Acceleration of the wedge over time.



(B) Maximum acceleration.

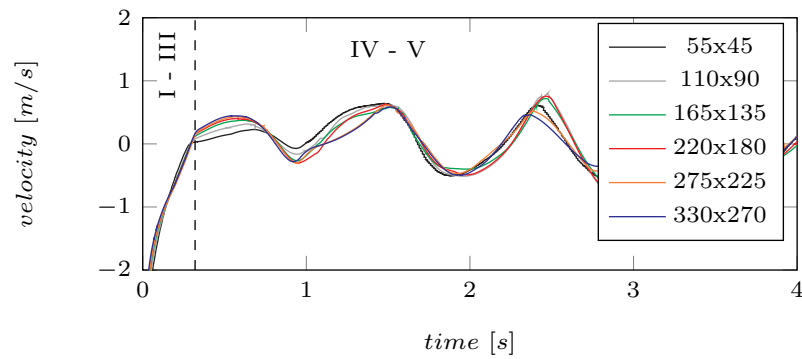


(C) Free surface at 0.02[s].

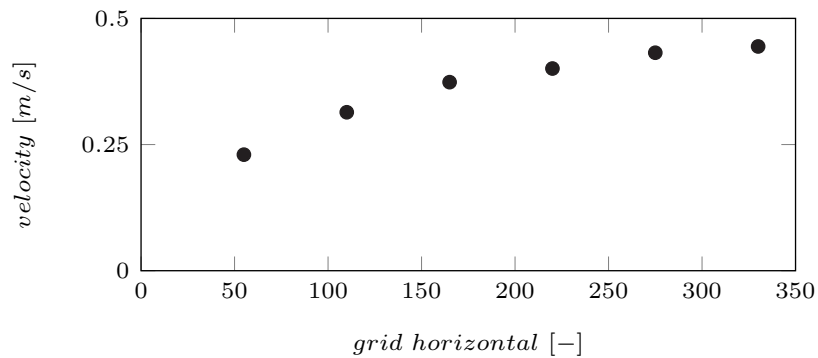


(D) Free surface at 0.08[s].

FIGURE 5.13. Numerical results for wedge with $\mu = 0.8$ for different grid resolutions. Stage number is included.



(E) Velocity of the wedge over time.



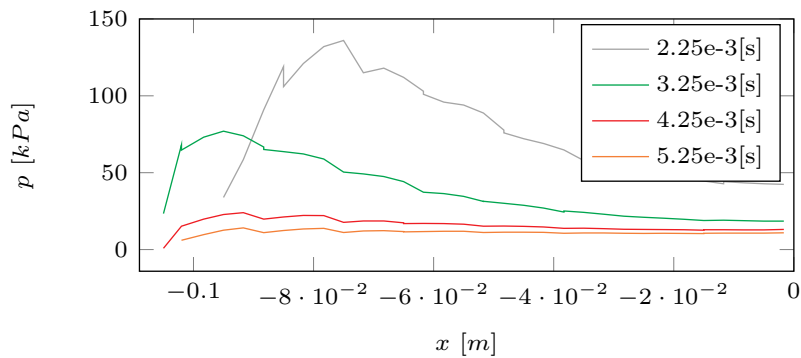
(F) First local velocity maximum.

FIGURE 5.13. Numerical results for wedge with $\mu = 0.8$ for different given grid resolutions. Stage number is included.

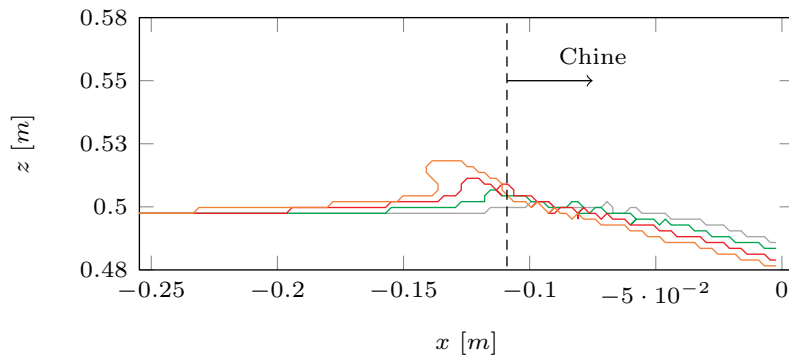
The heave frequency after the impact is found by extending the numerical simulation to 8[s] for a grid resolution of 220x180. The period of oscillation between consecutive local maxima is averaged over five oscillations. The resulting period is 0.89[s], which is slightly different from the 0.88[s] found with the experimental results. The difference is not large, but the most likely explanation is that the oscillation of the wedge is, in part, driven by the remaining free surface oscillations and that the free surface between experiment and simulation is slightly different because of wave breaking [179]. When the oscillation is considered completely free, the added mass factor associated with the period found is around 0.48.

Much literature has investigated the impact of a 2D wedge during the slamming stage, often with a constant fall velocity. Zhao, Faltinsen, and Aarsnes [316] showed that the position of maximum pressure is found at the spray roots before the free surface separates from the chine to form jets. After separation, the position of maximum pressure acting on the wedge moves toward the keel and the maximum pressure goes down. Results similar to Zhao, Faltinsen, and Aarsnes

[316] are found with the simulation at a grid resolution of 330×270 . The pressure along the bottom of the wedge is shown in Fig. 5.14 at four moments in time, at $t = 2.25 \times 10^{-3}$, 3.25×10^{-3} , 4.25×10^{-3} , and 5.25×10^{-3} [s] after the moment of first contact between wedge and free surface (not after maximum acceleration in this case). For those same moments in time, the free surface configuration near the wedge is shown in Fig. 5.14b. Note that the free surface separates from the chine between 3×10^{-3} and 4×10^{-3} [s]. Fig. 5.14c shows the total force on the wedge over time. The rise time of the force is 0.003 [s], a fact that was used starting from Fig. 5.7 to define an appropriate time for the origin of time axis. Due to the deceleration of the buoyant wedge, the total force already goes down before flow separation and jet formation. After separation of the free surface from the chine, the force drops more rapidly, which is consistent with the literature about wedges with a constant fall velocity.

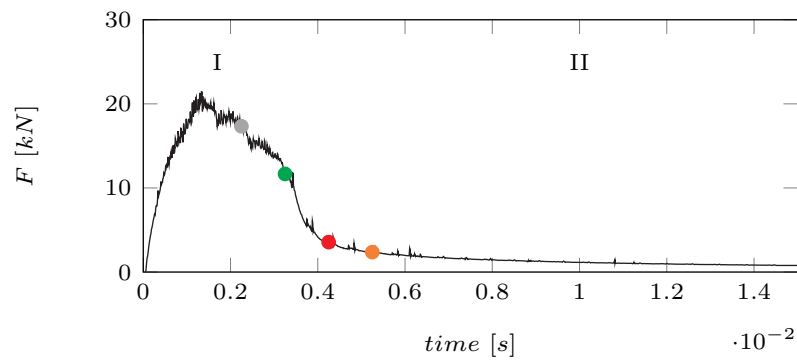


(A) Pressure along half of the bottom of the wedge, from chine to keel, at different times.



(B) Free surface configuration near the chine of the wedge, at different times.

FIGURE 5.14. Pressure distribution and free surface for wedge with $\mu = 0.8$ at different time instances indicated by the color. Flow separation takes place after reaching the end of the chine. The total force on the wedge over time is given.



(c) Total force on the wedge over time. Stage numbers in Fig. 5.1 included. Color indicates the time instance. Exact Moment of separation is not clear.

FIGURE 5.14. Pressure distribution and free surface for wedge with $\mu = 0.8$ at different time instances indicated by the color. Flow separation takes place after reaching the end of the chine. The total force on the wedge over time is given.

In the remainder, the numerical results are shifted in time, like the experimental results, so that $t = 0[s]$ corresponds with the moment of maximum deceleration. As there was a marginal difference between characteristic results for the high grid resolutions, all simulations discussed from here on are with a resolution of 330×270 . The moment when the separation stage starts is difficult to see with the results so far.

5.4 Simulations with an analytical approximation in space

Previous work on analytical methods for wedge entry focuses on the slamming stage and the beginning of the separation stage. Typically, the fall velocity is considered constant. Our aim is to extend the applicability of analytical methods and to consider buoyant wedges. To that end, an analytical method is derived so that a force decomposition can be made in order to study the relative contribution of the different force contributions in the different stages of wedge entry. The method is also used to investigate uncertainties in the experiment.

The modified Logvinovich model (MLM) [144] is implemented and extended, coupled with an equation of motion, and assessed up to the closure stage. As we have the required information from the experimental and numerical results, the fictitious body continuation (FBC) approach is applied, so that improved force predictions [257] can be made compared to bare MLM. A linear and a curved FBC are evaluated improved based on the free surface from the numerical simulations. A hydrostatic force is added to the method and its value is analyzed. Recent work [110] has assessed the FBC for asymmetric wedge entries (line between chines under an angle with the horizontal coordinate axis). Those

results inspired us to investigate the uncertainty in the experiment related to the tolerances of the guiding mechanism and the inclination angle of the wedge with respect to the initial free surface of the water. The main parameters for the derivation of the analytical approach are given in Fig. 5.15. They are explained when discussing the equations that feature the parameters.

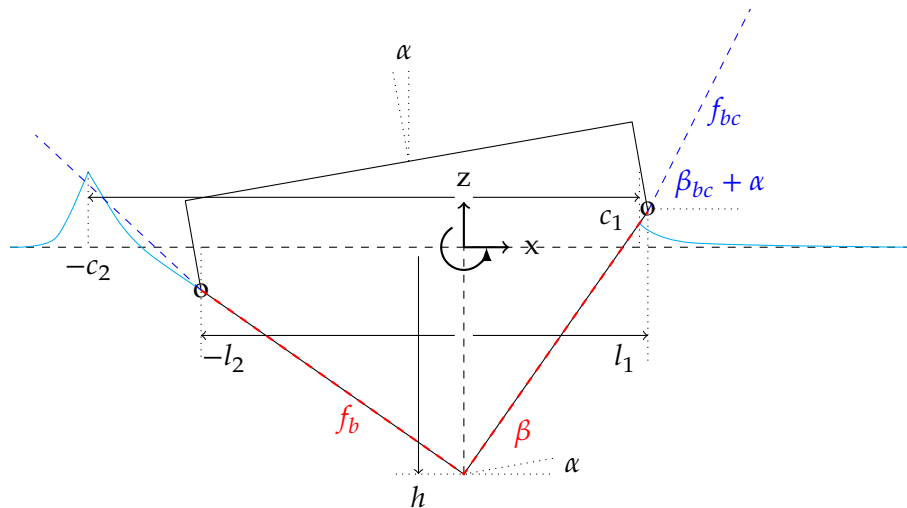


FIGURE 5.15. Parameters for analytic wedge entry. The wedge is allowed to have an angle α with respect to the horizontal. The wedge has a boundary f_b . The mark 'o' indicates the chines where flow separation occurs and continuation takes place with a fictitious body with boundary f_{bc} . The horizontal position of the chines are given by l . The position of the tip of the wedge with respect to the initial free surface is given by h . The wetted length of the wedge is defined by the range $-c_2$ to c_1 .

5.4.1 Free surface and body

Although the model of Logvinovich [162] is satisfactory for low deadrise angles, we choose to account for the shape of the body as in the MLM method, so that body contours other than wedges may also be evaluated. A continuous shape function for the body (f_b) is defined

$$f_b(x) = |x| \tan \left(\frac{1}{2} \frac{|x|}{x} (\beta_1 + \beta_2) + \frac{1}{2} (\beta_1 - \beta_2) \right) \quad (5.6)$$

in which β is the deadrise angle corrected by the inclination angle α to get $\beta_1 = \beta + \alpha$, and $\beta_2 = \beta - \alpha$. Coordinate $x = 0$ is defined at the horizontal position of the lowest point along the body contour. The description of the body contour in Eq. (5.6) is valid in the range $-l_2 < x < l_1$ in between the points where flow separation takes place. The fictitious body is defined outside of this range. For a

linear representation of the fictitious body [257] The linear approach of Tassin, Korobkin, and Cooker [257] is

$$f_{bc}(x) = f_b(l_1) + (x - l_1)\tan(\beta_{1,bc}), \quad (5.7)$$

a discrepancy in the force just after flow separation was found by Wen et al. [294] who compared the approach with numerical results. Therefore, the curved formulation of Wen et al. [294] is adopted, to which we have added the asymmetric aspect. For $x > l_1$, the description of the contour of the fictitious body then becomes

$$f_{bc}(x) = f_b(l_1) + (x - l_1)f_{x,b}(l_1) + \frac{l_1}{k}(A - \ln(1 + A))(\tan(\beta_{1,bc}) - f_{x,b}(l_1)), \quad (5.8)$$

in which

$$A = \frac{k(x - l_1)}{l_1}. \quad (5.9)$$

Parameters k and β_{bc} need to be determined from experimental or numerical results of the free surface deformation.

5.4.2 Wetted area

The pressure acts along the wetted length (or contact region) of the wedge. It depends on the depth of immersion h with respect to the undisturbed free surface and on the shape of the body shape f that consists of the actual body f_b and the fictitious body f_{bc} . Wagner's condition, which is the condition that keeps the free surface elevation restrained to the initial free surface, is used to determine the wetted length. The condition consists of two transcendental equations

$$\begin{aligned} \int_{-1}^1 f(x(\tau))\sqrt{\frac{1+\tau}{1-\tau}}d\tau &= \pi h(t), \\ \int_{-1}^1 f(x(\tau))\sqrt{\frac{1-\tau}{1+\tau}}d\tau &= \pi h(t). \end{aligned} \quad (5.10)$$

Wagner's condition implies that the wetted area only depends on the immersion depth of the body. Position x is approximated by piecewise-linear functions [145]

$$x(\tau) = \frac{1}{2}(c_1(t) + c_2(t))\tau + \frac{1}{2}(c_1(t) - c_2(t)), \quad (5.11)$$

in which the second part of the equation introduces the asymmetry. Depth h is found by integrating the body velocity (\dot{h}) over time

$$h(t) = \int_0^t \dot{h}(t)dt. \quad (5.12)$$

The two transcendental equations in Eq. (5.10) are split to solve for the wetted length in parts. Every part represents either the body or the fictitious body as follows

$$\int_{-1}^1 Ad\tau = \int_{b_1}^1 A_{bc}d\tau + \int_{-b_2}^{b_1} A_b d\tau + \int_{-1}^{-b_2} A_{bc}d\tau, \quad (5.13)$$

having abbreviated the integrand in Eq. (5.10) as A , and

$$\begin{aligned} b_1 &= \min\left(\frac{2l_1 - c_1 + c_2}{c_1 + c_2}, 1\right), \\ b_2 &= \min\left(\frac{2l_2 + c_1 - c_2}{c_1 + c_2}, 1\right). \end{aligned} \quad (5.14)$$

The wetted length of a wedge was derived by [145]

$$c_1(t) = \frac{\pi}{2\tan(\beta_1)} \frac{1 - \sin(-2\alpha)/\sin(2\beta)}{(1 - \nu)\sqrt{1 - \nu^2}} h(t) \quad \text{and} \quad c_2 = c_1(t) \frac{1 - \nu}{1 + \nu}, \quad (5.15)$$

with ν the solution of

$$\nu\sqrt{1 - \nu^2} + \arcsin(\nu) = \frac{\pi \sin(-2\alpha)}{2 \sin(2\beta)}. \quad (5.16)$$

5.4.3 Velocity potential

The angle between the initial free surface and body contour is assumed to be small. After linearisation of the boundary conditions at the undisturbed free surface and solving the boundary value problem, the velocity potential is derived, keeping only first-order terms (including the shape of the body) [144]

$$\phi(x, t) = -\dot{h}(t)\sqrt{(c_2(t) + x)(c_1(t) - x)} - \dot{h}(t)(f(x) - h(t) - d(t)), \quad (5.17)$$

The first term in Eq. (5.17) is the velocity potential for a flat plate [278]. The second term accounts for bodies of arbitrary shape that satisfy the assumption. In that second term, $d(t)$ equals zero when linearisation is applied around the initial free surface, and equals $f(c(t)) - h(t)$ when linearising around the instantaneous position of the free surface as it goes up along the contour of the body. Note that the linearisation of the boundary conditions does not lead to a linear problem, because the wetted length is unknown a priori [110]. A second-order analysis is more involved and reported by Oliver [197].

5.4.4 Pressure

Adding to prior assumptions that the liquid is assumed incompressible and irrotational, and that the effect of surface tension can be neglected, leads to a formulation of the (nonlinear) Bernoulli equation. Wagners' original approach for flat plates neglects higher-order terms, causing the pressure $p(x, t)$ to be overestimated [86]. When it is also assumed that the vertical forces are dominant over the horizontal ones, the MLM formulation of the Bernoulli equation along the body contour becomes [110, 144]

$$p(x, t) = -\rho \left[\phi_t + \frac{f_x \dot{h}}{1 + f_x^2} \phi_x + \frac{1}{2(1 + f_x^2)} (\phi_x^2 - \dot{h}^2) + gh \right], \quad (5.18)$$

to which we have added the hydrostatic pressure with gravitational constant g . Substituting the velocity potential with $d = 0$ gives a formulation similar to Hascoët et al. [110] with a pressure p_v that depends on the fall velocity \dot{h} of the wedge and a pressure p_a that depends on its acceleration \ddot{h} , but with a hydrostatic pressure p_h that depends on the vertical position

$$\begin{aligned}
 p(x, t) &= p_h(x, t) + p_v(x, t) + p_a(x, t) \\
 &= -\rho g \bar{h} \text{ (Buoyancy)} \\
 &\quad + \frac{1}{2} \rho \dot{h}^2 \max \left[\frac{dc_1}{dh} \sqrt{\frac{c_2 + x}{c_1 - x}} + \frac{dc_2}{dh} \sqrt{\frac{c_1 - x}{c_2 + x}} \text{ (Slamming)} \right. \\
 &\quad \quad \left. - \frac{1}{4} \frac{(c_1 - c_2 - 2x)^2}{(c_1 - x)(c_2 + x)(1 + f_x^2)} - 1 \text{ (Jets), } 0 \right] \\
 &\quad + \rho \ddot{h} \left[\sqrt{(\min(l_1, c_1) - x)(\min(l_2, c_2) + x)} + f(x) - \tilde{f}(x) \right] \text{ (Added mass)}.
 \end{aligned} \tag{5.19}$$

In Eq. (5.19), \tilde{f} is the fictitious body continuation for asymmetric bodies that accounts for both sides of the body not necessarily experiencing flow separation at the same moment. Parameter \bar{h} , a representative depth of immersion, can be defined with respect to the initial free surface ($\max(h(t) - f(x), 0)$) or with respect to another level. This is investigated later in this section.

The term p_v consists of two parts. One part, before the minus sign, is the slamming contribution found from the time derivative of the velocity potential; the other part is the pressure reduction due to the formation of jets. The term p_a represents the contribution of added mass.

The derivatives of the wetted length in Eq. (5.19) are solved after the wetted length has been solved, in the following way

$$\begin{aligned}
 \int_{-1}^1 f_x(x(\tau)) \frac{1}{2} (\tau + 1) \sqrt{\frac{1 + \tau}{1 - \tau}} d\tau &= \pi \frac{dh}{dc_1}, \\
 \int_{-1}^1 f_x(x(\tau)) \frac{1}{2} (\tau - 1) \sqrt{\frac{1 - \tau}{1 + \tau}} d\tau &= \pi \frac{dh}{dc_2}.
 \end{aligned} \tag{5.20}$$

Integral splitting, like in Eq. (5.13), is applied when necessary.

The pressure acts on the body along the length between contact points where the instantaneous free surface intersects with the body contour. That length can be expressed as the range $\min(-l_2, -c_2(t)) \leq x \leq \min(l_1, c_1(t))$. From here on ζ is used for the outcome of $\min(l, c)$. As a result of the quadratic terms in the nonlinear Bernoulli equation, the pressure in the contact points tends to negative infinity. Negative pressures are ignored [144] by using a max-function

for \tilde{p}_v as $\max(p_v, 0)$. Although there is no physical explanation for neglecting the negative pressure values, the results are satisfying.

The added mass pressure p_a does not level off after flow separation [257], whereas according to Iafrati and Korobkin [125] it should. A fictitious continuation of the body is needed for determining the submerged area [110]. Other than the MLM of Hascoët et al. [110] the added mass is not linearised at the initial free surface ($d(t) = 0$), but linearisation of the boundary conditions is performed at the instantaneous position of the free surface ($d(t) = f(c(t)) - h(t)$), similar to the generalized Wagner model of Mei, Liu, and Yue [178]. This requires a modification in the fictitious continuation compared to Hascoët et al. [110]. The new formulation is given in Eq. (5.21). A min-function in ζ for the fictitious continuation is used to ensure that the added mass does not keep growing after flow separation.

$$\tilde{f}(x) = f(-\zeta_2) + \frac{x + \zeta_2}{\zeta_1 + \zeta_2} (f(\zeta_1) - f(-\zeta_2)). \quad (5.21)$$

The effect of these changes compared to Hascoët et al. [110] is considered below.

5.4.5 Forces

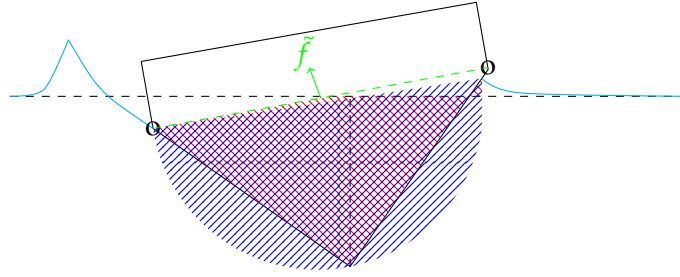
The added mass force, after integration of the added mass pressure, can be written in the following form

$$F_a = \rho \ddot{h} V_a, \quad (5.22)$$

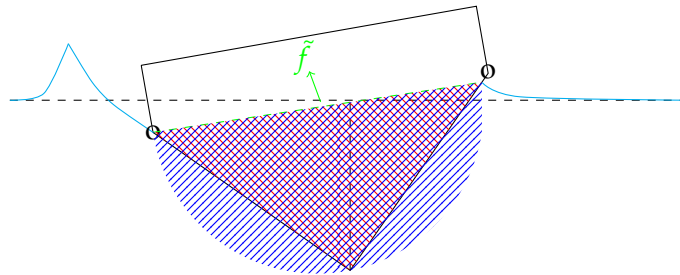
in which V_a is the volume of water that is accelerated by the body. The added volume is illustrated in Fig. 5.16. It has two contributions: a semi-circle with diameter $\zeta_1 + \zeta_2$ (indicated in blue in Fig. 5.16), and the submerged volume of the wedge that needs to be subtracted from the semi-circle (indicated in red)

$$V_a = \frac{1}{2} \frac{\pi}{4} (\zeta_1 + \zeta_2)^2 - \left(\frac{1}{2} (\zeta_1 + \zeta_2) (f(\zeta_1) + f(-\zeta_2)) - \int_{-\zeta_2}^{\zeta_1} f(x) dx \right). \quad (5.23)$$

The approach of Hascoët et al. [110] to the added mass is illustrated in Fig. 5.16a. Our approach with the new formulation for the fictitious condition \tilde{f} is shown in Fig. 5.16b. The formulation of the added mass is tested for two benchmarks in Sec. 5.4.7.



(A) Approach by Hascoët et al. [110], among others.



(B) Approach in this article with new formulation fictitious continuation \tilde{f} .

FIGURE 5.16. Illustration of added mass for an asymmetric wedge entry. Added mass is the difference between the first term of Eq. (5.23) (–) and the remaining part (–).

The force contribution that depends on the velocity of the wedge, slamming and the reduction due the formation of jets, is calculated as follows

$$F_v = \int_{-\xi_2}^{\xi_1} p_v dx. \tag{5.24}$$

The hydrostatic force contribution, F_h is calculated in the same way as the force contribution that depends on the velocity, but now with p_h .

5.4.6 Equation of motion

The motion of the wedge is determined using a state-space representation of Newton’s second law

$$\begin{aligned} m_b \frac{dh}{dt} &= F_v + F_a - m_b g, \\ \frac{dh}{dt} &= \dot{h}. \end{aligned} \tag{5.25}$$

in which m_b is the mass of the body. The inclination angle of the wedge α for asymmetric entry is kept constant here, but can be included in the state-space

5

representation as a time dependent variable. The system is solved by means of fourth-order Runge-Kutta time integration with the steps in the flow chart below.

FOR EACH TIME STEP

1. Use the velocity \dot{h} and the depth of immersion h at the old time level (Eq. (5.25))
2. Compute the wetted length (Eq. (5.13)) and its derivative (Eq. (5.20))
3. Compute the pressure along the contour of the body (Eq. (5.19))
4. Integrate the pressure along the wetted length to obtain the force, $F_v + F_a + F_h$ (Eqs. (5.22) and (5.24))
5. Integrate in time to obtain the new velocity \dot{h} and depth of immersion h (Eq. (5.25))

Input to the system are the shape of the body with deadrise angle β and inclination angle α , and the shape of the fictitious body with angle β_{bc} (and parameter k for it to be curved). Initial conditions are the velocity of the wedge upon impact \dot{h}_0 and the immersion depth $h_0 = 0$.

The following two subsections contain a verification of the analytical method with results of others that did not include a hydrostatic force. After verification, the method is tested with a buoyancy force and compared with our own numerical results during the slamming stage and the full separation stage up to the closure stage.

5.4.7 Verification symmetric entry and fictitious body

The analytical method is verified with the numerical results of Piro and Maki [211] and the analytical results of Tassin, Korobkin, and Cooker [257] (with an approach similar to Hascoët et al. [110]) for a wedge that decelerates after impact. The wedge has a deadrise angle $\beta = 10[\text{deg}]$ and an inclination angle $\alpha = 0[\text{deg}]$. Note that with $\alpha = 0$ the wedge entry is symmetric, so that $l_1 = l_2 = l$. The trajectory of the wedge is described by $h = (\dot{h}_1/2)t^2 + \dot{h}_0 t$. The velocity upon impact \dot{h}_0 is set to $4[\text{m/s}]$ and the constant deceleration \dot{h}_1 is such that the speed is equal to zero when the chine of the wedge reaches the initial water level. The input angle for the linear fictitious body is set to $\beta_{bc} = 45[\text{deg}]$ [257]. The force as a function of time is shown in Fig. 5.17 where "current" indicates our results, that are very close to those of Tassin, Korobkin, and Cooker [257] overall. The force has a maximum some time after impact. Flow separation starts at around $t/t_1 = 0.4$, where t_1 is the moment of minimum force, and gives a steep drop in

force. The force then tends to zero as the velocity tends to zero. It is not clear why the force in the numerical results of Piro and Maki [211] goes up again after reaching a minimum. The line "current + a.m." represents our results with the modification in the added mass term made above. The modification brings the results somewhat closer to the force maximum in the results of Piro and Maki [211], and causes somewhat larger forces overall.

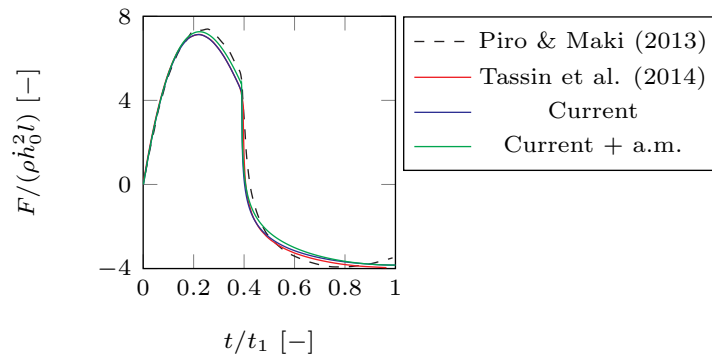


FIGURE 5.17. Force over time during wedge entry with $\alpha = 0$, $\beta = 10[\text{deg}]$ and $\beta_{bc} = 45[\text{deg}]$. Results of the method in the current article compared to numerical results (Piro and Maki [211]) and analytical results (Tassin, Korobkin, and Cooker [257]) from existing literature.

5.4.8 Verification asymmetric entry

The asymmetric implementation of wedge entry is verified based on numerical results of Hu et al. [119]. They used the domain setup of the 2D experiment conducted by Barjasteh, Zeraatgar, and Javaherian [10] and made a comparison. To our knowledge this is the first time that results of an analytic method are compared to Hu et al. [119]. A wedge with a deadrise angle of $\beta = 20[\text{deg}]$ enters the water with an initial impact velocity of $3.13[\text{m/s}]$ and a fixed inclination angle α . The inclination angle is varied four times: $0[\text{deg}]$, $5[\text{deg}]$, $10[\text{deg}]$, and $15[\text{deg}]$. The length of the chine of the wedge is $0.205[\text{m}]$ and the weight (m_b) is $44[\text{kg/m}]$. A comparison of the force in the numerical method versus the force in the analytical method is made in Fig. 5.18.

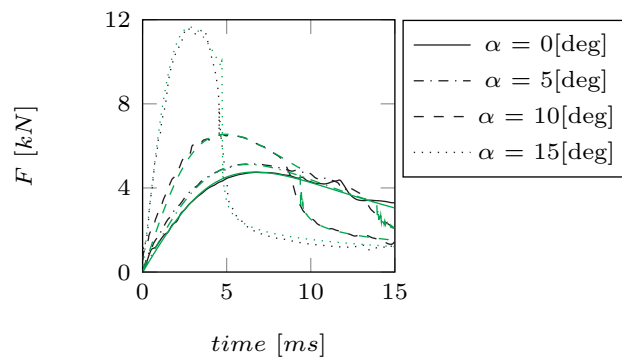


FIGURE 5.18. Wedge entry with $\beta = 20[\text{deg}]$ and $\beta_{bc} = 45[\text{deg}]$: acting forces over time compared for our analytical approach (—) and the numerical (–) model of Hu et al. [119].

In Fig. 5.18, good agreement between results of the numerical method and the analytical method is found, so that the analytical method we have derived can be considered suitable for asymmetric wedge entries. The main difference, however small, is that the decrease in force after separation of the jets around 5[ms] occurs more abruptly in the analytical results than in the numerical results. This finding is consistent with what is found from our numerical results for a symmetric wedge entry in Fig. 5.14c, where jet separation at 3.3[ms] (green dot) does not cause such an abrupt force reduction either.

5.4.9 Verification slamming and jet separation stage with numerical results

In order to compare the performance of the linear FBC to the performance of the curved FBC, the results of the analytical method are compared to the results of our numerical method in Figs. 5.13 and 5.14. According to Wen et al. [294], the difference between linear and curved FBCs starts to become important just after jet separation. The free surface contour at $5.25e-3[\text{s}]$, just after jet separation, is extracted from the numerical simulations and shown in Fig. 5.19. The figure shows the free surface contour to the right of the wedge's chine. The contour is given by $C_f = 0.9$. The horizontal position of the chine is indicated by a dashed vertical line. The end point of the wetted length of the wedge is indicated by a black circular marker. The marker is farther away from the center of the wedge than the chine, because the wedge is in the jet separation stage. The contours of the of the linear FBC and the curved FBC are also represented as dashed lines. Contrary to Wen et al. [294], who base their coefficients on the free surface positions at $1.25l$ and $1.5l$, with l equal to half the wetted length, our coefficients for the curved FBC come from a least-square fit of the free surface between the chine and the end point of the wetted length, yielding $\beta_{bc} = 54[\text{deg}]$ and $k = 30.0$. The linear FBC is shown with the same $\beta_{bc} = 54[\text{deg}]$.

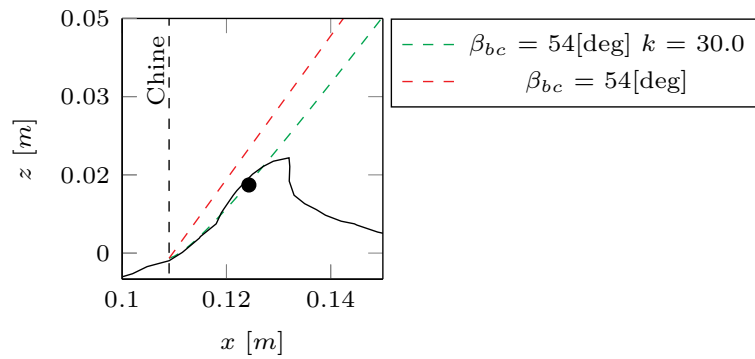
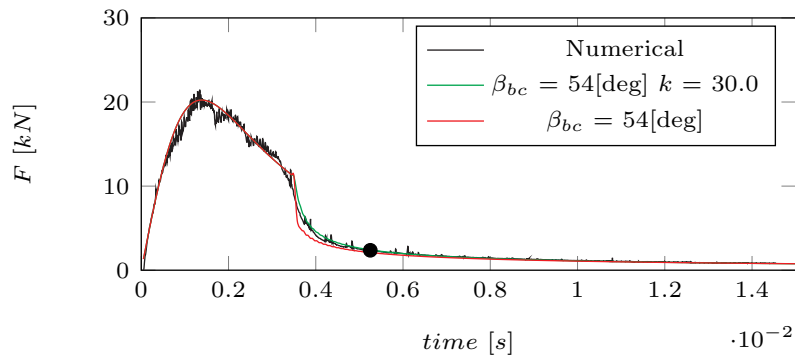


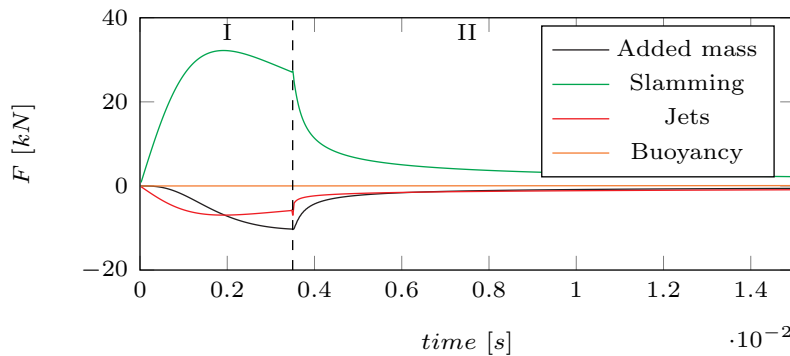
FIGURE 5.19. Comparing the linear and curved fictitious body continuation (FBC) to the right of the wedge’s chine with the free surface of our numerical method at $5.25\text{e-}3[\text{s}]$ using the contour given by volume fraction $C_f = 0.9$. The end point of wetted length at given time is indicated by marker ●.

Having all input needed for the analytical approach, the vertical force on the wedge over time is shown in Fig. 5.20a, in which the result of the numerical method for the wedge with $\mu = 0.8$ is compared to the result of the analytical method. The analytical result is in good agreement with the numerical result. The difference in force is never larger than 5%; the difference in force near the maximum at $0.015[\text{s}]$ is below 0.25%. With the curved FBC compared to the linear FBC, the analytical force is closer to the force from the numerical method for a longer duration after jet separation. The black circular marker in Fig. 5.20a indicates the time at which the coefficients β_{bc} and k were to the free surface of the numerical method.



(A) Result of numerical method compared to result of analytical method with linear and curved fictitious body continuation (FBC). Time $5.25\text{e-}3[\text{s}]$ when FBC is fit to numerical free surface is indicated with ●.

5



(B) Result of analytical method decomposed into different contributions (see Eq. 5.19) during slamming stage and jet separation stage with vertical dashed line at the time between stages.

FIGURE 5.20. Vertical force on wedge with $\mu = 0.8$ over time. Stage numbers are included.

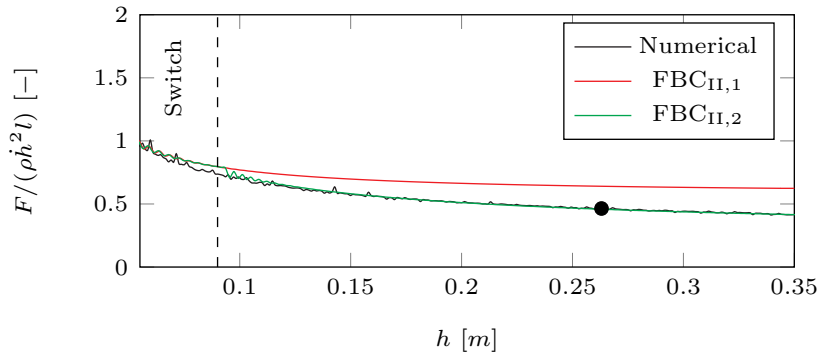
Fig. 5.20b shows how the force from the analytical method with $\beta_{bc} = 54[\text{deg}]$ and $k = 30.0$ is decomposed into different contributions in the slamming stage and in the jet separation stage. The following force contributions are distinguished: added mass, slamming, jet formation, and hydrostatic. The contribution of slamming is largest overall, especially during the slamming stage. The force contribution associated with jet formation subtracts from the slamming force. When represented as a force, the added mass contribution also subtracts from the contribution of slamming to for the total force on the wedge. The hydrostatic force during the slamming stage and the start of the jet separation stage is negligible compared to the other force contributions.

These results demonstrate that the analytical method, with some input from the numerical method to calibrate the FBC, can be used to determine the vertical force on the wedge with good accuracy during the slamming stage and the beginning of the separation stage. Linearising the added mass term at the instantaneous free surface position (discussed in Sec. 5.4.4) leads to an improved estimate of the added mass and maximum force compared to linearising at the initial free surface position. A difference is that the drop in force magnitude at the moment of flow separation (at around $3.5 \cdot 10^{-3}[\text{s}]$) is more abrupt in the analytical results than in the numerical results. The analytical method requires a couple of minutes to complete a simulation, with most of the computation time spent on finding the wetted length at each moment in time, whereas the numerical method requires several hours. With the limited computational effort required, the analytical method is better suited for the rapid assessment of small variations of the wedge's velocity and inclination angle during impact than the numerical method.

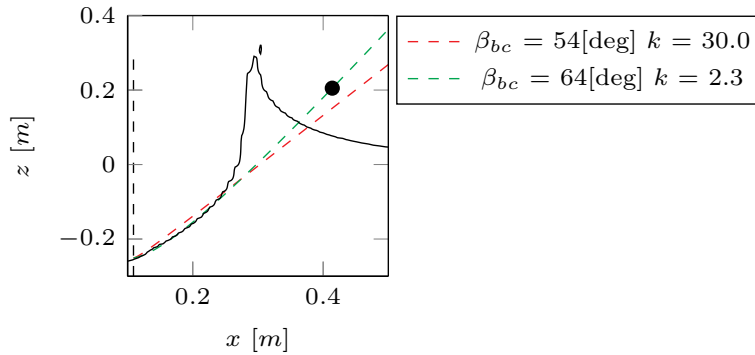
5.4.10 Extension until closure stage: change of the FBC

In literature, analytical methods have not yet been employed to determine forces on wedges until the closure stage. Also here the force as a function of time has thus far been presented until $t = 0.015$ [s]. The wedge's depth of immersion h and velocity \dot{h} at that time are 0.05 [m] and 2.5 [m/s]. During the slamming stage, the curve of the force as a function of immersion depth h strongly resembles the curve of the force as a function of time, shown in Fig. 5.20b. It was found that starting from $h = 0.06$ [m], the analytical results begin to deviate from the numerical results. The situation was analyzed by means of an additional numerical simulation with the same impact velocity of 6.4 [m/s], and the same grid cell size as the 330×270 grid, but with the gravity constant g set to 0 and with a larger domain and hence more grid cells. The domain was made larger to make sure that effects related to the size of the domain (boundary effects) were excluded from the comparison between numerical and analytical results during the separation stage (II). Note that boundary effects cannot have influenced the results during the slamming stage (I), because the size of the box was designed with that requirement in mind. The large numerical domain was 7.7 [m] wide with a water depth of 1.6 [m], which is a significant increase compared to the original domain of 1.1 [m] wide with a water depth of 0.495 [m]). Gravity was turned off to make sure that the buoyancy force did not impair the comparison between methods.

Fig. 5.21b shows the force on the wedge, made non-dimensional with $\rho \dot{h}^2 l$, from the numerical simulation in the larger domain for a range of immersion depths starting from $h = 0.05$ [m] ($\dot{h} = 2.5$ [m/s]) to a depth of 0.35 [m]. It also shows the force that resulted from the analytical method, obtained with the FBC for the first part of the separation stage with $\beta_{bc} = 54$ [deg] and $k = 30.0$. That FBC will be referred to as $\text{FBC}_{\text{II},1}$, with II the number of the stage from Fig. 5.1, from here on. Fig. 5.21b also contains a line indicated with $\text{FBC}_{\text{II},2}$ that is a better match to the numerical simulation results in the larger domain during the second part of the separation stage. $\text{FBC}_{\text{II},2}$ has values $\beta_{bc} = 64$ [deg] and $k = 2.3$. These values were found from fitting $\text{FBC}_{\text{II},2}$ to the free surface contour with $C_f = 0.9$ from the numerical simulation in the larger domain at an immersion depth $h = 0.26$ [m] of the wedge (at time $t = 0.15$ [s]). This depth is considered to be representative of the second part of the separation stage (II). Apparently, the FBC needs to change with changing depth and, hence, changing velocity. In the time span between 0.01 [s] and 0.04 [s], the velocity \dot{h} varies between 2.9 and 1.8 [m/s]. We found that a switch from $\text{FBC}_{\text{II},1}$ to $\text{FBC}_{\text{II},2}$ around 2.0 [m/s] leads to good agreement with the numerical results.



(A) Force as function of immersion depth of wedge during separation stage (II). Results of numerical method in larger domain and without gravity compared to results of analytical method with different values for the curved fictitious body continuation (FBC). Marker ● indicates the immersion depth at which $FBC_{II,2}$ was fit the numerical free surface.



(B) Free surface contour of the numerical simulation to the right of the wedge for an immersion depth $h = 0.26[m]$ (time $t = 0.15[s]$), together with the approximations of $FBC_{II,1}$ and $FBC_{II,2}$ to this contour. End point of wetted length at mentioned depth is indicated by marker ●.

FIGURE 5.21. Improved analytical representation of the force on the wedge with weight $\mu = 0.8$ during the separation stage, using a FBC with a better fit to the numerical free surface.

5.4.11 Extension until closure stage: buoyancy

Knowing that a buoyant wedge floats up after its vertical velocity has become zero, implies that the buoyancy force becomes dominant at some moment in the interaction with water. Typically buoyancy is modelled with a variable that is defined with respect to initial, undisturbed free water surface, such as the depth of immersion h of the wedge. Following Fairlie-Clarke and Tveitnes [85], the buoyancy force becomes $F_b = \rho g \int (h - f(x)) dx$. With zero or low vertical velocities and disregarding air cavities, it is natural to assume that the buoyancy force cannot become larger than $F_b = \rho g \nabla$, with ∇ the volume of the wedge, which when in 2D will also be called 'volume' for convenience.

The buoyancy force during impulsive interaction between wedge and water was found as the difference between forces from numerical simulations with and without gravity. The underlying assumption of the approach is that the free surface configuration near the wedge is sufficiently similar with and without gravity, so that the only difference in force must be due to the hydrostatic pressure. That appears to be true, at least until the beginning of the closure stage, as will be demonstrated below. The larger domain was used to avoid effects of the boundaries. Constant vertical velocities of the wedge were considered to facilitate interpretation of the force.

Fig. 5.23 shows the force difference ΔF , made non-dimensional with $\rho g \nabla$, as a function of immersion depth h for various constant vertical velocities ranging from 0.5[m/s] to 4.0[m/s]. The expression for the buoyancy force similar to Fairlie-Clarke and Tveitnes [85] is represented by a continuous black line. The value for the volume of the wedge ∇ is shown as a dotted horizontal black line. Vertical dashed lines are plotted in the colours of the wedge velocities they are associated with to mark out transitions between stages, with a roman numeral according to the number of the stage as in Fig. 5.1. For a wedge velocity of 0.5[m/s] we see that the buoyancy force first follows the line of Fairlie-Clarke and Tveitnes [85] until nearly the end of the closure stage (III), then changes trend when the enclosed stage starts (IV) and converges to the value of ∇ towards the Archimedal stage (V). Note that the maximum buoyancy force for this velocity is larger than the value for ∇ . The buoyancy force for $\dot{h} = 1.0$ [m/s] also follows the line of Fairlie-Clarke and Tveitnes [85] at first, but changes trend at a much lower value of the depth of immersion h and then continues to increase linearly with h but with a smaller slope compared to Fairlie-Clarke and Tveitnes [85]. Note that the stage transitions for the wedge with $\dot{h} = 1.0$ [m/s] occur at a larger depth of immersion compared to the wedge with $\dot{h} = 0.5$ [m/s]. The buoyancy force for all tested values of the vertical velocity higher than 1.0[m/s] also increases linearly with h but with an even lower slope compared to that for $\dot{h} = 1.0$ [m/s]. Interestingly, for all those vertical velocities of the wedge higher than 1.0[m/s] the slope of the buoyancy force as a function of depth is the same and equal to $0.56\rho gh$. This is a representative model for the buoyancy force on free falling wedges until the end of the separation stage (II).

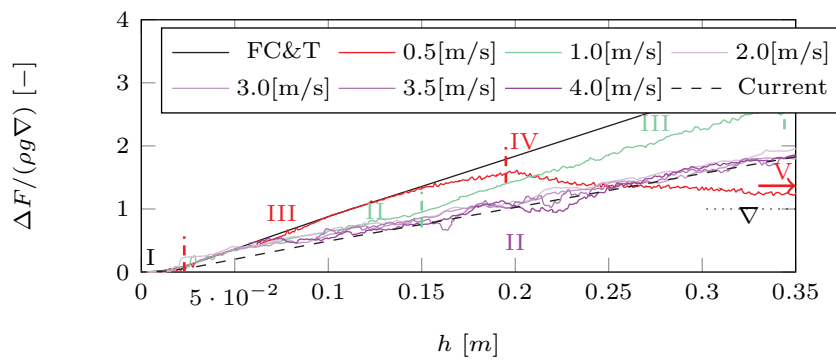


FIGURE 5.22. Buoyancy force on wedge obtained from the difference of forces on the wedge in simulations with and without gravity. Simulations were performed in the larger domain with a range of constant vertical velocities of the wedge. Vertical dashed lines give the transitions between stages. FC&T represents the model of Fairlie-Clarke and Tveitnes [85], ∇ the volume of the wedge. The dashed black line with a slope of $0.56h/\nabla$ gives the outcome of the current research that is used to model the buoyancy force for wedges with higher impact velocities than 1.0[m/s] .

It remains to be verified whether the free surface deformation near the wedge with and without gravity is sufficiently similar. Fig. 5.23 shows the free surface on either side of the wedge for a depth $h = 0.3\text{[m]}$ in the closure stage (III). The wedge has a constant vertical velocity of 3.0[m/s] . The free surface with gravity is coloured cyan, the free surface without is colored magenta. The colouring has reduced opacity so that the overlap shows as a bright purple. Apart from the jets, that overlap is nearly complete, meaning that we can say with some confidence that the difference between forces on the wedge from these simulations represents the buoyancy force. The figure also shows the initial free surface level as a dashed line, with h representing the distance between the dashed line and the tip of the wedge. The buoyancy force, apparently, needs to be evaluated with respect to a level that is almost halfway in between the initial free surface level and the tip of the wedge. Our best explanation for this is that the wedge at higher impact velocities creates its own, local free surface depression that affects the hydrostatic pressure.

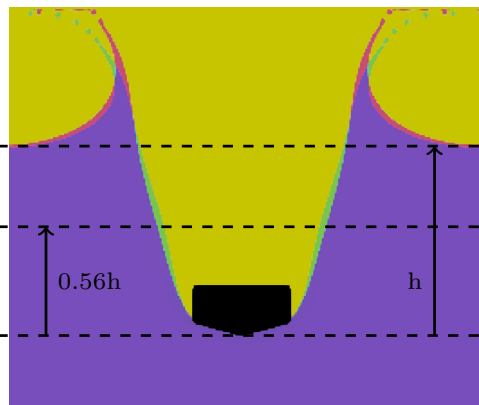


FIGURE 5.23. Free surface configuration at $h = 0.3$ [m] for constant wedge velocity of 3 [m/s] with gravity (cyan) and without (magenta). The overlap in purple shows how similar the free surface configurations are. The immersion depth h is given with respect to the initial free surface level. The buoyancy force found from this research needs to be modelled using a distance with respect to a level near halfway in between the initial free surface level and h .

Using the above, the different force contributions on the wedge can now be determined beyond the early separation stage and can be considered accurate until the closure stage. Starting at the moment in time when Fig. 5.20b stops, Fig. 5.24 gives the contributions of slamming, added mass, jets and buoyancy into the enclosed stage. Note that buoyancy force becomes dominant at the end of the separation stage (II), just before the transition to the closure stage (III).

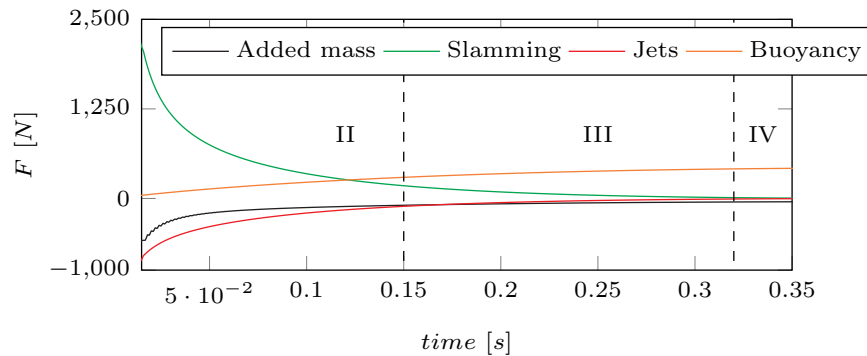


FIGURE 5.24. Force components of analytical method in stages beyond the slamming stage (I). Vertical dashed lines indicate transition between stages according to Fig. 5.1. The analytical model is tuned up to the end of stage II.

5

5.5 Synthesis of experimental, numerical, and analytical results

Before bringing everything together, there is one important step to consider. The analytical method is not bounded by side walls and a bottom of the water column as the tests of the experiment and the numerical simulations are. For later stages than slamming (I), boundary effects become apparent and it is discussed how they were accounted for. Then, the experimental, numerical and analytical results are compared between each other in terms of 1. the maximum vertical deceleration, 2. the velocity after impact and 3. the free surface configuration after impact. The results of the measurements are the average results from five repeated tests. In the simulations with the numerical method and the analytical method, the three wedges with weights $\mu = 0.8, 1.0$ and 2.0 are released with the average velocity at the moment of impact derived from the 200g accelerometer, Tab. 5.5c. Those are $6.39, 6.64$ and 6.99 [m/s], respectively. Grid 330×270 which was found from Sec. 5.3, is used in the numerical simulations in a domain with the inner dimensions of the box in the experiment. The analytical method was used with the modified fictitious body $FBC_{II,1}$, having parameters $\beta_{bc} = 54$ [deg] and $k = 30$ during the beginning of the separation stage, and $FBC_{II,2}$ with $\beta_{bc} = 64$ [deg] and $k = 2.3$ for $\dot{h} \leq 2.0$ [m/s] during the second part of the separation stage (II). The buoyancy force was modelled as $F_b = \rho g \int \bar{h} dx$, with $\bar{h} = \max(C_h h(t) - f(x), 0)$ and $C_h = 0.56$.

5.5.1 Boundary effects

The box in the experiment was sized such that it would not influence the force on the wedge during slamming stage (I), with the knowledge available before the experiment. It was found by comparing results of the analytical method with the experimental results that there were boundary effects during later stages than the slamming stage. Boundary effects were investigated with the numerical method using the larger domain of size 7.7×2.6 [m] and comparing those results to the result in a numerical domain the size of the box 1.10×0.495 [m]. The grid resolutions, as before, were the same for both domains.

The comparison between results in the larger and original domain shows that water piles up along the sides of the domain, which is also shown in Fig. 5.9, effectively increasing the mean water level in the domain. The boundary effects are included by adding a force with a linear dependency on the immersion depth h and some effect of the velocity of the wedge to the analytical method as

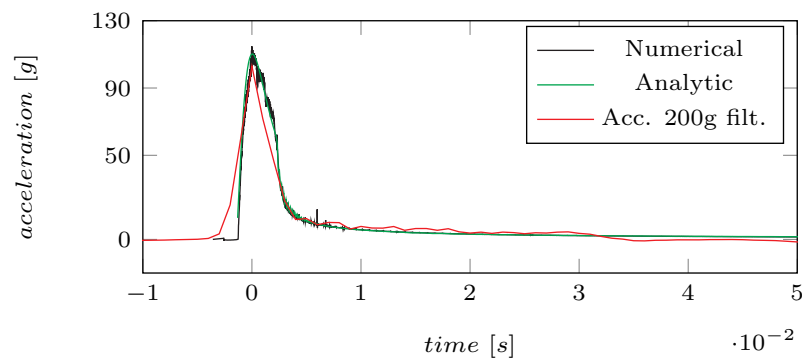
$$F_{BC} = 1.8h\rho\dot{h}^2l - (11.5h^2 - 2.1h)\rho g \nabla, \quad (5.26)$$

with l the wetted length of the wedge. The first term is related to boundary effects found without gravity and the second term for boundary effects with gravity during the separation stage (II). Note that the gravity related term is

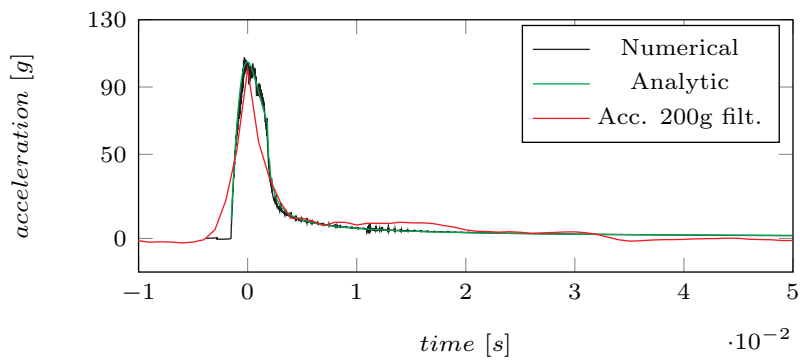
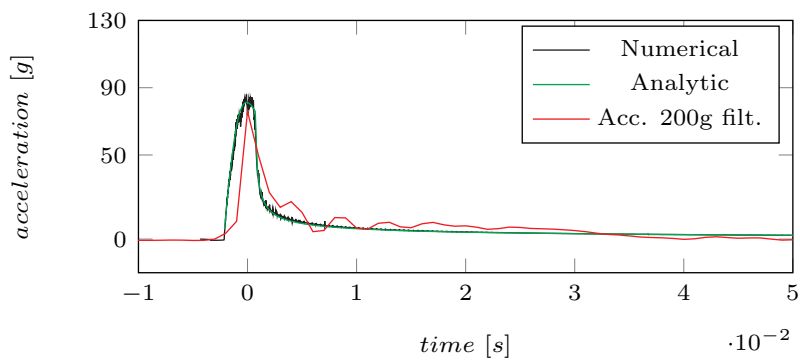
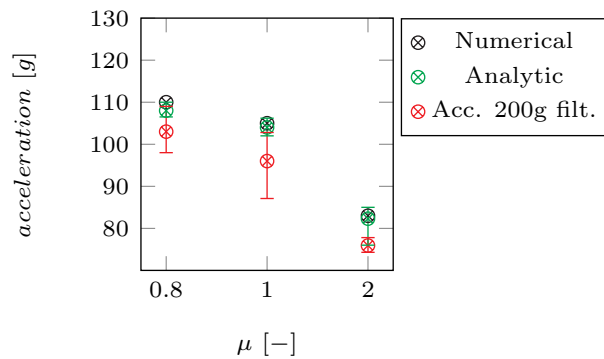
independent of velocity.

5.5.2 Vertical deceleration after impact

The vertical deceleration over time in terms of g has been plotted in Fig. 5.25 for the three different weights of the wedge. The time range includes the slamming stage (I) and the beginning of the separation stage (II). The maximum deceleration is taken from these graphs and shown separately in Fig. 5.25d, together with an uncertainty range. The uncertainty range for the experiment comes from the minimum and maximum values of the maximum acceleration from the five repetitions of the tests. The uncertainty range for the analytical method is found from two sources of uncertainty. The first source of uncertainty comes from the range of impact velocities derived from measurements of the 200g accelerometer (Tab. 5.5c). The second source of uncertainty stems from uncertainties in the setup regarding the guidance mechanism, the fall tower and the wedge. There was a distance of approximately 0.5[mm] in between carriage of the wedge and guiding rails. The maximum horizontal distance between any position over the height of the tower and the vertical line made by a level with a laser was 0.5[mm]. The uncertainty to which the deadrise angle of the wedge could be measured was 0.1[deg]. The sum of these uncertainties can be added up to a maximum uncertainty of the inclination angle α of the wedge of ± 0.2 [deg]. A number of values for α in between 0 and 0.2[deg] was used to determine the effect of varying the inclination angle on the maximum vertical acceleration. The results of these simulations are added to Fig. 5.25. Varying α , a maximum difference in maximum acceleration of around 0.1% is found, which is considered to be negligible compared the uncertainty in impact velocity.



(A) $\mu = 0.8$.

(b) $\mu = 1.0$.(c) $\mu = 2.0$.

(d) Maximum deceleration.

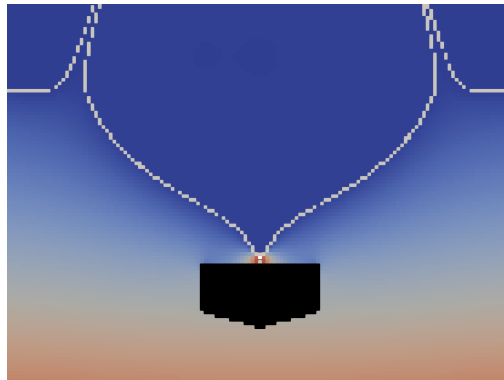
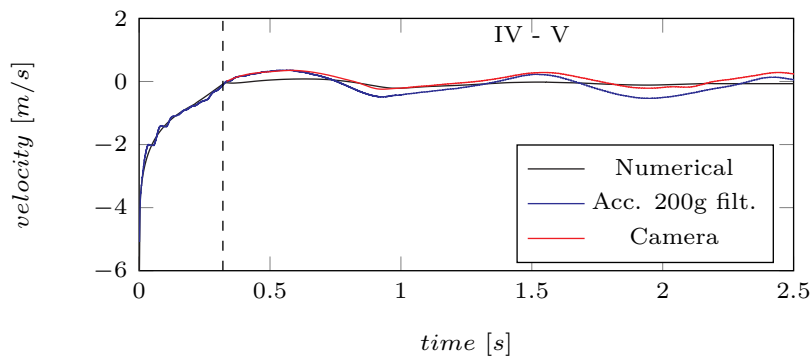
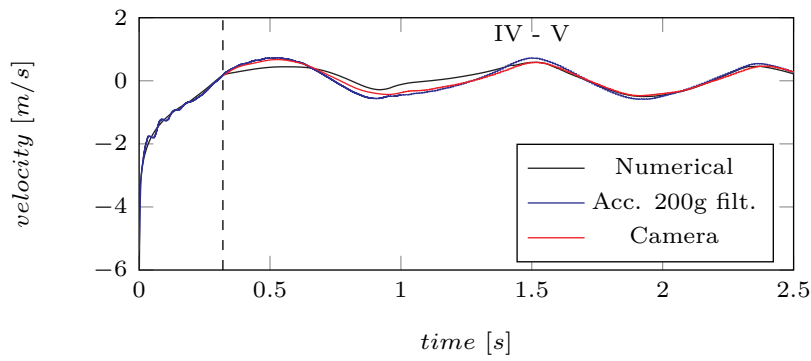
FIGURE 5.25. Deceleration of the wedges during the slamming stage (I) and the beginning of the separation stage (II), obtained from experiment, numerical simulations and simulations with the analytical method.

There is good visual agreement between the acceleration from the experiment, the numerical and the analytical simulations. Especially the accelerations from the two types of simulation are nearly identical. The increase in acceleration is not as steep in the experiment as it is in the simulations, which is likely due to a

combination of two things: (1) compressibility of the fluid, and (2) the (small) margins between wedge and box at the front and back end of the wedge. For pure water, compressibility could not be an explanation, but repeated violent interaction between wedge and water could have increased the air content in water. Only a fraction of air in water results in a much more compressible mixture [81]. The narrow opening between wedge and box in the experiment could have caused the pressure to be lower near the front and back end of the wedge, reducing the total force on the wedge at its acceleration at any moment. The maximum deceleration appears to be similar between all. Upon closer inspection of the maximum deceleration in Fig. 5.25d, however, it shows that the maximum is consistently lower in the experiments than it is in the simulations. The maximum acceleration from the simulations is also not in the uncertainty range of the measured acceleration, so that variability between experiments is not the explanation, but rather something systematic. As with the increase in acceleration, the most likely explanations for the systemic difference between experiments and simulations are compressibility of water and the openings between wedge and box. This needs to be investigated in future work.

5.5.3 *Velocity after impact*

The main reason for carrying out this study as we did, was to be able to investigate the entire process of wedges slamming into the free surface and re-emerging after their maximum submergence had been reached. During that time, the wedge experiences all stages in Fig. 5.1. Fig. 5.26 shows the velocity from $t = 0$ to 2.5[s] for the wedges with weights $\mu = 0.8$ and 1.0. The velocity for the wedge with $\mu = 2.0$ is not shown, because it hits the carriage end slot at around 0.17[s] after impact and never comes back to the free surface. The velocity obtained from consecutive camera images is now shown together with the velocity obtained from the 200g accelerometer. Note that the position measurements of the camera contained noise that was filtered out with a 8[Hz] low-pass filter. By comparing the velocities obtained in these two ways, we demonstrate that the velocity is only affected by differentiation errors and integration errors to a limited extent.



(c) Pressure plot with free surface for $\mu = 0.8$ showing moment at 0.32[s] when the cavity above the wedge closes.

FIGURE 5.26. Velocity of wedges with $\mu = 0.8$ and 1.0 during the five stages of impact until re-emergence. Vertical dashed line in the top two graphs indicates the moment of cavity closure, which for $\mu = 0.8$ occurs at 0.32[s]. From the moment of closure onward, 3D flow effects in the experiment prevent a formal comparison with the 2D numerical results.

The velocity obtained from the processed camera images is in good agreement with the velocity obtained from the acceleration measurements. From the measurements we find that the wedge with $\mu = 0.8$ floats back to the free surface faster than the wedge with $\mu = 1.0$, as expected. At the free surface, the wedges engage in a heaving motion, the wedge $\mu = 1.0$ with a different period of oscillation than the other.

The moment of closure, i.e. the transition from the closure stage (III) to the enclosed stage (IV), for $\mu = 0.8$ at around $0.32[s]$ is shown in Fig. 5.26c with a pressure contour plot of the numerical results. High pressures are observed on top of the wedge, where the free surface from either side of the wedge progresses over the deck until it meets in the middle. In the numerical simulations these pressures relate to such a high force on the wedge that it influences its motion on the way up. This moment is when the motion in the numerical simulation starts to deviate from the motion in the experiment. The difference is due to the free surface above the wedge in the experiment progressing as a dry bed surge, see Fig. 5.28d, with differences along the y -axis in the experiment – the 3D effects mentioned earlier – causing the force on the wedge in the experiment to be less pronounced than in the numerical simulations. The 3D flow features are comparable with steep breaking waves: breaking starts at one position along the crest of the wave, somewhat randomly, before the entire wave overturns [179]. For $\mu = 1.0$ the moment of closure occurs later because its higher velocity and weight cause it to immerse deeper and float back up later.

We zoom in on the time span until $0.4[s]$ in Fig. 5.27, showing the velocity of the wedges. Dashed vertical lines represent the transitions between stages. For the wedge with $\mu = 0.8$, the enclosed stage starts at around $0.32[s]$ when the free surface from either side of the wedge meets – approximately – in the middle of the deck above the wedge. The oscillation in the velocity record of the accelerometer corresponds with the $20[Hz]$ found in Fig. 5.7 and is not related to effects of air [75, 86]. The velocity of the wedge with $\mu = 2.0$ in Fig. 5.27c is shown only until $0.2[s]$, just after it hits the carriage end slot. This explains the sudden jump in velocity in the experimental results for that wedge. Up until that moment there is good agreement between the velocity in the measurements and the simulations. Considering all wedges with different weights, the general conclusion is that the numerical simulations show good agreement with the experiments until the moment of closure. Up to that moment our experimental setup can reliably be considered 2D. Future simulations will need to take the 3D flow features in the enclosed stage into account in order to be representative of the dynamics of buoyant wedges.

For wedges $\mu = 0.8$ and $\mu = 1.0$, the analytical method is in good agreement with the measurements and the numerical simulations up to the start of the

closure stage at around 0.20[s] (transition from stage II to stage III), as was our ambition. From that moment on, the free surface configuration does not satisfy the boundary conditions on the wedge and the FBC anymore, because the side walls of the wedge have become wet and the side walls are not part of the analytical method. For both wedges, the switch of FBC coefficients at a velocity of 2.0[m/s] leads to satisfactory results. For the wedge with $\mu = 2.0$ the agreement with measurements and numerical simulations is somewhat less. This is most likely due to the fact that the switch of FBC coefficients does not yet capture the full variation with velocity.

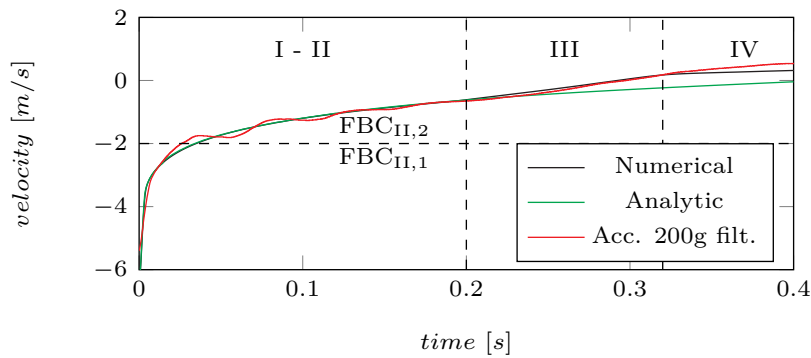
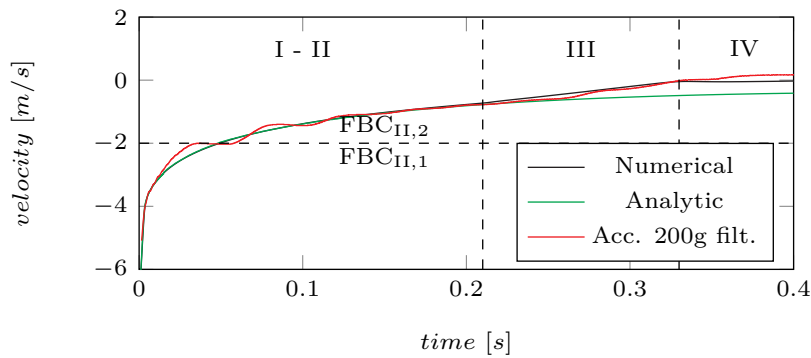
(A) $\mu = 0.8$.(B) $\mu = 1.0$.

FIGURE 5.27. Velocity of the wedge until 0.4[s] for the wedges with $\mu = 0.8$ and 1.0. For the wedge with $\mu = 2.0$, the velocity is shown until it hits the carriage end stop. Dashed vertical lines represent the transitions between stages.

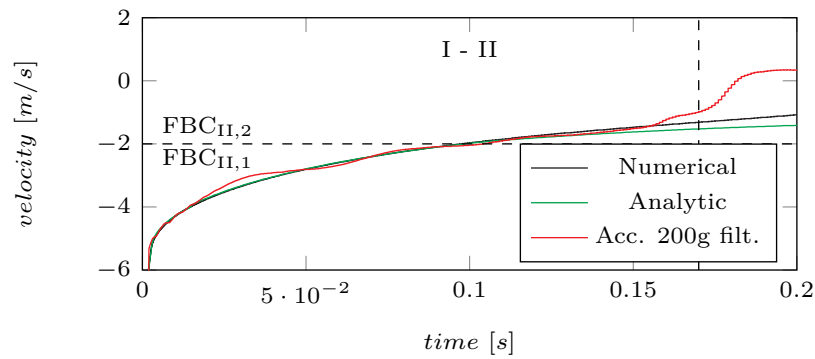
(c) $\mu = 2.0$.

FIGURE 5.27. Velocity of the wedge until 0.4[s] for the wedges with $\mu = 0.8$ and 1.0. For the wedge with $\mu = 2.0$, the velocity is shown until it hits the carriage end stop. Dashed vertical lines represent the transitions between stages.

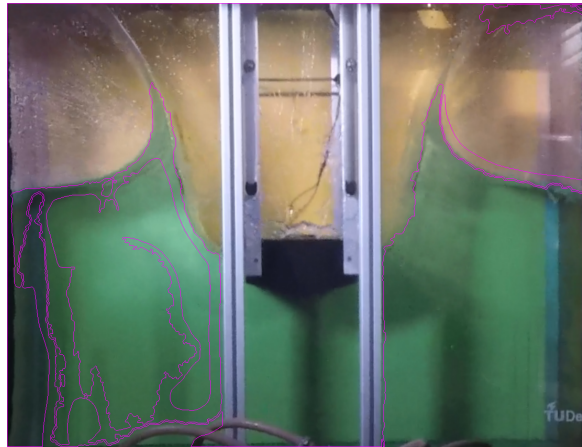
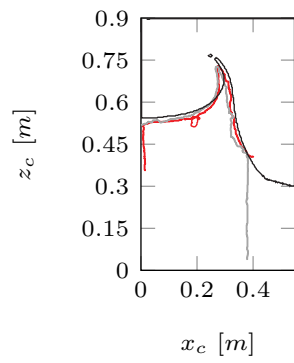
5.5.4 Free surface configuration

The free surface configuration during wedge entry with $\mu = 0.8$ is shown in Fig. 5.28. The free surface in the experiment is obtained from processing the camera images. The main calibration of the camera images is obtained from the four legs of the fall tower. The distance in between legs was carefully controlled during the setup of the experiment and gives a reliable measurement over the full height of the camera image. The calibration was checked by comparing the water level estimated from the camera images to the actual water level that was carefully controlled to 0.495[m] with a number of (closable) holes in the side of the box. Image processing yields contours that satisfy the criteria that were set; these contours are added to the camera images. The graph to the left of the camera images in Fig. 5.28 keeps the outermost contour that was recognized in the images and calls that the free surface position. The free surface position is given as a function of coordinate x_c (for width), that is zero at the left-most position of the box, and coordinate z_c , that is zero at the bottom of the box. The free surface position to the right of the wedge is mirrored on top of the left-hand side free surface position, so that the symmetry in the experiment can be investigated. The free surface from the numerical simulation is the contour where the filling ratio of cells C_f has a value of 0.9. The numerically obtained free surface is added to the graphs.

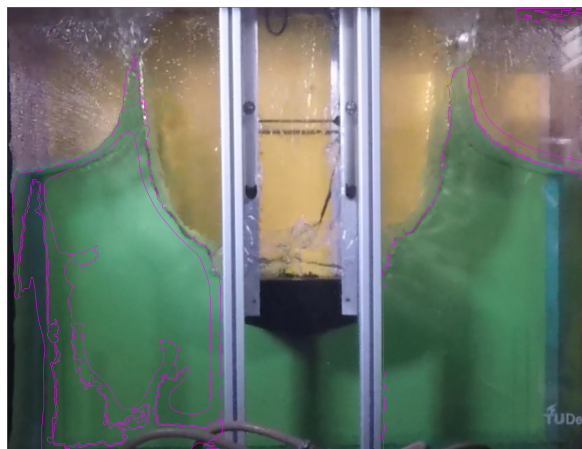
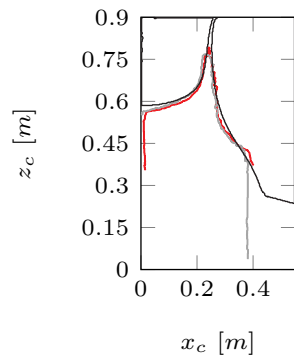
Considering the comparison between the contours found from the camera images and the images themselves, reveals that edge detection only captures the part of the free surface jets that can be considered water without air. It does not capture the parts of the jets that have turned into spray and droplets. The spray also obscures part of the jets from view, as we can see from Figs. 5.28b, and 5.28c. The free surface in the experiment is nearly symmetric. The free surface

from the numerical simulations is in close agreement with the free surface in the experiments, away from the jets. Protrusions of water from the free surface in the numerical simulation are nearly always matched in the experiment, except in Fig. 5.28f in the enclosed stage. The jets in the numerical simulations are more pronounced and give a better indication of the highest elevation of the jets than the contours extracted from the camera images. The breakup of the jets into spray and droplets is represented less well in the numerical simulations than in the experiment. Also, in Fig. 5.28d the jet that hits the top of the domain remains attached to the ceiling, whereas in the experiments that water start falling down earlier in the form of droplets. An interesting flow feature is observed in Fig. 5.28f. The wedge, on its way up, causes a low-pressure zone near the free surface at $x_c = 0.15$ [m], causing the free surface to entrap a pocket of air that breaks up into bubbles. Interestingly enough, although the numerical method cannot represent the breakup of an air pocket into bubbles, a depression in the free surface is observed in the numerical simulations at the position of the pocket of bubbles in the experiment. In the enclosed stage in Fig. 5.28f, more water appears to be above the wedge in the numerical simulation than in the experiment. The rise back to the free surface in the numerical simulations is slower than in the experiment, because of the large pressure that was generated when the cavity closed. Whether that is the only explanation needs to be investigated by means of 3D simulations.

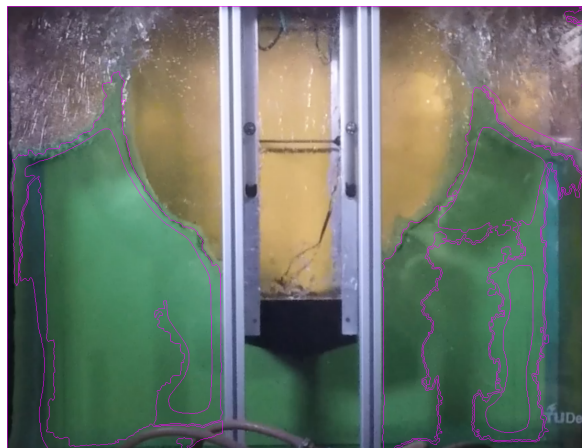
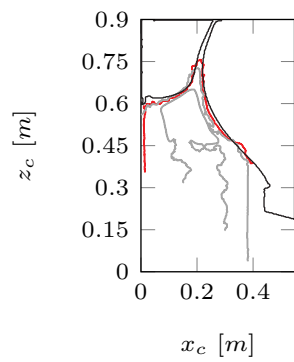
The free surface in the simulations is a good match to the free surface in the experiments. The quantification of the free surface position in the enclosed stage is more reliable in the experiments than in the simulations, because the experiments are asymmetric and the simulations are not. On the other hand, the numerical simulations give a better estimate of the elevation to which free surface jets may reach than the edge detection algorithm. This demonstrates that the combination of experiments and simulations gives more reliable results of the free surface position during wedge entry than either of them by themselves.



(A) 0.092[s] in stage II.

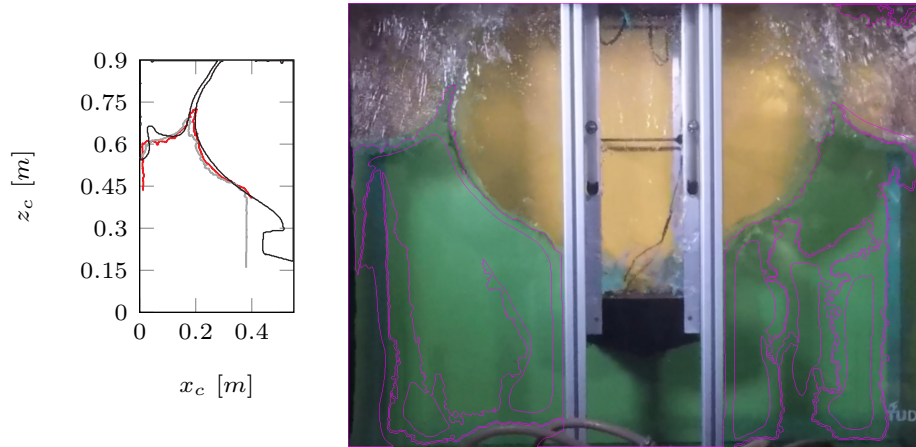


(B) 0.167[s] at the end of stage II.

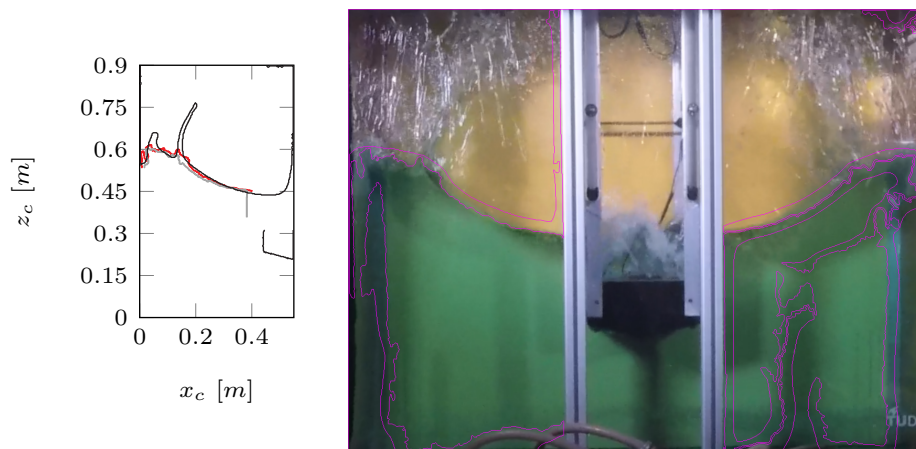


(C) 0.250[s] in stage III.

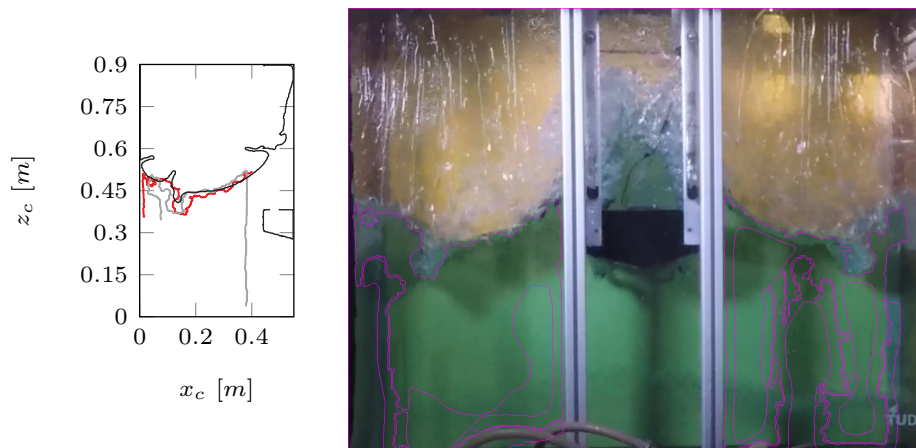
5



(D) 0.308[s] in stage III.



(E) 0.400[s] in stage IV.



(F) 0.571[s] in stage V.

FIGURE 5.28. Free surface configuration during wedge entry and re-emergence ($\mu = 0.8$);
 (—) experiment left, (—) experiment right, (—) numerical result.

5.6 Conclusion

Whereas most literature about wedge entry in water focuses on the initial impact between wedge and free surface, we have designed an experiment – 2D – that takes buoyant wedges from the slamming stage, through the stages of separation, closure and enclosed, to an Archimedal stage that ends with periodic vertical oscillation in the free surface. A new type of air cavity closure above the wedge was encountered, with strong implications for the comparison with simulations.

Three different weights of the wedge were tested; one lighter than the weight of its displaced volume of water, one with the same weight, and one heavier than its displaced amount of water. Impact velocities of up to 7[m/s] were found with a maximum deviation of 3% over five runs for the highest weight wedge. These impacts resulted in a deceleration higher than 100 times the gravitational constant with a maximum deviation of 7% for the wedge with the weight of its displaced volume of water, and 2% for the wedge with twice that weight. After having risen back up to the free surface, the buoyant wedges engage in a heave oscillation with a period from which an added mass could be derived that was the same as in literature.

The maximum acceleration of the wedge in simulations with our numerical method was always larger than the mean of the measurements in the experiment and the difference in acceleration up to the closure stage was never larger than 8%. The forces from the simulations could therefore be deemed representative of the forces in the experiment. The numerical simulations were used to identify with certainty those frequencies in the acceleration signal that correlate with the support structure of the wedge, rather than with the interaction between wedge and water. The free surface contours from the numerical simulations reliably show the position of free surface features such as jets, where in the experiment interpretation of the camera images was impeded by the break-up of these features into droplets. From the numerical simulations, it was also found that the assumption of the experiment being 2D does not hold any more after the closure stage. At the end of the closure stage, free-surface instabilities in the experiment, comparable to free surface wave breaking, cause variability in the direction perpendicular to the wedge's cross-section (y -direction) and subsequent fluid dynamics that are different from the simulations. Simulations beyond the moment of closure necessarily have to be performed in 3D.

An analytical method was extended for inclination angles of the wedge other than vertical (asymmetric impacts). The method was used to investigate the uncertainty regarding the inclination angle of the wedge as a result of the tolerances in the experimental setup. That uncertainty was found to cause a difference in wedge acceleration of no more than 0.1%. The concept of a fictitious body contin-

uation (FBC) was also extended to represent the wedge entry up to the closure stage. It was found that the FBC needs to change with velocity; we adopted one set of FBC coefficients for the beginning of the separation stage, and another set for the second part of the separation stage. It was also found that the buoyancy force on the wedge needs to be represented with a 44% lower coefficient than previously thought, because of the wedge's interaction with the free surface. Using these findings, simulation results of the analytical method up to the closure stage never deviated more than 1.5% from the numerical simulations.

Combining three methods of representing buoyant wedge entry in water in the way that has been described gives more reliable results in terms of acceleration, velocity, position and forces than would have been obtained from any of the methods separately.

AN EFFICIENT PRESSURE-BASED MULTIPHASE FINITE VOLUME METHOD FOR INTERACTION BETWEEN COMPRESSIBLE AERATED WATER AND MOVING BODIES

This chapter is reproduced from [77] :

M. van der Eijk and P. R. Wellens. "An efficient pressure-based multiphase finite volume method for interaction between compressible aerated water and moving bodies." *Journal of Computational Physics* (nd)

Abstract

Maritime structures in heavy seas can experience wave impact events with high loads. The loads can lead to structural failure and even loss of life. Wave breaking in said sea states causes air to be entrained in water as aeration clouds, remaining long enough to be transported and to play a role in the impulsive interaction with the structure. A small amount of air in water already forms a highly compressible mixture. Compressibility influences the magnitude of the impact loads.

A new Cartesian grid method for compressible multiphase flow is introduced to account for water, air and homogeneous mixtures of air and water. The method is designed to predict the hydrodynamic loads on moving bodies engaging with interfaces between fluids having large density ratios. Pressure-density relations are enforced meaning that the equation for conservation of energy is not explicitly solved. The interface between fluids is transported using a geometric Volume-of-Fluid method. The interface between fluids and structure is taken care of by a cut-cell method. An additional fraction field for the amount of air in water in combination with a new formulation for the multiphase speed of sound prevent overprediction of compressibility by artificial air entrainment.

New experimental data of 2D wedge impacts with aerated water are presented to demonstrate the validity of the numerical method. For low aeration levels, the simulation results in terms of the impact loads on the wedge and the frequencies of pressure waves generated upon impact are in good agreement with the experimental data. Increasing the level of aeration reduces the maximum impact load on the wedge. Reflected density waves lead to secondary loads on the wedge. The intensity of the secondary loads, relative to the primary load of impact, increases with the aeration level while the density wave frequency decreases.

6.1 Introduction

Maritime structures sail through heavy seas. Water waves encountered in these sea states can induce wave impacts on the structures and generate high loads. Wave loads have caused structural failure in the past [22, 120, 135, 286]. In some cases, wave loads have led to loss of life [153, 224].

Waves impact with structures like ships, quay walls, caisson breakwaters and the side walls of containment tanks. The impulsive interaction between water and structure can also be represented by a structure that falls onto a free surface. A theoretical account of a falling structure impacting with water is given by Von Karman [274]; experiments with like structures were performed by Greenhow [103]. Later work on impacts [102, 144, 279, 317] has in common that the water was assumed incompressible.

Heavy seas feature breaking waves. Wave overturning causes air pockets to be enclosed, which break up under water to form clouds of air bubbles, that are only a fraction of a wave height in size. The small air bubbles remain entrained for several wave periods [237], the entrained air making up in the order of a percent of the water volume [27, 206]. We refer to the process of air entrainment as aeration, and we call the mixture of water and air aerated water.

Due to aeration, the assumption of incompressibility of water is not always justified in modelling impulsive interaction of water with fixed structures [21, 27, 28, 112, 171]. Also for moving structures, experiments have demonstrated that aeration affects the results [81, 84, 169, 170]. A small amount of air in water already leads to a significant increase in the compressibility of the mixture [297]. The compressibility of aerated water can cause the peak of the impact load to be smaller and the duration of the load to be longer, compared to impacts with water that can be considered incompressible. Compressibility also allows for the generation of density waves. These waves are defined as short-period oscillations of density and pressure propagating through the mixture with the speed of sound.

An early theory to account for compressibility with aeration was given by Peregrine and Thais [206] for a rapidly filling cavity, inspiring numerical methods for modelling aerated water impacts on structures. These methods show similarities to those for the prediction of cavitation erosion [236], vaporization [73], compressible wave impacts [161] and underwater explosions [183].

There is a scale difference of $O(10^4)$ between a maritime structure and the aeration bubbles in the breaking waves that interact with the structure. A one-fluid formulation allows for coarser grids and likely has lower computational cost

compared to methods in which every air bubble near the structure is resolved or tracked [32–34]. The implications of using a one-fluid formulation is that air bubbles move with the same speed as the water containing them. This is a reasonable model for the situation half a wave period after a wave near a maritime structure has broken.

A one-fluid, weakly-compressible method for modeling homogeneous mixtures of air and water was introduced by Bredmose, Peregrine, and Bullock [22]. The method was based on the theoretical work of Peregrine and Thais [206]. The method solves for the conservation of mass (water and air), momentum, and energy. Aerated water is solved compressibly while the water remains incompressible in the energy equation. According to Ma et al. [168], the method features significant spurious oscillations in pressure and velocity near the interface between water and air. These oscillations are an artifact of a fully-conservative scheme [231] and can result in non-physical pressures and negative volumes of water [2].

The method proposed by Dias, Dutykh, and Ghidaglia [62] is similar to the method of Bredmose, Peregrine, and Bullock [22]. It was designed for large aeration levels, omitting tracking or reconstruction of the interface between fluids. Oscillations in pressure and velocity were not present any more, but the fluid-fluid interface became so diffuse that the distinction between the compressible fluids disappeared. A diffuse interface may prevent oscillations, but it introduces a non-monotonic behavior of the speed of sound across the fluid-fluid interface when using the one-fluid assumption. Non-monotonic behavior is the spurious reduction in speed of sound near the interface between air and water causing erroneous pressure oscillations.

Ma et al. [168] introduced a Kapila-based model [133] being quasi-conservative to prevent the unphysical oscillations around the interface. The method is able to account for moving bodies and interface tracking using a cut-cell method and a Volume-of-Fluid method. A third-order MUSCL reconstruction was used for the interpolation of density values from cell centers to cell faces. A HLCC approximate Riemann solver was used for transporting convective fluxes. Comparison with experimental data of a flat plate entry in aerated water [169] validates that the method can predict the hydrodynamic loads involved in such an entry. At the same time, interface diffusion across several mesh cells for large flow gradient regions was reported.

The model proposed by Plumerault et al. [214] omitted the energy equation by using equations of state that describe the pressure-density relation. They introduced a new fraction field indicating the amount of air in water. A pressure-relaxation method is used to solve the system of equations. A pressure equilibrium is solved

to compute the transport of the fluid-fluid interface, instead of solving a transport equation. Compared to the quasi-conservative model of Ma et al. [168], no assumption of the material derivative of entropy equal to zero is made. According to Ma et al. [168], the method of Plumerault et al. [214] is vulnerable to diffusion of the interface between fluids and to non-physical pressure oscillations at the density wave front, for similar reasons as for the method of Bredmose, Peregrine, and Bullock [22].

Others accounts of the effect of aeration are Elhimer et al. [81] and Hong, Wang, and Liu [117]. These are left out of the discussion due to significant differences in modeling but do contribute to the overview of existing literature made here.

The objective of this work is to introduce an efficient, quasi-conservative consistent numerical method for modeling the interaction between homogeneous aerated water and maritime structures. We are mainly aiming at quantifying how aeration affects the impact loads on arbitrarily-shaped structures in the presence of a complex configuration of the interface between fluids. A secondary interest pertains to the effect of density waves on the hydrodynamic load, i.e. capturing the pressure oscillations as a result of reflecting and refracting density waves rather than resolving the discontinuity of density at the density wave front in the greatest detail. The following can be considered novelties:

- compared to Bredmose, Peregrine, and Bullock [22], Plumerault et al. [214] and Ma et al. [168] that have a diffuse interface between fluids, the interfaces are kept sharp by means of a Volume-of-Fluid (VOF) method and geometric reconstruction of the fluid-fluid and fluid-body interface so that the moment of impact and the impact load are represented accurately;
- contrary to Plumerault et al. [214], a transport equation is solved for the additional volume fraction field so that, in future, the aeration level can vary near the free surface. At present, for verification purposes, the aerated water is homogeneous.
- the speed of sound in the aerated mixture is adapted near the interface between fluids with respect to Wood, Peregrine, and Bruce [299] to prevent a non-monotonic behaviour of the speed of sound upon impact with bodies;
- contrary to Ma et al. [168] that formulated their methods as a density-based solver, the numerical method is set up as a pressure-based solver like those found for underwater explosions [183]. For low Mach numbers a pressure based solver should be more efficient than a density-based solver, because the CFL number is not based on the speed of sound, but on the fluid velocities allowing for larger time steps;
- benchmark experimental data for aerated water entries are rare. An experiment with wedge in aerated water were performed specifically for the purpose of validating the numerical method in this work. Where most

investigations quantify only the effect of aeration on the magnitude of the primary impact peak, here also the post-impact, secondary loads from reflected density waves are considered.

The chapter starts with Sec. 6.2 introducing the variable definitions and the mathematical model in its conservative form. This mathematical model already begins with the assumption of a single fluid. The system of equations is closed by deriving the non-conservative formulation of the VOF transport equation and introducing pressure-density relations in Sec. 6.3. In Sec. 6.4 the grid structure is introduced, followed by Sec. 6.5 explaining the solution algorithm. In Sec. 6.6 the method is tested systematically against several benchmark 1D and 2D cases from literature. In Sec. 6.7 the wedge entry in aerated water is simulated and compared to the experiment that was set up specifically for validation of the method. The chapter ends with a summary of the conclusions.

6.2 Mathematical model

6.2.1 Interface capturing

Free surface' is used interchangeably with 'interface'. Computing the position of the fluid-fluid and the fluid-body interfaces accurately is relevant for determining the moment of impact. A color function $f(\mathbf{x}, t)$ is used to capture the position of the interface. Transport of the interface is described by

$$\frac{Df}{Dt} = \frac{\partial f}{\partial t} + (\mathbf{u} \cdot \nabla) f = 0, \quad (6.1)$$

in which $f(\mathbf{x}, t) = 0$ gives the position of the interface and \mathbf{u} the interface velocity.

A fixed cartesian grid is used to divide the domain in volumes. We make use of an interface-capturing Volume-of-Fluid (VOF) method, in which the color function f is replaced by a discrete volume fraction field. A volume fraction is the average of the continuous color function for a given volume.

The definition of the volume fractions given in Fig. 6.1. Volume fraction C_b indicates the part of a volume that is open to fluid. 'Body' is used interchangeably with 'structure'. Fraction $(1 - C_b)$ then represents the part of a volume that is occupied by the body. Volume fraction C_a indicates the part of a volume that is occupied with gas (air), where C_f gives the part of the volume occupied with liquid, either water or aerated water, a homogeneous mixture of air and water. This means that C_b is equal to the sum of C_f and C_a .

Following Plumerault, Astruc, and Maron [213], additional volume fraction fields are introduced to indicate the part by volume of the homogeneous mixture that is gas, β_g , and the part that is water β_l . These volume fractions are necessary for the formulation of the mathematical model.

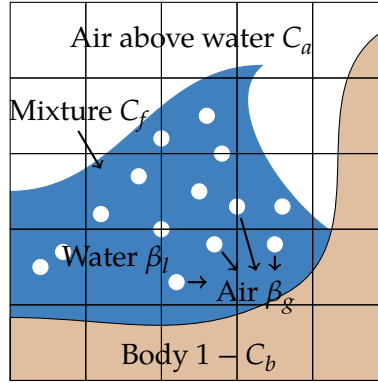


FIGURE 6.1. Illustration of the phases of matter in the solver and how they are represented discretely in the cartesian grid. Volume fraction C_f is used for representing aerated water, C_a for air above the water, β_l for the water part of the homogeneous air-water mixture, β_g for the air part. C_b gives the part of a volume not occupied by the body and open to fluid.

6.2.2 Fluids: conservative form

The governing equations for the mathematical model are formulated for a multiphase flow of immiscible Newtonian fluids. The one-fluid approximation is applied allowing for a single velocity and a single pressure field [188]. Equilibrium of pressure and a no-slip boundary condition between fluids is applied, which is justified by the fact that our emphasis is on short-duration impacts with aerated water.

For the air in aerated water, we neglect bubble interaction and effects of surface tension. The air bubbles are assumed to be sufficiently small [296]. The assumption of a homogeneous air-water mixture is valid when the eigenfrequencies of the pressure waveguide due to compressibility are well below the bubble resonance frequency [297], so that the mixture effectively behaves as a single medium. When translated to our simulation setups, this is a requirement that is met in all cases.

An equation for the conservation of mass, using a single velocity field \mathbf{u} , is formulated for each phase

$$\frac{\partial \alpha_k \rho_k}{\partial t} + \nabla \cdot (\alpha_k \rho_k \mathbf{u}) = 0, \quad k = a, l, g, \quad (6.2)$$

in which subscript a stands for air above water, l for the liquid part of the phase with aerated water, and g for the air part of the aerated water phase. Fractions α_k are defined as

$$\begin{aligned}\alpha_a &= \frac{C_a}{C_b}, \\ \alpha_l &= \frac{\beta_l C_f}{C_b}, \\ \alpha_g &= \frac{\beta_g C_f}{C_b}.\end{aligned}\quad (6.3)$$

Refer to Fig. 6.1 for the definition of the volume fractions.

The equation for the conservation of mass for the aggregate fluid is obtained from the sum of the equations for each phase

$$\frac{\partial \rho}{\partial t} + \nabla \cdot (\rho \mathbf{u}) = 0, \quad \rho = \frac{C_b - C_f}{C_b} \rho_a + \frac{(1 - \beta_g) C_f}{C_b} \rho_l + \frac{\beta_g C_f}{C_b} \rho_a. \quad (6.4)$$

Parameter ρ is the aggregate fluid density that is used together with the algebraic relations

$$\begin{aligned}\beta_g + \beta_l &= 1, \\ C_f + C_a &= C_b,\end{aligned}\quad (6.5)$$

Although not required, we now say that $\rho_g = \rho_a$ because for all our applications the gas entrained in water originates from the air above it.

The equations for the conservation of momentum, using again a single velocity field and a single pressure field read

$$\frac{\partial \rho \mathbf{u}}{\partial t} + \nabla \cdot (\rho \mathbf{u} \otimes \mathbf{u}) + \nabla p + \rho \mathbf{g} = 0. \quad (6.6)$$

Here, p is the pressure in the aggregate fluid and \mathbf{g} the vector of the acceleration of gravity. Note that the viscous term has been omitted from the momentum equation as mainly short-duration events will be considered, in which viscous effects such as the formation of boundary layers can be ignored.

6.2.3 Body motion

The body is assumed rigid and is displaced by a state-space representation of Newton's second law. The position of the body \mathbf{x}_b is found from

$$\frac{\partial \mathbf{x}_b}{\partial t} = \mathbf{u}_b, \quad (6.7)$$

and the body velocity \mathbf{u}_b , in turn, is found from

$$m_b \frac{\partial \mathbf{u}_b}{\partial t} = \mathbf{F}_b. \quad (6.8)$$

The mass of the body, m_b , is assumed constant. The force on the body, \mathbf{F}_b , includes the force of gravity and the force exerted by the fluid. Rotations of the body are not included.

The fluid force on the body is found from integrating the pressure in the normal direction to the boundary along the body contour. Viscous stresses on the body, as said, are not considered.

6.3 Closure of system of equations

6.3.1 Fluids: speed of sound

Sec. 6.2 described the system of equations consisting of three independent equations for the conservation of mass, equations for the conservation of momentum in the axis directions, and two equations for the state-space of the body. The pressure and velocity field are solved from this system. But the system of equations is not yet closed as it is not yet been defined how to solve for the density field. That is described in this section, with due attention to closure of the system in three-phase points where air, aerated water and body meet as we consider this a novelty with respect to the existing literature.

Densities are obtained algebraically using equations of state. These equations depend on the pressure and make the connection between the continuity equation (6.4) and the momentum equation (6.6) so that the change of density in time can be solved for. The relation between pressure and density can be written in a general form using the speed of sound. The speed of sound is the ratio of the change in density to the change in pressure. Assuming that changes are small and neglecting second order terms and higher, the equation of state for an individual fluid becomes

$$\frac{D\rho_k}{Dt} = \frac{1}{c_k^2} \frac{Dp}{Dt}, \quad k = a, l, g, \quad (6.9)$$

with c is the speed of sound, being the propagation rate of a pressure wave with infinitesimal amplitude through a fluid at rest. The derivatives are taken at constant entropy.

The conservation of mass equation in Eq. (6.4) contains an aggregate density field which needs to be solved. The equation is rewritten in Eq. (6.10) such that Eq. (6.9) can be used.

$$\frac{D\rho}{Dt} + \rho \nabla \cdot \mathbf{u} = 0, \quad (6.10)$$

in which the first term is the material derivative of the aggregate density ρ . The material derivative of the aggregate fluid cannot be replaced yet with Eq. (6.9). Additional explanation is needed for solving the aggregate density ρ and the material derivative of this density. Using Eq. (6.4), definitions for the air and water density, and the speed of sound c need to be formulated.

The material derivative of the aggregate density ρ in Eq. (6.10) is rewritten by substituting the formulation of the aggregate density in Eq. (6.4). The material derivatives of the individual fluids are replaced with Eq. (6.5). Accounting for the presence of the body through volume fraction C_b , the material derivative of the aggregate density becomes

$$\begin{aligned} \frac{D\rho}{Dt} = & \frac{C_b - C_f}{C_b} \frac{1}{c_a^2} \frac{Dp}{Dt} + \frac{C_f}{C_b} \left(\frac{\beta_g}{c_a^2} + \frac{1 - \beta_g}{c_l^2} \right) \frac{Dp}{Dt} + \\ & \frac{C_f}{C_b} (\rho_a - \rho_l) \frac{D\beta_g}{Dt} + \frac{1 - \beta_g}{C_b} (\rho_l - \rho_a) \frac{DC_f}{Dt}. \end{aligned} \quad (6.11)$$

The body is assumed rigid, resulting in $\frac{DC_b}{Dt} = 0$ and, therefore, not visible in Eq. (6.11). The remaining unknowns to be defined for the aggregate fluid and its material derivative are:

- the speeds of sound in air and water, c_a and c_l (Sec. 6.3.2), and
- the pressure-density relation for air and water, ρ_a and ρ_l (Sec. 6.3.2), and
- the material derivatives of β_g and C_f near the interface between air and aerated water, and the calculation of β_g (Sec. 6.3.3).

Resolving these unknowns in the next sections will lead to an equation of state of the aggregate fluid and a formulation of the aggregate speed of sound c , rather than separate equations for the constituent fluids.

6.3.2 Fluids: equations of state

The air above water, $C_a = 1 - C_f$, and the air in aerated water, β_g , are assumed compressible and to undergo isentropic compression. The relation between density and pressure under these circumstances is [183]

$$\frac{\partial \rho_a}{\partial p} = \frac{1}{c_a^2} = \frac{1}{a_c \gamma} \left(\frac{p}{a_c} \right)^{\frac{1-\gamma}{\gamma}} \quad \text{with } a_c = \frac{p}{\rho \gamma}, \quad (6.12)$$

in which γ is the ratio of specific heat of the gas at a constant pressure to its specific heat at a constant volume, and a_c the isentropic constant. Note that the right-hand side of Eq. (6.12) represents a relation for the speed of sound in air (c_a) and can be used for substitution in Eq. (6.11). The specific heat ratio for air is equal to 1.0 for isothermal conditions and 1.4 for adiabatic conditions.

Peregrine and Thais [206] showed the choosing a value of either 1.0 or 1.4 for the coefficient makes little difference for the loads generated during an impact. An adiabatic process happens relatively fast compared to an isothermal process like the propagation of sound. There is no time for heat exchange making $\gamma = 1.4$ a good assumption.

A nonlinear relation between density and pressure is derived from Eq. (6.12) by integration using $a_c = p_0/\rho_{a,0}^\gamma$. The formulation for ρ_a is needed in the material derivative in Eq. (6.11) and the aggregate density in Eq. (6.10).

$$\rho_a = \rho_{a,0} \left(\frac{p}{p_0} \right)^{\frac{1}{\gamma}} \quad (6.13)$$

Here, $\rho_{a,0}$ represents a reference value for the density. It is there to prevent "drifting" of the density during a simulation [292]. The reference value is chosen equal to the initial density, which is chosen equal to the density at atmospheric pressure.

The water part of the aerated water, β_l , is assumed weakly-compressible. For weakly compressible fluids, the relation between density and pressure is [183]

$$\frac{D\rho_l}{Dp} = \frac{1}{c_l^2}, \quad (6.14)$$

with c_l the speed of sound in water. The speed of sound in water is assumed constant and can be directly substituted in Eq. (6.11). The integration of Eq. (6.14) results in a linear relation between the density of the water and the pressure needed in Eq. (6.11) and Eq. (6.10) for the aggregate density.

$$\rho_l = \rho_{l,0} + \frac{1}{c_l^2} (p - p_0), \quad (6.15)$$

in which $\rho_{l,0}$ is the initial density to be chosen equal to the density of water under atmospheric conditions. Considering water weakly-compressible in this way will have little influence on the impact loads we are interested in, because for the pressure range we expect, the volume change of air in aerated water will be much larger than the volume change of water in aerated water. Hence, the major part of the volume change of the aerated water can be attributed to the volume change of air. Nevertheless, accounting for the compressibility of the liquid at this moment may extend the suitability of the method to applications not currently envisaged. Sec. 6.7.2 features a reflection on the pressure range in our current applications.

6.3.3 Fluids: volume fraction transport

In order to transport the interface between fluids, it is necessary to transport the volume fraction fields C_f and β_g . Also the material derivative for these volume

fractions, for use in Eq. (6.11), have not yet been derived.

The dominance of the inertial effects over buoyancy makes the assumption of a constant mass fraction μ_g valid. The mass fraction is the ratio of the mass of aeration over the mass of the mixture of water and air. The constant mass fraction μ_g is predefined by

$$\mu_g = \frac{\beta_g \rho_a}{m_f}, \quad (6.16)$$

means that $\frac{D\mu_g}{Dt} = 0$. Here, m_f is the mass of mixture air and water. The mass fraction can be rewritten to solve β_g , needed for solving the aggregate density ρ

$$\beta_g = \frac{\mu_g \rho_l}{(1 - \mu_g) \rho_a + \mu_g \rho_l}. \quad (6.17)$$

Substituting Eq. (6.16) in $D\mu_g/Dt = 0$ in combination with Eq. (6.9) results in the missing formulation of the material derivative of β_g in Eq. (6.11)

$$\frac{D\beta_g}{Dt} = \beta_g (1 - \beta_g) \left(\frac{1}{\rho_l c_l^2} - \frac{1}{\rho_a c_a^2} \right) \frac{Dp}{Dt}. \quad (6.18)$$

As mentioned in the introduction, a non-conservative formulation of the transport equation for C_f needs to be derived to prevent difficulties with spurious oscillations around the interface [2]. A formulation like this is found by considering mechanical equilibrium, i.e. equilibrium of pressure and velocity, between fluids [188].

The transport of the air-water interface with C_f needs a different formulation than the conservative form in Eq. (6.1). As mentioned in the introduction, a non-conservative formulation of the transport equation needs to be derived to prevent difficulties with spurious oscillations around the interface [2]. This formulation is found by using the mechanical (pressure and velocity) equilibrium between the fluids [188]. Summing all mass equations like for Eq. (6.4), as in Eq. (6.2), and using Eq. (6.9) for every phase results in an equation for total mass balance

$$\frac{Dp}{Dt} = - \frac{C_b}{\frac{\beta_g C_f + (C_b - C_f)}{\rho_a c_a^2} + \frac{(1 - \beta_g) C_f}{\rho_l c_l^2}} \nabla \cdot \mathbf{u}. \quad (6.19)$$

Filling in the sum of the mass balance of a and l results in

$$\frac{DC_f}{Dt} = -C_f \nabla \cdot \mathbf{u} - C_f \left(\frac{\beta_g}{\rho_a c_a^2} + \frac{1 - \beta_g}{\rho_l c_l^2} \right) \frac{Dp}{Dt}. \quad (6.20)$$

Note the independence of C_b which is essential for under- or overpredicting compressibility of a mixture and the similar form as the Kapila's one-dimensional

transport equation [133]. The equation has proved to be competent and easier to deal with than the fully conservative formulation [131, 231]. The right-hand side of Eq. (6.20) assures that the material derivative of the phase entropy is zero in the absence of shock waves.

The material derivative of C_f in Eq. (6.20) is needed to solve the transport of aerated water, but also for the material derivative of the aggregate density in Eq. (6.11). Substituting the missing unknowns defined in Sec. 6.3.1 in Eq. (6.11) results in the final formulation of the material derivative of the aggregate density needed for solving the total mass balance

$$\frac{D\rho}{Dt} = \rho \left(\frac{(1-\beta)C_f}{C_b} + \frac{C_b - C_f}{C_b} + \frac{\beta C_f}{C_b} \right) \frac{Dp}{Dt}. \quad (6.21)$$

6.3.4 Fluids: mixture speed of sound

The final formulation of the material derivative of the aggregate fluid is known in Eq. (6.21). This means that, using Eq. (6.9), a formulation for the aggregate speed of sound is derived

$$\frac{1}{\rho c^2} = \left(\frac{(1-\beta)C_f}{C_b} + \frac{C_b - C_f}{C_b} + \frac{\beta C_f}{C_b} \right). \quad (6.22)$$

For the air-water mixture let's define a mixture density (ρ_f) by splitting the formulation in Eq. (6.4)

$$\rho_f = (1 - \beta_g)\rho_l + \beta_g\rho_a, \quad \rho = \frac{C_f}{C_b}\rho_f + \frac{C_b - C_f}{C_b}\rho_a, \quad (6.23)$$

where ρ_f is the density of the aerated water. According to [297], the speed of sound formulation for homogeneous mixtures

$$\frac{1}{\rho_f c_f^2} = \frac{\beta_g}{\rho_a c_a^2} + \frac{1 - \beta_g}{\rho_l c_l^2} \quad (6.24)$$

and

$$\frac{1}{\rho c^2} = \frac{C_b - C_f}{C_b} \frac{1}{\rho_a c_a^2} + \frac{C_f}{C_b} \frac{1}{\rho_f c_f^2}. \quad (6.25)$$

The mixture speed of sound formulation of Wood is illustrated in Fig. 6.2. Fig. 6.2 shows a large decrease in speed of sound for a small fraction of β_g , even up to values lower than the speed of sound of air c_a and water c_l at atmospheric conditions.

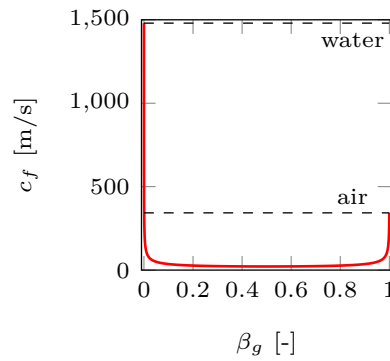


FIGURE 6.2. Woods' formulation in Eq. (6.24) for mixture sound of speed c_f . Plotted for air volume fraction β_g assuming $C_f = 1$.

The trend in Fig. 6.2 can be explained by looking to the general formulation of the speed of sound [296]

$$c_f = \frac{1}{\sqrt{\rho_f \kappa_f}}, \quad (6.26)$$

in which κ_f is the compressibility factor for the mixture. Assuming the compressibility factor for air and density for water constant (C) for a low volume fraction β_g , $\kappa_f \approx \kappa_a$, and $\rho_f \approx \rho_l$ results in

$$c_f = \frac{C}{\sqrt{\beta_g - \beta_g^2}}. \quad (6.27)$$

Where the density hardly changes, the mixture has the compressibility of air.

6.3.5 Fluids: new formulation speed of sound

For the speed of sound around the interface where a clear distinction is between air and water, the mixture speed of sound formulation of Woods' does in reality not hold [232]. There is no mixture between air and water at the fluid-fluid interface while we do use a homogeneous mixture model as stated in Sec. 6.2.2. The speed of sound at the interface is underestimated. The Woods' equation results in non-monotonic behavior and inaccurate wave transmission around the interface, getting worse for diffusive interfaces.

Ansari and Daramizadeh [3] gave another drawback for the mixture speed of sound relation in Eq. (6.25). The indicated problem is relevant for high-density ratio flows with large air volume changes and cavitation. The defined pressure-density relation in Sec. 6.3.1 can lead to negative densities when sub-atmospheric pressures play a role. A negative density results in a complex speed of sound for the mixture. As the introduction mentioned, aeration can lead to cavitation, meaning that the negative densities need to be prevented.

We decrease the effect of the non-monotonic behavior of the speed of sound across an interface by maintaining a sharp interface (explained in next Sec. 6.4). The consistent approach for determining the mass and momentum fluxes by [80] is used to deal with high-density ratio flows and sharp interfaces. The formulation of the air density by Wemmenhove [292] is used to prevent negative values when cavitation is involved. However, more attention needs to be paid when a rigid body, a cut-cell method, is involved.

Results in Sec. 6.6.4 showed that these measures were not enough when a body at the fluid-fluid interface is involved. The compressibility was not well predicted by comparing it with another numerical model. Saurel, Petitpas, and Berry [232] developed a formulation by adding an extra governing equation like the six-equations model of Hong, Wang, and Liu [116] to solve interface problems separated by compressible media. The corresponding formulation for the speed of sound is found called the frozen sound speed relation. This relation is the high-frequency limit of the particles with no mechanical equilibrium being the upper limit while the Woods' (mechanical equilibrium) speed of sound formulation is the lower limit. The particles are not able to adapt. Applying one of the two formulations was found to have small influence in the results [246]. In this work we did find differences when a body was involved. By not assuming a homogeneous mixture around the interface, a transmitted pressure wave by the interface is better predicted.

The use of the frozen speed-of-sound formulation at the fluid-fluid interface solved the compressibility issue at the interface when a body is involved; around the body, and the interface between the mixture, C_f , and air, $(1 - C_f)$. The new formulation for the speed of sound replaces Eq. (6.22) in Eq. (6.11) with

$$\frac{1}{\rho c^2} = \frac{C_b}{C_f \rho_f c_f^2 + (C_b - C_f) \rho_a c_a^2} \quad (6.28)$$

where c_f is given by mixture speed of sound formulation in Eq. (6.24) for volume fraction β_g .

The authors are aware that changing the mixture speed of sound violates the mathematical derivation of the model in Sec. 6.3. The combination of the frozen speed of sound for volume fraction C_f and the mixture speed of sound for volume fraction β_g , including a body with two unique volume fraction fields is new. The behavior of the new formulation is illustrated in Fig. 6.3 and can be compared with Fig. 6.2.

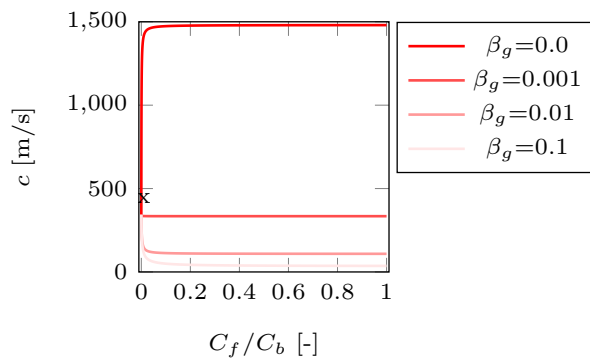


FIGURE 6.3. Frozen speed of sound for different mixtures β_g , varying C_f over C_b . The cross represent the speed of sound of air.

6.4 Grid structure

Before introducing the discretization of the governing equations, the grid structure is introduced with the definitions and notations needed to solve the system of equations. A brief account is provided of how to identify the material interface between water and air, of the arrangement of variables being solved for within a grid cell, and of the cut-cell method to incorporate moving bodies. This account follows the lines of the method introduced by Eijk and Wellens [80].

A fixed 2D cartesian grid is employed to divide the domain in cells. Cell labeling is used to identify the position of the interface within the grid. As stated in the introduction, the method should maintain a sharp interface to reduce the non-monotonic behavior of the speed of sound. Labeling aids in keeping the interface sharp because cells with air can be treated differently from cells with (aerated) water, and differently again from cells that contain the interface between air and (aerated) water. The cell labeling proposed by Eijk and Wellens [80] is used and illustrated in Fig. 6.4a. The choice of label is based on the volume fraction C_f . A cell completely filled by the body is labeled B and is not included in the system of equations. A cell without liquid ($C_f = 0$) is labeled E (empty, for historical reasons [142]). When a cell contains some fluid and is adjacent to an E-cell, it is given the S-label (surface). A cell with some fluid and adjacent diagonally to one empty cell is labeled as C. Remaining cells are labeled F (fluid, again for historical reasons). A F-cell is not allowed to connect with an E-cell. Note that a F-cell is not necessarily completely filled.

The standard Marker-and-Cell (MAC) staggered arrangement of variables within a grid cell is used, meaning that the scalar variables (pressure p , density ρ , and volume fractions C_f , C_b , β_g) are positioned in cell centers, and the components of the velocity vector normal to the cell faces ($\mathbf{u} = [u_1, u_2]^T$) are positioned at those faces. The arrangement of variables is shown in Fig. 6.4b. Control volumes

are employed to solve the governing equations. Two different kinds of control volume are used. Conservation of momentum is solved for in momentum control volumes, and continuity is solved for in mass control volumes. Mass control volumes coincide with grid cells, see Fig. 6.5a. Momentum control volumes lie staggered in the grid with respect to mass control volumes. All control volumes are shown in Fig. 6.5b. Averaging is needed to obtain values of the density at the positions of the velocity components. A consistent averaging procedure is described by Eijk and Wellens [80] and not discussed further here.

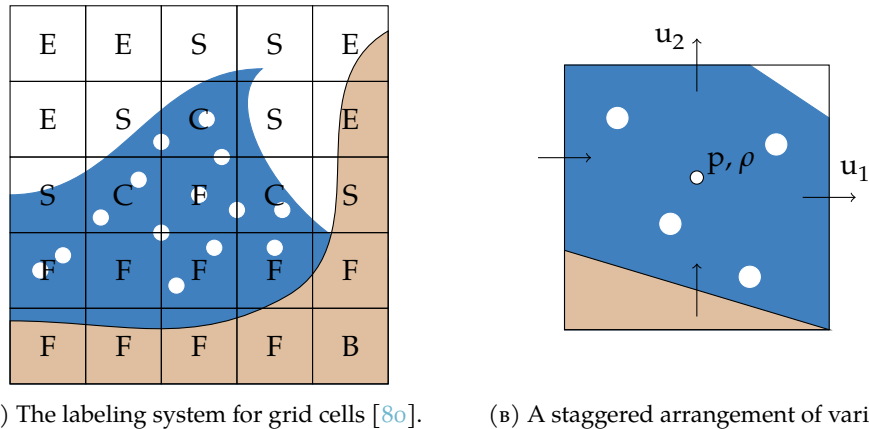
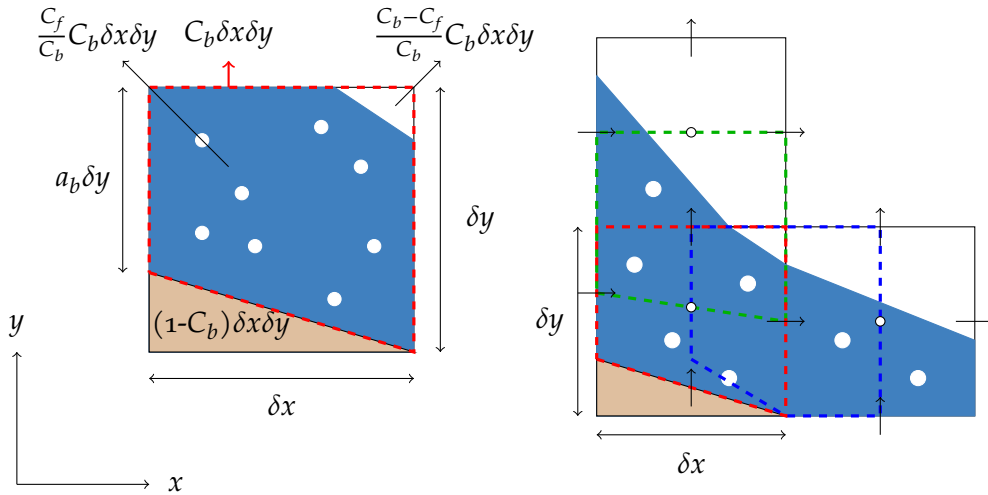


FIGURE 6.4. Fixed Cartesian grid structure with labels making a distinction between body, water, and air. Standard MAC configuration of variables (staggered); scalar variables (p and ρ) are defined in cell centers (\circ), the velocity field u is sampled at the faces of the cell (\rightarrow).

The body is represented using a cut-cell method [90]. A cell is called a 'cut cell' when part of the body's contour intersects with this cell. The part of the cell not occupied by body is referred to as volume fraction, or volume aperture, C_b . The interface between body and fluids cuts through the cell by means of piecewise-linear segments. Volume and face apertures are used to account for the presence of the body. Volume aperture C_b indicates the part of a grid cell's volume that is open to fluid. Face apertures a_b indicate the area of a grid cell's faces that is open to flow. Apertures are illustrated in Fig. 6.5a. Apertures scale the size of the control volumes so that the equations in cut cells are solved like those in uncut cells; the discretization of the equations does not change. A visual representation of the scaling of control volumes is given in Fig. 6.5b. The size of the mass control volume is $C_b \delta x \delta y$, and left-most part of the boundary of the control volume that is open to flow is $a_b \delta y$. More about the treatment of cut cells is given in Eijk and Wellens [80].



(A) Cut cell with volume aperture C_b indicating the part of the grid cell's volume open to fluid and face aperture a_b indicating the area of a grid cell's face open to flow. The mass control volume is shown as (-). The filling ratio of cells is administered in terms of C_f and C_b . (B) Staggered arrangement of control volumes within the grid. Mass control volumes coincide with grid cells.

FIGURE 6.5. Control volumes and cut cells. Cut cells are used to represent arbitrarily shaped moving bodies in the grid by means of piecewise-linear segments. Cut cells scale mass control volumes (-) and momentum control volumes with an averaging procedure, leading to this graphical representation of control volumes. Vertical momentum control volumes (-), and horizontal momentum control volumes (-) lie staggered with respect to mass control volumes.

6.5 Discretization and solution algorithm

The governing equations for conservation of mass (6.4) and conservation of momentum (6.6) of the fluids are discretized and combined with the discrete representations of the equations of motion of the body (6.7) and (6.8) into a system of equations for solving the pressure p and the body velocity \mathbf{u}_b . The fluid velocities \mathbf{u} are solved from the pressure gradients. The fluid and body velocities are used to transport the interface between fluids and the interface between fluids and body. Density ρ and the fraction of air in water β_g (aeration) are solved algebraically. The equations are combined into a solution algorithm.

The solution algorithm is an extension of the incompressible two-phase flow method in Eijk and Wellens [80], that uses the same discretization techniques for the mass, momentum and interface transport to obtain a consistent method. Without consistency, momentum losses and distortion of the interface are found for high-density ratio flows. A temporary continuity equation was used to obtain

consistency, solving it on momentum control volumes to prevent momentum losses as a result of the staggered grid.

A one-step projection method [41] is used for solving the pressure. Time levels are indicated using superscripts $n + 1$ and n . A $\bar{\cdot}$ above variables indicates an auxiliary step. The following discrete operators are used to compose the system of equations: $\Omega_f, \Omega_c, \mathcal{C}_f, M_c, M_f, A_c, \mathbf{I}$, in which subscript (f) or (c) is used to indicate whether the operator is applied on momentum or mass control volumes respectively. The symbols represent the discrete

- M : divergence operator, that depends on grid sizes and face apertures a_b [90].
- M^T : transpose of the divergence operator that equals the gradient operator, working on pressures that are considered constant within grid cells [39].
- \mathcal{C} : convective operator that retains the skew-symmetry of its continuous counterpart [269].
- Ω : volume operator representing the grid cell volume scaled by C_b [90].
- A : operator that integrates the pressure along the body contour using face apertures a_b [80].
- \mathbf{I} : identity matrix

The operators depend on time because of the volume and face apertures that change with the moving body.

The solution algorithm is explained as implemented.

FOR EACH TIME STEP

- a) Solve volume fraction transport for fluid and body (C_f^{n+1}, C_b^{n+1}) and reconstruct interfaces with face apertures a_b^{n+1}
- b) Solve auxiliary momentum field $\bar{\rho}\bar{\mathbf{u}}$ and ρ^n
- c) Solve auxiliary density and vector field $\bar{\rho}$ and $\bar{\mathbf{u}}$
- d) Solve vector field including all explicit terms $\tilde{\mathbf{u}}$ and ρ^{n+1} and β_g^{n+1}
- e) Solve new pressure field with δp and coupling with body \mathbf{u}_b^{n+1}
- f) Solve new fluid velocity field \mathbf{u}^{n+1}

After every time step, a Courant number is calculated for the new velocity field \mathbf{u}^{n+1} [80]. When the Courant number does not satisfy the criterion associated with the time integration, the time step is halved until it does. When the Courant number is below a user defined minimum Courant number for 10 time steps, then the time step is doubled.

The following describes the discretization in order of the steps in the solution algorithm in subsections that have the same number as the step in the algorithm. A final seventh subsection introduces an interface correction to the mixture speed of sound formulation compared to Eq. (6.25) to prevent artificial compressibility at the interface between fluids.

6.5.1 Interface transport

The interface capturing method consists of two steps: interface transport and geometrical reconstruction of the interface. Interface transport depends on the interface orientation and the discrete volume fraction field. The update for C_f is solved by means of the discrete representation of Eq. (6.20). The update for β_g is solved algebraically using Eq. (6.17). Transport equation (6.20) can be separated into an advective and a compressive part. For the advective part fluxes are computed along the boundary of a mass control volume. Fig. 6.6 shows a visual representation of a flux in a cut cell. Using fluxes, the discretization of the transport equation (6.20) becomes

$$C_f^{n+1} = C_f^n - \frac{1}{\delta x \delta y} \left[\sum_{sides} \delta C_{f,side} \right]^1 - \frac{\delta t}{\delta x \delta y} \left[\frac{C_f^n}{C_b^n} \left(\frac{\beta_g^n}{\rho_a^n (c_a^2)^n} + \frac{1 - \beta_g^n}{\rho_l^n (c_l^2)^n} \right) \frac{Dp}{Dt} \right]^2. \quad (6.29)$$

Boxed term 1 represents the advective part, boxed term 2 represents the compressive part. A flux δC_f is of the form

$$\delta C_f \propto \frac{C_f}{C_b} u_1 \delta t a_b \delta n, \quad (6.30)$$

with δn representing the cell face size which in 2D corresponds to either δx or δy . In the example in Fig. 6.6, δn is equal to δy .

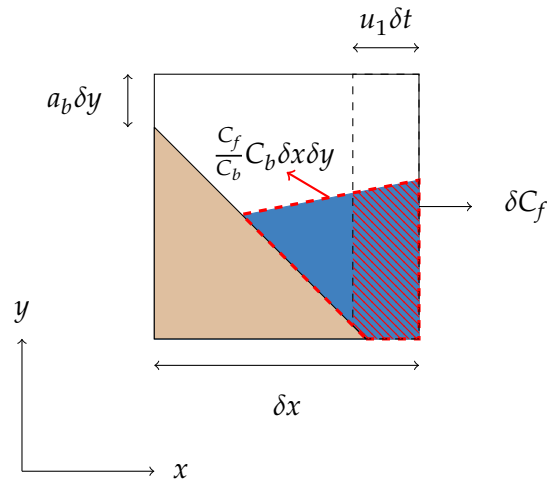


FIGURE 6.6. Flux in a cut-cell near the interface between air and aerated water. The hatched area (–) represents the size of the flux δC_f . The area surrounded by the dashed line (–) represents the volume of the air-water mixture $\frac{C_f}{C_b} \delta x \delta y$ in the mass control volume.

There is existing literature about using reconstruction after transporting the interface, to good effect [53, 192, 276]. Geometric reconstruction reduces mass loss and keeps the interface sharp. The piecewise linear interface calculation method (PLIC) of Parker and Youngs [202] is applied. The labelling system in Fig. 6.4a is used for marking out cells where the interface needs reconstruction; those are cells labeled with S or C. An example of a PLIC interface segment is shown in Figs. 6.5b and 6.5a.

The body is displaced similarly to Eq. (6.29). The difference is that the compressive term does not need to be computed. The transport equation for the body is

$$C_b^{n+1} = C_b^n - \frac{1}{\delta x \delta y} \sum_{sides} \delta C_{b,side}. \tag{6.31}$$

After updating C_b to C_b^{n+1} , the interface between body and fluids is reconstructed using the same PLIC method that is used for the interface between fluids. The face apertures a_b^{n+1} indicated in Fig. 6.5a are found by averaging end points of PLIC reconstruction lines in neighboring cells.

6.5.2 Auxiliary momentum field

The momentum equation (6.6) is solved in steps. First, an auxiliary momentum field $\bar{\rho} \bar{\mathbf{u}}$ is solved for

$$\frac{\bar{\rho} \bar{\mathbf{u}} - \rho^n \mathbf{u}^n}{\delta t} \Omega_f^{n+1} + \mathfrak{C}_f^n (\rho^* \{ \mathbf{u}^n, \mathbf{u}_b^n \}) \mathbf{u}^n. \tag{6.32}$$



Momentum $\rho^* \mathbf{u}$ is defined as the weighted average of momentum contributions from the two fluids that are modelled

$$\rho^* \mathbf{u} = (C\rho_f + (1 - C)\rho_a)\mathbf{u}, \quad (6.33)$$

in which C is a weight that is based on the mass fluxes

$$C = \frac{|\delta C_f|}{|\mathbf{u}|a_b \delta t \delta n}, \quad (6.34)$$

using δC_f from Eq. (6.30) to obtain consistency between mass and momentum.

Density field ρ^n is found using the values of p^n , C_f^n and C_b^n and the reconstruction of the interface from the mass control volumes that have overlap with the momentum control volume under consideration using the definition in Eq. (6.4). When the pressure at the position of a velocity in a cell is necessary, it is found as the average of the two nearest pressures in the direction of that velocity.

6.5.3 Auxiliary density

An auxiliary density field $\bar{\rho}$ is computed for the momentum control volume that complies with the discretization of the momentum fluxes and VOF fluxes by means of a temporary continuity equation. The auxiliary density field is needed due to the inconsistency between ρ^{n+1} and $\bar{\rho}$ [29, 80, 222]. The temporary continuity equation reads

$$\frac{\bar{\rho} - \rho^n}{\delta t} \Omega_f^{n+1} + M_f^n (\rho^* \{\mathbf{u}^n, \mathbf{u}_b^n\}) = 0. \quad (6.35)$$

using the following approach near the interface between fluids and body

$$M_f^n (\rho^n \{\mathbf{u}^n, \mathbf{u}_b^n\}) = M_f^n (\rho^n \mathbf{u}^n) + (1 - M_f^n) (\rho^n \mathbf{u}_b^n). \quad (6.36)$$

An auxiliary vector field $\bar{\mathbf{u}}$ is computed by dividing the auxiliary momentum field by the auxiliary density found from Eq. (6.35).

6.5.4 New density & new aeration fields

A second auxiliary velocity field $\tilde{\mathbf{u}}$ is constructed to contain the remaining terms of the momentum equation, that are integrated explicitly in time

$$\tilde{\mathbf{u}} = \bar{\mathbf{u}} - \delta t \left(\Omega_f^{n+1} \right)^{-1} \left(\frac{1}{\rho^{n+1}} (M_c^T)^{n+1} p^n + \mathbf{g} \right), \quad (6.37)$$

in which the new pressure field p^{n+1} is split into a temporal change δp and the pressure field at the old time level p^n .

Density field ρ^{n+1} is computed similarly to ρ^n . However, the new pressure field p^{n+1} , needed for equations of state of the fluids described in Sec. 6.3.1, remains as of yet unknown. In order to prevent having to iterate between density and pressure until convergence, which would involve a significant computational effort with solving a Poisson equation at every iteration, rather an auxiliary pressure field \tilde{p} is constructed. Even without iterating between density and pressure, the Poisson equation in the current method described here constitutes 90% of the total computational cost. The auxiliary pressure field is found from

$$\frac{\tilde{p} - p^n}{\delta t} \Omega_f^{n+1} + M_c^n (p^n \{\mathbf{u}^n, \mathbf{u}_b^n\}) - (p^n - \rho^n (c^2)^n) M_c^n (\{\mathbf{u}^n, \mathbf{u}_b^n\}) = 0. \quad (6.38)$$

Note that this equation is solved on mass control volumes. Then, using Eqs. (6.12) and (6.15) for the air density ρ_a^{n+1} and liquid density ρ_l^{n+1} , respectively, the new density field ρ^{n+1} is computed. The densities ρ_a^{n+1} and ρ_l^{n+1} are functions of p^* , but also of C_f^{n+1} and C_b^{n+1} , see Sec. 6.5.2.

The new aeration field β_g^{n+1} is computed using the new density values ρ_a^{n+1} and ρ_l^{n+1} , together with Eq. (6.17) in which the mass fraction μ_g is required to remain constant.

6.5.5 Pressure equation & coupling with body

The equation for the pressure change δp is obtained by taking the divergence (M_c) of the momentum equation and substituting it into the continuity equation by eliminating the velocity field at the new time step \mathbf{u}^{n+1} . The discrete continuity equation for a mass control volume equals

$$\frac{1}{\rho} \frac{D\rho}{Dt} + M_c^{n+1} (\{\mathbf{u}^{n+1}, \mathbf{u}_b^{n+1}\}) = 0. \quad (6.39)$$

After substituting the discrete momentum equation into Eq. 6.39 and rearranging terms, an equation for δp and \mathbf{u}_b^{n+1} is obtained

$$\delta t M_c^{n+1} (\Omega_f^{n+1})^{-1} \frac{1}{\rho^{n+1}} (M_c^T)^{n+1} \delta p - (1 - M_c^{n+1}) \mathbf{u}_b^{n+1} = M_c^{n+1} \tilde{\mathbf{u}} + \frac{1}{\rho} \frac{D\rho}{Dt}. \quad (6.40)$$

The material derivative density term in Eq. (6.40) is solved with Eq. (6.21)

$$\frac{1}{\rho} \frac{D\rho}{Dt} = \frac{1}{\rho^{n+1} (c^2)^{n+1}} \left(\frac{\delta p}{\delta t} \Omega_c^{n+1} + M_c^{n+1} (p^n \{\tilde{\mathbf{u}}, \tilde{\mathbf{u}}_b\}) - p^n M_c^{n+1} \{\tilde{\mathbf{u}}, \tilde{\mathbf{u}}_b\} \right), \quad (6.41)$$

from which the unsteady term with the pressure change δp needs to be moved to the left-hand side of Eq. (6.40). How the speed of sound (c) is computed is described in the last subsection of Sec. 6.3.

Body motion

The discrete representation of the equations of motion of the body Eq. (6.8) is given by

$$\frac{\mathbf{u}_b^{n+1} - \mathbf{u}_b^n}{\delta t} m_b + m_b \mathbf{g} + \mathcal{A}_c^{n+1} (\delta p + p^n), \quad (6.42)$$

in which \mathcal{A}_c is an operator that integrates the pressure over the surface of the body. Similar to the auxiliary velocity and pressure fields, an auxiliary body velocity $\tilde{\mathbf{u}}_b$ is formulated including terms that are integrated explicitly

$$\tilde{\mathbf{u}}_b = \mathbf{u}_b^n + \delta t m_b^{-1} (m_b \mathbf{g} + \mathcal{A}_c^{n+1} p^n). \quad (6.43)$$

Fluids and body are coupled through the pressure. The following system of equations needs to be solved to find the field of pressure change δp the body velocity \mathbf{u}_b

$$\begin{bmatrix} \mathcal{L}_p & -M_b^{n+1} \\ \delta t m_b^{-1} \mathcal{A}_c^{n+1} & \mathbf{I} \end{bmatrix} \cdot \begin{bmatrix} \delta p \\ \mathbf{u}_b^{n+1} \end{bmatrix} = \begin{bmatrix} \mathcal{R}_p \\ \tilde{\mathbf{u}}_b \end{bmatrix}, \quad (6.44)$$

in which

$$\begin{aligned} \mathcal{L}_p &= \delta t M_c^{n+1} (\Omega_f^{n+1})^{-1} \frac{1}{\rho^{n+1}} (M_c^T)^{n+1} - \frac{1}{\rho^{n+1} (c^2)^{n+1}} \delta t^{-1} \Omega_c^{n+1}, \text{ and} \\ \mathcal{R}_p &= M_c^{n+1} \tilde{\mathbf{u}} + \frac{1}{\rho^{n+1} (c^2)^{n+1}} (M_c^{n+1} (p^n \{\tilde{\mathbf{u}}, \tilde{\mathbf{u}}_b\}) - p^n M_c^{n+1} \{\tilde{\mathbf{u}}, \tilde{\mathbf{u}}_b\}). \end{aligned} \quad (6.45)$$

6.5.6 New fluid velocity field

Finally, after having solved for the pressure change and the body velocity, the new fluid velocity field is computed from

$$\frac{\mathbf{u}^{n+1} - \tilde{\mathbf{u}}}{\delta t} \Omega_f^{n+1} + (M_c^T)^{n+1} \delta p = 0. \quad (6.46)$$

6.5.7 Numerical model discretization schemes

In this section the time integration has been represented as implicit for the pressure and Forward Euler for the explicit terms. This was for the purpose of presenting an already complex combination of equations, and in the presentation we wanted to keep emphasis on the equations and not confound matters with the details of the discretization. The algorithm as presented works, but improvement with respect to the presented algorithm can be obtained with the discretization discussed here.

The convective term in Eq. (6.46) is solved on a momentum control volume. This term is discretized using the high-resolution scheme [114, 307]. The high-resolution scheme combines high-order accuracy with monotonicity and switches from second-order to first-order upwind near the interfaces between body and

fluids and between fluids. An explicit second-order Adams-Bashforth time stepping scheme then is employed for the convective term to allow for larger time steps. The suitable Courant restriction for the combination of these two schemes is 0.25 or lower [292].

The material derivative of the pressure is solved on mass control volumes. The advective term of the derivative is split into two terms as illustrated in Eq. (6.41). The divergence term of the pressure is discretized using arithmetic averaging of pressures. The pressure equation in Eq. (6.44) is solved monolithically with the equations of motion of the body. The equations of motion of the body are integrated in time using the Crank-Nicolson scheme [80].

The material interfaces defined using volume fractions C_f and $1 - C_b$ are transported using a direction-split scheme called COSMIC [155]. The COSMIC scheme is applied for the advective term in Eq. (6.29). A correction around the interface [295] is used to conserve mass for incompressible flows.

A final note on the discretization is that it was not designed to be completely mass conserving. It is quasi-conservative in which mass errors are carefully balanced against momentum errors and other errors that can be expected on the fairly coarse grids that cannot be avoided for the envisioned application of wave impacts on structures at sea. It is demonstrated next that the errors are well behaved and that the numerical results show good agreement with analytical solutions and experimental results.

6.6 Verification and validation with results from existing literature

Peregrine et al. [207] showed that it is likely that density waves are formed in the compressible medium after wave impacts of aerated water against structures. The capability of our method to represent the propagation of density waves is investigated by comparing with results of existing benchmark tests with compressibility from literature: a shock tube, a piston and a 2D shock bubble.

6.6.1 1D Shock tube

A shock tube is a 1D case in which a fluid or fluids at different initial pressure are separated before being released. The propagation of a density wave in a tube filled with air at different states initially was presented by Eijk and Wellens [75] using a similar numerical method. Two shock tube cases are considered here. One with water at high pressure on one side of the tube and air on the other, and one with aerated water at a higher pressure one side of the tube than the other. Gravitational effects are not relevant and are omitted from the simulations. For both cases, three different grid resolutions are used and the effect of the Courant number on the results is evaluated.

6.6.1.1 Shock tube with two separated fluids

The first case resolves a density wave through a shock tube with two fluids, water and air. A shock tube with water and air was investigated analytically by Sod [247]. The setup of the simulation is illustrated in Fig. 6.7.

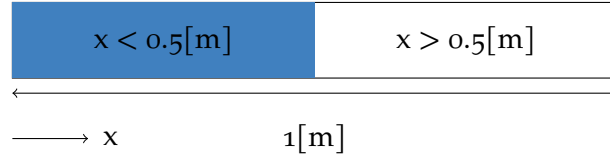


FIGURE 6.7. Setup of simulation of a shock tube with water (■) and air. Water initially at high pressure.

The fluid configuration, pressure and density satisfy the following initial conditions

$$C_f = \begin{cases} 1[-], & x < 0.5[\text{m}] \\ 0[-], & x > 0.5[\text{m}] \end{cases}, \quad p = \begin{cases} 1.0[\text{Pa}], & x < 0.5[\text{m}] \\ 0.1[\text{Pa}], & x > 0.5[\text{m}] \end{cases},$$

and

$$\rho = \begin{cases} 1.0[\text{kg}/\text{m}^3], & x < 0.5[\text{m}] \\ 0.125[\text{kg}/\text{m}^3], & x > 0.5[\text{m}] \end{cases}.$$

The initial velocity field is zero. Aeration is not considered, so $\beta_g = 0$. As equations of state, these relations are employed

$$\rho_l = p, \quad \rho_a = \left(\frac{p}{a_c} \right)^{\frac{1}{\gamma_a}},$$

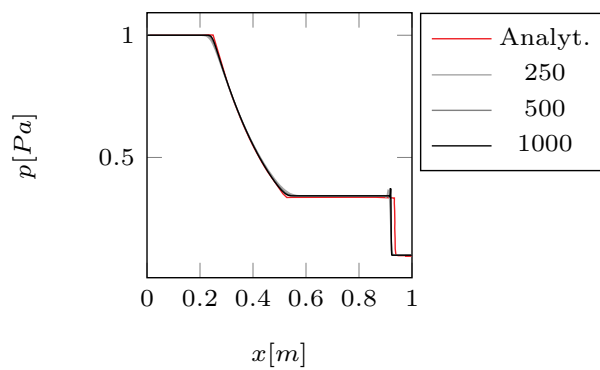
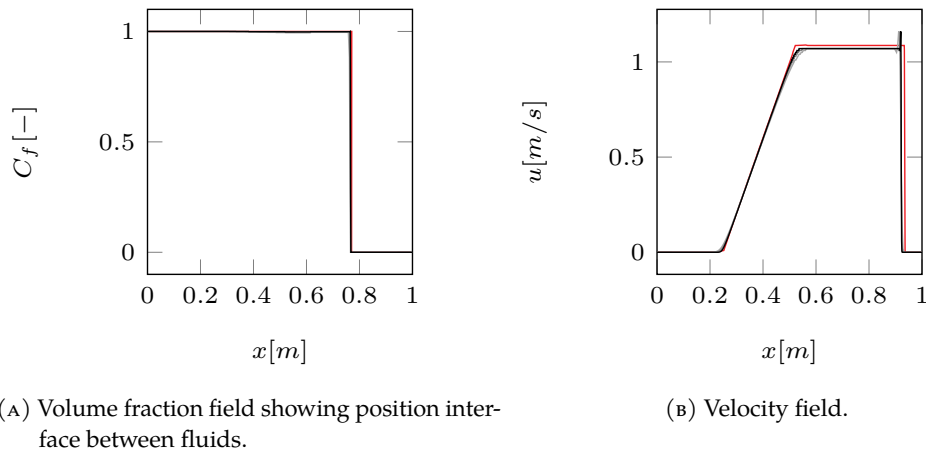
with ρ_l the density of water and $\rho_a, a_c = 1.34543$ and $\gamma_a = 1.25$ the density, specific heat ratio and isentropic constant for air, leading to the following expressions for the speed of sound in water and air respectively

$$\frac{1}{c_l^2} = 1, \quad \frac{1}{c_a^2} = \frac{1}{1.34543\gamma_a} \left(\frac{p}{1.34543} \right)^{\frac{1-\gamma_a}{\gamma_a}}.$$

The maximum Courant number, based on the instantaneous fluid velocities, equals 0.2. The final time for the simulations is set at 0.25[s]. Simulations are performed for several grid resolutions to investigate convergence. The resolutions are 250, 500, and 1000 cells over the tube length.

The simulation results are shown in Fig. 6.8 and compared to the analytical results of Sod [247]. The displacement of the interface between fluids is predicted well. The mass loss is never larger than 0.4% for the air phase and 0.01% for the liquid phase. A rarefaction wave propagates through the water in negative

x-direction and a compression wave propagates through the air in positive x-direction. The fluid velocity is continuous across the interface between water and air. The velocity gradients in the rarefaction wave ($0.2 < x < 0.5$) are smoothed by numerical viscosity, which decreases with increasing grid resolution. Note that the compression wave front is not a formal discontinuity in the method; the velocity jump is smeared out over a couple of grid cells. The numerical viscosity is not sufficient to prevent wiggles near the compression wave front: small spurious velocity oscillations are found there, but they are independent of the spatial grid size. The velocity of the compression wave front is underestimated by 1.0% and also the fluid velocities are somewhat underestimated compared to the analytical results. This could be due to using the non-conservative form of the equations in the method. The non-conservative form does not satisfy the same Rankine-Hugoniot conditions, describing the states of the fluid on either side of the compression wave front, as the conservative form.



(c) Pressure field.

FIGURE 6.8. Shock tube with water and air: numerical results compared to analytical solution [247] for three different grid resolutions at time $t = 0.25$ [s].

6.6.1.2 Shock tube with aerated water (water-air mixture)

The second case is a shock tube filled with aerated water, i.e. a homogeneous water-air mixture, with a higher pressure and density in the left-most half of the tube. An analytical solution for density wave propagation through dispersed fluids (mixtures) was reported in Franquet [93]. The assumption of homogeneity means that transport of the interface through C_f is not resolved; C_f is equal to one throughout the domain. The mass fraction of the air in water is $\mu_g = 1.31 \cdot 10^{-5}$ [-]. The initial conditions for the air volume fraction associated with that mass fraction, and for the pressure on either side of the shock tube are

$$\beta_g = \begin{cases} 1.95 \cdot 10^{-3}[-], & x < 0.5[\text{m}] \\ 1.00 \cdot 10^{-2}[-], & x > 0.5[\text{m}] \end{cases}, \quad p = \begin{cases} 10^6[\text{Pa}], & x < 0.5[\text{m}] \\ 10^5[\text{Pa}], & x > 0.5[\text{m}] \end{cases}.$$

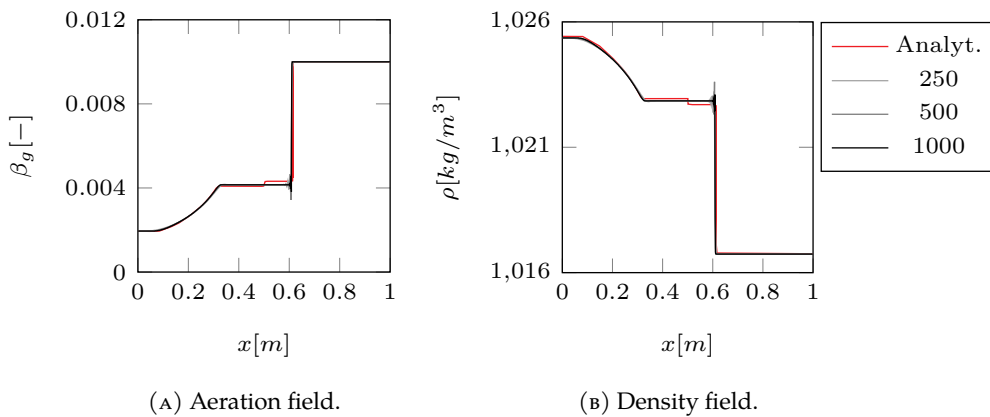
The initial conditions for the density of the air in water and for the density of the water are

$$\rho_a = \begin{cases} 6.91[\text{kg}/\text{m}^3], & x < 0.5[\text{m}] \\ 1.33[\text{kg}/\text{m}^3], & x > 0.5[\text{m}] \end{cases}, \quad \rho_l = \begin{cases} 1027.4[\text{kg}/\text{m}^3], & x < 0.5[\text{m}] \\ 1027.0[\text{kg}/\text{m}^3], & x > 0.5[\text{m}] \end{cases}.$$

The equations of state are the same as in Sec. 6.3.1.

At first a maximum Courant number based on the instantaneous fluid velocities of 0.001 is set. The final time of the simulations is $5.5137 \cdot 10^{-4}$ [s]. Simulations with three grid resolutions are performed, using 250, 500 and 1000 cells in the length of the tube.

The results of the simulations are shown in Fig. 6.9. The results are in agreement with the analytical solution. The slight jump in the aeration and density field near $x = 0.5$ [m] is caused by a temperature fluctuation, which our method does not solve for. Similar observations as for the shock tube with water and air separately can be made regarding numerical viscosity, the resolution of velocity gradients and oscillations near the compression wave front.



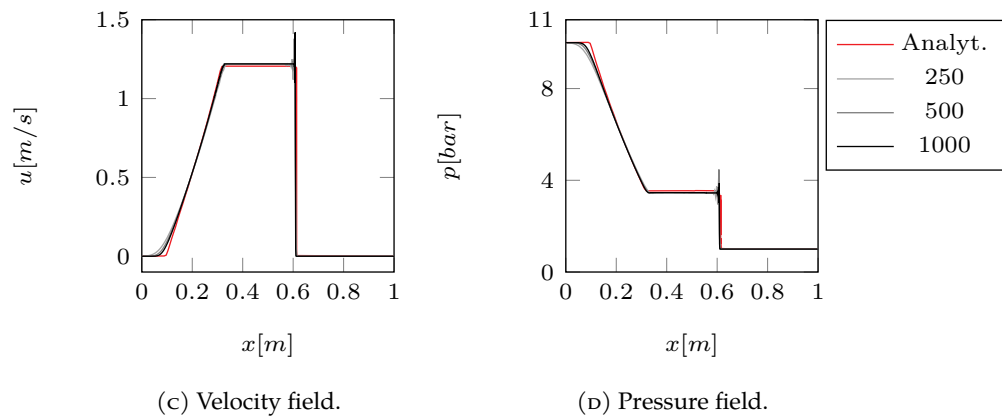


FIGURE 6.9. Shock tube aerated water: numerical results compared with analytical solution [93] for three different grid resolutions at time $t = 5.51 \cdot 10^{-4}$ [s].

Next, the effect of the maximum Courant number on the results is investigated. Simulations are performed in which the maximum Courant numbers are varied between $5 \cdot 10^{-4}$ and $1 \cdot 10^{-2}$ at a grid resolution of 1000 cells. The results are shown in Fig. 6.10, zooming in on the direct vicinity of the compression wave at time $t = 5.51 \cdot 10^{-4}$ [s]. The resolution of the jump in velocity over the compression wave front is strongly affected by the choice for the maximum Courant number. With a Courant number of $5 \cdot 10^{-4}$ the jump is resolved well but velocity oscillations (wiggles) are observed. The oscillations become smaller for higher Courant numbers, until for a value of $1 \cdot 10^{-2}$ no oscillations remain. But at a maximum Courant number of $1 \cdot 10^{-2}$, the jump in velocity near the compression wave front is also not resolved well anymore.

For the shock tube with aerated water the speed of the propagating density wave is close to 200 [m/s]. That means that for a Courant number based on the fluid velocities of $1 \cdot 10^{-2}$, the Courant number based on the speed of the density wave is approximately 2. Considering the shock tube with separated water and air with a Courant number based on fluid velocities of 0.2, the Courant number based on the density wave speed is 0.3. Note that the numerical method is not intended for an optimal representation of shock fronts, but for the representation of effects associated with compressibility in impacts between waves and structures. To obtain an adequate representation of the fluid properties on either side of the density wave front, the experience with the shock tubes gives us that the Courant number based on the speed of the density wave needs to be kept well below 1.

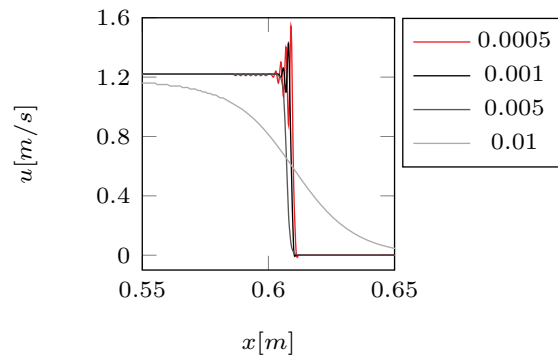


FIGURE 6.10. Shock tube aerated water: effect of maximum Courant number (based on instantaneous fluid velocity) on the velocity on either side of the compression wave front. Simulations performed with grid 1000 and velocity shown at time $t = 5.51 \cdot 10^{-4}$ [s].

6.6.2 Water or rigid body piston

To demonstrate the method's performance at capturing low-frequency, low-velocity, large scale compression of fluids that are separated by an interface, vertical 1D 'piston' simulations are performed [61, 168]. The piston is either a layer of water or a body initially placed in between two layers of air before releasing it to fall down due to gravity. The piston compresses the air below while gaining and losing inertia, after which the compressed air pushes the piston back up again. At these low velocities, the water piston, being weakly compressible, is expected to behave the same as the piston that is modelled as a moving body.

The piston simulation setup is shown in Fig. 6.11. The piston is hatched to indicate that it can either be a rigid body (C_b is transported) or water (C_f is transported). The initial air density is 1 [kg/m³], and the density of water and body is 1000 [kg/m³]. The pressure follows an aerostatic pressure distribution with value of $1 \cdot 10^5$ [Pa] at the bottom end of the domain. The gravity constant \mathbf{g} is $[0, -9.81]^T$ [m/s²]. The maximum Courant number is 0.2 . The velocity field when the simulations start, is zero.

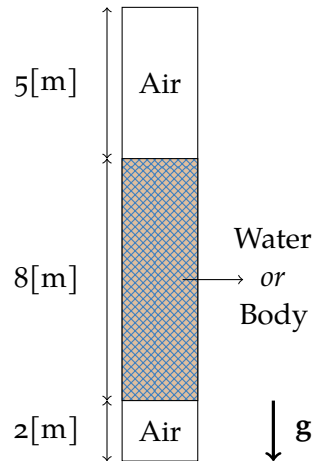
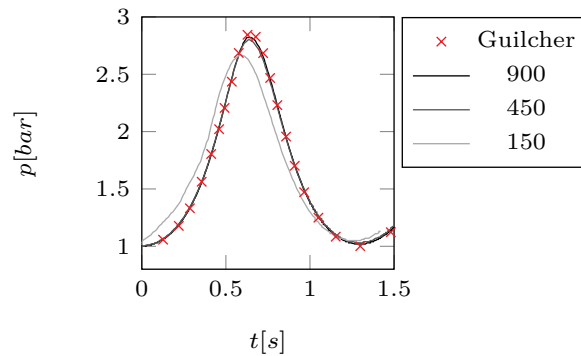
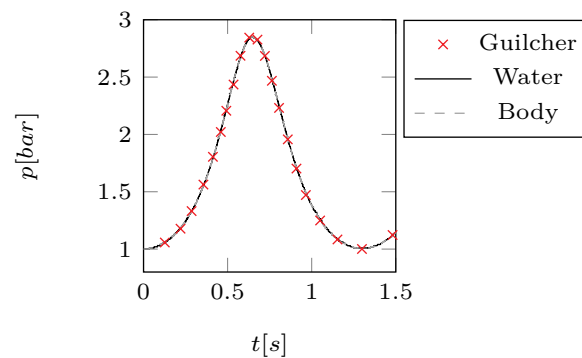


FIGURE 6.11. Piston: simulation setup. Hatched area indicates either water or a moving rigid body.

Results are given in Fig. 6.12 in terms of the pressure at the bottom end of the domain for different numbers of cells over the full height of the domain. Results are compared to those of Guilcher et al. [104]. The pressure over time with a piston composed of water in Fig. has converged for grid 450 and then matches the results of Guilcher et al. [104]. When the water is replaced by a moving rigid body for grid 450, the pressure in Fig. 6.12b, the pressure is a match to that below the water piston. Both piston motions have the same expected physical behavior, even though the transport algorithms for C_f and C_b are quite different.



(A) Pressure below water piston for different grids (maximum Courant number 0.2).



(B) Pressure below moving rigid piston compared to water piston for grid 450.

FIGURE 6.12. Piston: pressure below piston as a function of time when piston is either water or moving rigid body.

6.6.3 2D Shock bubble

The test case with a shock bubble is performed to investigate how density waves change direction and how they are transmitted between fluids in simulations with a compressible multiphase method. Helium shock-bubble experiments were performed by Haas and Sturtevant [105] and the results serve as a benchmark.

The simulation setup for the 2D helium shock bubble case is illustrated in Fig. 6.13. Air, initially, is in two states on either side of the domain, just as for the shock tube. A cylindrical helium bubble is placed in the air at one of these states, approximately in the middle of the domain. The domain boundaries are closed with atmospheric pressure prescribed on the left horizontal end of the domain. Because the simulation setup is symmetrical in y -direction only half of the domain in that direction is simulated. Three grid resolutions are used in half of the domain: 1200×150 , 800×100 , and 400×50 . A Courant number of 0.2 is used. The shock front arrives at the x -position of the helium bubble at $6 \cdot 10^{-5}$ [s] after the fluids are released. From here on, the moment the shock front arrives at the position of the bubble is defined as $t=0$ [s].

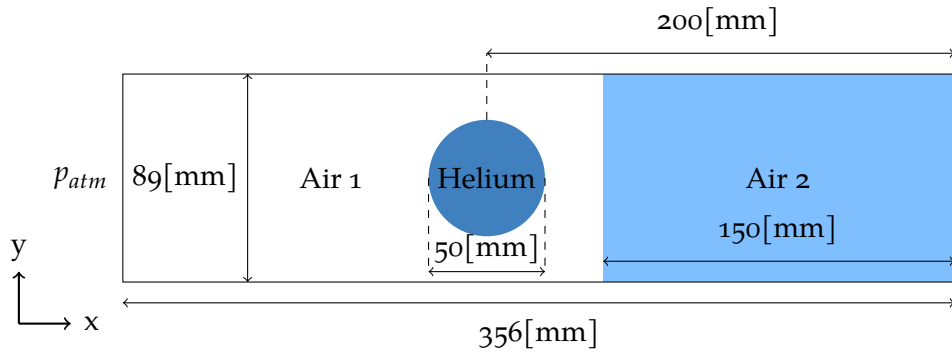


FIGURE 6.13. Shock bubble: simulation setup with air at two states of pressure, and helium bubble in the air at one of these states.

The helium bubble in the experiment was contaminated with 28% air (of mass) [105]. The fluid properties in Table 6.1 take the contamination into account and are given for a temperature of 25 degrees Celsius [105]. These properties, according to the Rankine-Hugoniot equations, are associated with an initial shock front speed of 420[m/s] and a Mach number of 1.22 [105, 221]. Quirk and Karni [221] conducted a detailed numerical study of the helium shock bubble. Kreeft and Koren [148] also simulated the shock bubble, but with different fluid properties using a density-based model solving Kapila’s five-equation model for inviscid, non-heat-conducting, compressible two-fluid flows. Even though the fluid properties they used were different, the same shock front speed as in the experiment was obtained [148].

	γ [-]	ρ [kg/m ³]	p [kg/ms ²]	C_f [-]	β [-]	u [m/s]
Air 1	1.4	1.168	$1.0 \cdot 10^5$	1.0	0	0
Air 2	1.4	1.612	$1.5698 \cdot 10^5$	1.0	0	-115.5
Helium	1.648	0.212	$1.0 \cdot 10^5$	0	0	0

TABLE 6.1. Initial fluid properties for helium shock bubble simulation [105].

In the simulations, the front of the density wave before interacting with the helium bubble at $t = 0[s]$, is smeared out over ten grid cells. We chose the position in the middle of these 10 cells as the position of the density wave front to compare with the results from literature. The results of the simulations are given in terms of the positions and the velocities of the interfaces and the density wave fronts. The definition of all interfaces and shock fronts is given in Fig. 6.14a. Interfaces and shock fronts are identified by their velocities v . Fig. 6.14b features a space-time plot of the interfaces, in which the results of the numerical method at three grid resolutions is compared with the results of Quirk and Karni [221]. The maximum Courant number is 0.2. The results of our numerical method have converged. Where the grid spacing used by Quirk and Karni [221]

6

was 0.056[mm], a relatively coarse grid is used in our simulations, with the 1200x150 grid having a spacing of 0.30[mm]. Spurious oscillations at the density wave front were not observed. Even at these coarse grids, the positions of the interfaces over time are in good agreement with Quirk and Karni [221]. A similar conclusion was found for the cases with the shock tube.

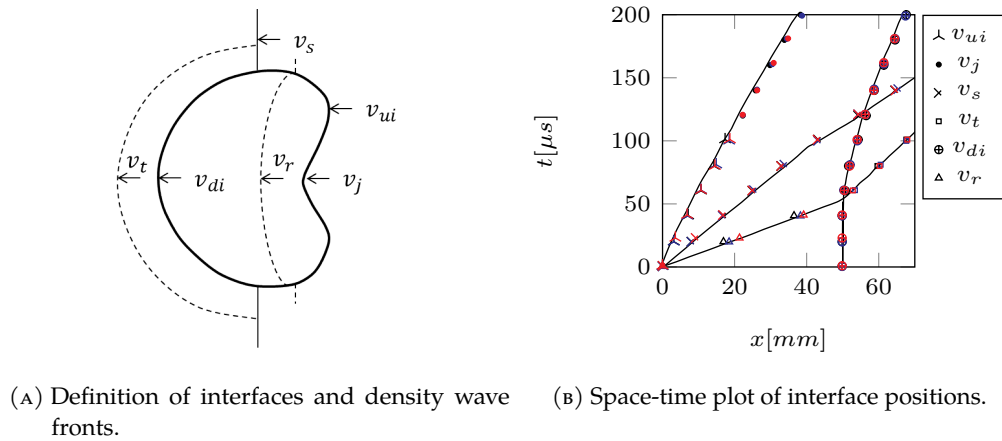


FIGURE 6.14. Shock bubble: definition of interfaces and density wave fronts together with a space time plot of the position of the interfaces and wave fronts. Numerical results (markers) at three grid resolutions: 400x50 ■, 800x100 ■ and 1200x150 ■, compared with Quirk and Karni [221] (solid lines). The maximum Courant number is 0.2.

The velocity magnitudes of the interfaces and the density wave fronts are compared with the experimental results of Haas and Sturtevant [105] and the numerical results of Quirk and Karni [221] and Kreeft and Koren [148] in Table 6.2. Good agreement is found between the results of our method using grid 1200x150 (maximum Courant number 0.2) and the existing results from literature.

	v_s	v_r	v_t	v_{ui}	v_{di}	v_j
Haas and Sturtevant [105]	410	900	393	170	145	230
Quirk and Karni [221]	422	943	377	178	146	227
Kreeft and Koren [148]	419	956	-	176	-	-
Present model 1200x150 CFL = 0.2	417	970	384	184	146	215

TABLE 6.2. Shock bubble: velocity magnitudes (in [m/s]) of interfaces and density wave fronts.

Density profiles at time $t = 1.4 \cdot 10^{-4}$ [s], taken at $y = 89$ [mm] at the top of the domain and at $y = 49.5$ [mm] in the middle of the domain, are shown for grid resolutions 400x150 and 1200x150 and Courant numbers 0.005 and 0.2. Comparing results for the same Courant number, but different spatial grid resolution, and for the same spatial resolution but different Courant numbers, shows that

increasing the spatial grid resolution and reducing the Courant number yield nearly the same effect: the density profile shows more variation and the density wave front is spread out less in space. The increase in grid resolution and the lowering of the Courant number did not significantly affect the position of the density wave front or the interface of the bubble themselves. The fluid interface between helium and air (at v_{di} and v_{ui}) is captured well and smeared out less due to the geometrical reconstruction.

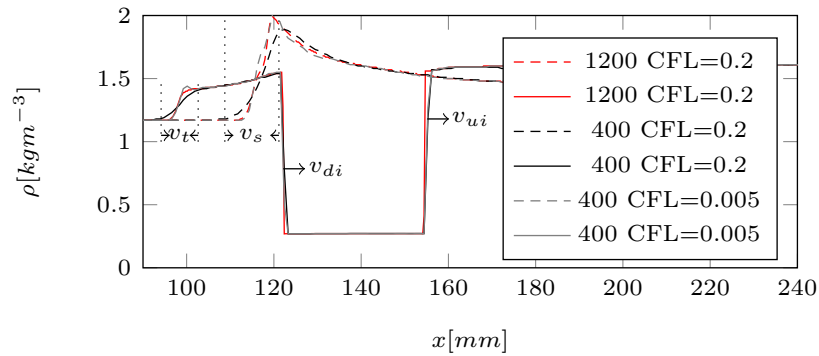


FIGURE 6.15. Shock bubble: density profile ρ at time $1.4 \cdot 10^{-4}$ [s] for different grid resolutions and Courant numbers. Dashed lines for ρ at $y = 89$ [mm]. Solid lines for ρ at $y = 49.5$ [mm].

6.6.4 2D wedge entry in incompressible water

The test case of a 2D wedge impact with incompressible water is considered to evaluate the new speed-of-sound formulation in Eq. (6.28). The setup of the simulation is shown in Fig. 6.16a, containing the dimensions of the domain and the wedge; it is the same setup as the one used in the next section about validation. The angle that the bottom planes of the wedge make with the horizontal, the so-called deadrise angle (α), is 15 [deg]. In the simulation the wedge falls down vertically and impacts with the water. The vertical velocity of the wedge upon impact (V_i) is 7.0 [m/s]. The grid is named for the number of cells that are used to represent the bottom plane of the wedge within the dashed box in Fig. 6.16a, because it is important to resolve the water jets formed in that box with sufficient accuracy. For the simulations described here, a grid resolution of 33×18 in the box is used.

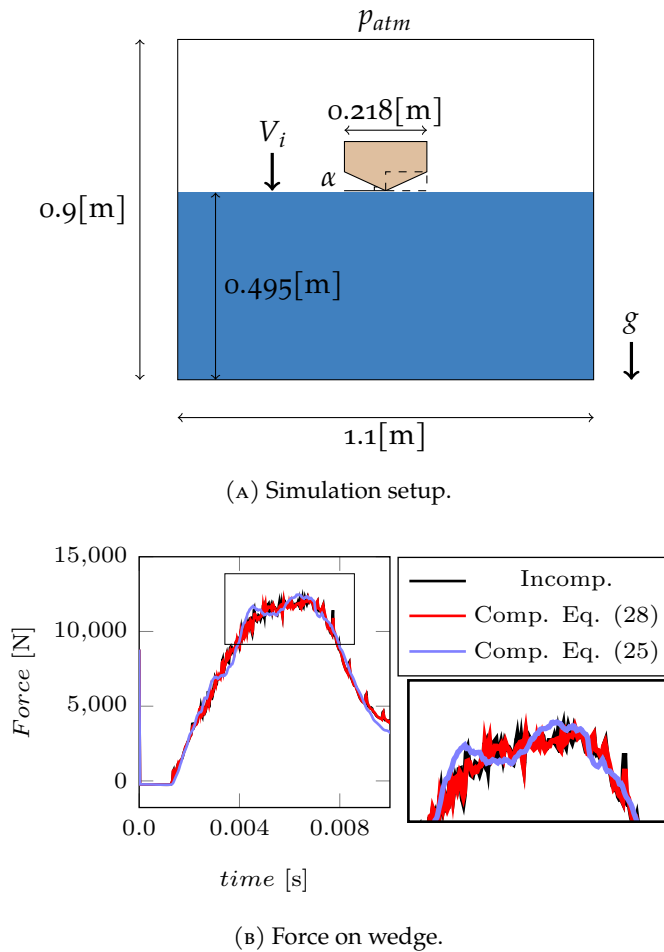


FIGURE 6.16. 2D wedge entry: simulation setup and force on wedge as a function of time. Force from the current method with $\beta_g = 0.0$ and two different formulations for the speed of sound compared with incompressible model from an earlier article [75]. Grid 33×18 used.

Two simulations without aeration, so that $\beta_g = 0.0$, are performed, from which the vertical force on the wedge over time is obtained. Without entrained air in water, the results of these simulations should be close to that of the incompressible method described in Eijk and Wellens [75]. One simulation is performed with an implementation of the traditional mixture speed of sound in Eq. (6.25). The other simulation is performed with an implementation of the new formulation for the speed of sound in Eq. (6.28). Zooming in on the peak of the force in Fig. 6.16b, one finds that the force from the implementation with new speed of sound in Eq. (6.28) is a near-exact match with the force from the incompressible method [75]. The force from the implementation with the traditional mixture speed of sound in Eq. (6.25), shows a low-frequency oscillation. The low-frequency oscillation is the result of a numerical artifact that we call ‘spurious compress-

ibility'. In violent free surface flow, grid cells labelled F can sometimes receive a lower value for the filling ratio C_f than 1. Using Woods' equation, Eq. (6.25), values for $1 - C_f$ are treated the same as aeration, so that a fluid containing an artifact of violent free surface flow can become misrepresented as a compressible fluid. Small values for $1 - C_f$ can already lead to a significant decrease of the speed of sound. The spurious compressibility shows up as force oscillations some moments after the wedge impacts with the water. Eq. (6.28) corrects for the presence of F-labelled cells with values for C_f lower than 1 and therefore does not lead to force oscillations that should not be there.

6.7 2D Wedge impact with aerated water

In order to evaluate the capabilities of the numerical method in terms of fluid-structure interaction with compressible aerated water, it is validated against a new experiment that was performed specifically for this work. Before motivating why it was necessary to conduct a new experiment, first an overview of existing literature about experiments with aerated water is provided.

6.7.1 Brief overview of experiments with aerated water

Experimental data for fluid-structure interaction with aerated water is rare [81, 118, 169–171], with Eroshin et al. [84] being an early account such an experiment. Hong, Wang, and Liu [118], Ma et al. [169], and Mai et al. [170] used a flat plate and Elhimer et al. [81] used 3D cones with different deadrise angles. A general conclusion they made is that the effect of aeration is relevant for designing maritime structures operating in heavy seas. A significant reduction of the impact loads is found compared to impacts with pure water.

For flat plate impacts, Ma et al. [169] found that increasing the level of aeration increases the rise time and fall time of the impact pressure on the plate. They added that with flat plate impacts cavitation likely plays a role. Mai et al. [170], also studying flat plate impacts, motivated that the high-frequency oscillations associated with the compressibility of the medium they found, can have consequences for the fatigue analysis of the structure, but that the standard regulations for taking impact pressures into account may be conservative in the presence of aeration, as these, being based on pure water, specify impact pressures that are too high. Their results are in agreement with the numerical results of Hong, Wang, and Liu [118].

For cone impacts with aerated water, Elhimer et al. [81] found a reduction of the wetted contact surface, a reduction of the impact pressure, and a reduction of the average pressure, compared to cone impacts with pure water. They showed that the edge Mach number (Ma_{edge}) is relevant for indicating the significance of aeration on the peak pressures. The edge Mach number is the ratio of the fluid

expansion velocity along the bottom of the body and the speed of sound of the mixture

$$Ma_{edge} = \frac{V_i}{\tan(\alpha)c_f'} \quad (6.47)$$

where c_f is found from Eq. (6.24) and α is the deadrise angle, that was illustrated in Fig. 6.16. Elhimer et al. [81] concluded that when the edge Mach number (Ma_{edge}) is above 0.05, compressibility has a relevant effect on the impact pressure. When Ma_{edge} is above 0.3, the type of nonlinearity related to that in the equation of state of the air-water mixture is found. In the range $0.05 < Ma_{edge} < 0.3$ the largest changes in impact pressures are found.

6.7.2 Experimental setup

The existing experiments in literature focus on finding the effect of aeration on the impact pressure. While that is certainly our motivation, too, validating the numerical method requires more than only the pressure. Because the speed of sound of the mixture has such a central role in the derivation of the closure model, the experiment for validation was designed to capture not only the pressure upon impact, but also the secondary pressure oscillations as a result of the reflected density waves. The body in the experiment is formed by a wedge, because the numerical method is not suited to capture the phase changes associated with cavitation encountered by Ma et al. [169].

The setup of the experiment consists of three parts: the box containing water, the fall tower and the wedge attached to a guiding mechanism within the fall tower. The fall height from the tip of the wedge to the initial free surface of the water is at most 2.83[m] so that, with friction, a maximum impact speed V_i up to 7.0[m/s] can be achieved. The box and wedge are illustrated in Fig. 6.17, in which α is the deadrise angle. The box is made of 36[mm] thick plywood, with a 30[mm] perspex front, having the overall inner dimensions of in-plane width×height×out-of-plane width = 1100×900×240[mm]. The out-of-plane width of the wedge is 238[mm]. This is somewhat smaller than the box to prevent contact between wedge and box, while minimizing 3D effects due to the gap between wedge and box. The width of the wedge between chines is 218[mm], being five times smaller than the width of the box. The water level in the box is 495[mm] with respect to the bottom of the box.

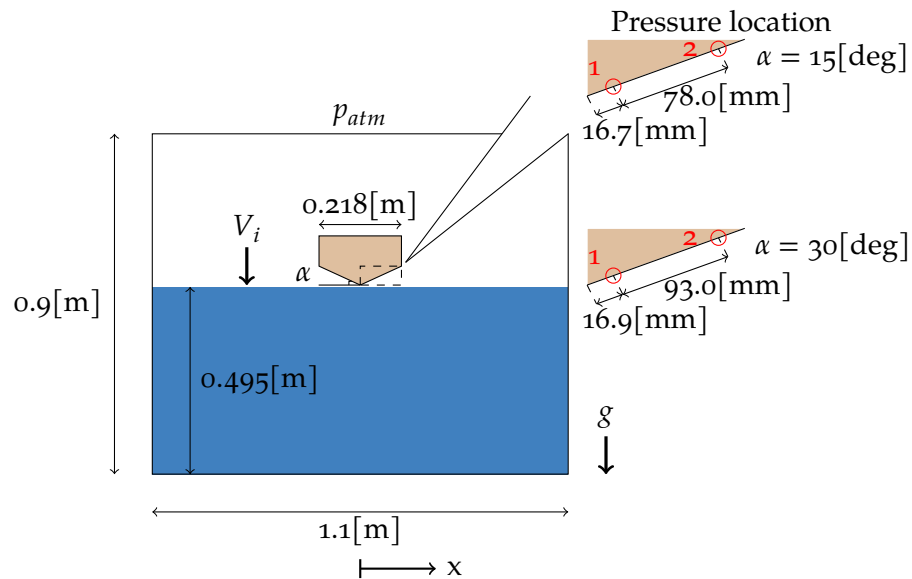


FIGURE 6.17. Setup of wedge impact experiment with aerated water. Dimensions of the experiment are also the dimensions of the numerical domain.

Two wedges are used, each with a mass of $31.78[\text{kg}/\text{m}]$, having different deadrise angles (α). one has a deadrise angle of $15[\text{deg}]$, the other of $30[\text{deg}]$. These deadrise angles are encountered frequently in industry at different cross-sections of high-speed vessels [79]. The side walls of the wedge above the chine are $0.20[\text{m}]$ high. The wedge is equipped with four pressure sensors, positioned along the bottom of the wedge. The positions of the sensors on one side of the wedge are shown in Fig. 6.17 for the two different deadrise angles. The other two pressure sensors are placed symmetrically at the other side of the wedge. The type of pressure sensor is 113B25 ICP of PCB Piezotronics, with a membrane diameter of $5.54[\text{mm}]$. This type measures impact pressures accurately during a short time, after which they are 'loaded' and need to 'discharge'. The pressure sensor closest to the tip of the wedge is called pressure sensor 1, the other, closest to the chine, is called 2. The sensors placed on the other side of the wedge are used as a measure of the variability of the pressure. A sampling frequency of $100[\text{kHz}]$ was used to record the pressure.

Air bubbles in water are created at the bottom of the box. A homogeneous (equal) distribution of air bubbles is approached through the use of sixteen AS23 fresh water air diffusers of Pentair equally distributed along the bottom of the box. The air diffusers create bubbles with varying size in the order of $1[\text{mm}]$ in diameter. The aeration level is measured with the approach of Ma et al. [169] (Eq. 2) using a cylindrical tube that is significantly larger than the size of the bubbles. The time it takes to fill the tube with air versus the rise time of the bubble determines the aeration level. The standard deviation and mean of the aeration levels β_g in

the experiment are shown in Fig. 6.18 for three different locations in the box. The position of the wedge in the box is indicated by the solid black lines near the origin of the horizontal axis. For every location, six aeration measurements are performed and expressed as volume of air over volume of water. The standard deviation of the six aeration measurement increases with increasing level of aeration. It is less than $1 \cdot 10^{-3}$ for the aeration levels approximating 1% by volume, rising to $2.5 \cdot 10^{-3}$ for the aeration levels close to 4% by volume. The variation between locations also increases with increasing level of aeration, being smaller than $3 \cdot 10^{-3}$ for the aeration level close to 1% and rising to more than $1 \cdot 10^{-2}$ for aeration levels of 4%. A homogeneous air-water mixture was not achieved, especially considering the aeration levels near the boundary of the box, but near the position of the wedge homogeneity is approximated reasonably well.

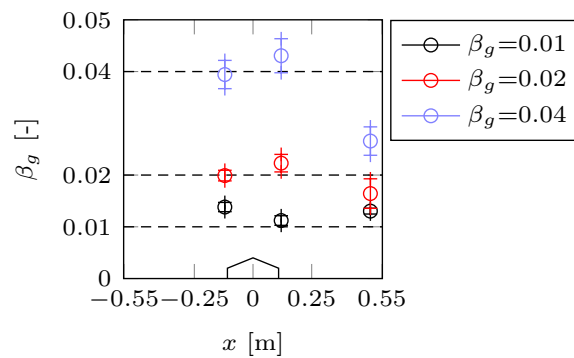


FIGURE 6.18. Aeration measurements represented as air volume over water volume at the free surface for different locations in the box. Position of the wedge is indicated by solid black lines at the bottom of the graph.

The experiment is conducted for combinations of four aeration levels ($\beta_g = 0.0, 0.01, 0.02, 0.04[-]$) and two deadrise angles ($\alpha = 15, 30[\text{deg}]$). The impact velocity of the wedge is kept constant at $V_i = 7[\text{m/s}]$. The combinations are illustrated with white circles in Fig. 6.19, showing the edge Mach number as a function of aeration level and deadrise angle. The maximum edge Mach number is the ratio of the maximum flow velocity along the "edge" of the wedge over the speed of sound. A Ma_{edge} equal to 0.5 is reached. Every test in the experiment is repeated five times and gives 10 data signals as a function time per pressure sensor (recall the symmetrically placed pressure sensors). The 10 data points per time step are used to determine the mean and the standard deviation of the pressure. The expected maximum pressure on the wedge is between 10^4 and $10^7[\text{Pa}]$, so that the density changes in the mixture can be attributed mainly to the air in water [81].

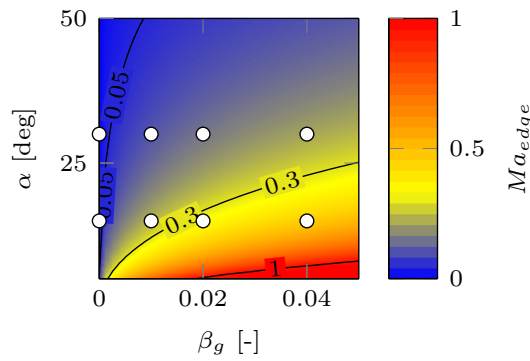


FIGURE 6.19. The edge Mach number (Ma_{edge}) depending on the impact velocity $V_i = 7$ [m/s] and the deadrise angle α of the wedge, and the aeration level β_g for a homogeneous mixture. The experimental tests are represented by \circ .

6.7.3 Numerical setup

The size of the domain in the numerical setup is given by Fig. 6.17. The top boundary of the domain is used to define the atmospheric pressure. The remaining walls are closed and can reflect density waves. The initial height of the bottom of the wedge above the initial waterline h_0 is 10[mm]. The air layer between the wedge and the interface is not expected to affect the loadings as the deadrise angles are too high [79, 318].

The relevant parameters for the fluids and wedge are given in Tab. 6.3a. The degrees of freedom of the wedge are limited to allow only vertical motion. The end time of the simulations is 0.10[s] so that the entire slamming stage of the interaction between wedge and aerated water is captured. A maximum Courant number of 0.2 is used. The impact velocity of the wedge in the simulations is $V_i = 7.0$ [m/s]. Simulations are performed for the same cases in Fig. 6.19, represented by the white dots, for which tests in the experiment were performed. The relevant parameters are also summarized in Tab. 6.3b. These cases cover the range of $0.05 < Ma_{edge} < 0.5$.

Parameter	Value
ρ_l [kg/m ³]	999.00
ρ_a [kg/m ³]	1.22
p_{atm} [Pa]	$1.00 \cdot 10^5$
h_0 [m]	0.01

(A) Initial conditions of fluids and wedge.

Variable	Values			
α [deg]	15	30		
β_g [-]	0.0	0.01	0.02	0.04

(B) Variables considered in the numerical simulations.

TABLE 6.3. Simulation parameters



A grid convergence test for the simulated pressure is conducted with $\alpha = 15[\text{deg}]$ and $\beta_g = 0.0[-]$. The dashed box in Fig. 6.17 is used as a reference for the grid resolution. The reported number of cells therefore is an indication of the number of cells in horizontal and vertical direction used to capture the slope of the bottom of the wedge. The simulation results of the grid convergence test are shown in Fig. 6.20. The figure shows the pressure obtained at the location of pressure sensor 1 (closest to the tip of the wedge) as solid lines, and the pressure at the location of pressure sensor 2 as dashed lines. The value of the pressure at any time is the average taken over the area of the sensor with diameter 5.54[mm].

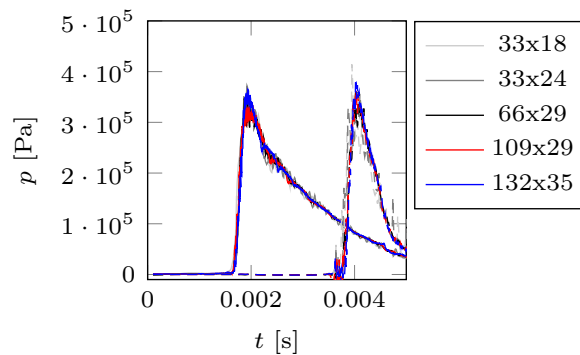


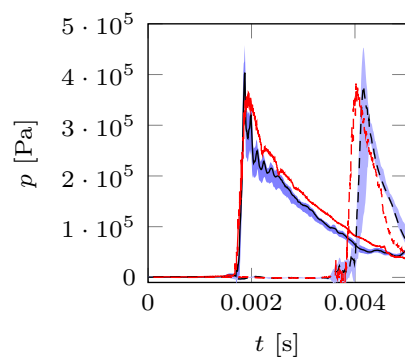
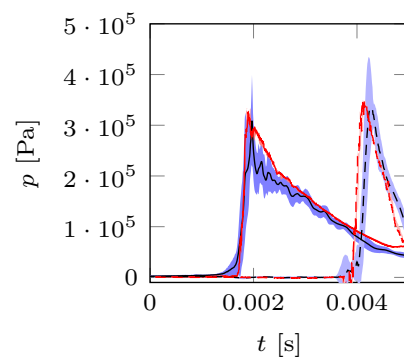
FIGURE 6.20. Simulation results for grid convergence test, using $\alpha = 15[\text{deg}]$ and $\beta_g = 0.0[-]$. Pressure sensor 1 represented by solid lines. Pressure sensor 2 represented by the dashed lines. Pressure is the average taken over the area of the sensor with diameter 5.54[mm].

The discussion of convergence will focus on pressure sensor 1; the results obtained for pressure sensor two follow a similar trend. One measure of grid convergence is to consider the pressure integrated over time up to 0.005[s], representing an equivalent of impulse. The pressure impulse converges rapidly. The pressure impulse on the finest grid of 135x35 has a value of 487.0[Pa·s]. The difference in pressure impulse with the coarsest grid was 1% of that value; a difference of 0.2% was obtained for 66x29; and a difference of 0.04% for 109x29. Another measure of grid convergence is to consider the maximum pressure during impact. The maximum pressure on the finest grid of 132x35 is $3.7 \cdot 10^5$. The difference in maximum pressure with the coarsest grid of 33x18 is 6.6% of that value. For grid 109x29 the difference in maximum pressure is 2.0% of that value. Grid convergence in terms of the maximum impact pressure therefore has not been obtained. As the convergence is not monotonous, we do not expect that formal grid convergence of the maximum pressure can be obtained. This needs to be accounted for in our interpretation of the comparison between experiment and simulations. All simulations from here on are performed with grid 109x29.

6.7.4 Comparison simulations and experiment: maximum pressures

Fig. 6.21 shows the pressures obtained from the numerical simulations with grid 109×29 together with the pressures obtained from the tests in the experiment. The atmospheric pressure was subtracted from all results. Solid blue lines are for pressure sensor 1 and dashed blue lines are for pressure sensor 2. The blue lines for the pressure from the experiment are the average of ten signals. A band is formed along the lines representing one standard deviation above and below the average. The lines from the experiment show that discharging the pressure sensors after impact leads to an increased bandwidth around the average pressure and increased uncertainty.

Red lines in Fig. 6.21 represent the pressures from the simulations, solid lines for pressure sensor 1 and dashed lines for pressure sensor 2. The lines are the average pressures obtained from two simulations at each aeration level β_g with the minimum and maximum value measured at that level on either side of the wedge, see Fig. 6.18. The following simulations were performed: β_g equals 1.0 and 1.5% for the aeration level of 1.0%; β_g equals 1.9 and 2.4% for a level of 2.0%; β_g equals 3.7 and 4.6% for the aeration level of 4.0%. The uncertainty found from the grid convergence test is not included in Fig. 6.21.

(A) $\beta_g = 0.0[-]$ and $\alpha = 15[\text{deg}]$.(B) $\beta_g = 0.01[-]$ and $\alpha = 15[\text{deg}]$.

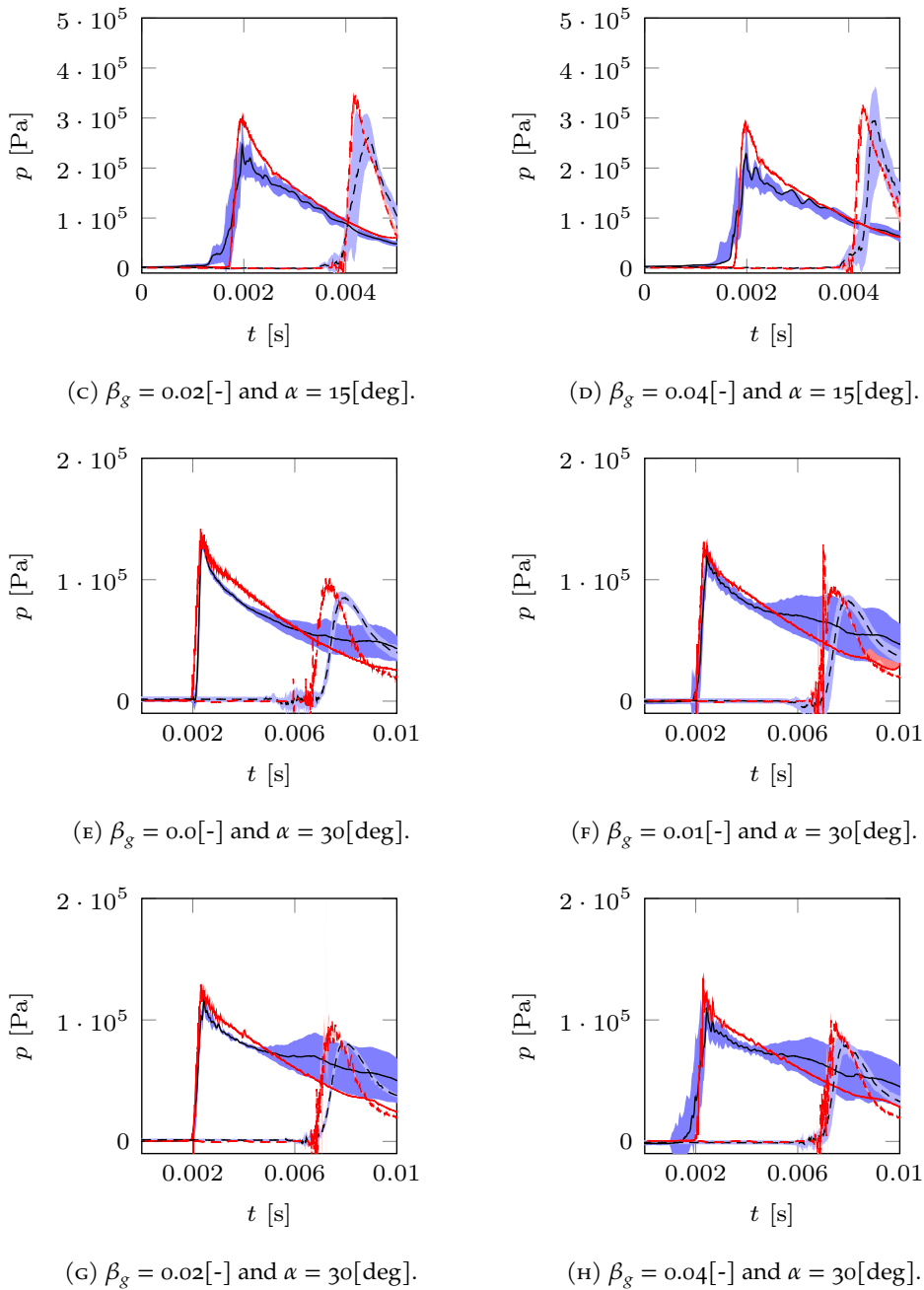


FIGURE 6.21. Impact pressures: numerical simulation results (—) with experimental results (---) for two pressure positions. Pressure sensor 1 is represented by solid lines (—). Pressure sensor 2 is represented by dashed lines (---). Band for the experiments composed of one standard deviation below and one above average pressure. Grid 109×29 was used for the simulations. Simulated pressures are the average of two simulations with the minimum and maximum value for aeration at that level. Band around numerical results formed by minimum and maximum. Uncertainty of grid convergence not included in graphs.

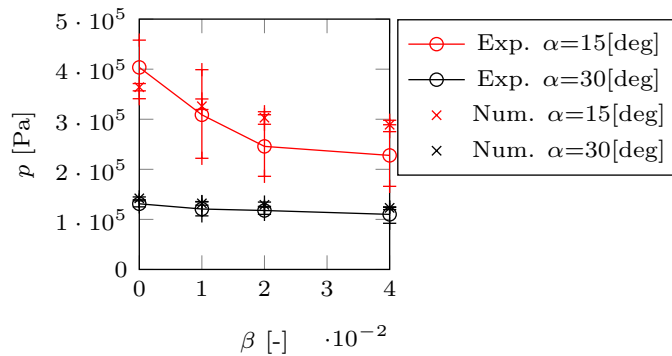
The simulated pressures show good visual agreement with the measured pressures for both deadrise angles and for all aeration levels. The pressures obtained during impacts with the 30[deg] deadrise angle wedge are hardly affected by the level of aeration. This conclusion is consistent between the simulation results and the experimental results. For the wedge with a deadrise angle of 15[deg], the maximum pressure during impact goes down with increasing level of aeration, both in the simulations and in the experiments. There are a number of differences between simulation results and measurements for this wedge. For pressure sensor 2, the pressure in the simulations rises before the pressure in the measurements rises, as if the water reaches pressure sensor 2 earlier in the simulations than it does in the experiments. The most likely explanation is that the jets of water formed by the wedge displacing water are fairly thin, and therefore underresolved in the simulations.

Although the maximum pressure in the measurements can be higher than the pressure in the simulations for some cases, the pressure in the simulations near the maximum pressure is consistently higher. We observed that before for simulations and experiments without aeration, and then it seemed to be due to 3D effects caused by the gaps between wedge and box at both out-of-plane endpoints of the wedge. These effects seem to decrease the pressures. That is, however, not the only explanation for the difference in pressure between simulations and experiment in this study, because the difference in pressure increases with increasing level of aeration. It seems that the aerated water in the experiments with higher levels of aeration than 1% is more compressible than what is modelled in the simulations.

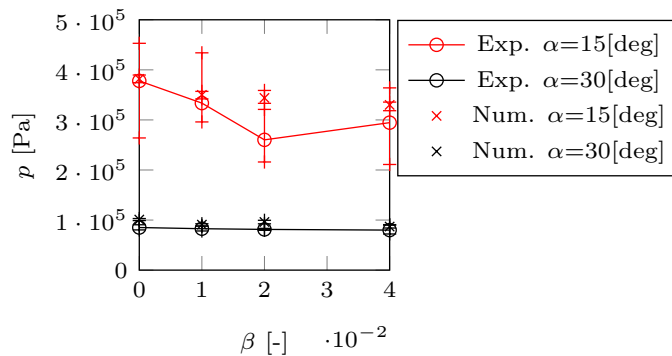
A final difference that is apparent, is that pressure sensor 1 (see Fig. 6.17) in the experiment registers a pressure rise before a pressure is registered in the numerical simulations. That difference in pressure between simulations and experiment before the maximum pressure is attained, becomes larger with increasing levels of aeration. Similar results were found by Elhimer et al. [81] and Ma et al. [168] who explained the difference by a layer of froth at the free water surface that becomes larger with higher levels of aeration. The explanation seems plausible and consistent with what can be observed from Fig. 6.21, but at present we lack the means to investigate this further.

The pressure maxima in simulations and experiment, with their respective bandwidths, are plotted as a function of level of aeration in Fig. 6.22. An uncertainty of 2%, as a result of the simulation results not being completely converged for maximum pressures, are included in the graph. Fig. 6.22 confirms that the level of aeration hardly affects the maximum impact pressures for the wedge with a deadrise angle of 30[deg]. The pressure maxima from the simulations are within the uncertainty band of the experiments, for both wedges at both pressure sensor

locations. For the wedge with a deadrise angle of 15[deg], the effect of aeration on the maximum impact pressure is significant. The trends for increasing levels of aeration between simulations and experiment are different. The aerated water in the experiment seems to become more compressible with increasing level of aeration than the modelled air-water mixture in the simulations. This could potentially have to do with the fact that ratio of air to water for higher levels of aeration is such that bubbles start to influence each other and that the assumption of homogeneity is not valid anymore.



(A) Pressure sensor 1.



(B) Pressure sensor 2.

FIGURE 6.22. Maximum impact pressures for different levels of aeration. Simulation results are compared with experimental result. The band around the experimental pressure maxima is formed by one standard deviation. The band around the simulated pressures is formed by the uncertainty due to the grid size and the variation in measured aeration values near each aeration level.

6.7.5 Comparison simulations and experiment: post-impact pressure oscillations and frequency analysis

The wedge impacting with the aerated water generates density waves due to the compressibility of the air-water mixture. The density wave reflect off of domain

boundaries and propagate back to the wedge. The back-and-forth propagation of the density waves causes pressure oscillations on the wedge. A time sequence of the simulated pressure after impact for the wedge with $\alpha = 15[\text{deg}]$ and for aerated water with $\beta_g = 0.04[-]$ is shown in Fig. 6.23. Grid 109×29 was used for the simulation. The density waves become apparent by their front, which shows as a barrier between regions with higher and lower pressure that propagates through the domain.

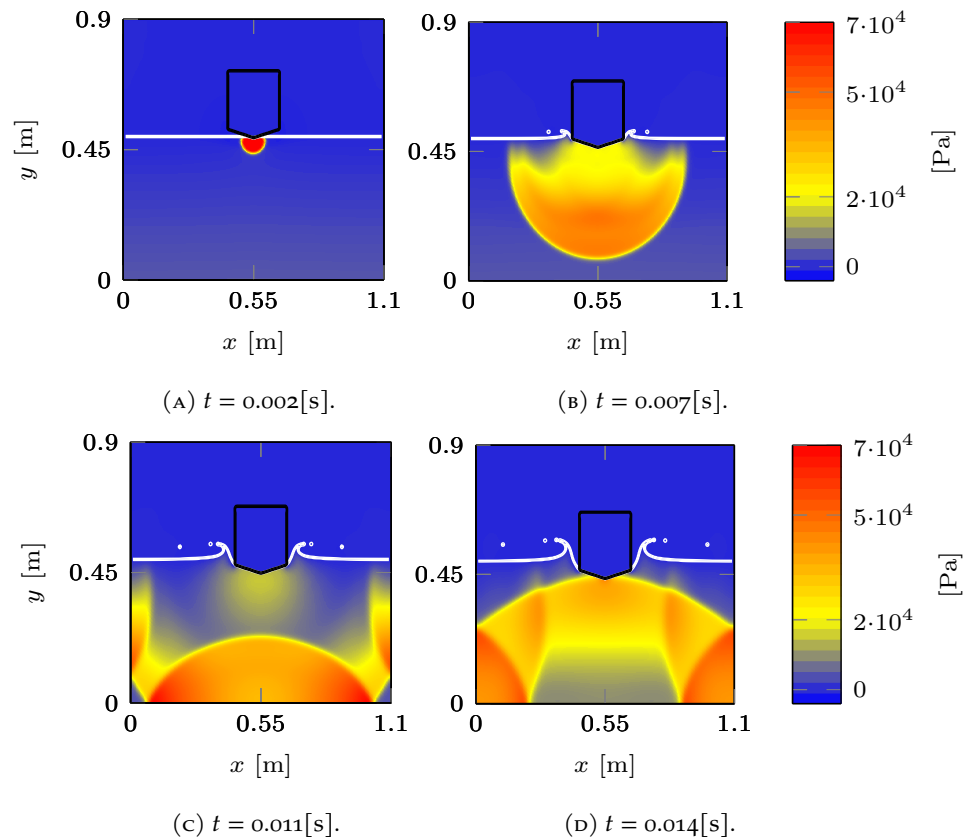


FIGURE 6.23. Time sequence of simulated pressure fields for wedge impact $\alpha = 15[\text{deg}]$ and $\beta_g = 0.04[-]$ at different time instances. From the sequence it becomes apparent that density waves are formed that propagate through the domain. The numerical grid was 109×29 .

In Fig. 6.24, the simulated pressure over time along the chine of the wedge with a deadrise angle of $\alpha = 15[\text{deg}]$ is shown for four levels of aeration. Grid 109×29 was used for the simulations. In the simulations, an increase in aeration level results in an increase in amplitude of the post-impact pressure oscillations.

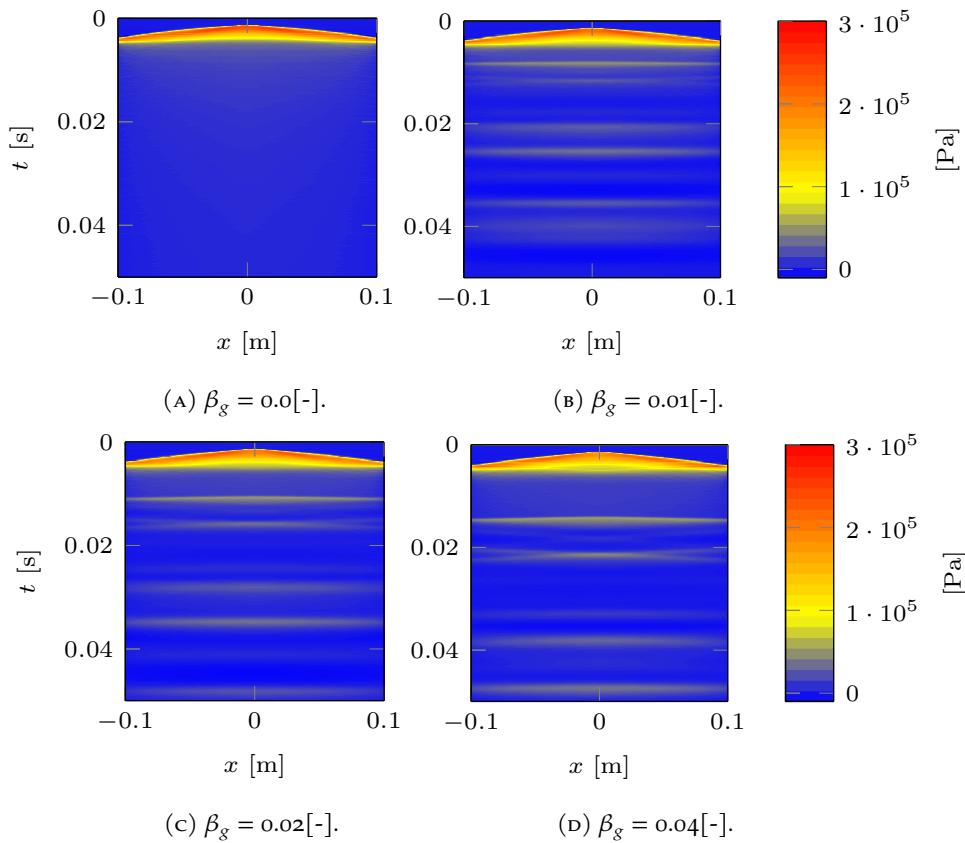


FIGURE 6.24. Simulated pressure along bottom of wedge ($\alpha = 15[\text{deg}]$) over time for different levels of aeration. Interaction of reflected density waves pressure oscillations on the wedge. Numerical grid used is 109×29 .

A Fourier analysis of the signal in Fig. 6.24 at the (inner positioned) pressure sensor 1 is illustrated in Fig. 6.25. For the aeration levels $\beta_g = 0.01, 0.02, 0.04[-]$ a speed of sound (c_f) of around 109, 77, 55[m/s] is found. The domain frequency related to the position of the bottom or the side walls of the domain can be calculated with $c_f/(2h_w)$ (where $h_w = 0.495[\text{m}]$). The time range the pressure signals are analyzed is from 0.002[s] after maximum pressure to $h_w/c_f[\text{s}]$ such that the density wave can be experienced two times after the peak pressure. The pressure oscillations are obtained by filtering the pressure signal with a high pass filter up to 40[Hz] for all aeration levels, not to interfere with the domain frequency and remove the “non-oscillating” signal. The same time signal for all cases, numerical and experimental, is used for equal comparison. A Fourier analysis of the obtained pressure oscillation signals is illustrated in Fig. 6.25. The magnitude is normalized by the maximum mean pressure peak found in the experiment for pressure sensor 1 in Fig. 6.22 to show the relevance of the post-impact loadings.

For aeration level $\beta_g = 0.0$ in Fig. 6.25a, a frequency in the experimental results is found of around 450[Hz] which could correspond with some air left in the water ($\beta_g = 0.0005$). The experimental frequency is also found for other aeration levels meaning that this is not the case and is related to the vibration of the setup. For this reason, we only look to lower frequency effects (< 400 [Hz]).

The experimental and numerical results show that an increase in aeration level resulted in a longer continuation of the pressure oscillations with a lower frequency. The domain frequency for the bottom, given by the straight dashed lines, and the sidewalls, given by the straight dotted lines, and their higher modes do fit with the governing frequencies. An increase in the aeration level results in a shift in frequencies. The shift in frequencies for increasing aeration is conform to the mixture speed of sound formulation in Eq. (6.24). The governing frequencies agree fairly with the double frequencies of the speed of sound ($c_f/(2h_w)$). The governing frequencies are slightly higher than the ones found with the dashed lines because of the shortened distance h_w due to the penetration of the wedge. The (relative) magnitude of the pressure oscillations increases with the aeration level up to 20% numerically and up to 4% experimentally which is in agreement with the results found in Fig. 6.23.

The difference between the experiment and numerical model, besides mentioned above in Sec. 6.7.4, need some explanation. Low aeration levels, like for the maximum pressure, are numerically better predicted. Higher aeration levels are conservatively predicted by the numerical model and shows a difference in physics accounting for. The density waves are more damped experimentally than numerically related to the homogeneous assumption. In the experiment the mixture is due to the bubbles not fully homogeneous leading to diffusion, and the bubbles do interact and can lead to reflection. The numerical homogeneous assumption results in a prediction of the shock front (a sharp jump in pressure) which is in the experiment not found. This is part of 3D effects, where 2D in essence result in higher loads [79]. The model does not account for air pocket fragmentation, bubbles are from nature 3D, which also could prevent damping.

The assumption made in this work for not correctly modeling the discontinuity shows therefore no problems for predicting impacts like the presented wedge impact. The homogeneous assumption is correct for low aeration levels, in this case up to 1%. Besides the agreement with the domain frequencies, a fair agreement for the governing frequencies is found between the experiment and numerical results.

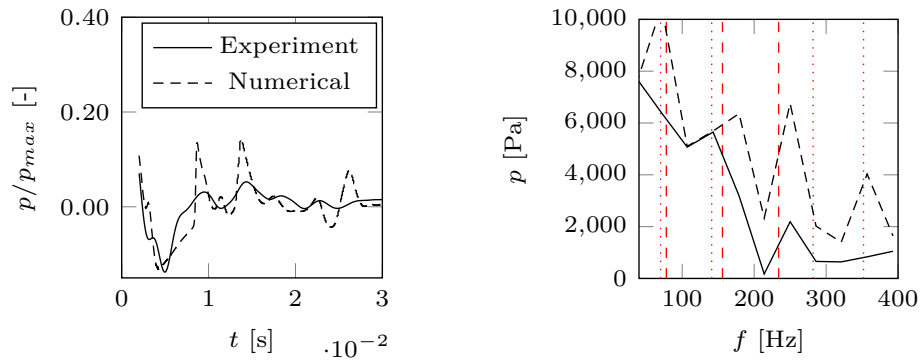
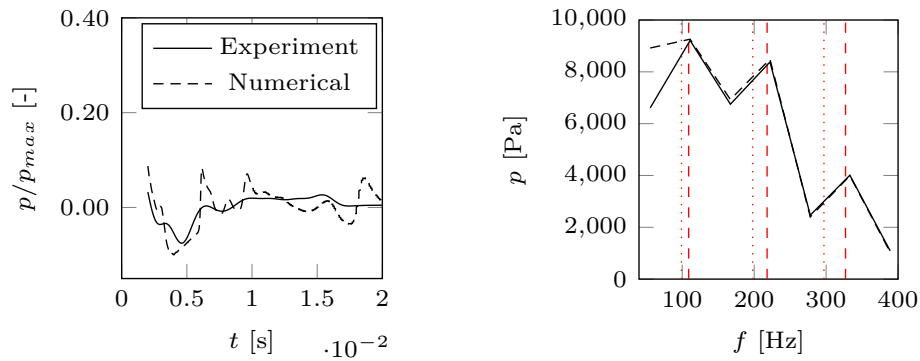
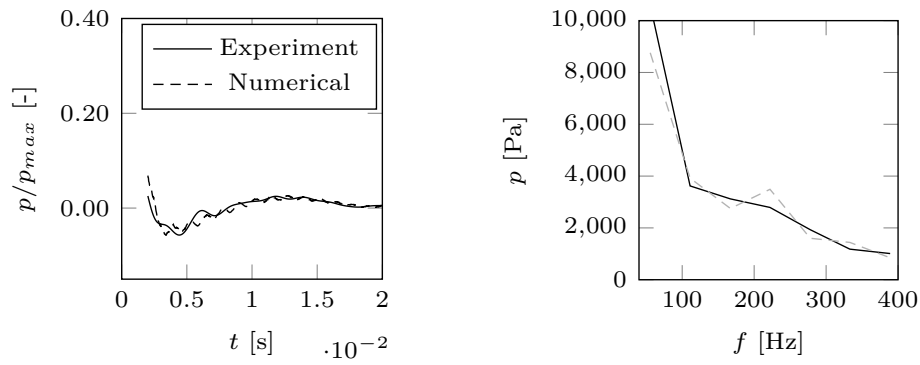
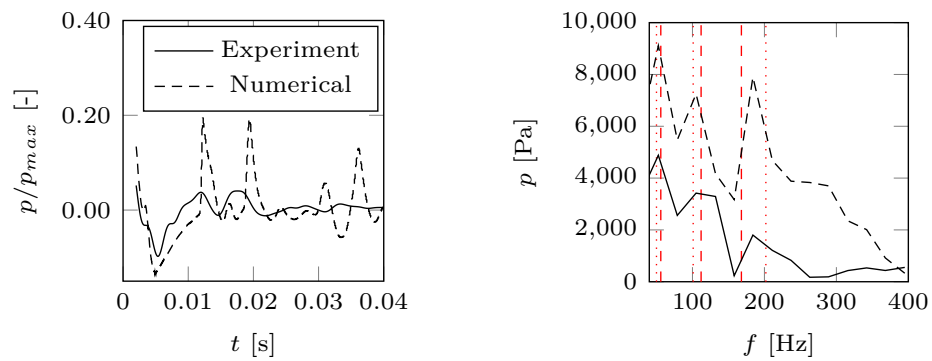


FIGURE 6.25. Signals found after subtraction and Fourier transform of the post-impact loadings for $\alpha = 15[\text{deg}]$. Signal used for analysis is $0.002[s]$ after impact. The signal is high-pass filtered ($40[\text{Hz}]$) resulting in the pressure oscillation caused by density waves. The numerical grid used is 109×29 . The red dashed lines indicate the domain frequencies from the bottom wall (longitudinal) and the red dotted lines from the side walls (transverse).



(G) Signal $\beta_g = 0.04[-]$ until $t = 0.04[s]$. (H) Fourier $\beta_g = 0.04[-]$ until $t = 0.04[s]$. Longitudinal (---) and transverse (····) mode.

FIGURE 6.25. Signals found after subtraction and Fourier transform of the post-impact loadings for $\alpha = 15[\text{deg}]$. Signal used for analysis is $0.002[s]$ after impact. The signal is high-pass filtered ($40[\text{Hz}]$) resulting in the pressure oscillation caused by density waves. The numerical grid used is 109×29 . The red dashed lines indicate the domain frequencies from the bottom wall (longitudinal) and the red dotted lines from the side walls (transverse).

6.8 Conclusion

A new compressible pressure-based multiphase model is presented for modeling the interaction of homogeneous aerated water with moving bodies. It is efficient because the operation that requires most computational effort is solving the Poisson problem for the pressure with a number of unknowns equal to the number of grid cells in the domain. The model can deal with high-density ratio compressible flows using a non-conservative formulation for transport of the interface. The unphysical increase of compressibility, caused by a non-continuous representation of the interface leading to artificial air entrainment, is prevented by means of an additional volume fraction field and a new formulation for the speed of sound.

The numerical results are in good agreement with solutions for traditional compressible multiphase flow cases: an oscillating water piston, a shock tube for separated and dispersed phases, and a cylindrical helium shock bubble. The test cases demonstrate the method's ability to handle contact discontinuities and rarefactions. Geometrical reconstruction of the fluid-fluid and fluid-body interfaces kept these interface sharp. Issues with wiggles around the contact discontinuity were not encountered, because the Courant limit of our formulation depends on the fluid velocities and not on the speed of the density waves. Even with coarse grid resolutions, the pressure levels in propagating density waves were well predicted, but the discontinuity between pressure levels was diffused over a couple of grid cells.

An 2D experimental setup for wedge impacts with water was converted specifically for this work to validate the numerical method for the interaction between aerated water and moving bodies in terms of the pressure. Air diffusion stones were placed on the bottom of a box with water to generate aeration levels up to four percent (by volume). We considered Mach numbers of up to 0.5, based on the maximum flow velocity of the jets and the mixture speed of sound. The numerical and experimental results are in good visual agreement for lower aeration levels, both showing a similar maximum pressure and development of the pressure over time. For a deadrise angle of the wedge of 15 degrees the differences at higher aeration levels are larger. For the higher aeration levels, the maximum pressures in the experiment during impact were lower than in the simulations. We believe this can be due to inhomogeneity of the mixture in the experiment at higher aeration levels.

The post-impact pressure oscillations due to density waves reflecting from the domain boundaries had higher amplitudes in the simulations than in the experiment. The post-impact oscillation amplitudes become larger when the aeration level, up to 4% of the maximum impact pressure in the experiment and up to 20% in the simulations. The governing frequencies of the post-impact oscillations were in good agreement. The speed of sound in the water-air mixture, therefore, is represented well. It is a matter of future study which parts of numerical method influence the amplitudes of the density waves after impact, so that the method becomes a better representation of the experiment. The assumption of homogeneity looks applicable for aeration levels up to 1%.



Part III

NUMERICAL IMPROVEMENTS FOR INTERFACE MODELING OF HIGH-DENSITY RATIO FLOWS

This part concerns the numerical improvements with respect to modeling the interfaces (Ch. 7), experienced for simulations involved with aeration using the fully compressible multiphase model in Ch. 6. A decrease of discontinuity in the free surface decreases the amount of artificial non-reconstructed air in water and increases accuracy of tracking. A mentioned inconsistency in the transport due to a reconstruction step needs to be prevented.

Photo: [181]

7

AN EFFICIENT 2D BILINEAR INTERFACE RECONSTRUCTION ALGORITHM AND CONSISTENT MULTIDIMENSIONAL UNSPLIT ADVECTION SCHEME FOR ACCURATE TRACKING OF HIGHLY-CURVED INTERFACIAL STRUCTURES ON UNIFORM GRIDS

This chapter is reproduced from [76] :

M. van der Eijk and P. R. Wellens. “An 2D efficient bilinear interface reconstruction algorithm and consistent multidimensional unsplit advection scheme for accurate tracking of highly-curved interfacial structures on uniform grids.” *Journal of Computational Physics* (nd)

Abstract

A new bilinear interface reconstruction algorithm (BLIC) is presented to capture highly-curved interfaces more accurately on structured grids without a significant increase in computational costs compared to the standard piecewise linear interface calculation (PLIC) methods. The new reconstruction algorithm uses the initial PLIC segment and improves continuity of the interface using an averaging method. A curvature-weighted method improves the repositioning of the linear segments.

A new unsplit donating quadrant advection (DQA) scheme is introduced that is conservative and can create consistency with the momentum flux for two-phase flow models with a staggered MAC arrangement of variables within a grid cell. The consistent discretization of the fluxes prevents spurious interface velocities, negative densities, and instabilities. Standard 2D test cases and benchmarks demonstrate the performance of the BLIC and the DQA scheme, showing high accuracy and low costs compared to other available methods.

7.1 Introduction

7.1.1 Motivation and Volume-of-Fluid method

Modeling an interface between two separated fluid structures is a general application in industry. An application example for interface modeling is breaking water waves. Breaking wave impacts can enforce high peak pressures on marine structures. The forces are difficult to predict due to the complex free surface configuration of a breaking wave. Analytical expressions, assumptions, and empirical relations are currently used for the prediction of these forces which do not account for all their physical variability, hence the need for accurate free surface resolving numerical methods.

Sophisticated low-cost numerical two-phase flow models would decrease the uncertainty in determining the acting forces on marine structures. These models can also be used for a better understanding of the physics. This work proposes two new low-cost algorithms that improve the accuracy of modeling an interfacial flow compared to state-of-the-art approaches: an interface reconstruction algorithm and a stable interface advection scheme, both for use in numerical two-phase flow models.

There are multiple ways of interface modeling available for a two-phase flow model. One type of categorization is that between interface-capturing and interface-tracking techniques. The interface-tracking approach is a technique that explicitly transports Lagrangian markers surrounding an interface [216]. Disadvantages of such an approach are the difficulty of handling arbitrary changes of the topology and complex operations like the merging and breakup of interfaces [234]. In this work, we consider interface-capturing. Many interface-capturing techniques exist, e.g. Volume-of-Fluid (VOF) methods using a discrete volume fraction field C_f having a value between 0 and 1 to identify the position of the interface, and level-set methods using the signed distance to the interface.

The level-set method is easily differentiable, but often not fully mass conserving without special measures [198, 253]. This work focuses on a VOF method that enforces strict volume conservation. A VOF method [115] uses a color function $f(\mathbf{x}, t)$ as an indicator of the material present at a defined position. The advection equation is

$$\frac{Df}{Dt} = \frac{\partial f}{\partial t} + (\mathbf{u} \cdot \nabla)f = 0, \quad (7.1)$$

where \mathbf{u} is the interface velocity. The interface motion is approximated on a numerical grid of discrete cells covering the physical domain at hand. Cells are control volumes for governing equations like Eq. (7.1). In the discrete representation of Eq. (7.1), volume fraction field C_f is the average of the continuous color

function over a given cell.

A VOF method for capturing the interface consists of two parts: the *geometrical interface reconstruction* and *fluid advection*. Geometrical interface reconstruction is required for finding the position of the interface from the color function. Fluid advection works by determining the donating regions and the fluxes. The donating region is the volume that is transported through the cell face while the flux is the quantity of the captured fluid going through the cell face. Our focus is on geometrical reconstruction using VOF although algebraic reconstruction [243, 302] or no reconstruction with compressive terms would also have been options when our interest would have been on only the two phases of fluid. There are faster methods than geometric reconstruction, using explicit analytic formulas (a Moment of Fluid method [182]). Algebraic reconstruction requires less complex coding and computational costs than geometrical reconstruction, but may have lower accuracy for similar grid resolutions. With this work, however, we aim to resolve challenges with two-phase flow modelling especially when an object is present, challenges that were encountered in our method [80] and in others. The implementation of the new schemes required to address the challenges is investigated in 2D on structured grids for two-phases. A reflection regarding their implementation in 3D is formulated.

7.1.2 Brief literature overview of geometrical interface reconstruction

Early algorithms to predict the interface orientation are the piecewise linear approximation [54], a stair case approximation [115], and simple line segments aligned with one of the grid axes (SLIC) [194]. These algorithms have a disadvantage that they can not keep fluid structures together due to the discontinuity in the interface from cell to cell; diffusion of the interface results in unphysical disconnecting droplets.

The Piecewise Line Interface Calculation (PLIC) method was an improvement over SLIC because it uses a linear function instead of a constant function of the spatial coordinates for determining the interface position in a grid cell. Even though the PLIC method still suffers from interface discontinuity at the faces of a grid cell, the PLIC method is often used to good effect. Many methods are available for determining the interface orientation, e.g. Parker and Youngs' method [202], (efficient) least square interface reconstruction (ELVIRA) [210], least-square gradient [226], height function scheme (Centered Columns) [210], Mixed Youngs-Centered (MYC) implementation [6], Centroid-Vertex Triangle-Normal Averaging (CVTNA) [160], piecewise continuous linear interface calculation (PCLIC) [271], and linear or quadratic fitting [235].

After the introduction of the PLIC method, other methods with higher-order functions in the spatial coordinates for the reconstruction were introduced. Price [217] proposed a parabolic reconstruction method (PPIC) based on a second-order equation for the interface segment. Similarly, Renardy and Renardy [223] presented a three-dimensional parabolic approach called PROST. Both methods showed an increase in accuracy but also in computational costs caused by iterative steps. The discussed parabolic reconstruction methods still display discontinuities in the interface. A reconstruction method that aims to reduce the discontinuity between the material interfaces is Patterned Interface Reconstruction (PIR) [186] using planar interfaces. This method is second-order accurate but does not fully satisfy continuity.

Further developed methods enforced the continuity of the interface. Sometimes even equality of the line segments' first derivative on either side of a cell faces is satisfied. The following references in this paragraph all found that a continuous representation of the interface reduces the diffusivity of the interface. Reconstruction methods based on cubic splines of Ginzburg and Wittum [100] and López et al. [163] (SIR) resulted in continuity and improved estimation of the curvature. However, the interfaces are wavy due to the non-locality of errors. Diwakar, Das, and Sundararajan [65] proposed the Quadratic Spline based Interface (QUASI) reconstruction algorithm satisfying the continuity and first derivative constraint. Although the QUASI method showed improved accuracy, the computational costs are an order higher than the standard low-order reconstruction methods. The noniterative PQLIC method [271] using quadratic lines has improved accuracy but, again, a significant increase in computational costs. Furthermore, the PQLIC method is not fully conservative. Another method worth mentioning is the piecewise circular arc interface calculation (PCIC) method [172] that makes use of a correction such that the interface is continuous. Other recently published methods provide higher-convergence rates but do not tackle topological changes of the interface like the methods discussed above [31, 313].

The reconstruction methods using higher-order functions are accompanied by an increase in the difficulty of flux calculations, computational costs, and sometimes additional computational (iterative) steps. For increasing the accuracy of representing an arbitrary (highly-curved) fluid structure like a breaking wave with small flow features, the accuracy and sharpness improvement of the interface does not always outweigh the increase in computational costs. An example of such a highly-curved fluid structure is illustrated in Fig. 7.1.

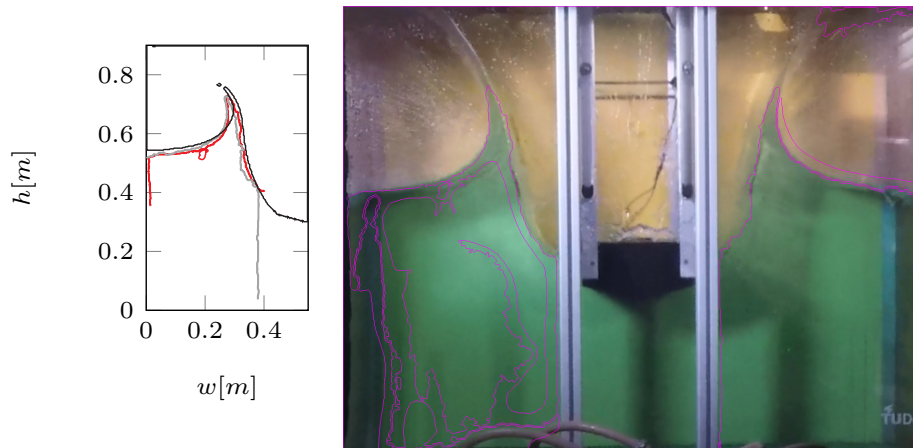


FIGURE 7.1. Comparison free surface experimental & numerical data of a 2D wedge entry representing a section of a marine structure [78]; — experiment left side, — experiment right side, — numerical result at 0.092[s]. The ‘h’ and ‘w’ indicate the height and width position, respectively. The impact speed is up to 7[m/s] for a wedge with with a deadrise angle of 15[deg] and a width of 0.218[m].

Our new reconstruction algorithm aims to improve the accuracy of reconstructing highly-curved interfaces without a significant increase in computational costs compared to a PLIC algorithm using the Volume of Fluid method. The algorithm should be robust for an accurate interface reconstruction; the implementation needs to be straightforward. An iterative scheme is avoided such that no thresholds are needed. Compared to a PLIC algorithm, the presented scheme should reconstruct the interface with higher accuracy. We call the new algorithm the BiLinear Interface Calculation (BLIC) method. It is discussed in Sec. 7.2.

7.1.3 Brief literature overview of fluid advection schemes

The second part of a VOF method is fluid advection. Fluid advection geometrically estimates the fluid fluxes through the faces of a grid cell as a means of transporting the interface. The donating region and the corresponding reconstructed interface determine the size of the fluid flux. A distinction between two kinds of fluid advection schemes is made: an operator-splitting advection scheme and an unsplit advection scheme.

The operator-splitting schemes are characterized by the ease of determining the donating region and by how many calculation steps are required for the final fluid flux. These calculation steps can be split into two parts; determining the fluid flux in one direction and intermediate geometrical interface reconstructions. The advantage of a direction-split scheme is that it is straightforward to implement and robust. However, they show numerical diffusion and geometrical splitting errors that distort the interface [210]. The Conservative Operator Splitting for Multidimensions with Inherent Constancy (COSMIC) scheme [155] tries

to minimize these errors and is used for comparison in this work with unsplit advection schemes. The choice for COSMIC as a reference is made because it was applied in our research field a number of times before [74, 80]. The focus of this work is on unsplit advection schemes.

The second kind of fluid advection algorithm, unsplit advection schemes, prevents geometrical errors and the intermediate reconstruction step(s) by fluxing at once, sometimes in multiple directions, based on a polygon forming the donating region. The polygon is a plane figure described by a finite number of line segments resulting in a closed shape for every cell face. The polygon represents the donating region used for determining the flux. Polygon reconstruction is based on the velocity magnitude at the cell face and the surrounding velocity field.

The majority of unsplit advection schemes discussed here are for structured grids, but it is worth mentioning two recently proposed unsplit advection schemes for unstructured grids without going into more detail: a new triangulation algorithm with a modified Swartz method (UFVFC-Swartz) that shows high accuracy on unstructured grids [175], and a blended high-resolution scheme described as simple and efficient [141].

Many (multidimensional) unsplit advection schemes for structured grids are available, but not all advection schemes are without problems. The problems are characterized by Comminal, Spangenberg, and Hattel [47]: overlapping of donating regions (non-conservative), gaps between the donating regions (diffusion of interface), and non-conforming donating regions (undershoot or overshoot because the edges of the adjacent donating regions do not have the same length).

Early unsplit advection schemes were introduced by Rider and Kothe [226], Pilliod Jr. and Puckett [210] and Puckett et al. [219], and Harvie and Fletcher [109]. The Rider and Kothe scheme estimates the donating regions by a polygon based on face-centered velocities. Where the advection scheme is straightforward and has low costs, it is non-conservative because of overlapping donating regions and the diffusivity of the interface. The conservative Defined Donating Region (DDR) scheme of Harvie and Fletcher [109] prevents the overlap but increases the diffusivity of the interface and has a lower order of accuracy. Higher accuracy is obtained by Puckett's scheme, allowing, in contrast to DDR, fluid to enter and exit a cell in one time step while still being conservative. None of the discussed schemes results in conforming donating regions.

López et al. [163] proposed the Edge-Matched Flux Polygon Advection (EMFPA) scheme. Different than the advection schemes above, it is based on vertex velocities instead of face-centered velocities. The EMFPA scheme is accurate and

conservative. However, the advection scheme did not initially result in conforming regions due to the volume corrections needed to satisfy the volume constraint, i.e. the volume of the polygon that satisfies the flux size based on the face-centered velocity.

More variations of the volume corrections of EMFPA are proposed [159, 180], but they did not solve the non-conforming regions. Cervone et al. [35] proposed an additional volume correction that solved the problem of conforming regions. The FMFPA-3D scheme of Owkes and Desjardins [199] showed another solution for having conforming donating regions using EMFPA. They added a simplex to the polygon to create a solenoidal fluid flux.

The advection schemes discussed above are based on polygons constructed of linear edges. More sophisticated advection schemes, like Cellwise Conservative Unsplit advection (CCU) [47] using streaklines and the Stream scheme [108] using stream tubes, are not discussed in this work because of the computational costs. The CCU scheme showed to be around seven times more expensive than the EMFPA scheme.

Conclusions found in existing literature for a consistent two-phase flow solver [80] are the reason for introducing a new fluid-advection scheme. Eijk and Wellens [80] use a consistent approach to determine the mass and momentum fluxes on a staggered MAC arrangement of variables. A temporary continuity equation and densities discretized with the mass fluxes are used for consistency [320]. Eijk and Wellens [80] concluded that a direction-split advection scheme, like the COSMIC scheme, leads to inconsistency between the mass and momentum transfer and an increase in instability of the interface. The inconsistency is caused by a combination of the intermediate geometrical interface reconstruction step and the staggered MAC arrangement of variables. The densities resulting from the temporary continuity equation can even be negative, leading to instability of the interface.

EMFPA [199] prevents the intermediate geometrical reconstruction step while remaining conservative. However, as EMFPA is based on cell-vertex velocities, the created polygon can result in a so-called "negative" donating region. An example is illustrated in Fig. 7.2. The blue donating region self-intersects through the cell face resulting in a donating and a receiving volume at the same time. The receiving volume is of the opposite sign than the velocity centered at the cell face (u_{face}). There is the possibility that the final flux (δC_f) found with the receiving region is larger than the donating region or even the volume constraint. This is not correct, because the flux and the face-centered velocity have opposite signs.

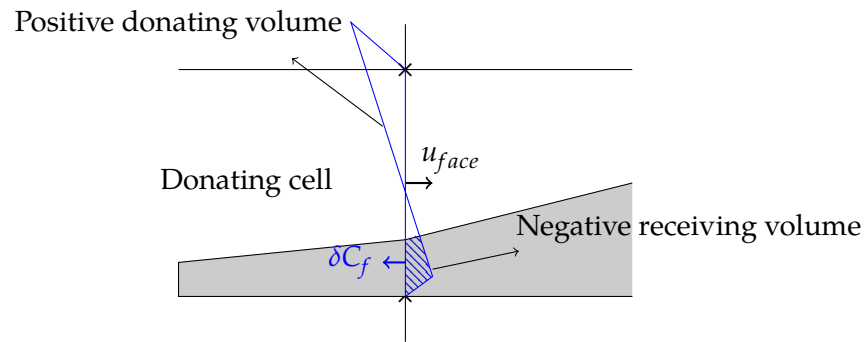


FIGURE 7.2. Example with EMFPA scheme resulting in a negative donating region. The donating region is given by the blue lines ■. This region can generate a receiving flux larger than the donating one for a geometrically reconstructed interface, which is incorrect. The geometric fluid structure is given by ■. The flux δC_f (hatched with -) has a different direction (indicated by a blue arrow) than the face-centered velocity u_{face} (indicated by a black arrow). The faces of a grid cell are given by -. A cell vertex is given by x.

From the authors' point of view, the donating region in Fig. 7.2 is in contradiction with the momentum fluxes for two-phase flow solvers in which the velocity is assumed constant over the cell face; the momentum flux and mass flux based on the face-centered velocity can have a different sign from the VOF flux. The negative region can result in negative densities for a two-phase flow solvers such as Eijk and Wellens [80]. The problems of splitting schemes and the negative densities with EMFPA are discussed in more detail in Sec. 7.6.

The new advection scheme introduced below is a multidimensional unsplit VOF advection scheme that is conservative, conforming, and allows the material to enter and exit a grid cell in one time step. Face-centered velocities are used to prevent negative regions. We call the advection scheme DQA, which stands for donating quadrant advection. It is seen as a modification of EMFPA and the Rider-Kothe scheme that should obtain similar accuracy to EMFPA.

7.1.4 Structure of this work

This work starts with the introduction of the BiLinear Interface Calculation (BLIC) algorithm. In Sec. 7.3 the new BLIC method is compared with two standard PLIC methods for the static reconstruction of two shapes. In Sec. 7.4 the donating quadrant advection (DQA) scheme is introduced. The combination of the BLIC and DQA schemes are compared with other available methods in terms of accuracy and computational costs for traditional transport benchmarks in Sec. 7.5. In Sec. 7.6 the consistent application of the advection scheme for a two-phase solver [80] with a staggered arrangement of variables is discussed. The occurrence of negative densities when using a split advection scheme or the EMFPA scheme is highlighted. Instabilities caused by the reconstruction step

and prevention of negative densities are illustrated in Sec. 7.6.4 for the example of a translating bubble. Conclusions are formulated in the final section.

7.2 BiLinear Interface Calculation

The new reconstruction method presented here will be called BiLinear Interface Construction (BLIC) method. It consists of the following steps:

1. Identification of the cells defined as interface.
2. An initial Piecewise Linear Interface Construction (PLIC) per cell is defined as an interface based on the gradient of the volume fraction and the volume in a cell C_f .
3. The determination of cell face values, which are a measure of the part of the cell face that is in contact with the captured fluid C_f .
4. The application of weighted averaging on either side of the cell face to create continuity of the interface.
5. Addition of a control point, resulting in a bilinear interface, to keep the volume of C_f the same.

The number of the step refers to the number of the subsection below in which the step is discussed. The method should remain low-in-costs, achieve higher accuracy for highly curved interfaces, and increase the continuity of the interface compared to PLIC methods. The scope of the implementation is limited to 2D. Considerations about extending the implementation to 3D are given at the end of this chapter. PLIC methods (e.g. Parker and Youngs, least-square gradient, ELVIRA) are portable to unstructured grids [128]. The BLIC method is a low-effort extension of PLIC which would be equally portable to unstructured grids.

7.2.1 Identification of the interface

Labeling of grid cells is used to account for the position of the interface between two fluids. The labels decide where the reconstruction of the interface takes place. The choice for the label of each cell is based on the volume fraction. The volume fraction C_f indicates the degree to which a grid cell is filled with fluid and takes a value between 0 and 1. We have adopted the labeling system of Eijk and Wellens [80], omitting solid structures (B label) for brevity. In Fig. 7.3, the labeling of the cells in a domain containing two fluids is illustrated, using label E(mpty) for cells completely filled with the lighter of the two fluids ($C_f = 0$), the label S(urface) for cells with some of the heavier of the two fluids adjacent to aligned E cells, and the label C(orner) for one diagonally neighboring E cell. A S-cell is found when $C_f > 0$ and a neighboring cell in the horizontal or vertical plane is E(mpty). A C-cell is labeled after finding the S-cells, when $C_f > 0$ in a cell and neighbours diagonally to a E-cell. Remaining cells are defined as F(luid) cells. S-labeled cells and C-labeled cells need reconstruction of the interface between the two fluids. Why S-cells and C-cells are labeled differently is because of continuity of the

interface and will become clear later in this section. S-cells and E-cells are also referred to as interface cells.

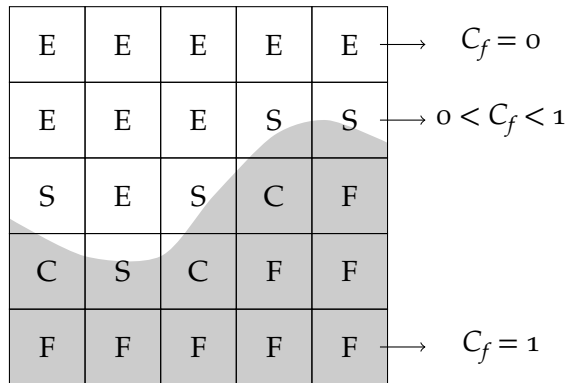


FIGURE 7.3. Labeling of cells [80]; labels F, S, C, and E. Fluid is indicated by ■ ($C_f > 0$).

7.2.2 Initial PLIC reconstruction

A PLIC method uses a piecewise linear segment that approximates the real physical interface in a cell. An example of such a linear segment is illustrated in Fig. 7.4. It is described by the following 2D equation

$$m_x x + m_y y = \alpha, \tag{7.2}$$

where $\mathbf{m} = [m_x, m_y]^T$ is the interface orientation, $\mathbf{x} = [x, y]^T$ the position vector of a point on the interface, and α the distance to the origin so that the interface satisfies the volume constraint C_f for the given interface orientation. The distance to the origin α of the interface is found analytically, as in Scardovelli and Zaleski [233], either in 2D or in 3D.

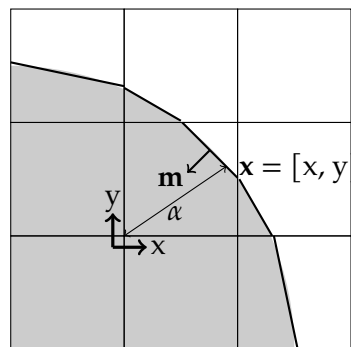


FIGURE 7.4. A quarter circle reconstructed using piecewise linear segments (PLIC); the normal vector \mathbf{m} and height value constant α for a random \mathbf{x} are illustrated for a 3×3 stencil. Fluid is indicated by ■ ($C_f > 0$).

The first step of a PLIC method is to identify the interface orientation, often based on the gradient of the volume fraction. Many methods to determine the interface orientation are published and discussed above. In the presented work, Parker and Youngs' method and Mixed Youngs-Centered (MYC) are discussed because of their ease of implementation and the relatively low costs [74]. Here, in any case, Parker and Youngs and MYC are compared to identify their effect on the final reconstruction. Diwakar, Das, and Sundararajan [65] mentioned that for their higher-order QUASI method, the interface orientation method for the initial PLIC is expected not to be relevant for the final reconstruction. We will find out if this is also the case for the BLIC method.

The Parker and Youngs' method, for a 2D grid, determines the gradients of the volume fraction C_f at four corners of the central grid cell using finite difference. The gradients are normalized and averaged, resulting in the interface orientation \mathbf{m} . The method is first-order accurate, but the errors in the reconstruction are comparable to second-order methods [210, 235].

The Mixed Youngs-centered (MYC) method [6] is a mix between the Parker and Youngs' method and the standard height function approach with a stencil of 3×3 grid cells. It is described as a fast and accurate way to compute the interface normal \mathbf{m} . Aulisa et al. [6] showed that the implementation outperforms the Parker and Youngs' method [202] in terms of accuracy and approaches second-order accuracy. Düz [74] reported the MYC implementation as a good compromise between accuracy and computational cost.

7.2.3 Face values

The next step of the BLIC method is determining the face values of the PLIC reconstruction. Every PLIC line contains two endpoints positioned at a cell face. An example is illustrated in Fig. 7.5. The face value is determined by a PLIC endpoint, illustrated by \bullet . A is a value between 0 and 1 that describes the part of a cell face that connects to the heavier fluid ($C_f = 1$). These endpoints are found analytically [233]. The 2D PLIC line forms a quadrangular or triangular shape, uniquely described by m_x , m_y , and α . For every cell with label S or C a PLIC line is computed. The endpoints of PLIC lines in the two cells on either side of a cell face in general do not coincide. The face apertures based on the PLIC lines left and right cell face, A_{left} and A_{right} , are combined so that face aperture A is the average of A_{left} and A_{right} .

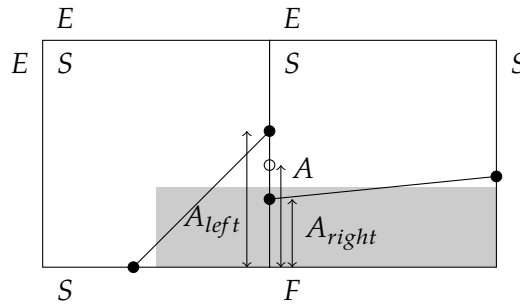


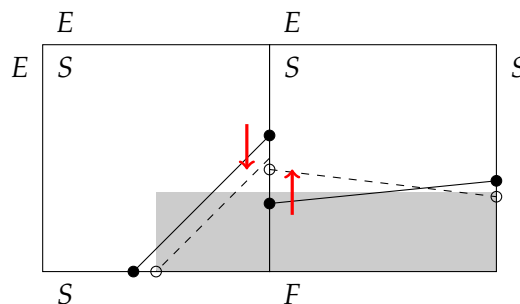
FIGURE 7.5. Definition of face values A . Fluid is indicated by ■. PLIC endpoints ●. A more continuous endpoint ○ is found by averaging PLIC endpoints. The labeling of the cells and the surrounding cells is shown by means of letters F , S and E .

The neighboring PLIC endpoints may be not positioned on the same cell face. This makes it harder to obtain continuity of the interface. Repositioning of the endpoints then is needed. Examples of how endpoints could be repositioned is illustrated in Fig. 7.6, which are inspired by the approach of Diwakar, Das, and Sundararajan [65]. The red arrows show the directions in which PLIC endpoints are moved. Every situation needs a different treatment to determine face aperture A , created by the more continuous interface that is represented by means of the dashed lines after repositioning the endpoints.

We want to avoid distinguishing between situations like in Fig. 7.6 to limit the involved computational effort. A such method should satisfy the following constraints

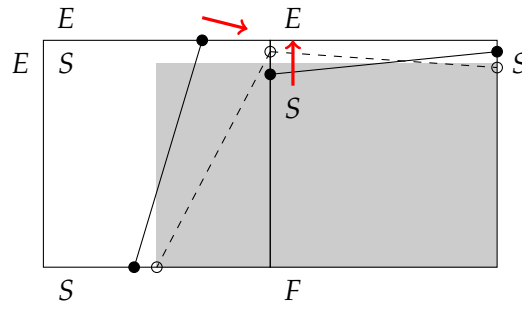
1. the face value A of an edge in an interface cell (S-or C-cell) neighboring a F-or E-cell is equal to 1 or 0, respectively;
2. a S-or C-cell has two face values A between 1 and 0;
3. the volume constraints are enforced without iteration or a significant increase in computational costs;

and is described in the next section.

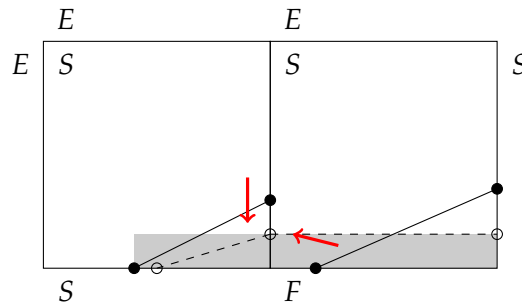


(A) Both values A_{left} and A_{right} between 0 and 1 on common edge.

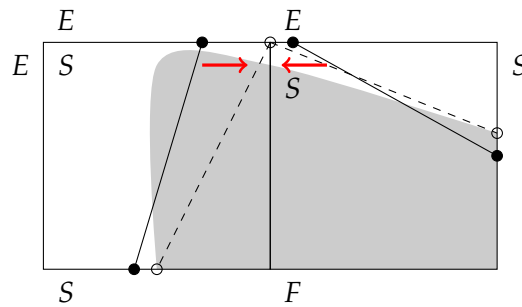




(B) Full face value on common edge; $A_{left} = 1$ and $0 < A_{right} < 1$.



(C) A zero face value on common edge; $0 < A_{left} < 1$ and $A_{right} = 0$.



(D) No common edge with face values A_{left} and A_{right} equal to 1.

FIGURE 7.6. Four different situations of PLIC reconstructions to obtain continuity along the interface without satisfying the volume constraint yet [65]. Each situation ask for a different treatment to find the endpoints, which requires computational effort. A method that avoids distinguishing between situations is proposed in Sec. 7.2.4. Fluid is indicated by ■. PLIC endpoint ●. Continuous endpoint ○. The labeling of the cells and the surrounding cells is shown by means of letters F , S and E .

7.2.4 Averaging method: curvature weighted

The proposed averaging method for determining the new face value A is based on the motto that *the curvature is more accurately predicted by a piecewise linear segment when the curvature is close to zero*. When averaging, the method gives more

weight to the parts of the interface that have low curvature. A piecewise linear representation for those parts is expected to be more accurate than for the parts of the interface with high curvature. Weighted averaging prevents the parts of the interface with high curvature from influencing the parts with low curvature, improving the overall accuracy of the interface reconstruction. A better curvature prediction gives a more accurate representation of the face values of the interface.

The curvature is calculated for interface cells (S-and C-cells). Curvature is not defined for the remaining labels. Many methods are available to predict curvature. In this work, we will only highlight two; the standard height function technique [50, 215] and the classic technique using finite difference [1, 202]. These methods are chosen for their relative ease of implementation.

The curvature (κ) is defined as

$$\kappa = -\nabla \cdot \left(\frac{\nabla \phi}{\|\nabla \phi\|} \right), \quad (7.3)$$

where ϕ can be a height value (a sum of aligned volume fractions) or just the volume fraction C_f . The standard height function technique is described by, for instance, Kleefsman et al. [142], using a 3×3 stencil. When the interface is more vertical than horizontal, the height function is defined parallel to the horizontal axis. The finite difference technique to calculate the curvature is based on the approach of Parker and Youngs [202]. The approach computes the normal vector to the interface at every corner of a cell. The difference in normal vectors at the corners results in the curvature of the free surface in that cell, defined at the cell center.

An example of a interface on a 3×3 stencil is shown in Fig. 7.7. The curvature at the corner of the fluid body in this example should approach infinity; the values for the height function technique and the classic finite difference technique are given. Fig. 7.7 is an extreme example, with a strongly underresolved free surface configuration, to exaggerate the issue with the standard height function technique. The issue with the standard height function technique is that applying the method at sharp corners of the interface can lead to negative values of the curvature. To avoid negative values for the curvature, we continue with the classic finite difference technique. For more information about accurate methods for determining curvature, one is referred to Popinet [215] and Abadie, Aubin, and Legendre [1], who resolved the issue with negative curvature by making the height function technique adaptive.

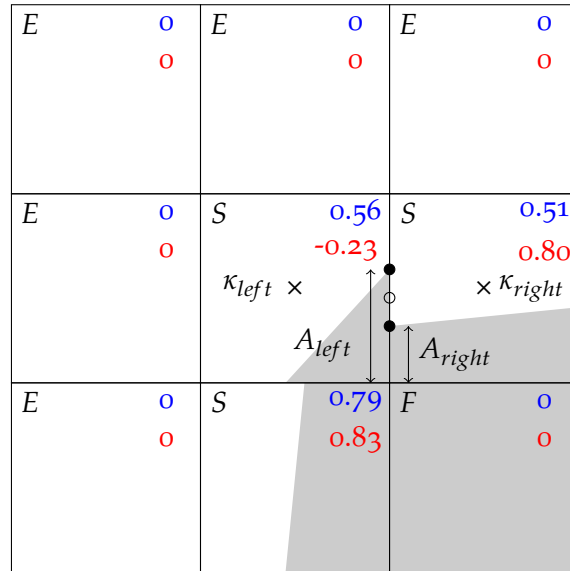


FIGURE 7.7. Prediction of the curvature (κ) using the volume fractions C_f with two different techniques; the classic technique (■), and the height function technique (■). Fluid is reconstructed with original PLIC indicated by ■ ($C_f > 0$). PLIC endpoint ●. Continuous endpoint resulting in A ○. Center grid cell where κ is defined (×).

The new face value A is calculated as

$$A = \frac{\kappa_{right}^{n_\kappa} A_{left} + \kappa_{left}^{n_\kappa} A_{right}}{\kappa_{left}^{n_\kappa} + \kappa_{right}^{n_\kappa}}, \tag{7.4}$$

where n_κ is a weighting factor. This weighting factor is a free parameter for which a value is found by comparing simulation results in Sec. 7.3 for the static reconstruction of two different shapes. Referring to the constraints given in Sec. 7.2.3, the formulated method ensures that the face values of a F-cell or E-cell are 1 and 0, respectively. Repositioning of the endpoints (see Fig. 7.6) is automatic when the curvature-weighted approach is used. The curvature weighted approach should ensure that when an interface cell has more than two neighboring interface cells in vertical and horizontal direction, the number of face values remains two by applying it only for the lower two values of A .

7.2.5 Addition of BLIC point

When the continuity is improved by averaging as in Fig. 7.8a, the reconstruction will not satisfy the volume constraint. Therefore an additional point is introduced which will make the reconstruction bilinear. The additional point is initially positioned in the middle of the reconstructed line, see the ● in Fig. 7.8b. The point moves perpendicular to the continuous reconstructed line until it satisfies the



volume constraint for C_f .

No iterations are needed to find the final position of the additional point. Using the definitions in Fig. 7.8c, the coordinates of the additional point (x_3, y_3) are found from

$$y_3 = \alpha(x_{3,0} + \beta) + b \text{ where } \alpha = -(x_1 - x_2)/(y_1 - y_2) \text{ and } b = y_1 - \alpha x_1. \quad (7.5)$$

The points are ordered counter clockwise. The third line can move over the line $y(\beta)$ with initial point

$$x_{3,0} = \frac{x_1 + x_2}{2} \text{ and } y_{3,0} = \frac{y_1 + y_2}{2}. \quad (7.6)$$

The value of β is found by

$$\beta = \frac{V_{final} - V_0}{\frac{1}{2}\alpha(x_2 - x_1) + \frac{1}{2}(y_1 - y_2)}, \quad (7.7)$$

where $V_{final} - V_0$ is the difference between the volume constraint and the volume before adding the extra control point.

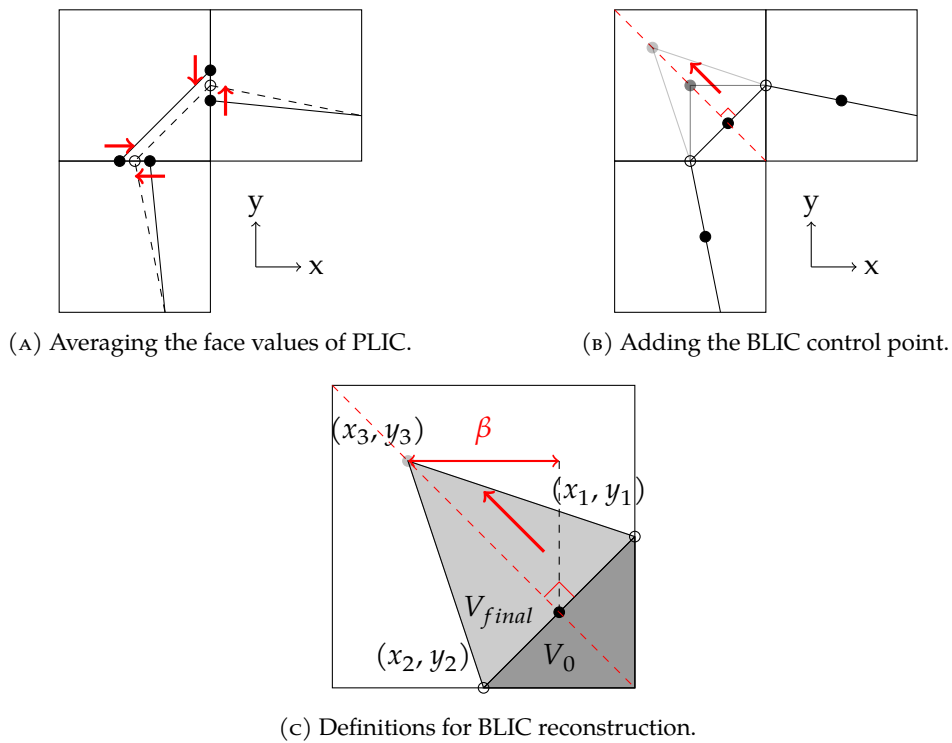


FIGURE 7.8. Procedure BLIC reconstruction to meet volume constraint. The volume V_0 after averaging the face values to A is ■. The final volume V_{final} satisfying the volume constraint is ■. BLIC additional point ●. Continuous endpoint ○.

7.2.6 Evaluation & Remark

The curvature-weighted averaging is evaluated for the reconstruction of a sharp corner in Fig. 7.9, including the additional point satisfying the volume constraint. Two values for n_κ , 0 and 2, are compared with the end-positioning approach of Diwakar, Das, and Sundararajan [65]. Note that n_κ equal to 0 is simply averaging. The approach of Diwakar, Das, and Sundararajan [65] needs special treatments for repositioning endpoints as mentioned in Sec. 7.2.3. Compared to Fig. 7.6b their approach ignores the information of A_{left} and assumes A is equal to A_{right} .

The results in Fig. 7.9 show that for this case, the proposed curvature-weighted averaging method is an improvement compared to the approach of Diwakar, Das, and Sundararajan [65]. The value of n_κ affects the reconstruction and therefore needs extra evaluation in Sec. 7.3.

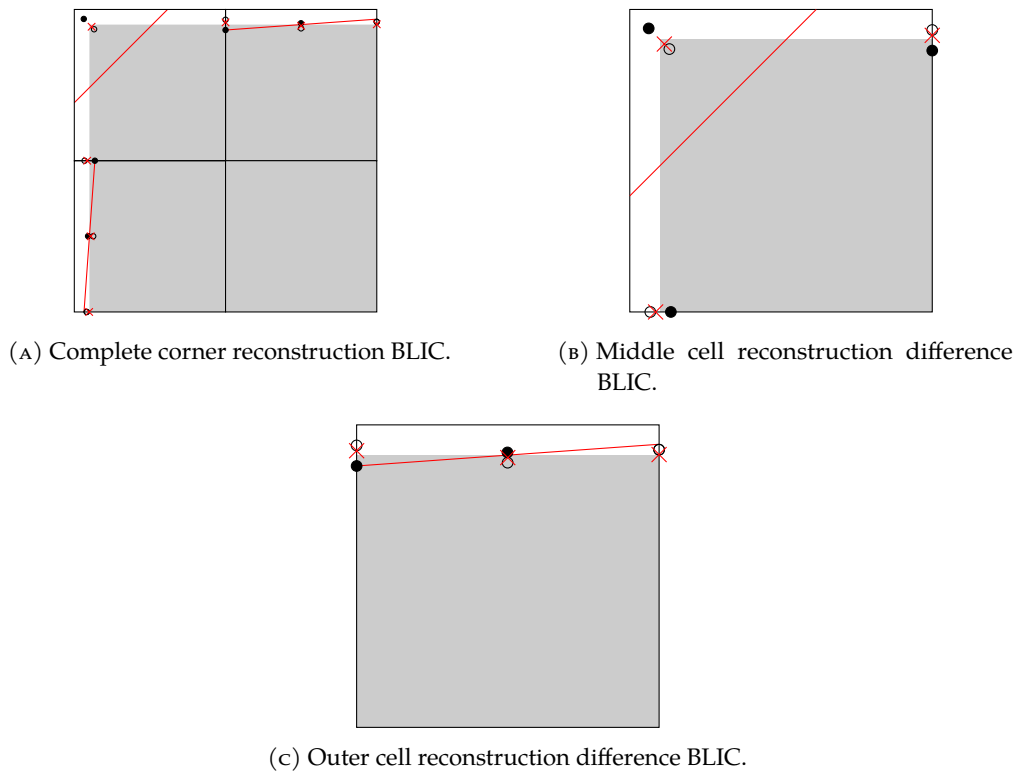


FIGURE 7.9. Continuous face value calculation A for a 90 degrees corner. Red line is PLIC Youngs reconstruction (-). ● is the approach of Diwakar, Das, and Sundararajan [65] for determining the face values. ○ is the averaging method for $n_\kappa = 0$. × is the weighted averaging method for $n_\kappa = 2$. Fluid is indicated by ■ ($C_f > 0$).

An additional remark concerns the BLIC point dividing the line segment. When this BLIC point is positioned outside of a grid cell, the initial PLIC line is used.



The interface in that case is not continuous anymore. This is most likely to happen for S and C-cells which are almost empty or almost full. How often this happens is evaluated for the reconstruction of circle with 64 grid cells in the diameter. The chance is in the order of 0.1% and decreases to zero with grid refinement. For the reconstruction of a square with its sides resolved by 64 grid cells, the same results are obtained. The test case in Sec. 7.5.2 elaborates on this by also considering underresolved structures and shows how accurate BLIC remains compared with PLIC.

Another remark concerns the C-cells which is a reason why S-and-C-cells do not have the same label. There is the chance that a C-cell, connected to two S-cells, has an original PLIC interface with an opposing orientation than the S-cells before applying BLIC. This works against creating a smooth continuous BLIC interface when using the curvature-weighted approach. For this situation, the normal of the interface in the C-cell is reoriented such that it points in the direction of the average of the normal vectors of the interfaces in the neighboring S-cells. After reorienting the normal vector, the face values A in the BLIC algorithm are determined. The situation of opposing orientations in neighboring interface cells is even rarer than BLIC points being positioned outside of grid cells.

A final remarks concerns the extension to 3D. The BLIC algorithm can be extended to 3D by following a similar procedure with planes and lines instead of lines and points. The BLIC algorithm presented in Sec. 7.2 can be formulated in 3D without increasing the complexity. The shape of the interface will be a pyramid after positioning the endpoints using the curvature-weighted approach. The cost increase of using BLIC instead of PLIC in 2D is evaluated in Sec. 7.5.3. The cost increase of using BLIC instead of PLIC in 3D is proportional to that in 2D.

7.3 Static reconstruction interface

The accuracy of the following reconstruction methods is compared for two static shapes: Parker and Youngs [202], Mixed Youngs Centered (MYC) [6], and BLIC. The transport of fluid is not involved, only reconstruction. The shapes that are evaluated are a circle and a square.

A domain of one by one is used. The width of the square is 0.512, and the circle radius is 0.368. The square is positioned in the center of the domain and the circle off-center at (0.525, 0.464) to prevent the reconstruction method from favoring a specific interface orientation [226]. The L_1 norm of the error between the exact interface and the reconstructed interface is calculated as

$$L_1 = \int \int |S_{exact}(x,y) - S_{reconstructed}(x,y)| dx dy, \quad (7.8)$$

in which S is the interface. The L_1 norm for both shapes and the different reconstruction methods is given in Tab. 7.1 as a function of the number of grid cells in the domain.

Grid	Youngs		Youngs + BLIC	
	Square	Circle	Square	Circle
10	4.81e-3	8.92e-4	3.51e-4	3.59e-4
20	6.81e-4 (2.82)	2.59e-4 (1.78)	7.61e-5 (2.21)	9.91e-5 (1.86)
40	2.48e-4 (1.46)	1.17e-4 (1.15)	2.57e-5 (1.57)	4.38e-5 (1.18)
80	7.20e-5 (1.79)	5.39e-5 (1.12)	5.62e-6 (2.19)	2.03e-5 (1.11)
160	4.06e-6 (4.15)	2.83e-5 (0.93)	1.90e-7 (4.89)	1.09e-5 (0.90)
320	1.79e-6 (1.18)	1.41e-5 (1.01)	6.24e-8 (1.60)	5.52e-6 (0.98)

Grid	MYC		MYC + BLIC	
	Square	Circle	Square	Circle
10	5.64e-3	9.76e-4	8.82e-4	4.63e-4
20	7.72e-4 (2.87)	2.35e-4 (2.05)	7.61e-5 (3.53)	1.21e-4 (1.94)
40	3.40e-4 (1.18)	6.91e-5 (1.77)	1.96e-5 (1.96)	3.41e-5 (1.83)
80	8.82e-5 (1.95)	3.02e-5 (1.19)	1.93e-6 (3.34)	1.53e-5 (1.16)
160	4.44e-6 (4.32)	1.57e-5 (0.94)	4.26e-7 (2.18)	7.91e-6 (0.95)
320	1.97e-6 (1.17)	7.71e-6 (1.03)	1.72e-7 (1.32)	3.86e-6 (1.03)

TABLE 7.1. Reconstruction error static square / circle for different grid resolutions with $n_\kappa = 2$. The order of convergence is given in between parentheses.

Circular shapes are common for fluid configurations, like droplets and bubbles. High accuracy in representing these shapes is important for contacts between bodies. The reconstruction using Parker and Youngs and MYC alone results in errors at least twice as high as when they are combined with BLIC.

Sharp corners in fluid bodies, like those in a square, are not present due to surface tension effects. However, when moving solid objects representing structures are present in a simulation, and when it is convenient to reconstruct the interface between solid objects and fluids in the same way as between fluids, then sharp corners do play a role. From that point of view, we want to know how the various reconstruction methods deal with sharp corners. The reconstruction error in the L_1 norm is reduced by an order of magnitude compared to Parker and Youngs and MYC when using the BLIC method.

The results in Tab. 7.1 show that when an underresolved material interface like the corner of a square is present, BLIC decreases the reconstruction error significantly with a higher order of convergence. For the circle, which is not underresolved, the results show that the decrease in error with BLIC is less. For the circle, the

reconstruction error with BLIC converges to the error obtained with PLIC on a grid that is twice as fine. This was expected because BLIC divides piecewise linear segments in two.

The effect of the magnitude of weighing factor n_κ on the reconstruction error in Eq. (7.4) is evaluated in Tab. 7.2 for BLIC (initialization with Parker and Youngs). The results show that the dependency on the curvature for the face apertures in the BLIC method improves the accuracy of reconstructing a square. For the square having sharp corners, the best performing value for n_κ is 2. A lower value for n_κ performs better than a high value for the reconstruction of a circle. BLIC performs, independent of the value of n_κ , better than Parker and Youngs when comparing the errors in Tab. 7.2 with Tab. 7.1. The reason for the improvement compared to PLIC when using higher values for n_κ is because the corners of a square in general are inherently underresolved, making PLIC so inaccurate. For circles, this inherent absence of resolution is not there, so that BLIC and PLIC have a comparable accuracy. Making n_κ adaptive is an interesting option for future research. In the remainder of this article, we will continue with n_κ is 2 with the underlying thought of representing fluid configurations with highly-curved interfaces.

n_κ	0		1		2	
	Square	Circle	Square	Circle	Square	Circle
10	1.26e-3	3.76e-4	4.68e-4	3.38e-4	3.51e-4	3.59e-4
20	8.00e-4	1.03e-4	3.18e-5	9.91e-5	7.61e-5	9.91e-5
40	8.25e-5	4.06e-5	5.93e-6	3.96e-5	2.57e-5	4.38e-5
80	1.75e-5	1.76e-5	5.04e-6	1.85e-5	5.62e-6	2.03e-5
160	4.44e-6	9.39e-6	2.47e-7	9.67e-6	1.90e-7	1.09e-5
320	1.97e-6	4.69e-6	1.41e-7	4.94e-6	6.24e-8	5.52e-6

n_κ	3		4	
	Square	Circle	Square	Circle
10	2.34e-4	4.22e-4	1.19e-4	7.05e-4
20	8.94e-5	9.85e-5	9.28e-5	9.79e-5
40	3.85e-5	4.58e-5	4.60e-5	4.67e-5
80	6.20e-6	2.13e-5	6.77e-6	2.19e-5
160	4.93e-7	1.15e-5	6.80e-7	1.18e-5
320	2.10e-7	5.84e-6	3.05e-7	6.02e-6

TABLE 7.2. Reconstruction error static square / circle with BLIC (with Parker and Youngs initialisation) for increasing value of n_κ , and therefore dependency of curvature κ .

The cost evaluation and comparison with other available reconstruction algorithms is done for the benchmarks in the next section.

7.4 Unsplit edge-matched upwind flux polygon advection scheme

A new unsplit multidimensional advection scheme has been developed. It is compared with a direction-split advection scheme, called COSMIC [155], for several benchmarks. Before introducing these advection schemes, a brief overview of the advection of the interface using the Volume-of-Fluid (VOF) approach is given.

7.4.1 VOF advection

The interface is captured using Eq. (7.1) under the assumption of incompressibility and the no-slip condition between the two fluids. In case of a Volume of Fluid (VOF) method, the color function f is replaced by a discrete volume fraction C_f . The discrete volume fraction indicates the filling ratio of one of the fluids in a grid cell and is the average of the color function.

The fluids are transported with the assumption of incompressibility

$$\begin{aligned} \int_{V_c} \frac{C_f^{n+1} - C_f^n}{\delta t} dV &= - \int_V (\mathbf{u} \cdot \nabla) C_f dV \\ &= - \int_V \nabla \cdot (\mathbf{u} C_f) dV \\ &= - \oint_{S_c} (\mathbf{u}^n C_f^n) \cdot \mathbf{n} dS, \end{aligned} \quad (7.9)$$

in which V and S are the volume and boundary of the grid cell, respectively. The superscript indicates the time level; $n + 1$ is the new time level and n is the old-time level. Eq. (7.9) is the basis for the discretization of the advection equation. A straightforward discretization of the advection equation reads

$$C_f^{n+1} = C_f^n - \frac{1}{V} \sum_{face} \delta C_{f,face}, \quad (7.10)$$

in which subscript $face$ refers to a cell face, and the VOF flux δC_f is the amount of fluid transported from one cell to the next. Similar to Fig. 7.2, Fig. 7.10 shows an example of a flux at the cell face and the donating region for a one-directional flow field. The velocity field is defined at the cell faces of a grid cell. The VOF flux is based on the reconstructed interface segment of the donating cell. The flux is of the form

$$\delta C_f \sim C_f \delta t \delta A, \quad (7.11)$$

where δA is the part of the area of a cell face in contact with the fluid being transported. The total area of the cell face in Fig. 7.10 is equal to δy . The naming of the cell faces, w(est), e(ast), n(orth), and s(outh), are illustrated.

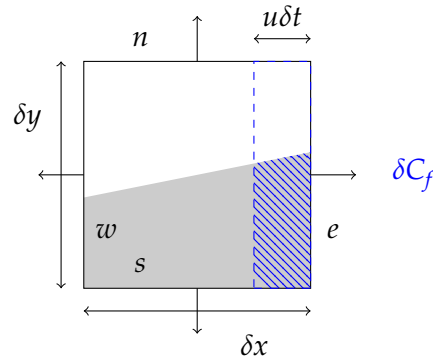


FIGURE 7.10. Flux is calculated in a grid cell. Fluid is indicated by ■. The other fluid is white. The amount of fluid being transported (fluxed δC_f) is hatched with —. The cell faces are named. The donating region is indicated by the dashed line.

7.4.2 COSMIC advection scheme

The COSMIC split scheme we compare the new method to consists of multiple transport and reconstruction steps [155]. The COSMIC scheme, in 2D, reads as follow

$$\begin{aligned} C_f^{*X} &= C_f^n - \frac{1}{V} \sum_{face=w,e} \delta C_{f,face}(u^n, C_f^n) + \frac{C_f^n}{V} \sum_{face=w,e} u_{face} \delta y, \\ C_f^{*Y} &= C_f^n - \frac{1}{V} \sum_{face=n,s} \delta C_{f,face}(v^n, C_f^n) + \frac{C_f^n}{V} \sum_{face=n,s} v_{face} \delta x, \end{aligned} \quad (7.12)$$

The interface of the intermediate volume fraction fields C_f^{*X} and C_f^{*Y} is again reconstructed, resulting in $C_f^{X, n+1/2}$ and $C_f^{Y, n+1/2}$. The superscripts * and $n + 1/2$ indicate intermediate time levels. A distinction is made between these two time levels (* and $n + 1/2$) for the discussion in Sec. 7.6 of why inconsistency can be found with COSMIC. Even though the values for C_f with time levels * and $n + 1/2$ in a cell are the same, the staggered arrangement of variables causes a difference for momentum control volumes after the reconstruction.

The new fraction field is found from

$$\begin{aligned} C_f^{n+1} &= C_f^n - \frac{1}{V} \sum_{face=w,e} \delta C_{f,face} \left(u^n, \frac{C_f^n + C_f^{Y, n+1/2}}{2} \right) \\ &\quad - \frac{1}{V} \sum_{face=n,s} \delta C_{f,face} \left(v^n, \frac{C_f^n + C_f^{X, n+1/2}}{2} \right). \end{aligned} \quad (7.13)$$

7.4.3 Proposed Donating Quadrant Advection (DQA) scheme

As mentioned in the introduction, we want the new advection scheme to satisfy the following conditions.

1. It will be an unsplit multidimensional scheme: to prevent distortion of the interface, and geometrical errors.
2. Be conservative and non-diffusive: no overlapping regions or gap between neighboring donating regions.
3. Feature conforming regions: the length of the edges of two neighboring donating regions should have the same length.
4. Allow fluid to enter and exit a grid cell in one time step.

The EMFPA [199] scheme meets these requirements. The computational costs and accuracy of the new scheme should not be inferior to the EMFPA scheme. It also, in contrast to EMFPA, needs to be consistent with the mass and momentum transfer of two-phase flow solvers similar as presented in Eijk and Wellens [80]. Therefore, the subsection explaining the new scheme consists of four steps: positioning and determining the linear edges of the donating region, volume correction by adding an extra control point to satisfy the volume constraint, and checking if the final donating region complies with the requirements.

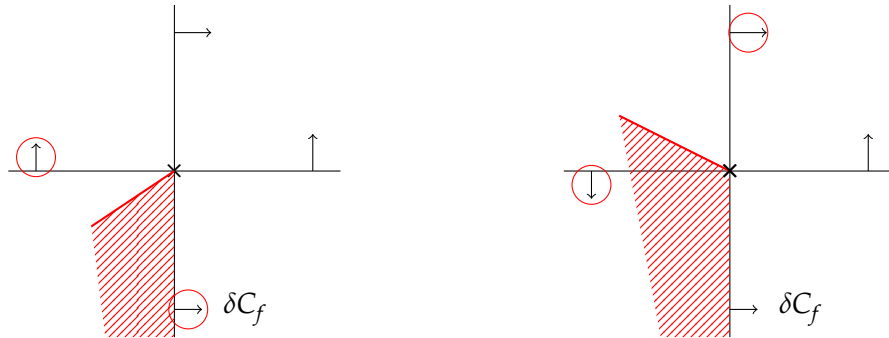
7.4.3.1 Positioning of the linear edges

The new scheme is based on face-centered velocities, like Rider-Kothe [226], to prevent the so-called negative donating flux-region, illustrated in Fig. 7.2. The negative donating region can result in a VOF flux of opposite sign than the fluxing face velocity. We consider this inconsistent with the direction of the face-centered velocity and the effect thereof is elaborated upon in Sec. 7.6. The donating region needs to be on one side of the cell face, given by the sign of the face velocity. In contrast to Rider-Kothe, the new scheme is conservative and has no overlap with neighboring donating regions. We will name the scheme DQA, short for Donating Quadrant Advection.

Three different situations for constructing a linear edge of the donating region are illustrated in Fig. 7.11. The difference between the vertex velocity-based EMFPA scheme in Figs. 7.11d, 7.11e, 7.11f and the new scheme in Figs. 7.11a, 7.11b, 7.11c is given. The encircled velocities in Fig. 7.11 are used for determining the magnitude and direction of the thick-lined linear edge. The vertex velocities used for EMFPA are found by averaging the surrounding face-centered velocities.

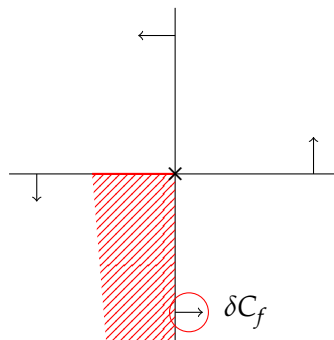
The DQA scheme depends on the direction of the fluxing face-centered velocity. The quadrant where the linear edge is positioned decides which single face-centered velocity is used. The linear edge is always positioned in a quadrant where, in 2D, two (vertical and horizontal) face-centered velocities are donating.

When no quadrant has two donating face-centered velocities, in Fig. 7.11c, a non-sloped linear edge is made to prevent a negative donating region. The use of this non-sloped linear edge has the disadvantage that it can lead to a gap between neighboring donating regions because the linear edge does not match with the linear edge for the donating region of the upper velocity in Fig. 7.11c. But enforcing a non-sloped edge is necessary to prevent negative donating regions. The loss of accuracy as a result of this procedure is checked for benchmarks in Secs. 7.5.1 and 7.5.2 by comparing with EMFPA. The results will show that DQA is competitive with EMFPA.

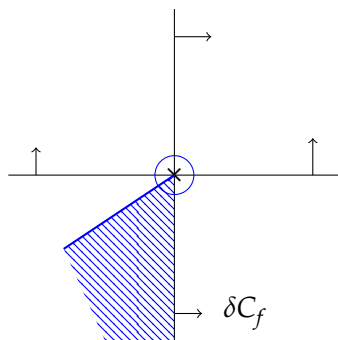


(A) DQA 1: Edge of polygon in the corresponding cell.

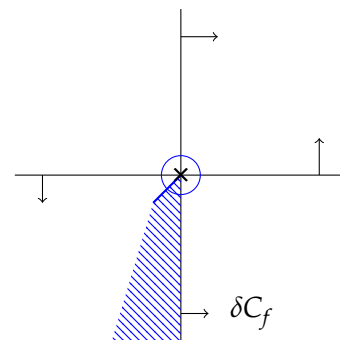
(B) DQA 2: Edge of polygon in another cell.



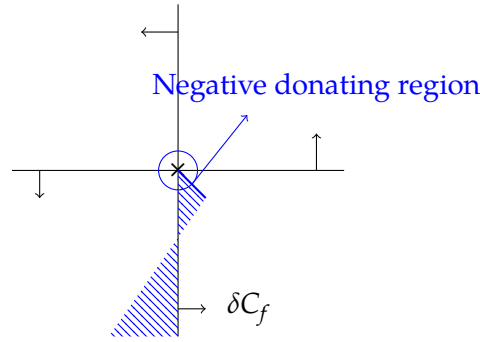
(C) DQA 3: Velocity change of sign.



(D) EMFPA 1: Edge of polygon in the corresponding cell.



(E) EMFPA 2: Edge of polygon in another cell.



(F) EMFPA 3: Velocity change of sign.

FIGURE 7.11. Three different situations of flux polygon construction using velocities defined on the cell faces. The thick linear edge is determined by the encircled velocities. Grid cells are illustrated with $-$. The amount of fluid being transported with DQA (fluxed δC_f) is virtual hatched with $-$ and with EMFPA is hatched with $-$. A cell vertex is given by \times where the velocities are averaged for EMFPA. A velocity position is given by an arrow.

7.4.3.2 Determination of the linear edges

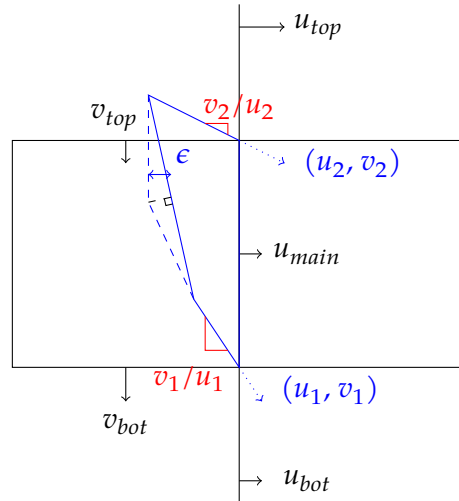
Determining the complete donating region with DQA, including the coordinates of the vertices, is based on Fig. 7.12. The flux velocity u_{main} determines the volume of the donating region. The vertical velocities v_{bot} and v_{top} are used to determine the slope of the linear edges. The distance value ϵ and slope value ϕ are related to the volume correction discussed in the next subsection.

The velocities are defined such that the positioning of the linear edges complies with the three situations illustrated in Fig. 7.11. The velocities in Fig. 7.12a for the linear edges of the donating region are defined as follow

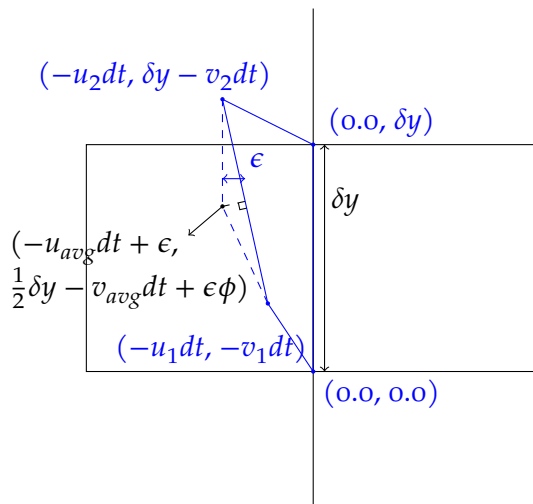
$$[u_1, v_1] = \begin{cases} [u_{main}, v_{bot}], & \text{if } \text{sign}(v_{bot}/u_{main}) \neq \text{sign}(u_{main}) \\ [u_{bot}, v_{bot}], & \text{else if } \text{sign}(u_{bot}) = \text{sign}(u_{main}) \\ [u_{main}, 0.0], & \text{otherwise} \end{cases} \quad (7.14)$$

$$[u_2, v_2] = \begin{cases} [u_{main}, v_{top}], & \text{if } \text{sign}(v_{top}/u_{main}) = \text{sign}(u_{main}) \\ [u_{top}, v_{top}], & \text{else if } \text{sign}(u_{top}) = \text{sign}(u_{main}) \\ [u_{main}, 0.0], & \text{otherwise} \end{cases}$$

Donating region construction in other directions is approached similarly. The scheme, like EMFPA [199], can be straightforwardly extended to 3D.



(A) Example of face-centered velocities needed.



(B) Coordinates defining the polygon; additional point is black.

FIGURE 7.12. Definition of DQA scheme; in case $u_1 = u_{main}$, $u_2 = u_{top}$, $v_1 = v_{bot}$, and $v_2 = v_{top}$. Donating region is given by $-$. Slopes are given by $-$. The volume correction with slope ϕ is illustrated for the approach of Owkes and Desjardins [199]. The cell face area δA is equal to δy .

7.4.3.3 Volume correction

The donating regions in Fig. 7.12 do not initially satisfy the volume constraint. Many volume correction methods are available [35, 159, 180, 199]. The correction method of Owkes and Desjardins [199] is adopted by adding an extra control point. This extra point ensures that the volume of the donating region satisfies the volume constraint. Conforming donating regions are found when applying



this correction method.

The distance value ϵ , illustrated in Fig. 7.12b, should result in a donating region with a volume of $u_{main}dt\delta A$ (the volume constraint). The additional point that satisfies the volume constraint is found with u_{avg} and v_{avg} being equal to $\frac{1}{2}(u_1 + u_2)$ and $\frac{1}{2}(v_1 + v_2)$, respectively. The distance is found from

$$\epsilon = dt \frac{-u_2v_1dt + u_1v_2dt + 2u_{main}\delta A - (u_1 + u_2)\delta A}{(v_2 - v_1)dt + (u_1 - u_2)\phi dt - \delta A}, \quad (7.15)$$

in which δA is equal to δy for Fig. 7.12.

The slope value ϕ can be determined in many ways. Evaluation of the effect of ϕ on the accuracy is needed. Owkes and Desjardins [199] uses the normal vector of the original linear edge as the direction for creating the additional point. This method is illustrated as an example in Fig. 7.12. Other ways to determine the slope value ϕ are

$$\begin{aligned} \phi &= \frac{v_2 - v_1}{u_2 - u_1} \quad (\text{Owkes and Desjardins [199]}), \\ \phi &= 0 \quad (\text{current called } zero), \\ \phi &= \frac{v_2 + v_1}{u_2 + u_1} \quad (\text{current called } avg). \end{aligned} \quad (7.16)$$

The evaluation of the slope value is done in the next section. The slope value of Owkes and Desjardins [199] is used for comparison with other computational methods.

The extra correcting point can result in a non-convex donating flux region. When the shape is non-convex, the donating region is split into multiple convex triangles. This increases the computational costs as the triangles are dealt with separately, but it solves the problem of determining the VOF flux of a non-convex region. The intersection points of the donating region with the BLIC interface are expensive to determine for non-convex shapes. The computational costs are analyzed in one of the following sections.

7.4.3.4 Reducing order with DDR scheme

Owkes and Desjardins [199] showed that their advection scheme is unconditionally stable. We want to discuss what constraints are needed to keep the two-phase solver described in Sec. 7.6 stable. When the volume correction is large, the additional point can lead to an overlap of the donating region with neighboring regions. Or it can result in a negative donating region. The DQA method can easily switch to a lower-order DDR scheme when this happens. The difference between DDR and DQA, illustrated in Fig. 7.13b, is that the donating polygon

never intersects a cell face; material cannot enter and exit a cell in one time step. The DDR scheme is found when the boxed step in Eq. (7.14) is omitted. DDR is robust and conservative, but increases the diffusivity of the interface.

The criteria to switch from DQA back to DDR are

1. The correcting point should not lead to overlap with neighboring polygons or the polygon itself to prevent mass changes.
2. The correcting point should not be at the opposite side of the cell face compared to the other points of the donating region (later referred to as 'negative donating region') because it can induce instability of the two-phase solver.

When these criteria are not met, one of the provided constraints is violated, and the DDR method is used for that particular cell face. Note that the correction method we use can also cause mass issues due to overlap when combined with EMFPA. Alternative correction methods will be a research topic of ours for the near future.

The chance that switching back to DDR occurs is negligible for cases with imposed velocity fields. However, for the case in Fig. 7.1, with large fluid deformations [78], the switch back provides robustness, in the sense that negative donating regions that can induce instabilities of the two-phase solver are prevented. For a case similar to the one shown in Fig. 7.1, using a relatively coarse grid resolution (roughly 100 cells in the width and height of the domain) and a Courant number of 0.50, the number of times the algorithm switches back to DDR is smaller than 1% of the total number of time steps. Switching back especially occurs when water and air near the interface have large velocities in opposite direction. At those moments, the correction to meet the volume constraint can lead to overlap or the situation discussed in the Sec. 7.4.3.5, so that switching back to DDR is necessary to prevent instability. The percentage of time steps, in which the algorithm switches back to DDR, decreases when lowering the Courant number. Grid refinement with a factor of two reduces the number of times the algorithm switches back with a power of two. We consider the chance of the algorithm switching back small. The effect of switching back to DDR on the accuracy is evaluated in Sec. 7.5.2.

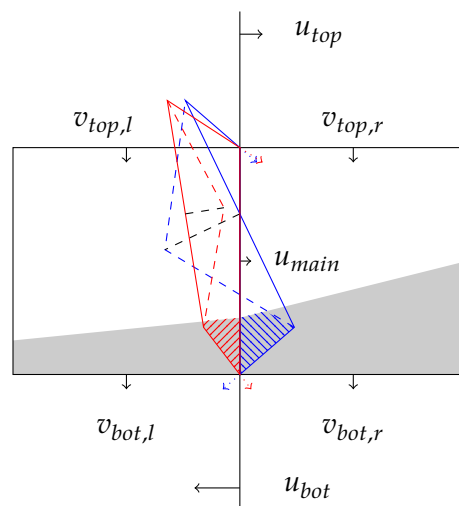
7.4.3.5 *Difference EMFPA and DQA for two examples*

In Fig. 7.13 the full donating region with EMFPA and DQA is compared for two cases. These two cases are considered to be the most different. The length of the velocity vectors is to scale. The flux size is illustrated by the hatched area. The volume correction method of Owkes and Desjardins [199] is used with both

EMFPA and DQA.

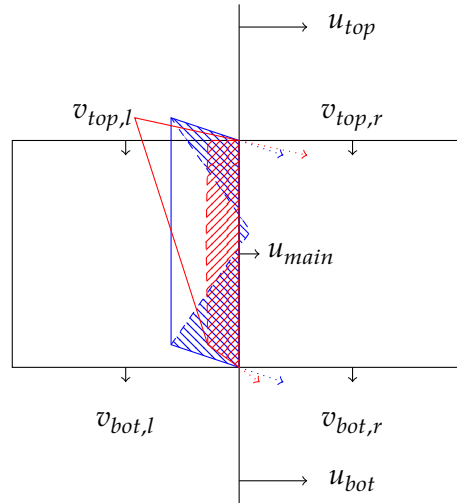
In Fig. 7.13a, a shear flow is considered, an example of EMFPA having a flux of opposite sign than the fluxing face-centered velocity. The DQA scheme prevents this by using the face-centered velocity based on the position of the linear edges of the donating region. In Fig. 7.13b, an example of DQA switching to DDR is given. A negative donating region is created due to the volume correction, which is allowed by EMFPA but not by the DQA scheme.

The authors want to point out that, even though the chance is small, EMFPA can result in a negative donating region that gives a flux larger than the volume constraint. In other words, the size of the hatched area can be larger than the sum of the receiving and the donating region. As a requirement, DQA strictly enforces volume conservation.



(A) Shear flow: presented scheme prevents flux of opposite sign than velocity.

FIGURE 7.13. Difference between EMFPA (■) and the DQA scheme (■) for two different case. The dashed line is the donating region after volume correction. The solid line is the original donating region. The hatched area is the flux δC_f . Liquid is indicated by ■. The air is white. Note that the hatched area for the EMFPA scheme can be larger than the volume constraint $u_{main} \delta t \delta A$, but DQA is not.



(B) In a wake: presented scheme uses DDR to prevent negative region.

FIGURE 7.13. Difference between EMFPA (■) and the DQA scheme (■) for two different case. The dashed line is the donating region after volume correction. The solid line is the original donating region. The hatched area is the flux δC_f . Liquid is indicated by ■. The air is white. Note that the hatched area for the EMFPA scheme can be larger than the volume constraint $u_{main} \delta t \delta A$, but DQA is not.

7.5 Fundamental transport cases

7.5.1 Zalesak slotted disk rotation

The first benchmark case with advection of a fluid structure to be discussed is the Zalesak slotted disk [312]. The Zalesak slotted disk is a well-known benchmark for volume-tracking methods. The disk is rotated for one complete anti-clockwise revolution in a velocity field with uniform vorticity

$$u = -\Omega(y - y_0), v = \Omega(x - x_0), \tag{7.17}$$

where $\mathbf{u}=[u, v]^T$ is the 2D velocity field, $\mathbf{x}=[x, y]^T$ the spatial position, and the position with subscript 'o' the axis of rotation. The domain is four by four with the center of rotation at coordinate (2.00, 2.00). The constant angular velocity Ω is 0.50. The disk has a radius of 0.50 and is initially positioned at coordinate (2.00, 2.75). The slot has a width of 0.12 and stops in the center of the disk. The grid resolution used for the benchmark is 200x200. These parameters are adopted from the work of Rudman [229] and Diwakar, Das, and Sundararajan [65]. The error is defined as

$$E^n = \frac{\sum_{i,j} |C_{f,i,j}^n - C_{f,i,j}^0|}{\sum_{i,j} C_{f,i,j}^0}, \tag{7.18}$$

in which n represents the number of revolutions of the slotted disk.



In Tab. 7.3, the errors of Eq. (7.18) for various reconstruction and advection schemes after one rotation of the disk are given with a reference to the article from which it was taken. The results of the newly presented reconstruction and advection scheme are compared with the state-of-the-art schemes in Tab. 7.3. For an equal comparison, a Courant number of 0.25 is used based on the maximum velocity [163]. The number of times DQA switches back to DDR, as discussed in Sec. 7.4.3.4, is 0%. López et al. [163] commented that the largest error for this case is typically found near the slot and Scardovelli and Zaleski [235] found that PLIC methods normally smooth out parts of the interface with high curvature, like the slot.

Algorithm	Error (E^1)
SLIC [194]	8.38e-2
Hirt-Nichols [115]	9.62e-2
CICSAM [265]	2.02e-2
High-resolution VOF - unstructured grid [141]	1.01e-2
Puckett - stream [108]	1.00e-2
Puckett - DDR [109]	9.73e-3
Puckett - EMFPA [163]	9.73e-3
Youngs - stream [108]	1.07e-2
Youngs - DDR [109]	1.56e-2
Youngs - EMFPA [163]	1.06e-2
QQ - THINC [303]	1.42e-2
SIR - EMFPA [163]	8.74e-3
ACLSVOF uniform triangular grid [5]	7.19e-3
ACLSVOF adaptive triangular grid [5]	1.25e-2
Linear ls. fit - EI-LE [235]	9.42e-3
Quadratic ls. fit - EI-LE [235]	5.47e-3
Quadratic ls. fit + continuity - EI-LE [235]	4.16e-3
QUASI - EMFPA [65]	2.69e-3
Youngs - DQA (current)	1.23e-2
Youngs - COSMIC (current)	1.25e-2
MYC - DQA (current)	1.06e-2
MYC - COSMIC (current)	1.09e-2
Youngs BLIC - DQA (current)	7.76e-3
MYC BLIC - COSMIC (current)	6.38e-3
MYC BLIC - DQA (current)	5.85e-3

TABLE 7.3. Error E^n for slotted disk rotation ($n = 1$). Other schemes are compared with the presented ones. Youngs is an abbreviation for the Parker and Youngs method. Least square is abbreviated with ls.. A Courant number of 0.25 is used.

Algorithm	50×50	100×100	200×200
MYC - DQA (current)	1.39e-1	3.45e-2 (2.01)	1.06e-2 (1.70)
MYC - COSMIC (current)	1.41e-1	3.47e-2 (2.02)	1.09e-2 (1.67)
MYC BLIC - COSMIC (current)	1.42e-1	2.08e-2 (2.77)	6.16e-3 (1.76)
MYC BLIC - DQA (current)	1.38e-1	2.30e-2 (2.58)	5.85e-3 (1.98)

TABLE 7.4. Error E^n for slotted disk rotation ($n = 1$) for different grid resolutions using MYC. A Courant number of 0.25 is used. The order of convergence is in between parentheses.

The error E^1 after one rotation of the disk and the order of convergence obtained when using the reconstruction and advection methods in this work, is shown in Tab. 7.4. For higher grid resolutions, the error can potentially be governed by the number of time steps [235]. Decreasing the Courant number results in higher errors E^1 , because it increases the number of reconstruction and advection steps. Where a Courant number of 1.00 with a grid of 200×200 (MYC BLIC - DQA) results in an error of 4.78e-3, a Courant number of 0.50 gives 5.30e-3, and 0.25 gives 5.85e-3. This effect is also mentioned by Diwakar, Das, and Sundararajan [65], showing that it does not happen with their QUASI scheme.

In Fig. 7.14, the application of BLIC showed that the corners of the slot are better represented than with PLIC. A more accurate PLIC method like MYC reduces the error compared to Paker and Youngs, also in combination with BLIC. The unsplit DQA advection scheme shows a slight reduction of the error compared to COSMIC and a similar error as EMFPA. The combination of DQA and MYC BLIC obtains similar accuracy for the slotted disk as higher-order methods like the Quadratic fit methods [235]. The computational costs are compared in Section 7.5.3.

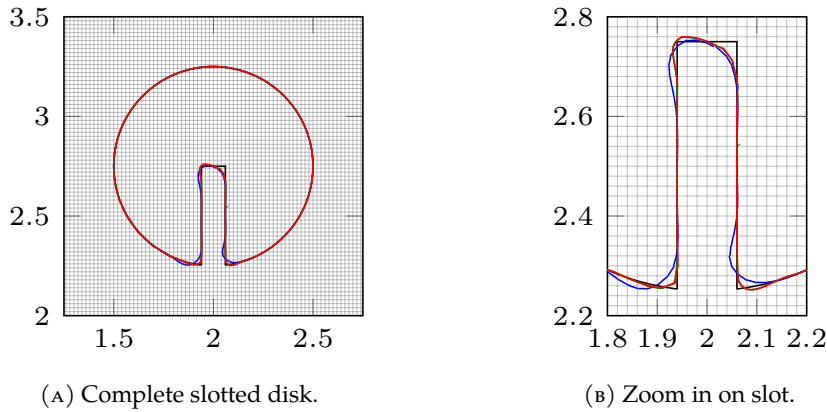


FIGURE 7.14. The interfaces of the Zalesak' slotted disk for one turn with 200×200 . MYC BLIC - DQA is indicated by ■. MYC BLIC - COSMIC is indicated by ■. MYC - COSMIC is indicated by ■. Reconstruction of interface is given for a number of rotations $n = 1$.

7.5.2 Rider–Kothe single vortex

A simple translation or solid body rotation of a fluid structure like the slotted disk by itself is not enough for testing interface modeling methods. No final judgment can be made because this kind of case is not realistic and more suitable for benchmarking and debugging [229]. A more physical case for interface modeling is the reversed single vortex field case by Bell, Colella, and Glaz [11], modified by Rider and Kothe [226].

A solenoidal velocity distribution is imposed for the reversed single vortex field in a domain of one by one. The velocity field is determined by the stream function field

$$\Psi(x, y, t) = \frac{1}{\pi} \sin^2(\pi x) \sin^2(\pi y) \cos\left(\frac{\pi t}{T}\right), \quad (7.19)$$

with T as the period of the reversed motion of the vortex. An initial circle with a radius of 0.15 is positioned at $(0.50, 0.75)$ and deformed until $t = T/2$. Hereafter, the deformed structure deforms back to its initial shape until $t = T$. The error E^T is determined by the difference between the initial and final volume fraction field multiplied by the grid spacing [65]

$$E^T = \sum_{i,j} \delta x_i \delta y_j |C_{f,i,j}^T - C_{f,i,j}^0|. \quad (7.20)$$

According to Scardovelli and Zaleski [235] the main error for the single vortex, as well as for the slotted disk, is caused by the number of reconstructions rather than the advection algorithm.

Period T is chosen to be 2.00. Tab. 7.5 shows the errors E^T for single vortex simulations with the advection and reconstruction methods presented in the

current work. The methods described here are compared to methods from the existing literature. Three different grid resolutions 32×32 , 64×64 , and 128×128 are considered. A Courant number of 0.95 is used, the Courant number at each time level being based on the maximum velocity component in the domain at that time level. In the existing methods, a Courant number of 1.00 was used, but for that number using DQA can lead to mass losses due to overlap in donating polygons caused by the correction point (see Sec. 7.4.3.4). This is elaborated upon below.

Algorithm	32x32	64x64	128x128
Hirt & Nichols + LHF [74]	1.01e-2	5.25e-3 (0.94)	2.47e-3 (1.09)
QQ - THINC [303]	6.70e-2	1.52e-2 (2.16)	3.06e-3 (2.29)
Puckett - stream [108]	2.37e-3	5.65e-4 (2.07)	1.32e-4 (2.10)
Puckett - Rider & Kothe [226]	2.36e-3	5.85e-4 (2.01)	1.31e-4 (2.16)
Puckett - EMFPA [163]	2.14e-3	5.39e-4 (1.99)	1.29e-4 (2.06)
Youngs - stream [108]	2.49e-3	7.06e-4 (1.82)	2.23e-4 (1.66)
Youngs - EMFPA [163]	2.31e-3	6.89e-4 (1.75)	2.25e-4 (1.61)
LSG - COSMIC [74]	2.74e-3	7.01e-4 (1.97)	1.96e-4 (1.84)
LSG - EI-LE [74]	2.70e-3	6.93e-4 (1.96)	1.89e-4 (1.87)
ELVIRA - COSMIC [74]	2.55e-3	6.50e-4 (1.97)	1.51e-4 (2.11)
ELVIRA - EI-LE [74]	2.54e-3	6.47e-4 (1.97)	1.45e-4 (2.16)
CVTNA - PCFSC [160]	2.34e-3	5.38e-4 (2.12)	1.31e-4 (2.04)
Linear ls. fit - EI-LE [235]	1.75e-3	4.66e-4 (1.91)	1.02e-4 (2.19)
Qls. fit - EI-LE [235]	1.88e-3	4.42e-4 (2.09)	9.36e-5 (2.24)
Qls. fit + cont. - EI-LE [235]	1.09e-3	2.80e-4 (1.96)	5.72e-5 (2.29)
Mixed VOF method [5]	1.00e-3	2.69e-4 (1.89)	5.47e-5 (2.30)
SIR - EMFPA [163]	8.62e-4	2.37e-4 (1.86)	5.62e-5 (2.08)
QUASI - EMFPA [65]	6.65e-4	1.57e-4 (2.08)	4.33e-5 (1.86)
PCIC - EMFPA [172]	5.61e-4	1.46e-4 (1.94)	4.17e-5 (1.81)
Youngs - DQA (current)	2.14e-3	5.15e-4 (2.05)	1.66e-4 (1.63)
MYC - DQA (current)	2.09e-3	4.32e-4 (2.27)	1.08e-4 (2.00)
MYC - COSMIC (current)	2.74e-3	6.96e-4 (1.98)	1.80e-4 (1.95)
Youngs BLIC - DQA (current)	1.23e-3	1.88e-4 (2.71)	6.25e-5 (1.60)
MYC BLIC - COSMIC (current)	1.68e-3	4.04e-4 (2.06)	1.40e-4 (1.53)
MYC BLIC - DQA (current)	1.21e-3	2.04e-4 (2.57)	4.42e-5 (2.20)

TABLE 7.5. Error E^T at different grid resolutions for the reversed single vortex field with $T = 2.00$ and Courant number 0.95. Methods presented in this article are compared with methods from the existing literature, for which a Courant number of 1.00 was used. Youngs is an abbreviation of the Parker and Youngs method. The order of convergence is in between parentheses. Quadratic least square is abbreviated with qls..

MYC BLIC - DQA has a lower error compared to other available methods. The method competes in terms of accuracy with higher-order methods like PCIC (piecewise circular arcs) and QUASI (quadratic splines). The choice for a more-accurate PLIC method, like MYC compared to Parker and Youngs, improves the result for reversed single vortex. For a period T of 2.0 and grid 128×128 , MYC BLIC - DQA has a similar error as PCIC - EMFPA. Referring back to Sec. 7.4.3.1, the accuracy of DQA is similar to EMFPA when comparing Youngs - DQA with Youngs - EMFPA. These results show that the use of a non-sloped linear edge has negligible influence on the accuracy for this case.

Fig. 7.15 shows the difference in interface at $t = T/2$ and $t = T$ for six of the single vortex simulations in Tab. 7.5, comparing methods on a grid of 32×32 and on a grid of 128×128 . The interface obtained with MYC BLIC - DQA on the coarser grid comes closest to the interface obtained on the finer grid. On the finer grid the difference between methods is not visible any more. Switching back from BLIC to PLIC was not necessary for the simulations used to make Fig. 7.15; they all met the constraints defined in Sec. 7.2.6.

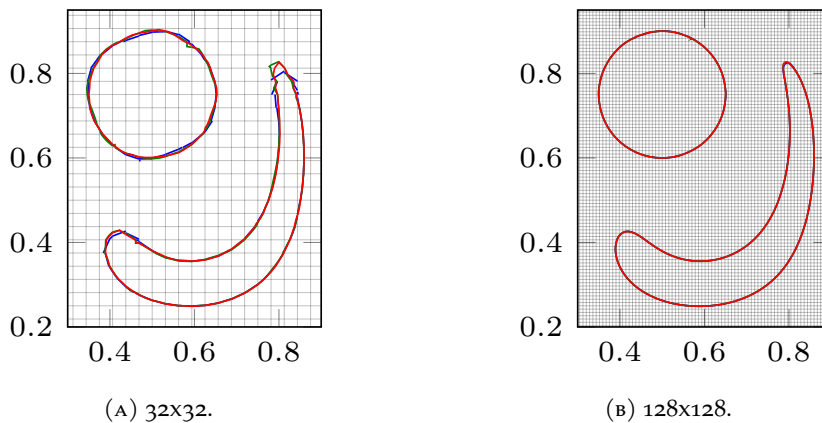


FIGURE 7.15. The interfaces for the reversed single vortex from Rider and Kothe [226] with $T = 2.00$ and Courant number 0.95. MYC BLIC - DQA is indicated by ■. MYC BLIC - COSMIC is indicated by ■. MYC - COSMIC is indicated by ■.

The effect of the Courant restriction on the accuracy of the simulations is evaluated for the methods discussed above. The error E^T , obtained using grid 128×128 , is shown in Tab. 7.6 for values of the Courant number 0.1, 0.5, 0.95 and 1.00. Similar to the slotted disk, a decrease in Courant number does not lower the error when using DQA. The larger error for lower Courant numbers is due to the increased number of reconstructions. When using COSMIC the error does decrease when going from Courant number 1 to Courant number 0.95, and from 0.95 to 0.5, but that due to the fact that COSMIC, with the reconstruction step, is not mass conserving for Courant numbers above 0.5 [295]. Note again that DQA

is not mass conserving either at a Courant number of 1.0 because of the overlap in donating regions. The mass losses for DQA depend on the grid size. The mass losses for MYC BLIC - DQA with Courant number 1.00 are 0.18%, 0.62% and 1.50% respectively, for grids 128×128 , 64×64 and 32×32 . For grids 128×128 and 64×64 DQA switched back to DDR in 0.00% of all time steps, for grid 32×32 DQA switched back in 0.50% of all time steps.

Courant number	0.1	0.5
Youngs - DQA (current)	3.06e-4 (0.00%)	2.66e-4 (0.00%)
MYC - DQA (current)	1.35e-4 (0.00%)	1.21e-4 (0.00%)
MYC - COSMIC (current)	1.39e-4 (0.00%)	1.30e-4 (0.00%)
Youngs BLIC - DQA (current)	2.23e-4 (0.00%)	8.22e-05 (0.00%)
MYC BLIC - COSMIC (current)	1.53e-4 (0.00%)	6.36e-05 (0.00%)
MYC BLIC - DQA (current)	1.34e-4 (0.00%)	4.99e-5 (0.00%)
Courant number	0.95	1.0
Youngs - DQA (current)	1.66e-4 (0.00%)	3.30e-4 (0.04%)
MYC - DQA (current)	1.08e-4 (0.00%)	2.49e-4 (0.18%)
MYC - COSMIC (current)	1.80e-4 (0.04%)	2.47e-4 (0.07%)
Youngs BLIC - DQA (current)	6.25e-5 (0.00%)	2.22e-4 (0.18%)
MYC BLIC - COSMIC (current)	1.40e-4 (0.04%)	1.98e-4 (0.08%)
MYC BLIC - DQA (current)	4.42e-5 (0.00%)	2.15e-4 (0.18%)

TABLE 7.6. Error E^T at grid resolution 128×128 for different Courant numbers. The mass changes are given as a percentage of the initial mass in between parentheses.

In Fig. 7.16, two different grid resolutions and time instances of the interface for a non-reversed single vortex are illustrated. The BLIC method keeps the fluid body better together than PLIC. The number of detached droplets is reduced when using BLIC. Sharper parts of the vortex, especially the front, and the tail are represented better with BLIC than with PLIC. With BLIC the interface could not always be reconstructed for grid resolution 32×32 and switched back to PLIC due to the correction point of BLIC being outside of a cell. The number of time steps BLIC switched to PLIC for that grid until $t = 3.0$ is 8.9% with MYC BLIC - DQA and 13.7% with MYC BLIC - COSMIC. Even when having to switch back to PLIC this many time, there is still an advantage of using BLIC because its error E^T is smaller than for plain PLIC. For grid 128×128 , BLIC switched back to PLIC in fewer than 0.3% of all time steps.

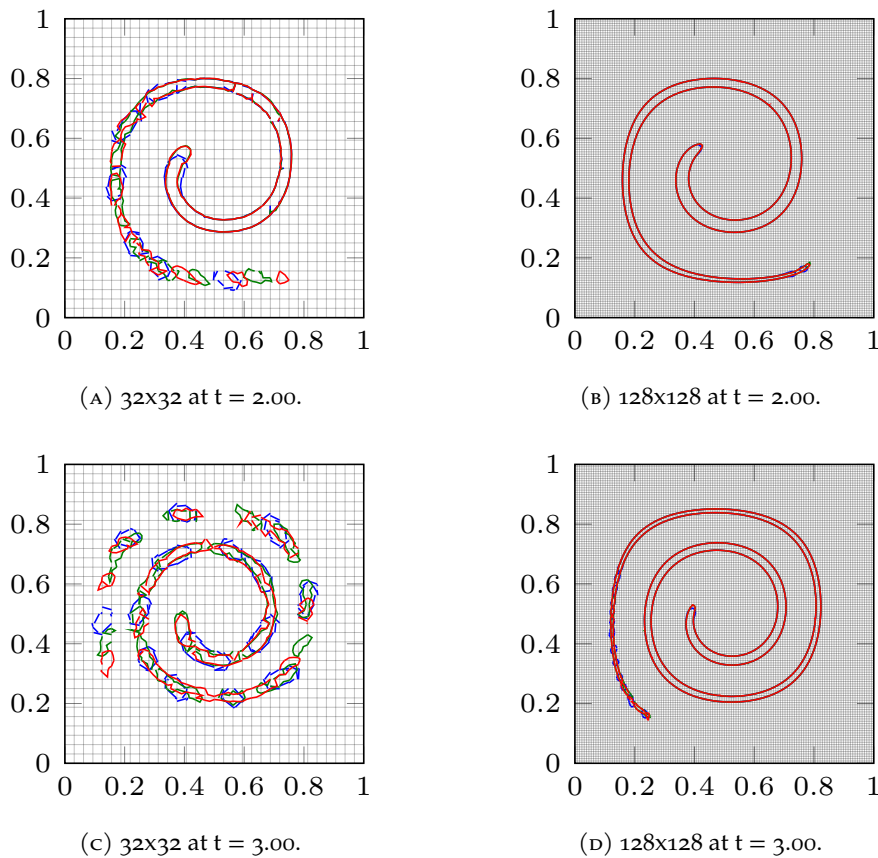


FIGURE 7.16. The interfaces for a non-reversed single vortex with different reconstruction and transport schemes at two time instances. MYC BLIC - DQA is indicated by ■. MYC BLIC - COSMIC is indicated by ■. MYC - COSMIC is indicated by ■.

The effect of determining the slope value ϕ for the DQA scheme is evaluated for the three approaches provided in Eq. (7.16). The results are given in Tab. 7.7 for the combination MYC BLIC - DQA. The volume correction of Owkes and Desjardins [199] has the best results for this case, even though they mentioned that the effect of the volume corrections is probably small.

ϕ	32x32	64x64	128x128
Owkes and Desjardins [199]	1.03e-3	2.18e-4	4.51e-5
zero	1.11e-3	2.22e-4	4.69e-5
avg	1.27e-3	2.52e-4	6.03e-5

TABLE 7.7. Error E^T for different ϕ in Sec. 7.4.3.3 with MYC BLIC - DQA for the reversed single vortex field with $T = 2.00$ and Courant number is 0.95.

7.5.3 Computational costs

The code is written in Python and compiled using the Numba package [151]. The compiled code is run on a 12-core stand-alone machine. In Fig. 7.17, the computational costs of the reconstruction and advection methods are compared for the reversed single vortex, normalized with the costs of the combination Parker and Youngs - COSMIC (Y-C). The costs at three different grid resolutions are compared. The average computational time is based on 384 time steps. The sensitivity of the costs is tested by repeating the same simulation on the same machine. After repeating five times, the cost variation is between 1% and 3%.

The application of the MYC reconstruction method over the Parker and Youngs' method is neglectable in computational costs. BLIC has between 20% and 1% more computational costs than Parker and Youngs. Similarly, as the results of Diwakar, Das, and Sundararajan [65], the costs relatively decrease by increasing the grid resolution.

The costs of the advection scheme become dominant for a higher grid resolution. The presented unsplit advection scheme (DQA) results in an average of around 5% less computational costs than the splitting scheme (COSMIC) when using a PLIC method. Similarly, the extra costs of using BLIC with the COSMIC scheme compared to the DQA scheme are even more dominant. The relative increase in computational costs is because of the additional intermediate reconstruction steps for COSMIC. The DQA scheme does not make use of intermediate reconstruction steps.

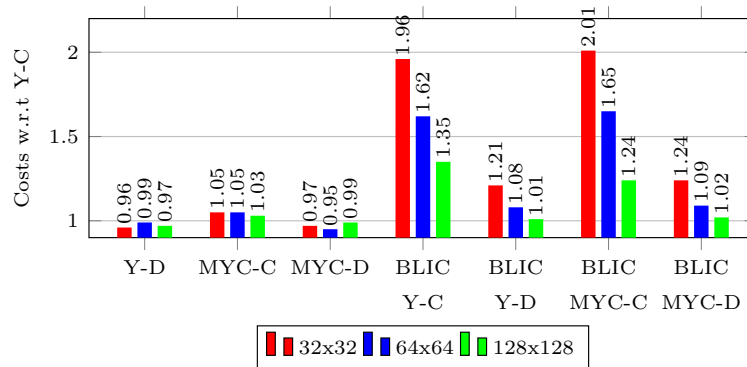


FIGURE 7.17. Comparison of computational costs normalized with the costs of Parker and Youngs - COSMIC (Y-C) for the single vortex case based on 384 timesteps for three different grid resolutions. (D) is DQA. (C) is COSMIC. (Y) is Parker and Youngs' method. (MYC) is Mixed Youngs and Centered method.

Compared to other reconstruction methods in the existing literature of which the costs are documented, BLIC appears to have fairly low costs. The quadratic

least-square reconstruction algorithm with continuity equation seems twice as costly as Parker and Youngs [235]. The QUASI method, showing high accuracy in representing the interface, is around 30 times higher in costs and ELVIRA 10 times compared to Parker and Youngs [65]. The computational costs of the SIR scheme are comparable with BLIC, around 1.1 times higher in costs than Parker and Youngs [163]. PCIC with continuity correction is around 15 times higher in costs compared to Parker and Youngs [172]. Note that it is difficult to compare with accuracy to the reported computational costs of methods in the existing literature. Not for every method cost indications are given. And for ELVIRA, for instance, reports [65, 163, 172] appeared inconsistent. Costs, moreover, depend on the efficiency of coding and the hardware that was used. For these reasons, the comparison in Fig. 7.17 can potentially be valuable, because all methods were implemented in the same code and run on the same machine.

7.6 Consistent mass-momentum transport

'Consistent' is the name used for two-phase methods with staggered variables that make sure that mass and momentum fluxes are determined in the same way, carefully considering that the control volumes for mass and momentum are also staggered with respect to each other [4, 80, 200, 230, 320]. Consistent modeling prevents momentum losses and prevents spurious velocities from being generated near the interface between fluids, that – in some cases – lead to instability.

Consistency is analyzed for the transport and reconstruction methods described in this work, in combination with the two-phase method of Eijk and Wellens [80]. The results of Eijk and Wellens [80] show temporal plots of momentum losses which are nearly zero. When spurious velocities do occur and when they can be explained in terms of the discretization of mass and momentum, we call them 'inconsistencies'. The discretization of the density is key for explaining the inconsistencies.

7.6.1 *Brief overview of two-phase solver*

A brief overview of the two-phase solver is needed to explain from where inconsistencies originate. The governing equations for two-phase flow are formulated as if it is a single homogeneous mixture [188]. The motion of the mixture is described in terms of a single velocity and a single pressure field, solving the continuity equation and the momentum equation, together with the advection equation for the interface. Viscous, capillary, and gravitational effects are neglected for the purpose of this work.

A 2D Cartesian grid of cells is adopted. According to the staggered MAC configuration of variables, velocities ($\mathbf{u} = [u, v]^T$) are defined in grid cell faces, and scalar variables, the pressures (p), volume fractions (C_f), and densities (ρ), are defined in grid cell centers. How continuity control volumes (V_c) and momentum control volumes (V_m), different for each velocity direction, are defined with respect to the grid cells is shown in Fig. 7.18.

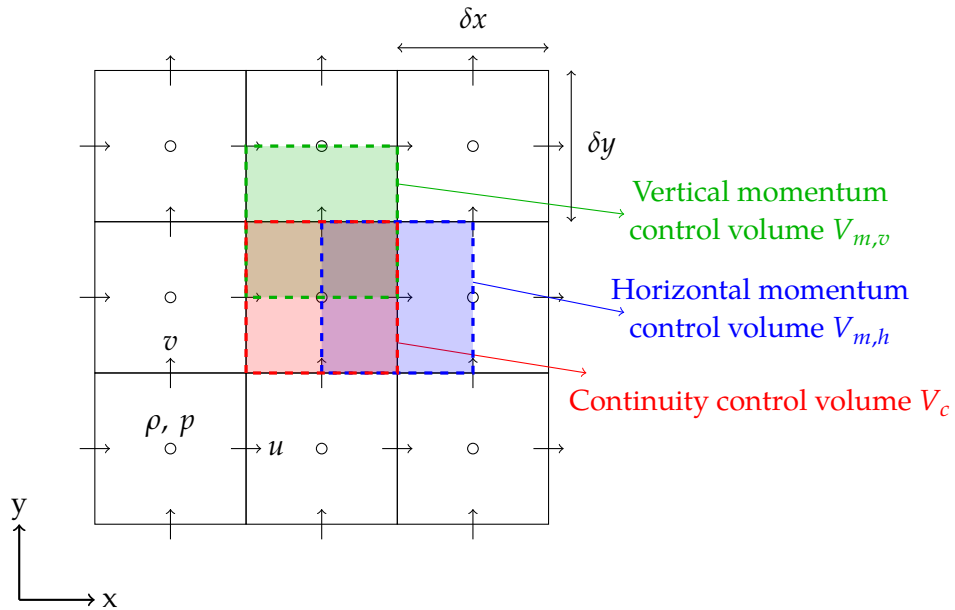


FIGURE 7.18. Standard MAC configuration of variables (staggered); pressure p is defined in the cell center (\circ), the horizontal velocity u field is sampled on the vertical faces (\rightarrow), the vertical velocity v is sampled on the horizontal faces (\uparrow). The overlap of the continuity control volume ($-$), with a vertical momentum control volume ($-$), and with a horizontal momentum control volume ($-$) is shown.

Considering the time discrete version of the continuity, momentum and advection equation, using Forward Euler in time for brevity of notation, the equations are integrated over control volumes to obtain the weak form. The weak form is the basis of the discretization in space. First, the fluids are advected using Eq. (7.9), repeated here without equation number to be complete

$$\int_{V_c} \frac{C_f^{n+1} - C_f^n}{\delta t} dV = - \oint_{S_c} \underbrace{(\mathbf{u}^n C_f^n)}_{consistent} \cdot \mathbf{n} dS.$$

Here, S_c refers to boundary of the control volume V_c shown in Fig. 7.18. Transport and reconstruction of the interface are solved for continuity control volumes

7

with labels S and C (refer to the labeling system in Sec. 7.2.1). Because the fluids are considered incompressible, the continuity equation reduces to

$$\oint_{S_c} \mathbf{u}^{n+1} \cdot \mathbf{n} dS = 0. \quad (7.21)$$

The time discrete momentum equation is solved in steps, the main step being

$$\int_{V_m} \frac{\rho^{n+1} \mathbf{u}^{n+1} - \rho^{n+1} \bar{\mathbf{u}}}{\delta t} dV = - \oint_{S_m} p^{n+1} \mathbf{n} dS, \quad (7.22)$$

in which auxiliary vector field $\bar{\mathbf{u}}$ in Eq. (7.22), without viscous, capillary and gravitational effects, is solved from

$$\int_{V_m} \frac{\bar{\rho} \bar{\mathbf{u}} - \rho^n \mathbf{u}^n}{\delta t} dV = - \oint_{S_m} \underbrace{\rho^* \mathbf{u}^n (\mathbf{u}^n \cdot \mathbf{n})}_{\text{consistent}} dS, \quad (7.23)$$

whereas auxiliary density $\bar{\rho}$ is solved with a temporary continuity equation that is integrated over momentum control volumes

$$\int_{V_m} \frac{\bar{\rho} - \rho^n}{\delta t} dV = - \oint_{S_m} \underbrace{(\mathbf{u}^n \rho^*) \cdot \mathbf{n}}_{\text{consistent}} dS. \quad (7.24)$$

Here, ρ^* is a density for which a consistent discretization in space is used. A *consistent* space discretization for momentum and mass is obtained when the advective terms indicated by the word 'consistent' are treated the same with continuity control volumes and with momentum control volumes, and when the spatial discretization of ρ^n and ρ^{n+1} is the same on continuity control volumes and on momentum control volumes. The density ρ^{n+1} is solved differently from $\bar{\rho}$.

The new density ρ^{n+1} is associated with the fluid volume in a momentum control volume. The fluid volume A in a momentum control volume is calculated with volume fraction field C_f^{n+1} and the fluid-interface orientation: $\rho = A\rho_f + (1 - A)\rho_{1-f}$, with ρ_f the constant density of the fluid that is advected (typically the heavier of the two fluids), and ρ_{1-f} the constant density of the other fluid.

The auxiliary density $\bar{\rho}$ is calculated using ρ^* . The value of ρ^* depends on the size of the VOF flux δC_f at the boundary of the momentum control volume, so that consistency is obtained between the mass flux and the momentum flux. The momentum flux $\rho^* \mathbf{u}$ is discretized using

$$\rho^* \mathbf{u} = (C\rho_f + (1 - C)\rho_{1-f}) \mathbf{u}, \quad (7.25)$$

in which C is a scalar fraction indicating the VOF flux normalized by the size of the donating region [320]. This discretization ensures consistency between mass and momentum flux.

$$C = \frac{|\delta C_f|}{|\mathbf{u}| \delta t \delta A}. \quad (7.26)$$

The density ρ^* is above zero by definition and, therefore, absolute values of flux and velocity are used.

7.6.2 Application of an advection scheme to the solver

Besides calculating the VOF fluxes around the faces of the continuity control volume for Eq. (7.6.1), additional VOF fluxes need to be calculated around the faces of the momentum control volumes for Eqs. (7.24) and (7.23) to find ρ^* . Owkes and Desjardins [200] dealt with this in a similar way. The VOF flux positions for all control volumes are illustrated in Fig. 7.19, including examples of donating regions for a flow that is directed to the right and to below. Fig. 7.19 shows one of the nine continuity control volumes in Fig. 7.18. The continuity control volume is subdivided in four quadrants so that fluxes of mass and momentum can be matched in continuity control volumes, horizontal and vertical control volumes. An arrow is drawn at every face of a quadrant, representing a VOF flux that requires computation. Per 2D grid cell, not four, but twelve VOF fluxes are calculated.

The thick-lined arrows in Fig. 7.19 are the cell-face-centered velocities solved from the system in Eq. (7.22). These velocities are assumed constant along a cell face. Therefore, the unknown sub-velocities for the faces of the quadrants are equal to the solved face-centered velocity, for instance for the velocities on the right-hand side of the cell: $u_{right} = u_{right,1} = u_{right,2}$. The same applies to u_{left} , v_{bot} , and v_{top} . The velocities in the middle of a grid cell (u_{mid} and v_{mid}) are not the same as the velocities in the cell faces. An averaging procedure is used to find these velocities. They are found from $v_{mid} = \frac{1}{2} (v_{top} + v_{bot})$ and $u_{mid} = \frac{1}{2} (u_{left} + u_{right})$. The sum of the two fluxes at the position of $v_{mid,1}$ and $v_{mid,2}$ in Fig. 7.19 results in the total VOF flux through the bottom face of the vertical momentum control volume needed for ρ^* . The same is true for the horizontal control volume fluxes at the position of u_{mid} .

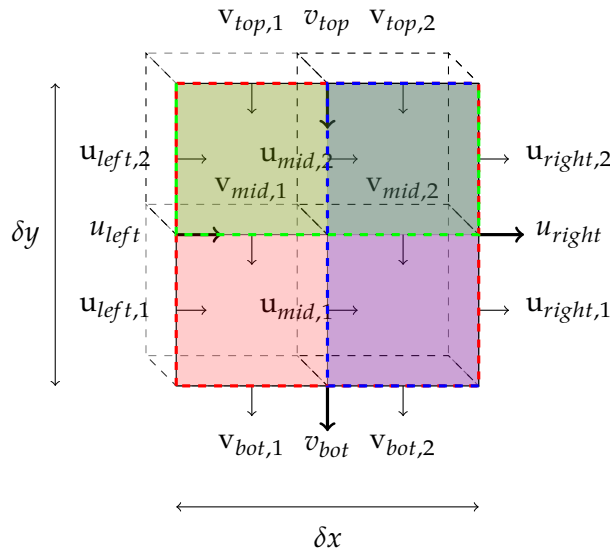


FIGURE 7.19. Subdivision of a grid cell in quadrants. DQA donating regions needed for a consistent discretization with a staggered arrangement are also indicated; solid black is the border of the grid cell and dashed black borders are the donating regions based on the sub-velocities. The u_{main} velocity for every donating region is given. Cell-face-centered velocities are thick-lined. The other arrows are sub-velocities. The overlap of the continuity control volume (—) with a vertical momentum control volume (—) is indicated, as well as the overlap with a horizontal momentum control volume (—).

The sub-velocities in Fig. 7.19 are used to reconstruct the donating region. The linear edges of the donating regions (black dashed lines in Fig. 7.19 representing the (sub-)donating regions) are calculated as in Sec. 7.4 using the sub-velocities of the cell quadrants. The sum of two donating regions along a cell face should be equal to the volume constraint, where ‘volume constraint’ means the total amount of fluid to be fluxed. For example, the volume constraint for the donating regions at the face indicated with *right* is $u_{right}\delta y = \frac{1}{2}u_{right,1}\delta y + \frac{1}{2}u_{right,2}\delta y$.

Similarities with Owkes and Desjardins [200] are found in dividing the cell into sub-cells. Even though they make use of vertex-centered velocities and adopt the method of Rudman [230], reconstructing the interface in sub-cells to create consistency and a conservative scheme, a difference is found in the way of correcting the donating region such that they comply with the volume constraint. In our case, for every sub-velocity a donating region with a correction is defined, resulting in a less complex system but more correction calculations.

7.6.3 Inconsistency

A method is considered to be fully consistent when the auxiliary density $\bar{\rho}$ is the same as ρ^{n+1} , see Eqs. (7.22) and (7.23). The method in Rudman [230] is fully

consistent with both transport and reconstruction of the interface taking place in cell quadrants, but also computationally expensive. Reconstruction handled in complete cells, instead of in cell quadrants, can lead to small inconsistencies. The overlap of the interface reconstruction in the continuity and momentum control volume is the reason for this. The problem is that $\bar{\rho}$ does not account for the reconstruction of the fraction field in a complete cell (or continuity control volume), while ρ^{n+1} does. Collocated approaches, like in Bussmann, Kothe, and Sicilian [29] and in Rudman [230], do not have this issue.

Zuzio et al. [320] use grid cells divided up in quadrants to determine mass fluxes, but reconstruct the interface in complete grid cells. In theory, reconstructing the interface in this way can lead to inconsistency because during reconstruction fluid can be moved from one quadrant to another, without having mass fluxes associated with that movement. Zuzio et al. [320] have demonstrated, however, without explicitly stating it in their article, that the effect of this type of inconsistency on the overall accuracy of the method is marginal, which was confirmed later by Eijk and Wellens [80] when using a similar approach in combination with the COSMIC transport method that reduces direction-split errors through an additional step including intermediate reconstruction.

An example of the non-problematic inconsistency described above with single-step advection methods is given in Fig. 7.20. The interface is transported in 1D with a constant velocity. The grey area shows the fluid configuration before transport. The hatched area shows the fluid configuration after transport. The numbers represent the volume fraction in half of a momentum control volume (in blue), normalized by the size of the momentum control volume. Fig. 7.20a gives the configuration of the fluid after transport (net value of all fluxes), but before reconstruction. The volume fraction in the halves of the momentum control volume then has a value that correspond to the fluxes. After reconstruction, in Fig. 7.20b, the volume fraction in the halves of the momentum control volume has changed. And because density field $\bar{\rho}$ is based on the VOF fluxes, and density field ρ^{n+1} is based on the volume fraction, an inconsistency between $\bar{\rho}$ and ρ^{n+1} arises.

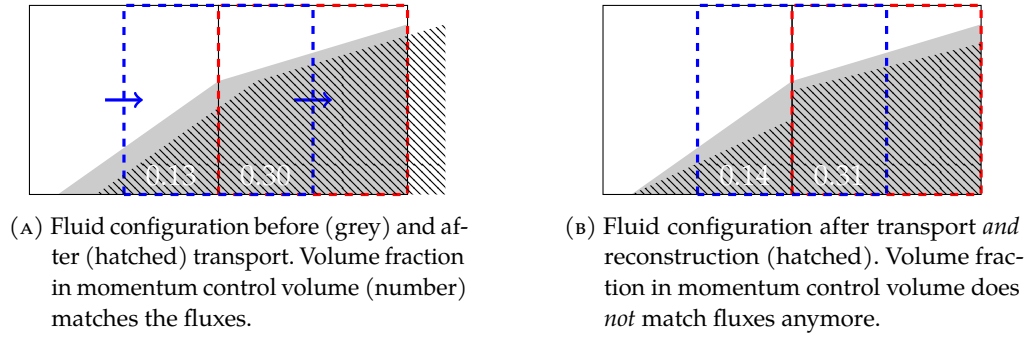


FIGURE 7.20. Interface transport and reconstruction resulting in inconsistency between $\bar{\rho}$ and ρ^{n+1} , because $\bar{\rho}$ is based on the fluxes (leading to fluid configuration in (a)) and ρ^{n+1} is based on the volume fraction after reconstruction (fluid configuration in (b)). Volume fraction before transport is indicated by ■. Volume fraction after transport is indicated by hatched area. The cell boundary (—), the horizontal momentum control volume (---), and continuity control volume (---) are also shown. The arrows represent the VOF fluxes through the faces of the momentum control volume. The values give the volume fraction of half the momentum control volume, normalized by the size of the total momentum control volume.

For incompressible flow modeling using the mixture formulation, the conditions $\rho_{1-f} < \bar{\rho} < \rho_f$ and $\rho_{1-f} < \rho^{n+1} < \rho_f$ for $\rho_{1-f} < \rho_f$ need to hold. Density ρ^{n+1} is associated with the volume fractions in a momentum control volume. As \mathcal{A} , as well as C_f , is bounded between 0 and 1, ρ^{n+1} always satisfies these criteria. Density $\bar{\rho}$ is based on the VOF fluxes. It therefore depends on the advection scheme whether $\bar{\rho}$ satisfies the conditions.

Upon more careful consideration, it was found that the intermediate reconstruction in COSMIC lead to a more substantial inconsistency, resulting in spurious velocities, negative densities $\bar{\rho}$ and even instability. Compared with the non-problematic reconstruction step discussed above, this intermediate reconstruction does violate the criteria given. The mechanism is explained below and is true for all direction-split schemes that include intermediate reconstruction (another example is the MACHO scheme [155]).

A sequence of steps of how a negative value for $\bar{\rho}$ can come about with COSMIC is given in Fig. 7.21 using the notations in Sec. 7.4.2. The hatched area indicates the size of the flux. The advection of the interface is split in fluxing the vertical direction first (Fig. 7.21a) to obtain the intermediate volume fraction field C_f^* , then reconstructing the interface to obtain $C_f^{n+1/2}$ (Fig. 7.21b), followed by fluxing in horizontal direction to obtain C_f^{n+1} (Fig. 7.21c).

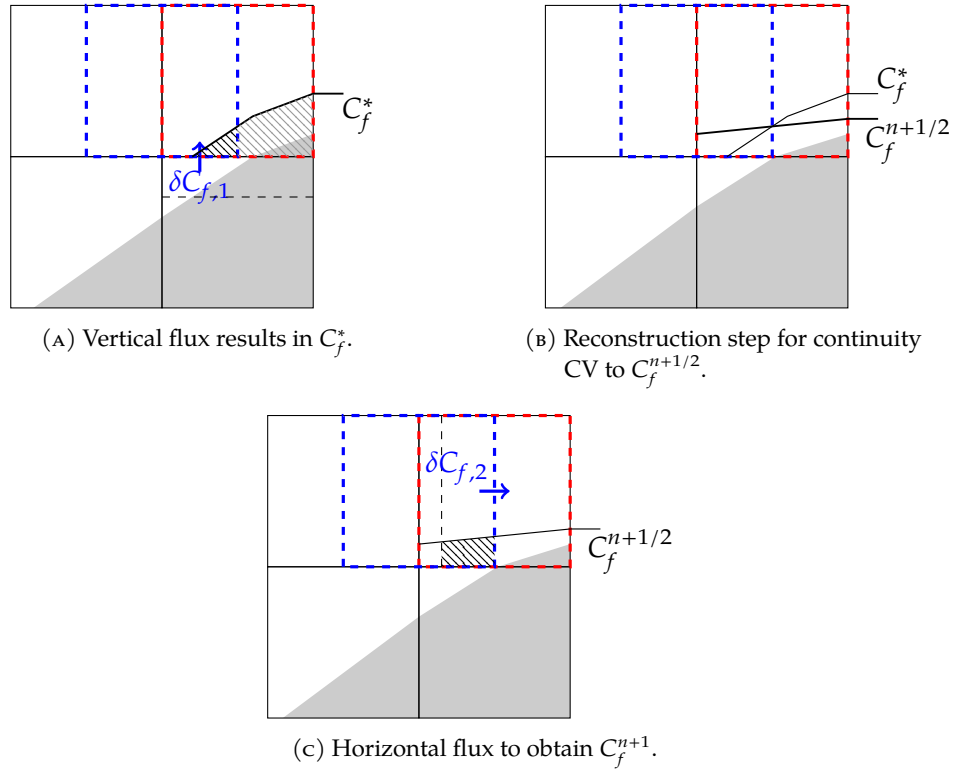


FIGURE 7.21. Problematic inconsistency due to intermediate reconstruction in COSMIC. Fluid C_f^n is indicated by ■. The cell boundary (—), the horizontal momentum control volume (—), and continuity control volume (—) are shown. The black hatched area indicates the flux for the momentum control volume. The black dashed line is the donating region for the given face-centered velocity.

The initial density ρ^n in Fig. 7.21 is equal to zero inside the momentum control volume. Using the variables from the situation of Fig. 7.21 in Eq. (7.24) results in an expression like

$$\bar{\rho} = -\frac{1}{\delta V_m} (\delta C_{f,2} - \delta C_{f,1}) \rho_f \tag{7.27}$$

in which it is assumed that the only non-zero VOF fluxes are $\delta C_{f,1}$ and $\delta C_{f,2}$, that δV_m is the size of the momentum control volume, and that $\rho_f \gg \rho(1-f)$. When, due to intermediate reconstruction $\delta C_{f,2}$ is larger than $\delta C_{f,1}$, so when the hatched area in Fig. 7.21c is larger than in Fig. 7.21a, then a negative value for $\bar{\rho}$ is obtained. Our experience is that negative densities lead to spurious velocities, which affect the time step through the Courant criterion. When the time step is kept the same, the spurious velocity may lead to instability.

Solutions to prevent negative densities could be to apply reconstruction in cell quadrants as in Rudman [230] with much increased computational effort. Another solution altogether could be to adopt a discretization based on a collocated



arrangement of variables and control volumes. The solution we chose to obtain a robust, accurate and consistent method for two-phase flow simulations was to develop DQA, an unsplit advection method.

DQA is inspired by EMFPA. When researching the application of EMFPA for our applications, another problematic inconsistency was encountered that can lead to negative values of $\bar{\rho}$, and even instability, when the VOF flux is of opposite sign from the velocity in the same control volume face. Where the donating region for direction-split methods is always solely on one side of the control volume face, a multidimensional unsplit advection scheme like EMFPA can generate negative donating regions, as shown in Figs. 7.2, 7.11f, and 7.13b. Negative donating regions can result in a VOF flux δC_f directed inwards of a momentum control volume, while the velocity \mathbf{u} points outwards.

An example of a negative donating region is illustrated in Fig. 7.22, in which the VOF flux δC_f is larger than the available fluid volume. Using Eq. (7.25) results in momentum $\rho^* u$ of opposite sign from the VOF flux. Using Eq. (7.24)

$$\bar{\rho} = \left(A^n - \frac{\delta C_f}{\delta V_m} \right) \rho_f \tag{7.28}$$

for the situation in Fig. 7.22, in which the value of A^n is smaller than the VOF flux $\frac{\delta C_f}{\delta V_m}$, while assuming that $\rho_f \gg \rho_{(1-f)}$, leads to a negative value for $\bar{\rho}$, spurious velocities and, potentially, instability. There is even the chance with EMFPA, although small, that the VOF flux δC_f in the negative donating region is larger than the volume constraint $u \delta t \delta A$. Then, fraction C in front of fluid ρ_{1-f} in Eq. (7.25) becomes negative, at which time mass conservation is not longer enforced. DQA, which does not allow for negative donating regions by design, prevents the problematic inconsistency.

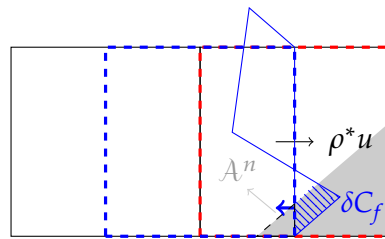


FIGURE 7.22. Negative donating region when using EMFPA. Volume fraction C_f is indicated by ■. The donation region is shown in (-). The hatched area is the VOF flux δC_f . Momentum flux $\rho^* u$ is of opposite direction from the VOF flux δC_f . In case the fluid volume (A^n) is smaller than the VOF flux δC_f , a negative density $\bar{\rho}$ is found, potentially leading to spurious velocities and instability.

7.6.4 The effect of the advection scheme on stability

Simulations with the two-phase solver of Eijk and Wellens [80] are performed to demonstrate the effect of inconsistency on the results. Two cases are considered. The first is designed to show the negative densities associated with the intermediate reconstruction step when using COSMIC for fluid transport. The second case is designed to show the negative densities resulting from negative donation regions when using EMFPA for fluid transport. The results of both cases are compared with the simulation results in which DQA is used for fluid transport. In all simulations, BLIC-MYC is used to reconstruct the interface.

The setup of the first case is shown in Fig. 7.23. A 2D cylinder (circle) composed of high-density fluid is translated diagonally through the domain at a constant velocity of 14.14[m/s] . The cylinder is surrounded by a low-density fluid with a uniform velocity of the same magnitude and in the same direction as the velocity of the high-density cylinder. The relative velocity between fluids, therefore, is zero and further velocity changes should not occur. The density ratio between fluids is 10^6 . The effect of the grid resolution on the results is investigated by considering three grid resolutions with 40×40 , 80×80 , and 120×120 grid cells. The time step is kept restrained at a value corresponding to an initial Courant number of 0.2. The Courant number is based on the size of the momentum control volume. The simulations finish after 100 time steps.

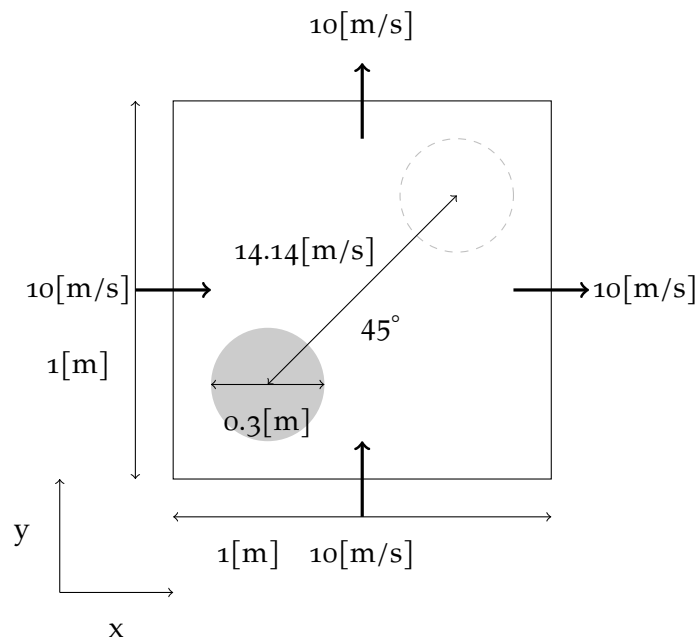


FIGURE 7.23. Simulation setup with cylinder of high-density fluid translating diagonally through low-density fluid at zero relative velocity.

The results of the 40×40 simulation with the diagonal translation of the fluid cylinder are shown in Fig. 7.25. Contour plots of the pressure after 50 time steps are given. The pressure distribution in the simulation with COSMIC is showing a region with lower pressure and a region with higher pressure which is unexpected for a simulation with zero relative velocity between the high-density fluid cylinder and the surrounding fluid. These regions are caused by spurious velocities that themselves are caused by the negative density that has developed according to the mechanism described above. As shown on the right of Fig. 7.25, a simulation with DQA instead of COSMIC, but otherwise the same, yields the expected results and does not show any pressure gradients.

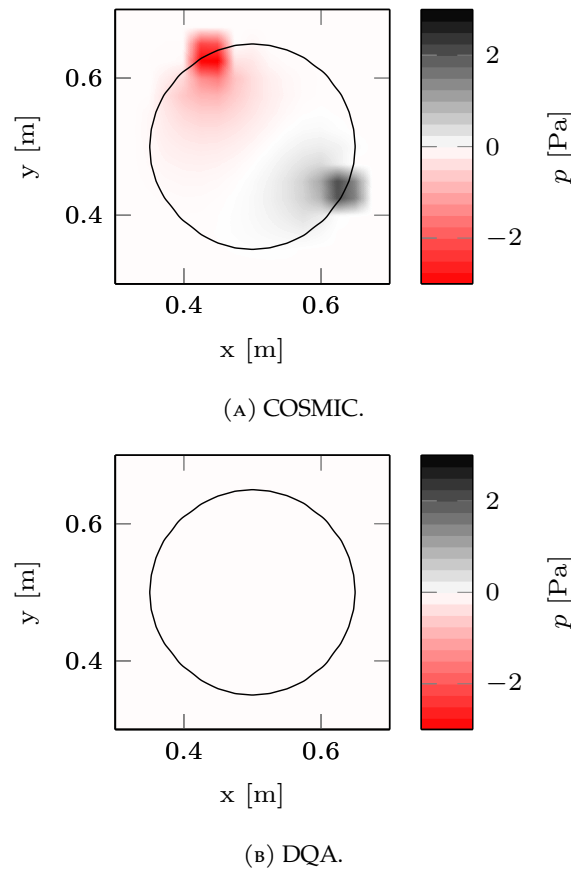


FIGURE 7.24. Contour plot of pressure in 40×40 simulation after 50 time steps. The interface is shown as a continuous black line. Results with COSMIC, to the left, feature regions of low and high pressure caused by spurious velocities. The simulation with DQA gives the expected results for this case without pressure gradients.

Fig. 7.25 compares the interfaces between COSMIC and DQA for two grid resolutions, 80×80 and 120×120 . For both grid resolutions, the interface with COSMIC

is highly distorted as a result of the spurious velocities, whereas the interface with DQA is as expected. The interface distortion does decrease with increasing grid resolution. Both simulations with COSMIC became unstable, but the simulation with a grid resolution of 120×120 became unstable at a later time step than the simulation with a grid resolution of 80×80 .

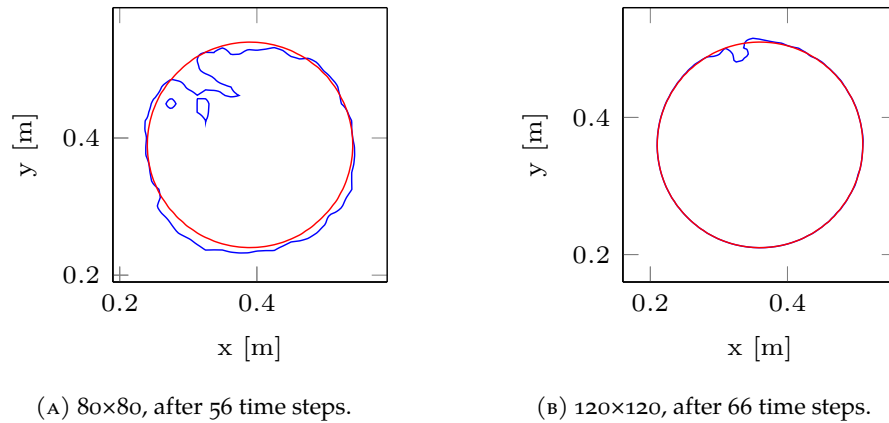


FIGURE 7.25. The interface between fluids in 80×80 and 120×120 simulations at two time levels. COSMIC is $-$. DQA is $-$. The interface in the simulations with COSMIC is highly distorted, whereas the simulations with DQA give the expected results.

The density $\bar{\rho}$ should be in between ρ_f and ρ_{1-f} . However, the simulation with COSMIC resulted for every time step in over- and undershoots of the density $\bar{\rho}$ in the order of 50. The over- and undershoots increase when the simulation becomes unstable until it crashes. An overshoot of $50[\text{kg}/\text{m}^3]$ compared to a density ratio of 10^6 seems small but can result in instability. The spurious velocities are smaller for lower density ratios. It must be noted that the simulations became unstable because we did not allow the time step to decrease according to the Courant criterion.

It is our experience, from Eijk and Wellens [80] and the present work, that exaggerating the density ratio with respect to more common ratios such as for water and air, helps trigger issues when they are there. The undershoots and overshoots of the intermediate density $\bar{\rho}$ seemed inconspicuous, but set a chain of events into motion that can even lead to unstable simulations.

The second case is designed to demonstrate the effect of having negative donating regions when using the EMFPA unsplit advection scheme in a two-phase flow solver with a high-density ratio between fluids. Negative donating regions can also lead to negative densities and spurious velocities. The mechanism is different from that with COSMIC, but the effect on the robustness of the solver

is the same. The previous case discussed does not show any issues for EMFPA because no negative donating regions are created with the imposed constant velocity field. The chance of negative donating regions increases for shear flows as in Fig. 7.13a.

The simulation setup is shown in Fig. 7.26. A 2D square of high-density fluid is at rest while being surrounded by low-density fluid moving with an undisturbed velocity magnitude of 10[m/s] . The density ratio between fluids is 10^6 . Two grid resolutions, 86×86 and 87×87 , are considered to show how sensitive EMFPA can be for the specific configuration of fluids. The time step is allowed to vary so that at any time the Courant number is lower than 0.4 . The simulations end at $t = 0.05\text{[s]}$. The thought behind the setup is to represent a shear flow, in which negative donating regions are constructed with EMFPA as in Fig. 7.13a. DQA does not allow negative regions to be formed. In absence of gravity and viscous stresses, the setup should not result in deformation or movement of the square of fluid. The differences between the simulation results with EMFPA and with DQA will be discussed.

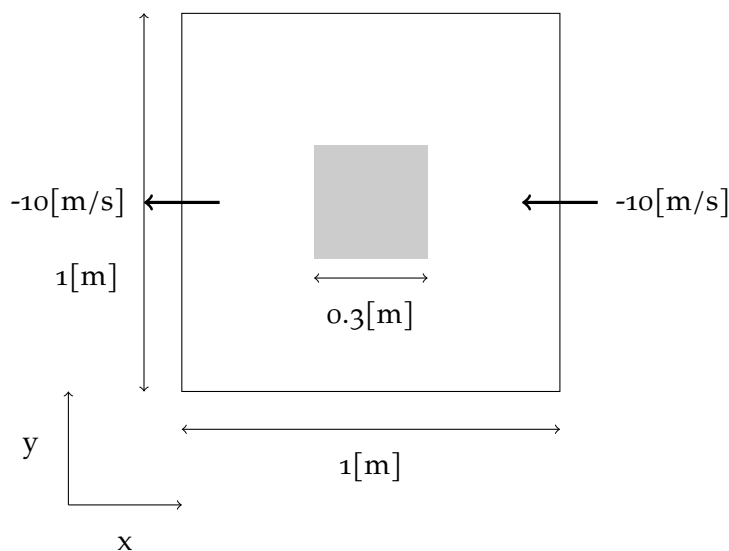
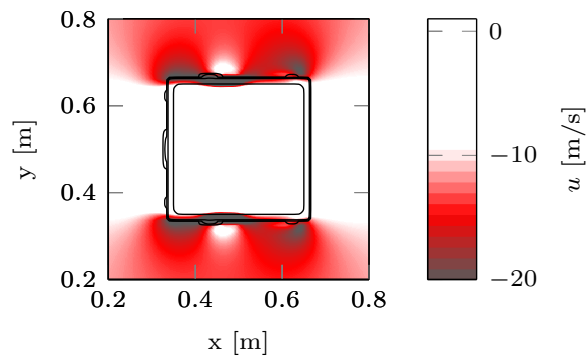
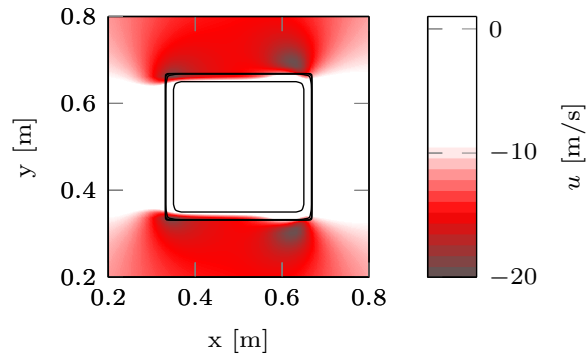
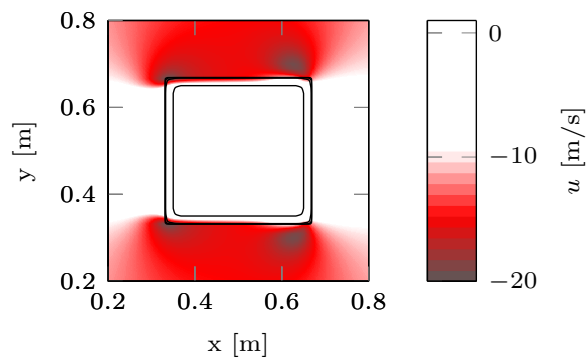


FIGURE 7.26. Simulation setup with square of high-density fluid at rest surrounded by low-density fluid moving with an undisturbed velocity magnitude of 10 m/s .

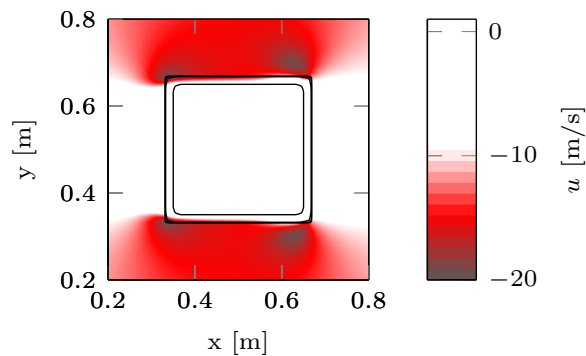
The differences between the simulation results with EMFPA and with DQA are most apparent when the horizontal velocity field is shown together with the interface between fluids. Fig. 7.27 shows the horizontal velocity and interface of four simulations at time $t = 0.005\text{[s]}$. The top row in Fig. 7.27 is for grid resolution 86×86 and has the EMFPA results on the left and the DQA results on

the right. The EMFPA results for grid 86×86 feature a distorted interface caused by negative densities, resulting in spurious velocity oscillations that attain a magnitude as high as 70 [m/s] (the scale in the plot goes until 20 to be able to compare with the other plots in the figure). The bottom row of Fig. 7.27 shows the results of the simulation with a grid resolution of 87×87 , again with EMFPA on the left and DQA on the right. For grid 87×87 , the results of EMFPA and DQA are the same and equal to what could be expected. The difference between the results of the simulations with EMFPA, with a marginal difference in grid resolution, indicates how sensitive a two-phase flow solver can be to negative densities.

(A) EMFPA 86×86 .(B) DQA 86×86 .



(c) EMFPA 87×87.



(d) DQA 87×87.

FIGURE 7.27. Contour plot of horizontal velocity and interface at $t = 0.005$ [s] in simulations with EMFPA and DQA at slightly different grid resolutions. Contour levels of the interface represent volume fraction values of 0.5, 0.01, 0.001, and 0.0001, becoming smaller from the high-density square towards the low-density surrounding fluid. EMFPA generates spurious velocities near -70 [m/s] (not shown, minimum of scale is -20 [m/s]).

The interface deformation with EMFPA is related to the specific position of the interface in a grid cell with a grid resolution of 86×86 and to EMFPA using vertex velocities. When a grid cell containing the interface is nearly filled, then, due to the high velocity of the low-density fluid, a negative donating region can be formed with a VOF flux of the opposite sign from the main velocity in that cell (see Fig. 7.13a). That VOF flux deforms the interface, which induces a negative density. With grid resolution 87×87 , the grid cells near the interface have a lower volume fraction which prevents the negative donating region from being formed. DQA is not sensitive to this mechanism because it does not allow the creation of negative donating regions.

The spurious horizontal velocities in the 86×86 EMFPA simulation are a consequence of negative densities which are caused by the VOF fluxes in interface

cells of opposite sign from the velocity in those cells. Negative densities $\bar{\rho}$ were computed with values up to $-350[\text{kg}/\text{m}^3]$ in more than 50% of the time steps according to the mechanism explained above: solving the velocity field $\bar{\mathbf{u}}$ in Eq. (7.23), using Eqs. (7.25) and (7.24) yields a negative density $\bar{\rho}$, resulting in a change in sign of the velocity. The pressure field needs to ensure a divergence-free field and, therefore, induces a larger correction of the velocity field, giving even higher velocities.

7.7 Conclusion

A new bilinear interface calculation (BLIC) method is introduced for reconstructing the interface in a 2D Volume-of-Fluid (VOF) method. A new multidimensional consistent unsplit VOF advection method, DQA, which is short for Donating Quadrant Advection, is presented using face-centered velocities that is conservative, low-cost, and accurate. It allows the fluid to enter and exit a cell in a time step.

Both BLIC and DQA are tested with standard 2D benchmarks like static reconstruction of two different shapes, Zalesak's slotted disk, and a reversed single vortex field. The BLIC method uses a robust curvature-weighted averaging method with a piecewise linear segment as starting point to create continuity of the interface along the cell faces. Weighting using the curvature increases the accuracy of the BLIC method, especially for underresolved material interfaces. The accuracy of BLIC for higher grid resolutions converges to the accuracy of PLIC on a grid twice as fine. The additional computational costs compared to Parker and Youngs' PLIC method is up to 20%, decreasing to 1% for higher grid resolutions. However, the increase in accuracy of representing the interface is up to an order of magnitude. The BLIC method needs a less dense grid and less computational time to reach similar accuracies as the PLIC method.

The DQA scheme we present shows similar accuracy as the state-of-the-art vertex velocities-based EMFPA scheme for traditional benchmarks. The computational costs of the unsplit DQA scheme are lower than for a direction-split scheme like COSMIC, mostly because of the intermediate reconstruction steps a direction-split scheme uses. The combination of the BLIC and DQA methods is competitive with higher-order methods in terms of accuracy but outperforms most of them in computational cost based on provided data from literature.

An important additional benefit of the DQA scheme is introduced to ensure consistency for an existing consistent two-phase flow solver with a staggered arrangement of variables. Consistency means using the same discretization techniques for determining the momentum, mass, and VOF fluxes and carefully matching them in the different control volumes that are staggered with respect

to each other. Consistency is achieved by incorporating the VOF fluxes in the discretization of the density. Negative densities due to inconsistency are found for an intermediate reconstruction step in COSMIC, and for a VOF flux of the opposite sign than the velocity in EMFPA. The negative densities result in spurious velocities and instability near the fluid interface. The DQA scheme prevents these negative densities and remains stable and accurate in a simulation of a translating high-density cylinder in a low-density fluid, for which COSMIC fails, and in a simulation with a square of high-density fluid in a shear flow with low-density fluid, for which EMFPA fails.

CONCLUSIONS AND FUTURE WORK

This chapter outlines the main results and findings of each part of this thesis and suggests any future research work.

8.1 Results and main findings

The overarching objective in this thesis is the development of a new pressure-based compressible multiphase flow model that can account for the effect of a compressible air-water mixture on the loadings on a freely-moving body. The emphasis lies on building a fast and robust model from scratch where well-considered decisions are made for numerical techniques. The capability of the method should be modeling the compressibility of the air-water mixture, high-density ratio flows, and presence of pressure waves when it gets in contact with a moving body.

In order to obtain this method, the starting point is the one-phase flow model in ComFLOW, used because of being fast and robust for the prediction of water-wave impacts. The thesis is separated in three parts:

1. Develop an adequate semi-compressible pressure-based two-phase method that can model high-density ratio flows, represent the compressibility effects of a well resolved entrapped air pocket, and account for the interaction between a moving body and the fluids.
2. Extend the semi-compressible model to a full compressible multiphase flow model that can account for the presence of air in water as a homogeneous mixture and quantify the abilities of this model by comparing with new experimental data.
3. Improve the model based on the experienced difficulties of modeling high-density ratio interfaces and compressibility due to impacts.

The aim is to use this final model to analyze the effect of air in water on, e.g., slamming and green-water events. It was necessary to conduct experiments for validation as a sub objective of this thesis.

Part I: Modeling of high-density ratio flows, compressible entrapped air-pocket oscillations, and fluid-body interaction

ComFLOW showed that the effect of the compressibility of air between the free surface and a high-speed vessel dropping with an average deadrise angle of 30 degrees into the water is negligible. Based on these results, the choice is made to use a one-phase flow model to compare the numerical model with the experimental results of a high-speed vessel in irregular head waves. The one-phase flow model was shown to outperform a state-of-the-art strip-theory method in terms of accuracy with an improvement of up to 20% for the vertical acceleration and is seen as an adequate tool for improving analytical methods like the strip-theory.

The one-phase model could simulate the impacts of a vessel in irregular waves and, therefore, be used as a basis to develop an in-house model from scratch. This in-house model is extended to a semi-compressible two-phase flow model where the air above the free surface is considered as compressible.

The semi-compressible model is applied for simulating the dynamics of an entrapped air pocket due to an overturning wave. For traditional test cases, the extended model showed that the air pocket dynamics are well captured. The effect of compression waves in the air dominates the dynamics of an entrapped air pocket, and surface tension had no effect on this scale. The pressure waves generated by the pulsation of the air pocket can be in the same order as the maximum pressure induced by the wave impact on the wall. However, the 2D simulations are overpredicting the pressures compared to experimental data because of the restricted movement of the fluids in 2D.

Around the interface between the fluids spurious velocities were present, even though multiple density averaging methods were tested that should have prevented this. The spurious velocities resulted in unphysical free-surface distortion and needed to be prevented.

Literature showed that high-density ratio interface flows are challenging and can easily result in unphysical free surface distortion. The staggered arrangement of variables can lead to a non-consistent discretization of the mass and momentum fluxes due to the difference in control volumes. A non-consistent discretization can cause momentum losses. A consistent discretization technique for momentum and mass is obtained when the fluxes along faces of control volumes and the spatial discretization of the densities are treated the same for all control volumes. Additionally, a new label is added to the cell labeling system to improve the sharpness of the interface. The model is extended with a cut-cell method that can represent a body. A monolithic coupling between the fluids and body is implemented to model two-way interaction. The consistent discretization of

cut-cells and high-density ratio flows gave an order of magnitude decrease in momentum losses for fluid-body interaction compared with the old non-consistent discretization technique. Comparison with experimental data showed numerical results closer to the measurements.

Part II: Experiments and numerics with aeration

In the second part of this thesis, the model is extended to account for the effect of air homogeneously distributed in water and the interaction with freely moving bodies. Validation with experimental data is necessary to show that the model produces reliable results. Before the extension is implemented, an experimental setup is presented. The setup includes a buoyant falling and emerging wedge in "2D". The provided experimental data can be used as a 2D benchmark for violent fluid-body interaction and improvement of 2D strip theories for ship motion. The numerical results with the semi-compressible two-phase model showed good agreement with the experimental results for free surface deformation and body motion. The combination of both numerical and experimental results provides a better understanding of when 3D effects are relevant; the moment when the cavity becomes unstable and closes, created in the wake of the body after it penetrated the water. The combination of experiment and numerical simulations reduces uncertainties, and leads to a better understanding of physics.

A new fully compressible pressure-based multiphase flow model is presented that can account for the effect of a constant mass fraction of air in the water and the interaction between the air above the free surface, the air-water mixture, and a body. The model releases the need for exact mass conservation using a non-conservative formulation for the interface transport which prevents unphysical oscillations around the interface, and the need to capture the sharp discontinuity of pressure waves due to the use of continuous spatial discretization schemes. The model enforces pressure-density relations that neglect the effect of temperature changes. A new formulation of the speed of sound and adding another volume fraction field indicating the aeration level prevented artificial compressibility effects due to unphysical air entrainment around the interfaces and cell label changes. The model showed good results for traditional benchmarks where the propagation of pressure waves through a fluid and through an interface are measured, even though the discontinuity of the waves is smeared out over a couple of grid cells.

The 2D experimental setup is extended to account for aeration, resulting in compressibility effects due to the ratio of maximum fluid velocity over the speed of sound of up to 0.5. The numerical and experimental results are in good agreement for low aeration levels, but start to deviate for higher aeration levels. Compared to the numerical results, the cushioning effect of the experiment is higher. The

post-impact loadings on the wedge caused by reflected pressure waves were less present for the experiment than for the numerical model. 3D bubble effects, not allowing for air pocket fragmentation, a not fully homogeneous mixture in the experiment, not being numerically mass conserving, and enforcing pressure-density relations can be an explanation for the remaining differences in the experimental and numerical results. The high frequencies of the post-impact loadings found with the numerical model are in good agreement with the experimental results for relatively high aeration levels because, related to the Courant restriction, the fluid velocities are in the same order as the pressure wave velocities. The post-impact loading variations become larger (compared to the maximum pressure at impact) when the aeration level increases and are likely to play a role in fatigue of structures.

Part III: Numerical improvements for interface modeling of high-density ratio flows

The artificial compressibility effects, when aeration is involved, are partly caused by the discontinuous interface reconstruction across the numerical grid. A new low-cost bilinear interface calculation method is introduced to enforce interface continuity with a curvature-weighted approach. Direction-split methods with a reconstruction step in combination with the staggered arrangement leave unresolved inconsistencies between the mass and momentum fluxes. These are minimized by introducing a new unsplit interface advection scheme. It prevents the inconsistencies that can result in an unstable interface. The new advection scheme also showed to be more shape preserving than the direction-split scheme used by the original method. The combination of both new schemes is competitive with higher-order methods in terms of accuracy but outperforms in costs.

8.2 Outlook

Suggested future research work is separated in two parts: improvements of the numerical model, and extensions for the experimental setup.

Numerical model

A 2D environment is a convenient place to develop a numerical model. However, many times it was experienced that 3D effects play a role and result in a deviation compared to the 2D results. Developing a 2D experimental setup was experienced as difficult, explaining why there are not many truly 2D benchmarks. Extending the presented numerical model to 3D should be one of the next steps.

The numerical model did not consider air pocket fragmentation during the simulation due to the assumption of homogeneity. The experiments for the wedge entry showed that air entrainment happens during the entry and emergence. The use of subgrid models beyond the assumption of a constant mass fraction of air in water is a step that can be made to include fragmentation without significantly

increasing the computational costs.

More attention is needed for handling cut cells at the fluid-fluid interface and face apertures of moving bodies for preventing unphysical air entrainment beneath the free surface. The calculation of the triple point where two interfaces come together, body-fluid and fluid-fluid interface, and the reconstruction of the fluid-fluid interface is relevant for the propagation of a jet along the boundary of a body. When the interface is not kept sharp, artificial air entrainment or unphysical detaching of droplets can happen. Applying the bilinear interface calculation method and the donating quadrant advection scheme for moving bodies needs evaluation.

Other steps that need consideration are comparing the staggered arrangement with a collocated arrangement of variables for momentum losses by fluid-body interaction, quarter cell reconstruction to reduce the momentum losses and prevent inconsistency due to interface reconstruction, and the implementation of shape-preserving body rotation or deformable bodies.

Experimental setup

The proposed experimental setup with a wedge is a fundamental case that makes it easier to understand what happens during an aerated water-wave impact. New experimental setups that can consider multiple water-penetrating bodies, green water events, breaking waves, and cases that approach reality can be next steps when there is more understanding of these kinds of impacts.

For this experimental setup, 3D effects and the homogeneous distribution of air need evaluation. An attempt needs to be made to visualize the propagating pressure waves by looking at the motion of the tiny air bubbles with a high-speed camera, by positioning pressure sensors at the domain boundaries, and by considering the deformation of the free surface for different aeration levels. Even a flexible wedge could help to identify pressure waves. Measuring the aeration level and the distribution with optical probes should decrease the uncertainty in air content. With the recordings of a high-speed camera, the air entrainment during impact could be derived. This requires the use of markers to control distortion. The measurements will yield a better understanding and can be the basis of a subgrid model for air entrainment.

-
- [1] T. Abadie, J. Aubin, and D. Legendre. "On the combined effects of surface tension force calculation and interface advection on spurious currents within Volume of Fluid and Level Set frameworks." *Journal of Computational Physics* 297 (2015), pp. 611–636 (cit. on pp. [54](#), [96](#), [256](#)).
- [2] R. Abgrall and S. Karni. "Computations of compressible multifluids." *Journal of Computational Physics* 169.2 (2001), pp. 594–623 (cit. on pp. [191](#), [199](#)).
- [3] M. R. Ansari and A. Daramizadeh. "Numerical simulation of compressible two-phase flow using a diffuse interface method." *International Journal of Heat and Fluid Flow* 42 (2013), pp. 209–223 (cit. on p. [201](#)).
- [4] T. Arrufat, M. Cialesi-Esposito, D. Fuster, Y. Ling, L. Malan, S. Pal, R. Scardovelli, G. Tryggvason, and S. Zaleski. "A mass-momentum consistent, Volume-of-Fluid method for incompressible flow on staggered grids." *Computers & Fluids* 215 (2021), p. 104785 (cit. on p. [281](#)).
- [5] E. Aulisa, S. Manservigi, and R. Scardovelli. "A mixed markers and volume-of-fluid method for the reconstruction and advection of interfaces in two-phase and free-boundary flows." *Journal of Computational Physics* 188.2 (2003), pp. 611–639 (cit. on pp. [273](#), [276](#)).
- [6] E. Aulisa, S. Manservigi, R. Scardovelli, and S. Zaleski. "Interface reconstruction with least-squares fit and split advection in three-dimensional Cartesian geometry." *Journal of Computational Physics* 225.2 (2007), pp. 2301–2319 (cit. on pp. [245](#), [253](#), [260](#)).
- [7] A. G. Avci and B. Barlas. "An experimental and numerical study of a high speed planing craft with full-scale validation." *Journal of Marine Science and Technology* 26.5 (2018), pp. 617–628 (cit. on p. [17](#)).
- [8] C. M. Bao, G. X. Wu, and G. D. Xu. "Simulation of water entry of a two-dimension finite wedge with flow detachment." *Journal of Fluids and Structures* 65 (2016), pp. 44–59 (cit. on p. [133](#)).
- [9] A. Baraldi, M. S. Dodd, and A. Ferrante. "A mass-conserving volume-of-fluid method: volume tracking and droplet surface-tension in incompressible isotropic turbulence." *Computer & Fluids* 96 (2014), pp. 322–337 (cit. on pp. [56](#), [96](#)).

- [10] M. Barjasteh, H. Zeraatgar, and M. J. Javaherian. "An experimental study on water entry of asymmetric wedges." *Applied Ocean Research* 58 (2016), pp. 292–304 (cit. on pp. 133, 166).
- [11] J. B. Bell, P. Colella, and H. M. Glaz. "A second-order projection method for the incompressible Navier-Stokes equations." *Journal of Computational Physics* 85.2 (1989), pp. 257–283 (cit. on p. 275).
- [12] C. E. Blenkinsopp and J. R. Chaplin. "Void fraction measurements and scale effects in breaking waves in freshwater and seawater." *Coastal Engineering* 58.5 (2011), pp. 417–428 (cit. on p. 4).
- [13] W. J. C. Boef. "Launch and impact of free-fall lifeboats. Part I. Impact theory." *Ocean Engineering* 19.2 (1992), pp. 119–138 (cit. on p. 128).
- [14] H. Bogaert, S. Léonard, L. Brosset, and M. L. Kaminski. "Sloshing and scaling: results from the Sloshel project." *The 20th International Offshore and Polar Engineering Conference*. OnePetro. 2010 (cit. on p. 2).
- [15] A. D. Boon and P. R. Wellens. "Probability and distribution of green water events and pressures." *Ocean Engineering* 264 (2022), p. 112429 (cit. on pp. 128, 135).
- [16] R. W. Bos, J. H. Den Besten, and M. L. Kaminski. "A reduced order model for structural response of the Mark III LNG Cargo Containment System." *International Shipbuilding Progress* 66.4 (2019), pp. 295–313 (cit. on p. 44).
- [17] R. W. Bos and P. R. Wellens. "Fluid structure interaction between a pendulum and focused breaking waves." *Physics of Fluids* 33.6 (2021), p. 062118 (cit. on p. 2).
- [18] R. W. Bos, M. van der Eijk, J. H. den Besten, and P. R. Wellens. "A reduced order model for FSI of tank walls subject to wave impacts during sloshing." *International Shipbuilding Progress* Preprint (2022), pp. 1–20 (cit. on pp. 84, 99, 135, 150).
- [19] J. U. Brackbill, D. B. Kothe, and C. Zemach. "A continuum method for modeling surface tension." *Journal of Computational Physics* 100.2 (1992), pp. 335–354 (cit. on pp. 45, 53–55, 96).
- [20] G. Bradski. "The OpenCV library." *Dr. Dobb's Journal: Software Tools for the Professional Programmer* 25.11 (2000), pp. 120–123 (cit. on p. 146).
- [21] H. Bredmose, G. Bullock, and A. Hogg. "Violent breaking wave impacts. Part 3. Effects of scale and aeration." *Journal of Fluid Mechanics* 765 (2015), pp. 82–113 (cit. on pp. 4, 190).

- [22] H. Bredmose, D. H. Peregrine, and G. N. Bullock. "Violent breaking wave impacts. Part 2: modelling the effect of air." *Journal of Fluid Mechanics* 641 (2009), pp. 389–430 (cit. on pp. 2, 5, 44, 62, 128, 190–192).
- [23] S. Brizzolara, N. Couty, O. Hermundstad, A. Ioan, T. Kukkanen, M. Viviani, and P. Temarel. "Comparison of experimental and numerical loads on an impacting bow section." *Ships and Offshore Structures* 3.4 (2008), pp. 305–324 (cit. on p. 133).
- [24] R. Broglia and D. Durante. "Accurate prediction of complex free surface flow around a high speed craft using a single-phase level set method." *Computational Mechanics* 62.3 (2018), pp. 421–437 (cit. on p. 16).
- [25] B. Buchner. "Green water from the side of a weathervaning FPSO." *International Conference on Offshore Mechanics and Arctic Engineering*. 1999 (cit. on p. 44).
- [26] B. Buchner. "Green water on ship-type offshore structures." PhD thesis. Delft University of Technology, 2002 (cit. on p. 135).
- [27] G. N. Bullock, A. R. Crawford, P. J. Hewson, M. J. A. Walkden, and P. A. D. Bird. "The influence of air and scale on wave impact pressures." *Coastal Engineering* 42.4 (2001), pp. 291–312 (cit. on pp. 3, 4, 6, 7, 24, 190).
- [28] G. N. Bullock, C. Obhrai, D. H. Peregrine, and H. Bredmose. "Violent breaking wave impacts. Part 1: Results from large-scale regular wave tests on vertical and sloping walls." *Coastal Engineering* 54.8 (2007), pp. 602–617 (cit. on pp. 3, 4, 190).
- [29] M. Bussmann, D. B. Kothe, and J. M. Sicilian. "Modeling high density ratio incompressible interfacial flows." *ASME 2002 Joint US-European Fluids Engineering Division Conference*. American Society of Mechanical Engineers Digital Collection. 2002, pp. 707–713 (cit. on pp. 76, 77, 85, 94, 101, 209, 286).
- [30] A. Calderer, S. Kang, and F. Sotiropoulos. "Level set immersed boundary method for coupled simulation of air/water interaction with complex floating structures." *Journal of Computational Physics* 277 (2014), pp. 201–227 (cit. on p. 132).
- [31] B. K. Campbell. "An arbitrarily high-order three-dimensional Cartesian-grid method for reconstructing interfaces from volume fraction fields." *Journal of Computational Physics* 426 (2021), p. 109727 (cit. on p. 246).
- [32] P. M. Carrica, D. Drew, F. Bonetto, and R. T. Lahey Jr. "A polydisperse model for bubbly two-phase flow around a surface ship." *International Journal of Multiphase Flow* 25.2 (1999), pp. 257–305 (cit. on p. 191).

- [33] A. M. Castro and P. M. Carrica. "Eulerian polydispersed modeling of bubbly flows around ships with application to Athena R/V." *International Shipbuilding Progress* 60.1-4 (2013), pp. 403–433 (cit. on p. 191).
- [34] A. M. Castro, J. Li, and P. M. Carrica. "A mechanistic model of bubble entrainment in turbulent free surface flows." *International Journal of Multiphase Flow* 86 (2016), pp. 35–55 (cit. on pp. 5, 191).
- [35] A. Cervone, S. Manservigi, R. Scardovelli, and S. Zaleski. "A geometrical predictor–corrector advection scheme and its application to the volume fraction function." *Journal of Computational Physics* 228.2 (2009), pp. 406–419 (cit. on pp. 249, 268).
- [36] W. H. R. Chan, P. L. Johnson, P. Moin, and J. Urzay. "The turbulent bubble break-up cascade. Part 2. Numerical simulations of breaking waves." *Journal of Fluid Mechanics* 912 (2021), A43 (cit. on p. 2).
- [37] A. Z. Chaudhry, Y. Shi, and G. Pan. "Recent developments on the water entry impact of wedges and projectiles." *Ships and Offshore Structures* 17.3 (2022), pp. 695–714 (cit. on p. 133).
- [38] Y. Cheny and O. Botella. "The LS-STAG method: A new immersed boundary/level-set method for the computation of incompressible viscous flows in complex moving geometries with good conservation properties." *Journal of Computational Physics* 229.4 (2010), pp. 1043–1076 (cit. on p. 78).
- [39] Y. Cheny and O. Botella. "The LS-STAG method: A new immersed boundary/level-set method for the computation of incompressible viscous flows in complex moving geometries with good conservation properties." *Journal of Computational Physics* 229.4 (2010), pp. 1043–1076 (cit. on p. 206).
- [40] B. Y. Choi and M. Bussmann. "A piecewise linear approach to volume tracking a triple point." *International Journal for Numerical Methods in Fluids* 53.6 (2007), pp. 1005–1018 (cit. on p. 89).
- [41] A. J. Chorin. "Numerical solution of the Navier-Stokes equations." *Mathematics of computation* 22.104 (1968), pp. 745–762 (cit. on pp. 8, 206).
- [42] E. D. Christensen. "Large eddy simulation of spilling and plunging breakers." *Coastal Engineering* 53.5-6 (2006), pp. 463–485 (cit. on p. 5).
- [43] S.-L. Chuang. "Experiments on flat-bottom slamming." *Journal of Ship Research* 10.01 (1966), pp. 10–17 (cit. on p. 133).
- [44] S.-L. Chuang. "Experiments on slamming of wedge-shaped bodies." *Journal of Ship Research* 11.03 (1967), pp. 190–198 (cit. on p. 133).

- [45] S.-L. Chuang and D. T. Milne. *Drop tests of cones to investigate the three-dimensional effects of slamming*. Tech. rep. David W. Taylor Naval Ship Research and Development center Bethesda M.D., 1971 (cit. on p. 134).
- [46] G. Colicchio, M. Greco, M. Miozzi, and C. Lugni. “Experimental and numerical investigation of the water-entry and water-exit of a circular cylinder.” *The 24th International Workshop on Water Waves and Floating Bodies*. 2009, pp. 19–22 (cit. on pp. 114, 116–119, 121, 122, 133).
- [47] R. Comminal, J. Spangenberg, and J. H. Hattel. “Cellwise conservative unsplit advection for the volume of fluid method.” *Journal of Computational Physics* 283 (2015), pp. 582–608 (cit. on pp. 248, 249).
- [48] A. R. Crawford. “Measurement and analysis of wave loading on a full scale coastal structure” (1999) (cit. on pp. 3, 4).
- [49] A. Crawford, G. Bullock, P. Hewson, and P. Bird. “Wave impact pressures and aeration at a breakwater.” *Ocean Wave Measurement and Analysis*. ASCE. 1998, pp. 1366–1379 (cit. on p. 4).
- [50] S. J. Cummins, M. M. Francois, and D. B. Kothe. “Estimating curvature from volume fractions.” *Computers & Structures* 83.6-7 (2005), pp. 425–434 (cit. on p. 256).
- [51] G. Cuomo, W. Allsop, and S. Takahashi. “Scaling wave impact pressures on vertical walls.” *Coastal Engineering* 57.6 (2010), pp. 604–609 (cit. on p. 4).
- [52] G. Cuomo, W. Allsop, T. Bruce, and J. Pearson. “Breaking wave loads at vertical seawalls and breakwaters.” *Coastal Engineering* 57.4 (2010), pp. 424–439 (cit. on p. 3).
- [53] S. T. Dang, E. A. Meese, J. C. Morud, and S. T. Johansen. “Numerical approach for generic three-phase flow based on cut-cell and ghost fluid methods.” *International Journal for Numerical Methods in Fluids* 91.9 (2019), pp. 419–447 (cit. on p. 208).
- [54] R. DeBar. “Fundamentals of the KRAKEN code.” *Technical Report UCIR-760* (1974) (cit. on p. 245).
- [55] G. B. Deane and M. D. Stokes. “Scale dependence of bubble creation mechanisms in breaking waves.” *Nature* 418.6900 (2002), p. 839 (cit. on p. 4).
- [56] L. Deike, L. Lenain, and W. K. Melville. “Air entrainment by breaking waves.” *Geophysical Research Letters* 44.8 (2017), pp. 3779–3787 (cit. on p. 3).

- [57] L. Deike, W. K. Melville, and S. Popinet. "Air entrainment and bubble statistics in breaking waves." *Journal of Fluid Mechanics* 801 (2016), pp. 91–129 (cit. on p. 2).
- [58] A. Del Buono, G. Bernardini, A. Tassin, and A. Iafrati. "Water entry and exit of 2D and axisymmetric bodies." *Journal of Fluids and Structures* 103 (2021), p. 103269 (cit. on p. 132).
- [59] S. S. Deshpande, L. Anumolu, and M. F. Trujillo. "Evaluating the performance of the two-phase flow solver interFoam." *Computational Science & Discovery* 5.1 (2012), p. 014016 (cit. on p. 58).
- [60] O. Desjardins and V. Moureau. "Methods for multiphase flows with high density ratio." *Center for Turbulent Research, Summer Programm* 2010 (2010), pp. 313–322 (cit. on p. 77).
- [61] F. Dias and L. Brosset. "Comparative numerical study: description of the calculation case." *The 20th International Offshore and Polar Engineering Conference*. Vol. 3. 2010 (cit. on p. 217).
- [62] F. Dias, D. Dutykh, and J.-M. Ghidaglia. "A two-fluid model for violent aerated flows." *Computer & Fluids* 39.2 (2010), pp. 283–293 (cit. on p. 191).
- [63] F. Dias and J.-M. Ghidaglia. "Slamming: Recent progress in the evaluation of impact pressures." *Annual Review of Fluid Mechanics* 50 (2018), pp. 243–273 (cit. on p. 128).
- [64] N. de Divitiis and L. M. de Socio. "Impact of floats on water." *Journal of Fluid Mechanics* 471 (2002), pp. 365–379 (cit. on p. 5).
- [65] S. V. Diwakar, S. K. Das, and T. Sundararajan. "A quadratic spline based interface (QUASI) reconstruction algorithm for accurate tracking of two-phase flows." *Journal of Computational Physics* 228.24 (2009), pp. 9107–9130 (cit. on pp. 246, 253–255, 259, 272–276, 280, 281).
- [66] Z. N. Dobrovol'Skaya. "On some problems of similarity flow of fluid with a free surface." *Journal of Fluid Mechanics* 36.4 (1969), pp. 805–829 (cit. on p. 133).
- [67] M. S. Dodd and A. Ferrante. "A fast pressure-correction method for incompressible two-fluid flows." *Journal of Computational Physics* 273 (2014), pp. 416–434 (cit. on p. 55).
- [68] S. Dong and X. Wang. "A Rotational Pressure-Correction Scheme for Incompressible Two-Phase Flows with Open Boundaries." *PLOS ONE* 11.5 (May 2016), pp. 1–38 (cit. on p. 55).
- [69] S. Downes, A. Knott, and I. Robinson. "Towards a shock tube method for the dynamic calibration of pressure sensors." *Philosophical Transac-*

- tions of the Royal Society A: Mathematical, Physical and Engineering Sciences 372.2023 (2014), p. 20130299 (cit. on p. 63).
- [70] D. A. Drew. “Mathematical modeling of two-phase flow.” *Annual Review of Fluid Mechanics* 15.1 (1983), pp. 261–291 (cit. on p. 9).
- [71] M. Dröge. “Cartesian grid methods for turbulent flow simulation in complex geometries.” PhD thesis. University of Groningen, 2007 (cit. on p. 153).
- [72] V. Duclaux, F. Caillé, C. Duez, C. Ybert, L. Bocquet, and C. Clanet. “Dynamics of transient cavities.” *Journal of Fluid Mechanics* 591 (2007), pp. 1–19 (cit. on pp. 128, 132).
- [73] B. Duret, R. Canu, J. Reveillon, and F. X. Demoulin. “A pressure based method for vaporizing compressible two-phase flows with interface capturing approach.” *International Journal of Multiphase Flow* 108 (2018), pp. 42–50 (cit. on pp. 76, 190).
- [74] B. Düz. “Wave generation, propagation and absorption in CFD simulations of free surface flows.” PhD thesis. Delft University of Technology, 2015 (cit. on pp. 22, 248, 253, 276).
- [75] M. van der Eijk and P. R. Wellens. “A compressible two-phase flow model for pressure oscillations in air entrapments following green water impact events on ships.” *International Shipbuilding Progress* 66.4 (2019), pp. 315–343 (cit. on pp. 5, 18, 21, 43, 77, 78, 84, 85, 91, 92, 99, 110–113, 120, 150, 180, 212, 223).
- [76] M. van der Eijk and P. R. Wellens. “An 2D efficient bilinear interface reconstruction algorithm and consistent multidimensional unsplit advection scheme for accurate tracking of highly-curved interfacial structures on uniform grids.” *Journal of Computational Physics* (nd) (cit. on pp. 150, 152, 243).
- [77] M. van der Eijk and P. R. Wellens. “An efficient pressure-based multiphase finite volume method for interaction between compressible aerated water and moving bodies.” *Journal of Computational Physics* (nd) (cit. on pp. 150, 189).
- [78] M. van der Eijk and P. R. Wellens. “Experimental, numerical and analytical evaluation of the buoyant wedge entry problem with reemergence in 2D.” *Journal of Fluid Mechanics* (nd) (cit. on pp. 6, 127, 247, 270).
- [79] M. van der Eijk and P. R. Wellens. “Experimental and numerical assessment of vertical accelerations during bow re-entry of a RIB in irregular waves.” *International Shipbuilding Progress* 67 (2020), pp. 1–26 (cit. on pp. 3, 15, 114, 128, 132, 137, 150, 154, 226, 228, 236).

- [80] M. van der Eijk and P. R. Wellens. "Two-phase free-surface flow interaction with moving bodies using a consistent, momentum preserving method." *Journal of Computational Physics* 474 (2023), p. 111796 (cit. on pp. 75, 133, 135, 149–152, 202–206, 209, 212, 245, 248–252, 265, 281, 286, 290, 292).
- [81] M. Elhimer, N. Jacques, A. E. M. Alaoui, and C. Gabillet. "The influence of aeration and compressibility on slamming loads during cone water entry." *Journal of Fluids and Structures* 70 (2017), pp. 24–46 (cit. on pp. 6, 7, 178, 190, 192, 224, 225, 227, 232).
- [82] R. N. Elias and A. L. G. A. Coutinho. "Stabilized edge-based finite element simulation of free-surface flows." *International Journal for Numerical Methods in Fluids* 54.6-8 (2007), pp. 965–993 (cit. on p. 66).
- [83] *Environmental conditions and environmental loads*. Det Norske Veritas Oslo, Norway, 2000 (cit. on p. 3).
- [84] V. A. Eroshin, A. V. Plyusnin, N. I. Romanenkov, Y. A. Sozonenko, and Y. L. Yakimov. "Influence of the atmosphere on the magnitude of the hydrodynamic forces in the case of a disk in a flat encounter with the surface of a compressible liquid." *Fluid Dynamics* 19.3 (1984), pp. 350–355 (cit. on pp. 190, 224).
- [85] A. C. Fairlie-Clarke and T. Tveitnes. "Momentum and gravity effects during the constant velocity water entry of wedge-shaped sections." *Ocean Engineering* 35.7 (2008), pp. 706–716 (cit. on pp. 171–173).
- [86] O. M. Faltinsen. *Hydrodynamics of High-Speed Marine Vehicles*. Cambridge University Press, 2006 (cit. on pp. 26, 150, 161, 180).
- [87] O. M. Faltinsen, O. F. Rognebakke, I. A. Lukovsky, and A. N. Timokha. "Multidimensional modal analysis of nonlinear sloshing in a rectangular tank with finite water depth." *Journal of Fluid Mechanics* 407 (2000), pp. 201–234 (cit. on p. 5).
- [88] K. Farkhodov, S.-H. Lee, and K.-R. Kwon. "Object Tracking using CSRT Tracker and RCNN." *Conference on Bioimaging*. 2020, pp. 209–212 (cit. on pp. 138, 147).
- [89] G. Fekken, A. E. P. Veldman, and B. Buchner. "Simulation of green-water loading using the Navier-Stokes equations." *The 7th International Conference on Numerical Ship Hydrodynamics*. 1999 (cit. on pp. 18, 44).
- [90] G. Fekken. "Numerical simulation of free-surface flow with moving rigid bodies." PhD thesis. University of Groningen, 2004 (cit. on pp. 18, 82, 98, 150, 152, 204, 206).

- [91] G. Z. Forristall et al. "Wave crest heights and deck damage in hurricanes Ivan, Katrina, and Rita." *Offshore Technology Conference*. Offshore Technology Conference. 2007 (cit. on p. 76).
- [92] M. M. Francois, S. J. Cummins, E. D. Dendy, D. B. Kothe, J. M. Sicilian, and M. W. Williams. "A balanced-force algorithm for continuous and sharp interfacial surface tension models within a volume tracking framework." *Journal of Computational Physics* 213.1 (2006), pp. 141–173 (cit. on pp. 51, 53, 54).
- [93] E. Franquet. "Modélisation eulérienne d'écoulements multiphasiques en présence d'ondes de chocs, de détonations et d'interfaces matérielles. Application aux matériaux énergétiques nanostructurés." PhD thesis. University of Pau and the Adour Region, 2006 (cit. on pp. 215, 216).
- [94] T. C. Fu, K. A. Brucker, S. M. Mousaviraad, C. M. Ikeda, E. J. Lee, T. T. O'shea, Z. Wang, F. Stern, and C. Q. Judge. "An assessment of computational fluid dynamics predictions of the hydrodynamics of high-speed planing craft in calm water and waves." *The 30th Symposium on Naval Hydrodynamics*. 2014, pp. 2–7 (cit. on p. 17).
- [95] A. Fyfe and E. Ballard. "Prediction of green water events on FPSO vessels." *International Conference on Offshore Mechanics and Arctic Engineering*. Vol. 36827. 2003, pp. 443–451 (cit. on p. 135).
- [96] S. Gekle, I. R. Peters, J. M. Gordillo, D. van der Meer, and D. Lohse. "Supersonic air flow due to solid-liquid impact." *Physical Review Letters* 104.2 (2010), p. 024501 (cit. on p. 132).
- [97] J. Gerrits. "Dynamics of liquid-filled spacecraft: numerical simulation of coupled solid-liquid dynamics." PhD thesis. University of Groningen, 2001 (cit. on pp. 5, 8, 18–20, 50).
- [98] S. Ghods and M. Herrmann. "A consistent rescaled momentum transport method for simulating large density ratio incompressible multiphase flows using level set methods." *Physica Scripta* 2013.T155 (2013), p. 014050 (cit. on pp. 77, 101).
- [99] T. Gilet and L. Bourouiba. "Fluid fragmentation shapes rain-induced foliar disease transmission." *Journal of the Royal Society Interface* 12.104 (2015), p. 20141092 (cit. on p. 128).
- [100] I. Ginzburg and G. Wittum. "Two-phase flows on interface refined grids modeled with VOF, staggered finite volumes, and spline interpolants." *Journal of Computational Physics* 166.2 (2001), pp. 302–335 (cit. on p. 246).

- [101] K. Gong, H. Liu, and B.-L. Wang. "Water entry of a wedge based on SPH model with an improved boundary treatment." *Journal of Hydrodynamics* 21.6 (2009), pp. 750–757 (cit. on p. 132).
- [102] O. M. Greco M .and Faltinsen and M. Landrini. "Shipping of water on a two-dimensional structure." *Journal of Fluid Mechanics* 525 (2005), pp. 309–332 (cit. on p. 190).
- [103] M. Greenhow. "Wedge entry into initially calm water." *Applied Ocean Research* 9.4 (1987), pp. 214–223 (cit. on pp. 132, 133, 190).
- [104] P.-M. Guilcher, G. Oger, E. Jacquin, L. Brosset, N. Grenier, and D. Le Touzé. "Simulation of liquid impacts with a two-phase parallel SPH model." *The 20th International Offshore and Polar Engineering Conference*. 2010 (cit. on p. 218).
- [105] J.-F. Haas and B. Sturtevant. "Interaction of weak shock waves with cylindrical and spherical gas inhomogeneities." *Journal of Fluid Mechanics* 181 (1987), pp. 41–76 (cit. on pp. 219–221).
- [106] F. Ham and Y.-N. Young. "A Cartesian adaptive level set method for two-phase flows." *Center for Turbulence Research Annual Research Briefs 2003* (2003) (cit. on p. 58).
- [107] D. J. E. Harvie, M. R. Davidson, and M. Rudman. "An analysis of parasitic current generation in volume of fluid simulations." *Applied mathematical modelling* 30.10 (2006), pp. 1056–1066 (cit. on p. 51).
- [108] D. J. E. Harvie and D. F. Fletcher. "A new volume of fluid advection algorithm: the stream scheme." *Journal of Computational Physics* 162.1 (2000), pp. 1–32 (cit. on pp. 249, 273, 276).
- [109] D. J. E. Harvie and D. F. Fletcher. "A new volume of fluid advection algorithm: the defined donating region scheme." *International Journal for Numerical Methods in Fluids* 35.2 (2001), pp. 151–172 (cit. on pp. 248, 273).
- [110] R. Hascoët, N. Jacques, Y.-M. Scolan, and A. Tassin. "A two-dimensional analytical model of vertical water entry for asymmetric bodies with flow separation." *Applied Ocean Research* 92 (2019), p. 101878 (cit. on pp. 128, 132, 158, 161–165).
- [111] M. Hattori, A. Arami, and T. Yui. "Wave impact pressure on vertical walls under breaking waves of various types." *Coastal Engineering* 22.1 (1994), pp. 79–114 (cit. on p. 3).

- [112] M. Hattori, A. Arami, and T. Yui. "Wave impact pressure on vertical walls under breaking waves of various types." *Coastal Engineering* 22.1-2 (1994), pp. 79–114 (cit. on p. 190).
- [113] P. D. Hieu and K. Tanimoto. "Verification of a VOF-based two-phase flow model for wave breaking and wave–structure interactions." *Ocean Engineering* 33.11-12 (2006), pp. 1565–1588 (cit. on p. 5).
- [114] C. Hirsch. *Numerical computation of internal and external flows: The fundamentals of computational fluid dynamics*. Butterworth-Heinemann, 2007 (cit. on p. 211).
- [115] C. W. Hirt and B. D. Nichols. "Volume of fluid (VOF) method for the dynamics of free boundaries." *Journal of Computational Physics* 39.1 (1981), pp. 201–225 (cit. on pp. 8, 9, 244, 245, 273).
- [116] Y. Hong, B. Wang, and H. Liu. "Aeration Effects on Hydrodynamic Loads of Circular Cylinder's High-speed Water Entry." *International Journal of Offshore and Polar Engineering* 29.04 (2019), pp. 446–451 (cit. on p. 202).
- [117] Y. Hong, B. Wang, and H. Liu. "Numerical study of hydrodynamic loads at early stage of vertical high-speed water entry of an axisymmetric blunt body." *Physics of Fluids* 31.10 (2019), p. 102105 (cit. on pp. 6, 7, 192).
- [118] Y. Hong, B. Wang, and H. Liu. "Experimental and numerical study on hydrodynamic impact of a disk in pure and aerated water." *Proceedings of the Institution of Mechanical Engineers, Part M: Journal of Engineering for the Maritime Environment* 235.1 (2021), pp. 152–164 (cit. on p. 224).
- [119] Z. Hu, X. Zhao, M. Li, Z. Fang, and Z. Sun. "A numerical study of water entry of asymmetric wedges using a CIP-based model." *Ocean Engineering* 148 (2018), pp. 1–16 (cit. on pp. 166, 167).
- [120] W. Huang and H. Xiao. "Numerical modeling of dynamic wave force acting on Escambia Bay Bridge deck during Hurricane Ivan." *Journal of Waterway, Port, Coastal, and Ocean Engineering* 135.4 (2009), pp. 164–175 (cit. on pp. 2, 128, 190).
- [121] F. J. Huera-Huarte, D. Jeon, and M. Gharib. "Experimental investigation of water slamming loads on panels." *Ocean Engineering* 38.11-12 (2011), pp. 1347–1355 (cit. on p. 3).
- [122] *Hull structural design ships with length 100 metres and above*. Det Norske Veritas Oslo, Norway, 2009 (cit. on p. 3).
- [123] S.-R. Hysing, S. Turek, D. Kuzmin, N. Parolini, E. Burman, S. Ganesan, and L. Tobiska. "Quantitative benchmark computations of two-dimensional bubble dynamics." *International Journal for Numerical Meth-*

- ods in Fluids* 60.11 (2009), pp. 1259–1288 (cit. on pp. 59, 62, 110, 113, 120).
- [124] A. Iafrati and D. Battistin. “Hydrodynamics of water entry in presence of flow separation from chines.” *The 8th International Conference on Numerical Ship Hydrodynamics*. 2003, pp. 22–25 (cit. on pp. 128, 132).
- [125] A. Iafrati and A. A. Korobkin. “Hydrodynamic loads during early stage of flat plate impact onto water surface.” *Physics of Fluids* 20.8 (2008), p. 082104 (cit. on p. 163).
- [126] R. A. Ibrahim. “Assessment of breaking waves and liquid sloshing impact.” *Nonlinear Dynamics* 100.3 (2020), pp. 1837–1925 (cit. on p. 3).
- [127] Y. A. Ilinskii, E. A. Zabolotskaya, T. A. Hay, and M. F. Hamilton. “Models of cylindrical bubble pulsation.” *The Journal of the Acoustical Society of America* 132.3 (2012), pp. 1346–1357 (cit. on p. 70).
- [128] K. Ito, T. Kunugi, H. Ohshima, and T. Kawamura. “A volume-conservative PLIC algorithm on three-dimensional fully unstructured meshes.” *Computers & Fluids* 88 (2013), pp. 250–261 (cit. on p. 251).
- [129] U. Jain, V. Novaković, H. Bogaert, and D. van der Meer. “On wedgeslamming pressures.” *Journal of fluid mechanics* 934 (2022) (cit. on pp. 132, 134, 150).
- [130] M. Jemison, M. Sussman, and M. Arienti. “Compressible, multiphase semi-implicit method with moment of fluid interface representation.” *Journal of Computational Physics* 279 (2014), pp. 182–217 (cit. on p. 76).
- [131] E. Johnsen and T. Colonius. “Implementation of WENO schemes in compressible multicomponent flow problems.” *Journal of Computational Physics* 219.2 (2006), pp. 715–732 (cit. on p. 200).
- [132] L. A. R. Jones. *HMS Nottingham braves rough Atlantic seas*. [Online; accessed August 22, 2022]. 2004. URL: https://commons.wikimedia.org/wiki/File:HMS_Nottingham_braves_rough_Atlantic_seas._MOD_45143881.jpg (cit. on p. 13).
- [133] A. K. Kapila, R. Menikoff, J. B. Bdzil, S. F. Son, and D. S. Stewart. “Two-phase modeling of deflagration-to-detonation transition in granular materials: Reduced equations.” *Physics of Fluids* 13.10 (2001), pp. 3002–3024 (cit. on pp. 191, 200).
- [134] G. K. Kapsenberg. “Slamming of ships: where are we now?” *Philosophical Transactions of the Royal Society A: Mathematical, Physical and Engineering Sciences* 369.1947 (2011), pp. 2892–2919 (cit. on pp. 3, 6).

- [135] J. Kay. "UK storms destroy railway line and leave thousands without power." See <http://www.bbc.co.uk/news/uk-26042990> (2014) (cit. on pp. 2, 128, 190).
- [136] C. E. Kees, I. Akkerman, M. W. Farthing, and Y. Bazilevs. "A conservative level set method suitable for variable-order approximations and unstructured meshes." *Journal of Computational Physics* 230.12 (2011), pp. 4536–4558 (cit. on p. 66).
- [137] D. M. Kelly, A. Dimakopoulos, and P. H. Caubilla. *Advanced numerical modelling of wave structure interaction*. CRC Press, 2021 (cit. on p. 4).
- [138] J. A. Keuning, G. L. Visch, J. L. Gelling, L. W. de Vries, and G. Burema. "Development of a new SAR boat for the Royal Netherlands Sea Rescue Institution." *The 11th International Conference on Fast Sea Transportation*. 2011 (cit. on pp. 18, 31, 38).
- [139] J. A. Keuning. "Nonlinear behaviour of fast monohulls in head waves." PhD thesis. Delft University of Technology, 1996 (cit. on p. 16).
- [140] K. T. Kiger and J. H. Duncan. "Air-Entrainment Mechanisms in Plunging Jets and Breaking Waves." *Annual Review of Fluid Mechanics* 44.1 (2012), pp. 563–596 (cit. on p. 3).
- [141] D. Kim, C. B. Ivey, F. E. Ham, and L. G. Bravo. "An efficient high-resolution Volume-of-Fluid method with low numerical diffusion on unstructured grids." *Journal of Computational Physics* 446 (2021), p. 110606 (cit. on pp. 248, 273).
- [142] K. M. T. Kleefsman, G. Fekken, A. E. P. Veldman, B. Iwanowski, and B. Buchner. "A volume-of-fluid based simulation method for wave impact problems." *Journal of Computational Physics* 206.1 (2005), pp. 363–393 (cit. on pp. 5, 8, 9, 16, 18, 21, 22, 25, 27, 48, 50, 80, 85, 87, 94, 95, 98, 132, 203, 256).
- [143] A. A. Korobkin. "Water impact problems in ship hydrodynamics." *Advances in Fluid Mechanics*. 1996, pp. 323–371 (cit. on p. 131).
- [144] A. A. Korobkin. "Analytical models of water impact." *European Journal of Applied Mathematics* 15.6 (2004), pp. 821–838 (cit. on pp. 131, 132, 158, 161, 162, 190).
- [145] A. A. Korobkin and S. Malenica. "Modified Logvinovich model for hydrodynamic loads on asymmetric contours entering water." *International Workshop on Water Waves and Floating Bodies*. 2005 (cit. on pp. 131, 132, 160, 161).

- [146] A. A. Korobkin and V. V. Pukhnachov. "Initial stage of water impact." *Annual Review of Fluid Mechanics* 20.1 (1988), pp. 159–185 (cit. on pp. 128, 131).
- [147] S. Koshizuka. "A particle method for incompressible viscous flow with fluid fragmentation." *Computational Fluid Dynamics Journal* 4 (1995), pp. 29–46 (cit. on p. 66).
- [148] J. J. Kreeft and B. Koren. "A new formulation of Kapila's five-equation model for compressible two-fluid flow, and its numerical treatment." *Journal of Computational Physics* 229.18 (2010), pp. 6220–6242 (cit. on pp. 220, 221).
- [149] I. Lagrange, A. Orazzo, D. Zuzio, and J.-L. Estivalèzes. "Immersed Interface Method for the Direct Numerical Simulation of air-blast primary atomization." *Conference ILASS-Americas*. May 2017 (cit. on p. 78).
- [150] C. Lai, A. W. Troesch, et al. "Modeling issues related to the hydrodynamics of three-dimensional steady planing." *Journal of Ship Research* 39.01 (1995), pp. 1–24 (cit. on p. 16).
- [151] S. K. Lam, A. Pitrou, and S. Seibert. "Numba: A llvm-based python jit compiler." *The 2nd Workshop on the LLVM Compiler Infrastructure in HPC*. 2015, pp. 1–6 (cit. on p. 280).
- [152] H. Lamb. *Hydrodynamics*. Cambridge university press, 1932 (cit. on pp. 55, 58).
- [153] U. Laur, K. Lehtola, and A. L. Eksborh. "Final Report on the capsizing on 28 september 1994 in the Baltic Sea of the ro-ro passenger vessel MV Estonia" (1997) (cit. on pp. 2, 128, 190).
- [154] V. Le Chenadec and H. Pitsch. "A monotonicity preserving conservative sharp interface flow solver for high density ratio two-phase flows." *Journal of Computational Physics* 249 (2013), pp. 185–203 (cit. on p. 76).
- [155] B. P. Leonard, A. P. Lock, and M. K. MacVean. "Conservative explicit unrestricted-time-step multidimensional constancy-preserving advection schemes." *Monthly Weather Review* 124.11 (1996), pp. 2588–2606 (cit. on pp. 87, 88, 212, 247, 263, 264, 287).
- [156] S. G. Lewis, D. A. Hudson, S. R. Turnock, and D. J. Taunton. "Impact of a free-falling wedge with water: synchronized visualization, pressure and acceleration measurements." *Fluid Dynamics Research* 42.3 (2010), p. 035509 (cit. on p. 134).
- [157] S. G. Lewis, D. A. Hudson, S. R. Turnock, J. I. R. Blake, R. Sheno, et al. "Predicting motions of high speed RIBs: A comparison of non-linear

- strip theory with experiments." *The 5th International Conference on High-performance Marine Vehicles*. 2006, p. 210 (cit. on p. 17).
- [158] G. Li, L. Yongsheng, Y. Guo, M. Jemison, M. Sussman, T. Helms, and M. Arienti. "Multiphase flow and Encapsulation simulations using the moment of fluid method." *International Journal for Numerical Methods in Fluids* 79 (2015), pp. 456–490 (cit. on p. 76).
- [159] P. Liovic and D. Lakehal. "A Newton–Krylov solver for remapping-based Volume-of-Fluid methods." *SIAM Journal on Scientific Computing* 31.2 (2009), pp. 865–889 (cit. on pp. 249, 268).
- [160] P. Liovic, M. Rudman, J.-L. Liow, D. Lakehal, and D. Kothe. "A 3D unsplit-advection volume tracking algorithm with planarity-preserving interface reconstruction." *Computer & Fluids* 35.10 (2006), pp. 1011–1032 (cit. on pp. 245, 276).
- [161] S. Liu, I. Gatin, C. Obhrai, M. C. Ong, and H. Jasak. "CFD simulations of violent breaking wave impacts on a vertical wall using a two-phase compressible solver." *Coastal Engineering* 154 (2019), p. 103564 (cit. on p. 190).
- [162] G. V. Logvinovich. "Hydrodynamics of flows with free boundaries." *Kyiv: Naukova Dumka* (1969), p. 215 (cit. on pp. 131, 132, 159).
- [163] J. López, J. Hernández, P. Gómez, and F. Faura. "A volume of fluid method based on multidimensional advection and spline interface reconstruction." *Journal of Computational Physics* 195.2 (2004), pp. 718–742 (cit. on pp. 152, 246, 248, 273, 276, 281).
- [164] P. Lubin and S. Glockner. "Numerical simulations of three-dimensional plunging breaking waves: generation and evolution of aerated vortex filaments." *Journal of Fluid Mechanics* 767 (2015), pp. 364–393 (cit. on pp. 3, 5).
- [165] P. Lubin, S. Vincent, S. Abadie, and J.-P. Caltagirone. "Three-dimensional large eddy simulation of air entrainment under plunging breaking waves." *Coastal Engineering* 53.8 (2006), pp. 631–655 (cit. on p. 5).
- [166] C. Lugni, M. Miozzi, M. Brocchini, and O. M. Faltinsen. "Evolution of the air cavity during a depressurized wave impact. I. The kinematic flow field." *Physics of Fluids* 22.5 (2010), p. 056101 (cit. on p. 3).
- [167] C. Lugni, M. Brocchini, and O. M. Faltinsen. "Evolution of the air cavity during a depressurized wave impact. II. The dynamic field." *Physics of Fluids* 22 (2010) (cit. on pp. 2, 4).

- [168] Z. H. Ma, D. M. Causon, L. Qian, C. G. Mingham, H. B. Gu, and P. M. Ferrer. "A compressible multiphase flow model for violent aerated wave impact problems." *Proceedings of the Royal Society A: Mathematical, Physical and Engineering Sciences* 470.2172 (2014), p. 20140542 (cit. on pp. 5, 191, 192, 217, 232).
- [169] Z. H. Ma, D. M. Causon, L. Qian, C. G. Mingham, T. Mai, D. M. Greaves, and A. Raby. "Pure and aerated water entry of a flat plate." *Physics of Fluids* 28.1 (2016), p. 016104 (cit. on pp. 6, 7, 190, 191, 224–226).
- [170] T. Mai, C. Mai, A. Raby, and D. M. Greaves. "Aeration effects on water-structure impacts: Part 1. drop plate impacts." *Ocean Engineering* 193 (2019), p. 106600 (cit. on pp. 6, 7, 190, 224).
- [171] T. Mai, C. Mai, A. Raby, and D. M. Greaves. "Aeration effects on water-structure impacts: Part 2. Wave impacts on a truncated vertical wall." *Ocean Engineering* 186 (2019), p. 106053 (cit. on pp. 3, 4, 190, 224).
- [172] R. K. Maity, T. Sundararajan, and K. Velusamy. "An accurate interface reconstruction method using piecewise circular arcs." *International Journal for Numerical Methods in Fluids* 93.1 (2021), pp. 93–126 (cit. on pp. 246, 276, 281).
- [173] J. Marges. *FRISC kent eigen kracht niet*. https://magazines.defensie.nl/allehens/2018/01/00_frisc. 2018 (cit. on p. 16).
- [174] M. Marghany. "Chapter 1 - Nonlinear ocean motion equations: Introduction and overview." *Nonlinear Ocean Dynamics*. Ed. by M. Marghany. Elsevier, 2021, pp. 1–44 (cit. on p. 1).
- [175] T. Marić, H. Marschall, and D. Bothe. "An enhanced un-split face-vertex flux-based VoF method." *Journal of Computational Physics* 371 (2018), pp. 967–993 (cit. on p. 248).
- [176] J. C. Martin, W. J. Moyce, J. C. Martin, W. J. Moyce, W. G. Penney, A. T. Price, and C. K. Thornhill. "Part IV. An experimental study of the collapse of liquid columns on a rigid horizontal plane." *Philosophical Transactions of the Royal Society of London. Series A, Mathematical and Physical Sciences* 244.882 (1952), pp. 312–324 (cit. on pp. 65, 66).
- [177] E. Medina-Lopez, W. Allsop, A. Dimakopoulos, and T. Bruce. "Conjectures on the Failure of the OWC Breakwater at Mutriku." *Coastal structures and solutions to coastal disasters 2015: Resilient coastal communities*. American Society of Civil Engineers Reston, VA, 2017, pp. 592–603 (cit. on p. 4).

- [178] X. Mei, Y. Liu, and D. K. P. Yue. "On the water impact of general two-dimensional sections." *Applied Ocean Research* 21.1 (1999), pp. 1–15 (cit. on pp. 131, 163).
- [179] W. K. Melville. "The instability and breaking of deep-water waves." *Journal of Fluid Mechanics* 115 (1982), pp. 165–185 (cit. on pp. 115, 156, 180).
- [180] J. Mencinger and I. Žun. "A PLIC–VOF method suited for adaptive moving grids." *Journal of Computational Physics* 230.3 (2011), pp. 644–663 (cit. on pp. 249, 268).
- [181] S. Merino. *Anlegen in der Klimakrise*. [Online; accessed August 22, 2022]. 2021. URL: <https://www.bkb.ch/de/privatkunden/anlegen/chancen/2021/anlegen-in-der-klimakrise> (cit. on p. 241).
- [182] T. Milcent and A. Lemoine. "Moment-of-fluid analytic reconstruction on 3D rectangular hexahedrons." *Journal of Computational Physics* 409 (2020), p. 109346 (cit. on p. 245).
- [183] S. T. Miller, H. Jasak, D. A. Boger, E. G. Paterson, and A. Nedungadi. "A pressure-based, compressible, two-phase flow finite volume method for underwater explosions." *Computer & Fluids* 87 (2013), pp. 132–143 (cit. on pp. 190, 192, 197, 198).
- [184] N. Mohd, M. M. Kamra, M. Sueyoshi, and C. Hu. "Three-dimensional Free Surface Flows Modeled by Lattice Boltzmann Method: a comparison with Experimental Data." *Evergreen* 4 (2017) (cit. on p. 66).
- [185] B. Molin and A. A. Korobkin. "Water entry of a perforated wedge." *The 16th International Workshop on Water Waves and Floating Bodies*. 2001 (cit. on p. 131).
- [186] S. Mosso, C. Garasi, and R. Drake. "A smoothed two-and three-dimensional interface reconstruction method." *Computing and Visualization in Science* 12.7 (2009), pp. 365–381 (cit. on p. 246).
- [187] S. M. Mousaviraad, Z. Wang, and F. Stern. "URANS studies of hydrodynamic performance and slamming loads on high-speed planing hulls in calm water and waves for deep and shallow conditions." *Applied Ocean Research* 51 (2015), pp. 222–240 (cit. on p. 17).
- [188] A. Murrone and H. Guillard. "A five equation reduced model for compressible two phase flow problems." *Journal of Computational Physics* 202.2 (2005), pp. 664–698 (cit. on pp. 9, 46, 76, 79, 150, 194, 199, 281).

- [189] S. Muzaferija. "A two-fluid Navier-Stokes solver to simulate water entry." *The 22nd Symposium on Naval Architecture*. National Academy Press, 1999, pp. 638–651 (cit. on p. 22).
- [190] N. Nangia, B. E. Griffith, N. A. Patankar, and A. P. S. Bhalla. "A robust incompressible Navier-Stokes solver for high density ratio multiphase flows." *Journal of Computational Physics* 390 (2019), pp. 548–594 (cit. on pp. 76, 77, 94).
- [191] Y. T. Ng, C. Min, and F. Gibou. "An efficient fluid–solid coupling algorithm for single-phase flows." *Journal of Computational Physics* 228.23 (2009), pp. 8807–8829 (cit. on p. 78).
- [192] V.-T. Nguyen and W.-G. Park. "A free surface flow solver for complex three-dimensional water impact problems based on the VOF method." *International Journal for Numerical Methods in Fluids* 82.1 (2016), pp. 3–34 (cit. on p. 208).
- [193] B. Y. Ni and G. X. Wu. "Numerical simulation of water exit of an initially fully submerged buoyant spheroid in an axisymmetric flow." *Fluid Dynamics Research* 49.4 (2017), p. 045511 (cit. on p. 133).
- [194] W. F. Noh and P. Woodward. "SLIC (simple line interface calculation)." *The 5th International Conference on Numerical Methods in Fluid Dynamics*. 1976, pp. 330–340 (cit. on pp. 245, 273).
- [195] C. O'Connor, S. Mohajernasab, and N. Abdussamie. "Numerical investigation into water entry problems of a flat plate with air pockets." *Journal of Ocean Engineering and Science* (2022) (cit. on p. 6).
- [196] C. Obhrai, G. Bullock, G. Wolters, G. Müller, D. H. Peregrine, H. Bredmose, and J. Grüne. "Violent wave impacts on vertical and inclined walls: large scale model tests." *Coastal Engineering*. World Scientific, 2005, pp. 4075–4086 (cit. on p. 44).
- [197] J. M. Oliver. "Second-order Wagner theory for two-dimensional water-entry problems at small deadrise angles." *Journal of Fluid Mechanics* 572 (2007), pp. 59–85 (cit. on p. 161).
- [198] E. Olsson and G. Kreiss. "A conservative level set method for two phase flow." *Journal of Computational Physics* 210.1 (2005), pp. 225–246 (cit. on p. 244).
- [199] M. Owkes and O. Desjardins. "A computational framework for conservative, three-dimensional, unsplit, geometric transport with application to the volume-of-fluid (VOF) method." *Journal of Computational Physics* 270 (2014), pp. 587–612 (cit. on pp. 249, 265, 267–270, 279).

- [200] M. Owkes and O. Desjardins. “A mass and momentum conserving unsplit semi-Lagrangian framework for simulating multiphase flows.” *Journal of Computational Physics* 332 (2017), pp. 21–46 (cit. on pp. 76, 281, 284, 285).
- [201] R. Panciroli, S. Abrate, G. Minak, and A. Zucchelli. “Hydroelasticity in water-entry problems: Comparison between experimental and SPH results.” *Composite Structures* 94.2 (2012), pp. 532–539 (cit. on pp. 132, 133).
- [202] B. J. Parker and D. L. Youngs. *Two and three dimensional Eulerian simulation of fluid flow with material interfaces*. 1992 (cit. on pp. 88, 208, 245, 253, 256, 260).
- [203] J. K. Patel and G. Natarajan. “A generic framework for design of interface capturing schemes for multi-fluid flows.” *Computer & Fluids* 106 (2015), pp. 108–118 (cit. on p. 77).
- [204] J. K. Patel and G. Natarajan. “A novel consistent and well-balanced algorithm for simulations of multiphase flows on unstructured grids.” *Journal of Computational Physics* 350 (2017), pp. 207–236 (cit. on p. 77).
- [205] A. Pathak and M. Raessi. “A three-dimensional volume-of-fluid method for reconstructing and advecting three-material interfaces forming contact lines.” *Journal of Computational Physics* 307 (2016), pp. 550–573 (cit. on p. 88).
- [206] D. H. Peregrine and L. Thais. “The effect of entrained air in violent water wave impacts.” *Journal of Fluid Mechanics* 325 (1996), pp. 377–397 (cit. on pp. 3, 4, 190, 191, 198).
- [207] D. H. Peregrine, H. Bredmose, G. Bullock, C. Obhrai, G. MüLLER, and G. Wolters. “Violent water wave impact on a wall.” *The 14th Aha Huliko Winter Workshop*. 2005 (cit. on pp. 5, 212).
- [208] C. S. Peskin. “Numerical analysis of blood flow in the heart.” *Journal of Computational Physics* 25.3 (1977), pp. 220–252 (cit. on p. 78).
- [209] R. Peterson, E. Pierce, B. Price, and C. Bass. *Shock mitigation for the human on high speed craft: development of an impact injury design rule*. Tech. rep. Naval Surface Warfare Center Panama City (FL), 2004 (cit. on p. 16).
- [210] J. E. Pilliod Jr. and E. G. Puckett. “Second-order accurate volume-of-fluid algorithms for tracking material interfaces.” *Journal of Computational Physics* 199.2 (2004), pp. 465–502 (cit. on pp. 245, 247, 248, 253).

- [211] D. J. Piro and K. J. Maki. "Hydroelastic analysis of bodies that enter and exit water." *Journal of Fluids and Structures* 37 (2013), pp. 134–150 (cit. on pp. 132, 165, 166).
- [212] L.-R. Plumerault. "Numerical modelling of aerated-water wave impacts on a coastal structure." PhD thesis. University of Pau and Pays de l'Adour, 2009 (cit. on pp. 9, 44, 49, 62, 70).
- [213] L.-R. Plumerault, D. Astruc, and P. Maron. "The influence of air on the impact of a plunging breaking wave on a vertical wall using a multfluid model." *Coastal Engineering* 62 (2012), pp. 62–74 (cit. on p. 193).
- [214] L.-R. Plumerault, D. Astruc, P. Villedieu, and P. Maron. "A numerical model for aerated-water wave breaking." *International Journal for Numerical Methods in Fluids* 69.12 (2012), pp. 1851–1871 (cit. on pp. 5, 191, 192).
- [215] S. Popinet. "An accurate adaptive solver for surface-tension-driven interfacial flows." *Journal of Computational Physics* 228.16 (2009), pp. 5838–5866 (cit. on p. 256).
- [216] S. Popinet and S. Zaleski. "A front-tracking algorithm for accurate representation of surface tension." *International Journal for Numerical Methods in Fluids* 30.6 (1999), pp. 775–793 (cit. on p. 244).
- [217] G. R. Price. *A piecewise parabolic volume tracking method for the numerical simulation of interfacial flows*. University of Calgary, 2000 (cit. on p. 246).
- [218] A. Prosperetti. "Motion of two superposed viscous fluids." *The Physics of Fluids* 24.7 (1981), pp. 1217–1223 (cit. on pp. 55, 56).
- [219] E. G. Puckett, A. S. Almgren, J. B. Bell, D. L. Marcus, and W. J. Rider. "A high-order projection method for tracking fluid interfaces in variable density incompressible flows." *Journal of Computational Physics* 130.2 (1997), pp. 269–282 (cit. on p. 248).
- [220] H. Qin, L. Zhao, and J. Shen. "A modified Logvinovich model for hydrodynamic loads on an asymmetric wedge entering water with a roll motion." *Journal of Marine Science and Application* 10.2 (2011), pp. 184–189 (cit. on p. 132).
- [221] J. J. Quirk and S. Karni. "On the dynamics of a shock–bubble interaction." *Journal of Fluid Mechanics* 318 (1996), pp. 129–163 (cit. on pp. 220, 221).
- [222] M. Raessi and H. Pitsch. "Consistent mass and momentum transport for simulating incompressible interfacial flows with large density ratios using the level set method." *Computer & Fluids* 63 (2012), pp. 70–81 (cit. on pp. 76, 77, 85, 94, 101, 110, 209).

- [223] Y. Renardy and M. Renardy. "PROST: a parabolic reconstruction of surface tension for the volume-of-fluid method." *Journal of Computational Physics* 183.2 (2002), pp. 400–421 (cit. on pp. 58, 246).
- [224] "Report on the investigation of the structural failure of MSC Napoli English Channel." *Marine Accident Investigation Branch, London* 9 (2007) (cit. on pp. 2, 128, 190).
- [225] G. Riccardi and A. Iafrati. "Water impact of an asymmetric floating wedge." *Journal of Engineering Mathematics* 49.1 (2004), pp. 19–39 (cit. on p. 5).
- [226] W. J. Rider and D. B. Kothe. "Reconstructing volume tracking." *Journal of Computational Physics* 141.2 (1998), pp. 112–152 (cit. on pp. 245, 248, 260, 265, 275–277).
- [227] A. A. K. Rijkens. "Proactive control of fast ships: improving the seakeeping behaviour in head waves." PhD thesis. Delft University of Technology, 2016 (cit. on p. 18).
- [228] Y. Ropert-Coudert, D. Grémillet, P. Ryan, A. Kato, Y. Naito, and Y. Le Maho. "Between air and water: the plunge dive of the Cape Gannet *Morus capensis*." *International Journal of Avian Science* 146.2 (2004), pp. 281–290 (cit. on p. 128).
- [229] M. Rudman. "Volume-tracking methods for interfacial flow calculations." *International Journal for Numerical Methods in Fluids* 24.7 (1997), pp. 671–691 (cit. on pp. 272, 275).
- [230] M. Rudman. "A volume-tracking method for incompressible multifluid flows with large density variations." *International Journal for Numerical Methods in Fluids* 28.2 (1998), pp. 357–378 (cit. on pp. 45, 51, 76, 77, 109, 150, 281, 285, 286, 288).
- [231] R. Saurel and R. Abgrall. "A multiphase Godunov method for compressible multifluid and multiphase flows." *Journal of Computational Physics* 150.2 (1999), pp. 425–467 (cit. on pp. 5, 191, 200).
- [232] R. Saurel, F. Petitpas, and R. A. Berry. "Simple and efficient relaxation methods for interfaces separating compressible fluids, cavitating flows and shocks in multiphase mixtures." *Journal of Computational Physics* 228.5 (2009), pp. 1678–1712 (cit. on pp. 6, 201, 202).
- [233] R. Scardovelli and S. Zaleski. "Analytical relations connecting linear interfaces and volume fractions in rectangular grids." *Journal of Computational Physics* 164.1 (2000), pp. 228–237 (cit. on pp. 252, 253).

- [234] R. Scardovelli and S. Zaleski. "Direct numerical simulation of free-surface and interfacial flow." *Annual Review of Fluid Mechanics* 31.1 (1999), pp. 567–603 (cit. on p. 244).
- [235] R. Scardovelli and S. Zaleski. "Interface reconstruction with least-square fit and split Eulerian–Lagrangian advection." *International Journal for Numerical Methods in Fluids* 41.3 (2003), pp. 251–274 (cit. on pp. 245, 253, 273–276, 281).
- [236] S. Schenke and T. J. C. van Terwisga. "An energy conservative method to predict the erosive aggressiveness of collapsing cavitating structures and cavitating flows from numerical simulations." *International Journal of Multiphase Flow* 111 (2019), pp. 200–218 (cit. on p. 190).
- [237] J. C. Scott. "The role of salt in whitecap persistence." *Deep Sea Research and Oceanographic Abstracts*. Vol. 22. 10. 1975, pp. 653–657 (cit. on pp. 3, 190).
- [238] C. M. Seddon and M. Moatamedi. "Review of water entry with applications to aerospace structures." *International Journal of Impact Engineering* 32.7 (2006), pp. 1045–1067 (cit. on p. 128).
- [239] J. H. Seo and R. Mittal. "A sharp-interface immersed boundary method with improved mass conservation and reduced spurious pressure oscillations." *Journal of Computational Physics* 230.19 (2011), pp. 7347–7363 (cit. on p. 153).
- [240] S. A. Shah, A. C. Orifici, and J. H. Watmuff. "Water Impact of Rigid Wedges in Two-Dimensional Fluid Flow." *Journal of Applied Fluid Mechanics* 8.2 (2015) (cit. on pp. 132, 133).
- [241] A. Shams, M. Jalalisendi, and M. Porfiri. "Experiments on the water entry of asymmetric wedges using particle image velocimetry." *Physics of Fluids* 27.2 (2015), p. 027103 (cit. on p. 133).
- [242] S. Shao, C. Ji, D. I. Graham, D. E. Reeve, P. W. James, and A. J. Chadwick. "Simulation of wave overtopping by an incompressible SPH model." *Coastal Engineering* 53.9 (2006), pp. 723–735 (cit. on p. 5).
- [243] F. Shyue K.-M/ and Xiao. "An Eulerian interface sharpening algorithm for compressible two-phase flow: The algebraic THINC approach." *Journal of Computational Physics* 268 (2014), pp. 326–354 (cit. on p. 245).
- [244] B. Skuse. "The third pillar." *Physics World* 32.3 (2019), p. 40 (cit. on p. 1).
- [245] R. Smith. *A large wave washing over a ship*. [Online; accessed August 22, 2022]. 2017. URL: https://www.reddit.com/r/HeavySeas/comments/7oz4c7/a_large_wave_washing_over_a_ship/ (cit. on p. 125).

- [246] K. K. So, X. Y. Hu, and N. A. Adams. “Anti-diffusion interface sharpening technique for two-phase compressible flow simulations.” *Journal of Computational Physics* 231.11 (2012), pp. 4304–4323 (cit. on p. 202).
- [247] G. A. Sod. “A survey of several finite difference methods for systems of nonlinear hyperbolic conservation laws.” *Journal of Computational Physics* 27.1 (1978), pp. 1–31 (cit. on pp. 213, 214).
- [248] I. Stenius, A. Rosén, and J. Kuttenukeuler. “Explicit FE-modelling of fluid–structure interaction in hull–water impacts.” *International Shipbuilding Progress* 53.2 (2006), pp. 103–121 (cit. on p. 132).
- [249] *Structural design of offshore ships*. Det Norske Veritas Oslo, Norway, 2002 (cit. on p. 3).
- [250] C. Sun. *Crossing The Drake Passage For Antarctica*. [Online; accessed January 20, 2020]. 2013. URL: <https://www.shell.com/inside-energy/all-in-the-family-the-brent-pioneers.html> (cit. on p. 44).
- [251] Z. Sun, X.-P. Sui, A. A. Korobkin, L. Zou, and Z. Zong. “Slamming force decomposition with gravity effect.” *Journal of Fluids and Structures* 114 (2022), p. 103694 (cit. on p. 131).
- [252] M. Sussman and E. G. Puckett. “A coupled level set and volume-of-fluid method for computing 3D and axisymmetric incompressible two-phase flows.” *Journal of Computational Physics* 162.2 (2000), pp. 301–337 (cit. on p. 110).
- [253] M. Sussman, P. Smereka, and S. Osher. “A level set approach for computing solutions to incompressible two-phase flow.” *Journal of Computational physics* 114.1 (1994), pp. 146–159 (cit. on p. 244).
- [254] M. Sussman, A. S. Almgren, J. B. Bell, P. Colella, L. H. Howell, and M. L. Welcome. “An adaptive level set approach for incompressible two-phase flows.” *Journal of Computational Physics* 148.1 (1999), pp. 81–124 (cit. on p. 110).
- [255] C. K. Svihla and H. Xu. “Simulation of free surface flows with surface tension with ANSYS CFX.” *International ANSYS Conference*. 2006 (cit. on pp. 56–58).
- [256] H. Takemoto. “Water impact test of a wedge with rectangular plates and its analysis.” *Journal of the Society of Naval Architects of Japan* 1984.156 (1984), pp. 306–313 (cit. on p. 133).
- [257] A. Tassin, A. A. Korobkin, and M. J. Cooker. “On analytical models of vertical water entry of a symmetric body with separation and cavity

- initiation." *Applied Ocean Research* 48 (2014), pp. 33–41 (cit. on pp. 128, 131, 132, 158, 160, 163, 165, 166).
- [258] A. Tassin, D. J. Piro, A. A. Korobkin, K. J. Maki, and M. J. Cooker. "Two-dimensional water entry and exit of a body whose shape varies in time." *Journal of Fluids and Structures* 40 (2013), pp. 317–336 (cit. on p. 132).
- [259] S. Tavakoli, S. Najafi, E. Amini, and A. Dashtimanesh. "Performance of high-speed planing hulls accelerating from rest under the action of a surface piercing propeller and an outboard engine." *Applied Ocean Research* 77 (2018), pp. 45–60 (cit. on p. 16).
- [260] M. Tenzer, O. el Moctar, and T. E. Schellin. "Experimental investigation of impact loads during water entry." *Ship Technology Research* 62.1 (2015), pp. 47–59 (cit. on p. 133).
- [261] T. T. Truscott, B. P. Epps, and J. Belden. "Water entry of projectiles." *Annual Review Fluid Mechanics* 46.1 (2014), pp. 355–378 (cit. on p. 132).
- [262] T. T. Truscott and A. H. Techet. "Water entry of spinning spheres." *Journal of Fluid Mechanics* 625 (2009), pp. 135–165 (cit. on p. 132).
- [263] Y.-H. Tseng and J. H. Ferziger. "A ghost-cell immersed boundary method for flow in complex geometry." *Journal of Computational Physics* 192.2 (2003), pp. 593–623 (cit. on p. 78).
- [264] T. Tveitnes, A. C. Fairlie-Clarke, and K. Varyani. "An experimental investigation into the constant velocity water entry of wedge-shaped sections." *Ocean Engineering* 35.14 (2008), pp. 1463–1478 (cit. on p. 134).
- [265] O. Ubbink and R. I. Issa. "A method for capturing sharp fluid interfaces on arbitrary meshes." *Journal of Computational Physics* 153.1 (1999), pp. 26–50 (cit. on p. 273).
- [266] H. S. Udaykumar, R. Mittal, P. Rampunggoon, and A. Khanna. "A sharp interface Cartesian grid method for simulating flows with complex moving boundaries." *Journal of Computational Physics* 174.1 (2001), pp. 345–380 (cit. on p. 78).
- [267] A. F. J. Van Deyzen. "Improving the operability of planing monohulls using proactive control: from idea to proof of concept." PhD thesis. Delft University of Technology, 2014 (cit. on pp. 16, 18).
- [268] G. Vaudor, T. Ménard, W. Aniszewski, M. Doring, and A. Berlemont. "A consistent mass and momentum flux computation method for two phase flows. Application to atomization process." *Computer & Fluids* 152 (2017), pp. 204–216 (cit. on p. 76).

- [269] R. W. C. P. Verstappen and A. E. P. Veldman. "Symmetry-preserving discretization of turbulent flow." *Journal of Computational Physics* 187.1 (2003), pp. 343–368 (cit. on pp. 78, 206).
- [270] T. M. Vestbstad. "Relative wave motion along the side of an FPSO hull." *The 18th International Conference on Offshore Mechanics and Arctic Engineering*. 1999 (cit. on p. 44).
- [271] T. G. Vignesh and S. Bakshi. "Noniterative interface reconstruction algorithms for volume of fluid method." *International Journal for Numerical Methods in Fluids* 73.1 (2013), pp. 1–18 (cit. on pp. 245, 246).
- [272] L. Vincent, T. Xiao, D. Yohann, S. Jung, and E. Kanso. "The Dynamics of Water Entry." *Journal of Fluid Mechanics* 846 (July 2017) (cit. on pp. 128, 132, 134).
- [273] S. Vincent, J. C. B. De Motta, A. Sarthou, J.-L. Estivalezes, O. Simonin, and E. Climent. "A Lagrangian VOF tensorial penalty method for the DNS of resolved particle-laden flows." *Journal of Computational Physics* 256 (2014), pp. 582–614 (cit. on p. 78).
- [274] T. Von Karman. "The impact on seaplane floats during landing" (1929) (cit. on pp. 131, 190).
- [275] H. A. Van der Vorst. "Bi-CGSTAB: A fast and smoothly converging variant of Bi-CG for the solution of nonsymmetric linear systems." *SIAM Journal on scientific and Statistical Computing* 13.2 (1992), pp. 631–644 (cit. on p. 22).
- [276] T. V. Vu, S. Homma, G. Tryggvason, J. C. Wells, and H. Takakura. "Computations of breakup modes in laminar compound liquid jets in a coflowing fluid." *International Journal of Multiphase Flow* 49 (2013), pp. 58–69 (cit. on p. 208).
- [277] J. H. Vughts. "The hydrodynamic coefficients for swaying, heaving and rolling cylinders in a free surface." *International Shipbuilding Progress* 15.167 (1968), pp. 251–276 (cit. on p. 149).
- [278] H. Wagner. "The phenomena of impact and planing on water." *National Advisory Committee for Aeronautics Translation* 1366, ZAMM 12 (1932), pp. 193–215 (cit. on pp. 131, 161).
- [279] H. Wagner. "Über stoß- und gleitvorgänge an der oberfläche von flüssigkeiten." *Journal of Applied Mathematics and Mechanics/Zeitschrift für Angewandte Mathematik und Mechanik* 12.4 (1932), pp. 193–215 (cit. on p. 190).

- [280] G. Wang, S. Tang, Y. Shin, et al. "A Direct Calculation Approach For Designing a Ship-shaped FPSO's Bow Against Wave Slamming Load." *The 12th International Offshore and Polar Engineering Conference*. International Society of Offshore and Polar Engineers. 2002 (cit. on p. 44).
- [281] J. Wang, C. Lugni, and O. M. Faltinsen. "Analysis of loads, motions and cavity dynamics during freefall wedges vertically entering the water surface." *Applied Ocean Research* 51 (2015), pp. 38–53 (cit. on pp. 129, 132).
- [282] J. Wang, C. Lugni, and O. M. Faltinsen. "Experimental and numerical investigation of a freefall wedge vertically entering the water surface." *Applied Ocean Research* 51 (2015), pp. 181–203 (cit. on pp. 128, 129, 132, 134).
- [283] S. Wang, H. B. Luo, and C. G. Soares. "Explicit FE simulation of slamming load on rigid wedge with various deadrise angles during water entry." *Maritime Engineering and Technology* (2012), pp. 399–406 (cit. on p. 132).
- [284] S. Wang and C. G. Soares. "Effects of compressibility, three-dimensionality and air cavity on a free-falling wedge cylinder." *Ocean Engineering* 217 (2020), p. 107589 (cit. on p. 132).
- [285] S. Wang, Y. Su, X. Zhang, and J. Yang. "RANSE simulation of high-speed planning craft in regular waves." *Journal of Marine Science and Application* 11.4 (2012), pp. 447–452 (cit. on p. 17).
- [286] K. Wei, J. Hong, M. Jiang, and W. Zhao. "A review of breaking wave force on the bridge pier: Experiment, simulation, calculation, and structural response." *Journal of Traffic and Transportation Engineering* (2022) (cit. on pp. 2, 128, 190).
- [287] P. R. Wellens and M. van der Eijk. *Experimental data of buoyant wedge entries with reemergence in 2D*. 4TU.ResearchData. 2023. doi: [10.4121/a698656f-2648-4bc7-99ae-4f9a27fd869c](https://doi.org/10.4121/a698656f-2648-4bc7-99ae-4f9a27fd869c) (cit. on p. 135).
- [288] P. R. Wellens. *Experimental data for a Rigid Inflatable Boat (RIB) undergoing slamming in irregular waves*. 2020. doi: [10.4121/13078601](https://doi.org/10.4121/13078601) (cit. on pp. 15, 18).
- [289] P. R. Wellens and M. Borsboom. "A generating and absorbing boundary condition for dispersive waves in detailed simulations of free-surface flow interaction with marine structures." *Computer & Fluids* 200 (2020), p. 104387 (cit. on pp. 20, 36).
- [290] P. R. Wellens. "Wave simulation in truncated domains for offshore applications." PhD thesis. Delft University of Technology, 2012 (cit. on pp. 35, 55).

- [291] R. Wemmenhove, R. Luppés, A. E. P. Veldman, and T. Bunnik. "Numerical simulation of hydrodynamic wave loading by a compressible two-phase flow method." *Computer & Fluids* 114 (2015), pp. 218–231 (cit. on pp. 5, 45, 49–51, 60, 69, 72, 97).
- [292] R. Wemmenhove. *Numerical simulation of two-phase flow in offshore environments*. University of Groningen, 2008 (cit. on pp. 8, 9, 18, 19, 26, 47–49, 61, 68, 95, 198, 202, 212).
- [293] X. Wen, A. Del Buono, P. Liu, Q. Qu, and A. Iafrati. "Acceleration effects in slamming and transition stages for the water entry of curved wedges with a varying speed." *Applied Ocean Research* 128 (2022), p. 103294 (cit. on p. 128).
- [294] X. Wen, Q. Qu, P. Liu, and S. Ding. "Theoretical study on slamming and transition stages of normal impacts of symmetrical bodies on calm and wavy water surfaces." *Applied Ocean Research* 119 (2022), p. 102986 (cit. on pp. 131, 160, 167).
- [295] G. D. Weymouth and D. K.-P. Yue. "Conservative Volume-of-Fluid method for free-surface simulations on Cartesian-grids." *Journal of Computational Physics* 229.8 (2010), pp. 2853–2865 (cit. on pp. 87, 212, 277).
- [296] P. S. Wilson and R. A. Roy. "An audible demonstration of the speed of sound in bubbly liquids." *American Journal of Physics* 76.10 (2008), pp. 975–981 (cit. on pp. 194, 201).
- [297] A. B. Wood. "A textbook of Sound, 578 pp." *Bell, London* (1941) (cit. on pp. 190, 194, 200).
- [298] A. B. Wood and R. B. Lindsay. "A textbook of sound." *Physics Today* 9.11 (1956), p. 37 (cit. on p. 5).
- [299] D. J. Wood, D. H. Peregrine, and T. Bruce. "Wave impact on a wall using pressure-impulse theory. I: trapped air." *Journal of waterway, port, coastal, and Ocean Engineering* 126.4 (2000), pp. 182–190 (cit. on p. 192).
- [300] J. Wrighton. *All in the family: the Brent pioneers*. [Online; accessed August 16, 2022]. 2016. URL: <https://www.shell.com/inside-energy/all-in-the-family-the-brent-pioneers.html> (cit. on p. 2).
- [301] G. X. Wu, H. Sun, and Y. S. He. "Numerical simulation and experimental study of water entry of a wedge in free fall motion." *Journal of Fluids and Structures* 19.3 (2004), pp. 277–289 (cit. on p. 133).
- [302] F. Xiao, Y. Honma, and T. Kono. "A simple algebraic interface capturing scheme using hyperbolic tangent function." *International Journal for Numerical Methods in Fluids* 48.9 (2005), pp. 1023–1040 (cit. on p. 245).

- [303] B. Xie and F. Xiao. "Toward efficient and accurate interface capturing on arbitrary hybrid unstructured grids: The THINC method with quadratic surface representation and Gaussian quadrature." *Journal of Computational Physics* 349 (2017), pp. 415–440 (cit. on pp. 273, 276).
- [304] H. Xie, F. Liu, P. Yu, and H. Ren. "Comparative study on fluid dynamic behavior and slamming loads of two bow-flare sections entering into water." *International Journal of Mechanical Sciences* 166 (2020), p. 105177 (cit. on p. 133).
- [305] H. Xie, X. Wei, F. Liu, H. Ren, X. Liu, and Z. Chen. "An experimental study on water entry of a 3D bow-flare model with pitch angles." *Ocean Engineering* 219 (2021), p. 108282 (cit. on p. 133).
- [306] Z. Xie, P. Lin, and T. Stoesser. "A conservative and consistent implicit Cartesian cut-cell method for moving geometries with reduced spurious pressure oscillations." *Journal of Computational Physics* 459 (2022), p. 111124 (cit. on pp. 78, 82).
- [307] Z. Xie and T. Stoesser. "A three-dimensional Cartesian cut-cell/volume-of-fluid method for two-phase flows with moving bodies." *Journal of Computational Physics* 416 (2020), p. 109536 (cit. on p. 211).
- [308] Y. Yamamoto, H. Ohtsubo, and Y. Kohno. "Water impact of wedge model." *Journal of the Society of Naval Architects of Japan* 1984.155 (1984), pp. 236–245 (cit. on p. 133).
- [309] E.-M. Yettou, A. Desrochers, and Y. Champoux. "Experimental study on the water impact of a symmetrical wedge." *Fluid Dynamics Research* 38.1 (2006), p. 47 (cit. on pp. 130, 134).
- [310] D. L. Youngs. "An interface tracking method for a 3D Eulerian hydrodynamics code." *Atomic Weapons Research Establishment Technical Report* 44.92 (1984), p. 35 (cit. on p. 22).
- [311] Z.-M. Yuan, X. Zhang, C.-Y. Ji, L. Jia, H. Wang, and A. Incecik. "Side wall effects on ship model testing in a towing tank." *Ocean Engineering* 147 (2018), pp. 447–457 (cit. on p. 30).
- [312] S. T. Zalesak. "Fully multidimensional flux-corrected transport algorithms for fluids." *Journal of Computational Physics* 31.3 (1979), pp. 335–362 (cit. on p. 272).
- [313] Q. Zhang. "Fourth-and higher-order interface tracking via mapping and adjusting regular semianalytic sets represented by cubic splines." *SIAM Journal on Scientific Computing* 40.6 (2018), pp. 3755–3788 (cit. on p. 246).

- [314] S. Zhang, D. K. P. Yue, and K. Tanizawa. "Simulation of plunging wave impact on a vertical wall." *Journal of Fluid Mechanics* 327 (1996), pp. 221–254 (cit. on p. 5).
- [315] R. Zhao. "A simplified nonlinear analysis of a high-speed planing craft in calm water." *The 4th International Conference on Fast Sea Transportation* (1997) (cit. on p. 16).
- [316] R. Zhao, O. M. Faltinsen, and J. Aarsnes. "Water entry of arbitrary two-dimensional sections with and without flow separation." *The 21st Symposium on Naval Hydrodynamics*. 1996, pp. 408–423 (cit. on pp. 5, 22, 24, 27, 131, 133, 156).
- [317] R. Zhao and O. M. Faltinsen. "Water entry of two-dimensional bodies." *Journal of Fluid Mechanics* 246 (1993), pp. 593–612 (cit. on p. 190).
- [318] X. Zhu, O. M. Faltinsen, and C. Hu. "Water Entry and Exit of a Horizontal Circular Cylinder." *Journal of Offshore Mechanics and Arctic Engineering* 129.4 (2006), pp. 253–264 (cit. on p. 228).
- [319] K. Zuiderveld. "Contrast limited adaptive histogram equalization." *Graphics gems* (1994), pp. 474–485 (cit. on p. 146).
- [320] D. Zuzio, A. Orazzo, J.-L. Estivalèzes, and I. Lagrange. "A new efficient momentum preserving Level-Set/VOF method for high density and momentum ratio incompressible two-phase flows." *Journal of Computational Physics* 410 (2020), p. 109342 (cit. on pp. 77, 78, 85, 87, 91, 92, 94, 100, 101, 120, 249, 281, 283, 286).

A deeper understanding of physics is required when the complexity of events increases. A complex event consists of many detailed interacting processes. The complete picture asks for an understanding of each of the processes individually. Numerical computing in the maritime industry is becoming more relevant due to the increase in usability and relatively low costs compared to experiments. The numerical results allow for analysis at the required level of detail. The complexity of water-wave impacts on offshore structures necessitates innovative numerical approaches because conventional analytical techniques fall short of representing the non-linearity in these events.

Large amplitude waves can break and cause impacts with damages to structures that lead to catastrophic failure and even loss of people. Even though these structures are designed according to the regulations, the lack of understanding of these extreme wave impacts can result in these failures. This is the motive of recent studies about large breaking waves.

A breaking wave can result in air entrapment followed by air entrainment due to fragmentation. The entrained air bubbles can remain in the water for several wave periods up to several percent in volume. The highly-compressible air bubbles in water (a homogeneous mixture of water and air) increase the mixture compressibility and decrease the speed of sound significantly. The mixture results in different loadings than pure water. A cushioning effect on the impact, distribution of the impact pressure over a larger area, increase in rise and fall time of the pressure, cavitation, and pressure waves can be due to air in water.

The overarching topic of this thesis is to gain more understanding of the effect of air entrapment and entrainment on wave impact loadings on floating bodies. An innovative fast computational model is developed that can account for these highly deformable interface flows. The model should deal with high-density ratio flows, sharp interface modeling for predicting the moment of impact, compressible entrapped air pockets, and a compressible homogeneous mixture of air and water. An experimental setup was needed that includes the effect of air entrainment in fluid-structure interaction. The results are used for model verification.

This dissertation consists of three parts. In the first part, the one-phase flow model of ComFLOW is introduced as starting point for further development. This method has a major application in predicting hydrodynamic wave loading

on offshore structures. The numerical model is characterized by the following terms: finite-volume method, Volume-of-Fluid interface capturing, geometrical interface reconstruction, pressure-based solver, one-fluid formulation, the staggered arrangement of variables on a fixed Cartesian grid, and a cut-cell method to account for moving rigid bodies. Results obtained with the one-phase flow model are compared with in-house conducted towing tank results of a high-speed vessel in moderate to high irregular head waves and a calibrated state-of-the-art strip theory method. The large vertical accelerations are well captured by the one-phase flow model, outperforming the strip-theory method in terms of accuracy. This creates opportunities for using the numerical model in seakeeping optimization and improving strip-theory methods.

Large breaking waves can result in the entrapment of highly compressible air pockets. The one-phase flow model is extended to a semi-compressible two-phase flow model accounting for the compressibility of the air phase. The dynamics of such an enclosed air pocket are characterized by the position of the free surface, surface tension, viscosity, and compressibility. The semi-compressible two-phase flow model incorporates a continuum surface model for surface tension and is tested for these characteristics by simulating traditional benchmarks. The results are in good agreement with the benchmarks. A wave impact case on a vertical wall with an overturning wave entrapping an air pocket shows that the compression of the air pocket dominates the dynamics. Pressure oscillations have amplitudes in the order of the pressure caused by the initial impact on the wall.

The interface modeling of two-phase flows is challenging due to the high-density ratio. A consistent discretization of mass and momentum transport is applied to prevent distortion, spurious velocities, and numerical instability. The model is extended for fluid-structure interaction using a cut-cell method. Simulations of newly devised fluid-structure interaction benchmark simulations show that using a consistent discretization reduces the momentum losses by an order of magnitude compared to non-consistent discretization. The reduction gets more apparent for high-density ratios. Results obtained with the consistent discretisation are closer to experimental measurements.

In the second part of the dissertation, an experiment with a wedge entry that is as 2D as possible is presented. This setup makes it possible to focus on complicated interactions between bodies and free surfaces with a large amount of detail. The experimental results act as a basis for the extension to simulate aerated water wave impacts and can be used as a benchmark for violent fluid-structure interaction. The free surface deformation and the dynamics of a buoyant wedge entering and emerging from the water are analyzed and compared with the semi-compressible two-phase numerical model. The combination of the experimental and numerical results reduces the uncertainty concerning chaotic aspects of the

flow and measurement errors and it results in a better understanding of when 3D effects take place.

The experimental setup is extended for pressure measurements on the wedge and injecting a homogeneously distributed air bubble field. The numerical model is extended to a new fully compressible pressure-based multiphase model. Pressure density relations are enforced, and the assumption of a homogeneous mixture is made to reduce costs by preventing the tracking of every single tiny bubble around a large structure. An additional fraction field indicating the aeration level and a new formulation for the speed of sound are described. This is to prevent artificial air entrainment that overestimates compressibility around the fluid-fluid interface. Comparing the numerical and experimental results shows the cushioning effect and rise and fall time of the pressure on the wedge increasing for a large amount of air in water. The sequential post-impact loadings on the wedge due to reflected pressure waves are increasing for a higher air content in water relative to the maximum pressure. The governing frequencies of these sequential loadings are decreasing in agreement with the speed of sound formulation. These may play a significant role in the fatigue of marine structures.

The numerical air entrainment is likely caused by discontinuities in the approximation of the interface. In the third part, a new bilinear interface reconstruction algorithm is presented, enforcing continuity using a curvature-weighted approach and the initiation of piecewise linear interface segments. Applying this algorithm leads to a neglectable increase in computational costs compared to standard piecewise linear interface calculation methods, but an order reduction in the error for shape preservation for traditional benchmarks like the Zalesak slotted disk and the reversed single-vortex. The new reconstruction outperforms higher-order methods of other literature in terms of costs by having similar accuracy. A new unsplit face-matched upwind-based flux polygon advection scheme is proposed to prevent inconsistency between mass and momentum fluxes due to using interface reconstruction and a staggered arrangement of variables. A translation of a high-density cylinder in low-density fluid verifies the improvement of consistency by not getting unstable.

Overall, this thesis sheds light on a stable and accurate numerical model for high-density ratio interface flows, discontinuous interface reconstruction, compressible entrapped air pocket oscillations, and fluid-structure interaction. The main outcome is an approach of modeling impacts of (moving) structures in aerated water, and the validation of the numerical model.

Een dieper begrip van de fysica is vereist wanneer de complexiteit van gebeurtenissen toeneemt. Een complexe gebeurtenis bestaat uit vele gedetailleerde op elkaar inwerkende processen. Het complete plaatje vraagt om inzicht in elk van deze processen afzonderlijk. Numeriek rekenen in de maritieme industrie is steeds relevanter door de toename in bruikbaarheid en relatief lage kosten in vergelijking met experimenten. De numerieke resultaten maken analyse op het vereiste detailniveau mogelijk. De complexiteit van golfklappen op offshore constructies vereist innovatieve numerieke benaderingen omdat conventionele analytische technieken de niet-lineariteit in deze complexe gebeurtenissen niet kunnen weergeven.

Golven met grote amplitude kunnen breken en inslaan, met als gevolg schade aan constructies, catastrofaal falen en zelfs het overlijden van mensen. Ook al zijn deze constructies volgens de regelgeving ontworpen, het gebrek aan inzicht in extreme golfklappen kan tot ongelukken leiden. Dit is de motivatie om onderzoek naar brekende golven te doen.

Een brekende golf kan lucht insluiten, waarna de luchtinsluiting fragmenteert tot luchtbellens. De meegevoerde luchtbellens kunnen meerdere golfperioden in het water blijven met een volume van enkele procenten van het watervolume. De sterk samendrukbare luchtbellens in water (een homogeen mengsel van water en lucht) verhogen de samendrukbaarheid van het mengsel en verlagen de geluidssnelheid aanzienlijk. Het mengsel resulteert in andere golfbelastingen dan zuiver water. Een verend effect op de maximale belasting, verdeling van de drukbelasting over een groter gebied, toename in stijg- en daaltijd van de druk, cavitatie en drukgolven kunnen te wijten zijn aan lucht in water.

Het overkoepelende onderwerp van dit proefschrift is om meer inzicht te krijgen in het effect van lucht -als insluiting of als mengsel met water- op belastingen op drijvende lichamen. Er is een innovatief snel rekenmodel ontwikkeld dat rekening kan houden met deze sterk vervormbare grensvlak stromingen. Het model moet omgaan met een hoge dichtheidsverhouding rond het grensvlak, het scherp modelleren van het grensvlak tussen twee vloeistoffen voor het voorspellen van het moment dat belasting plaatsvindt, samendrukbare ingesloten luchtvolumes en een samendrukbaar homogeen mengsel van lucht en water. Er was een experimentele opstelling nodig die het effect van het meevoeren van lucht op de interactie tussen vloeistof en structuur kan beschrijven. De experi-

mentele resultaten zijn gebruikt voor het valideren van het numeriek model.

Dit proefschrift bestaat uit drie delen. In het eerste deel is het één-fase stromingsmodel ComFLOW geïntroduceerd als uitgangspunt voor verdere ontwikkeling. Deze methode wordt toegepast bij het voorspellen van hydrodynamische golfbelastingen op offshore constructies. Het model is gekenmerkt door de volgende termen: eindige-volumemethode, Volume-of-Fluid voor het benaderen van het grensvlak, het geometrische reconstrueren van het grensvlek tussen twee vloeistoffen, vergelijkingen oplossen op basis van de drukterm, het formuleren van de stroming als een gemengde vloeistof, de verspringende rangschikking van variabelen op een vast Cartesiaans rooster en een methode die gebruikmaakt van cut cells om rekening te houden met bewegende niet-vertormbare lichamen. Resultaten verkregen met het één-fase stromingsmodel zijn vergeleken met intern uitgevoerde sleeptankresultaten van een hogesnelheidsvaartuig in matige tot hoge onregelmatige kopgolven en een gekalibreerde state-of-the-art striptheoriemethode. De grote verticale versnellingen zijn goed gerepresenteerd door het één-fase stromingsmodel dat qua nauwkeurigheid beter presteert dan de striptheoriemethode. Dit creëert mogelijkheden om het numeriek model te gebruiken bij optimalisatie van zeegang en het verbeteren van striptheoriemethoden.

Grote brekende golven kunnen leiden tot het insluiten van zeer samendrukbare lucht volumes. Het één-fase stromingsmodel is uitgebreid tot een twee-fase stromingsmodel dat rekening houdt met de samendrukbaarheid van de lucht. De dynamica van zo'n ingesloten luchtvolume is gekenmerkt door de positie van het vrij vloeistofoppervlak, oppervlaktespanning, viscositeit en samendrukbaarheid. Het twee-fase stromingsmodel bevat een continuüm-oppervlaktemodel voor oppervlaktespanning en is op deze kenmerken getest door traditionele gebeurtenissen te simuleren. De numerieke resultaten komen goed overeen met de traditionele simulaties. Een golfklap op een verticale wand met een omslaande golf die een luchtvolume vasthoudt, laat zien dat de samendrukbaarheid van het luchtvolume dominant aanwezig is in de druk. De drukschommelingen hebben amplitudes in de orde grootte van de initiële piekbelasting op de muur.

Het modelleren van het grensvlak tussen twee vloeistoffen is een uitdaging vanwege de hoge dichtheidsverhouding. Een consistente discretisatie van massa en momentumtransport is toegepast om vervorming, onechte snelheden en numerieke instabiliteit te voorkomen. Deze is uitgebreid voor vloeistof-lichaam interactie met behulp van cut cells. Nieuw ontworpen situaties voor vloeistof-lichaam interactie laten zien dat het gebruik van een consistente discretisatie de momentumverliezen met een orde van grootte reduceert in vergelijking met niet-consistente discretisatie. De reductie is duidelijker voor verhoudingen met een hogere dichtheid. De verkregen resultaten met de consistente discretisatie

liggen dicht bij de experimentele metingen.

In het tweede deel van het proefschrift is een experiment gepresenteerd met een vallende wig in water die zo 2D mogelijk is. Deze opstelling maakt het mogelijk om te focussen op de details van de gecompliceerde interacties tussen lichamen en vloeistoffen. De experimentele resultaten dienen als basis voor de uitbreiding om golfbelastingen met lucht in het water te simuleren en kunnen worden gebruikt als maatstaf voor hevige vloeistof-lichaam interactie. De vervorming van het vrije oppervlak en de dynamica van een drijvende wig die het water binnenkomt en uitgaat zijn geanalyseerd en vergeleken met het semi-samendrukbare twee-fase numerieke model. De combinatie van de experimentele en numerieke resultaten vermindert de onzekerheid over chaotische aspecten van de stroming en over meetfouten en leidt tot een beter begrip van wanneer 3D-effecten optreden.

De experimentele opstelling is hierna uitgebreid voor drukmetingen op de wig en het injecteren van een homogeen verdeeld luchtbellenveld. Het numerieke model is uitgebreid naar een nieuw, volledig samendrukbaar, op druk-gebaseerd meer-fasen model. Drukdichtheidsrelaties zijn afgeleid en de aanname van een homogeen mengsel is gemaakt om de kosten te verlagen. Deze aannames voorkomen dat elke kleine luchtbel rond een groot lichaam moet worden gevolgd. Een extra fase die het beluchtingsniveau aangeeft is toegevoegd en een nieuwe formulering voor de geluidssnelheid is gepresenteerd. Dit is om het kunstmatig meevoeren van lucht te voorkomen die de samendrukbaarheid rond het vloeistof-vloeistofgrensvlak overschat. Vergelijking van de numerieke en experimentele resultaten laat zien dat het verend effect en de stijg- en daaltijd van de druk op de wig toenemen voor een grotere hoeveelheid lucht in water. De repeterende belastingen op de wig als gevolg van gereflecteerde drukgolven nemen toe voor een hoger luchtgehalte in water. De frequenties van deze repeterende belastingen nemen af in overeenstemming met de snelheid van het geluid. Deze repeterende belastingen kunnen een belangrijke rol spelen bij de vermoeiing van maritieme constructies.

Het numeriek insluiten van lucht is waarschijnlijk veroorzaakt door discontinuïteiten in de benadering van het vrij vloeistofoppervlak. In het derde deel van het proefschrift is een nieuw bilineair reconstructiealgoritme gepresenteerd voor het vloeistofoppervlak dat continuïteit afdwingt met behulp van een met kromming gewogen benadering en de initiatie van simpele lineaire segmenten. De toepassing van deze method leidt tot een verwaarloosbare toename van de rekenkosten in vergelijking met standaard stuksgewijs lineaire segmenten, maar reductie in de fout voor vormbehoud met een orde van grootte voor traditionele simulaties zoals de Zalesak-schijf met sleuven en de omgekeerde enkele draaikolk. De nieuwe reconstructie presteert qua kosten beter dan methodes van hogere orde voor vergelijkbare nauwkeurigheid. Een nieuw verplaatsingsalgoritme

ritme is voorgesteld om inconsistentie tussen massa- en momentumtransport te voorkomen als gevolg van het gebruik van oppervlakreconstructie met de door ons gebruikte verspringende plaatsing van variabelen. De verplaatsing van een cilinder met hoge dichtheid in een vloeistof met lage dichtheid verifieert de verbetering van de consistentie door niet instabiel te worden.

Al met al werpt dit proefschrift licht op het stabiel en nauwkeurig numeriek modelleren van oppervlaktestromingen met een hoge dichtheidsverhouding tussen fases, discontinue oppervlaktereconstructie, oscillaties in ingesloten samendrukbare luchtvolumes en interactie tussen vloeistoffen en lichamen. Het belangrijkste resultaat is een nieuw model voor golfbelastingen op (bewegende) constructies met lucht in water, en de validatie van het model.

ACKNOWLEDGMENTS

First of all, I would like to thank my daily supervisor **Peter Wellens** who introduced me to the world of computational fluid dynamics and allowed me to do my first finite-volume discretization of the conservation laws. After these four years, I think I can say for both sides that you were not only my supervisor, but we also started to become friends. Besides having "serious" talks, we also had, let's say, enjoyable boy talks that could escalate in many directions. Thank you very much for pleasantly guiding me, sharing your broad knowledge, and endless rereading to improve my work. Thank you EVA.

Second, I would like to thank my promoter **Bendiks Jan Boersma** for his trust and for giving me the freedom I needed.

I would also like to express my gratitude to the people working in the towing tank for helping, providing, constructing, and supporting; **Sebastian, Peter, Pascal, Jennifer**, and **Frits** thank you for your time. I want to thank **Jasper** for his handcraft skills and knowledge but above all the nice chats we had.

Furthermore, I would like to thank the (old) students **Marnix, Robert, Bauke, Tijs**, and others for their contribution in coding, conducting experiments, and performing numerical simulations.

Thanks goes to my old work-related friends and roomies, but also the new ones. **Hugo** thank you for the privilege of having a friend who is smart but also dirty-minded, and **Pengpeng** thank you for the warm welcome and nice chats we had. **Jacob** and **Filippo** thank you for withstanding me. **Marco** thanks for your help and for having somebody with whom I could go into detail. The old guards **Reinier, Gabriele, Bart, Arno, Xiaobo**, and the new revelation **Wei Jun, Anna, Mohammed, Vasu**, thank you.

On a more personal note, I would like to thank my friends **Twan** and **Michel** for sometimes being stupid and weird but, above all, being ready for me. I would also like to thank my "not-yet" in-laws for their support and for being a positive distraction for me; **Paula, Amanda, Sarah, Michael**, and **Jouri**.

I would like to thank my own family, who supported me not only during my Ph.D. but also during my whole life. This is a good place to thank you for all these enjoyable moments. My parents **Rinie** and **Marjolein**, my brother **Leo** and his wife **Catriona**, thank you.

And finally, of course, **Iris** thank you for being sometimes down to earth, distracting me from my work, but most of all, the moments of love and being present for me. These moments were important to me. The same is true for my dog **Milko**. Love you both.

*Martin van der Eijk
Delft, September 2023*

Martin van der Eijk

Martin van der Eijk was born on 4 August 1995 in Nieuwerkerk aan den IJssel, the Netherlands. His research interests include fluid flows, dynamics, and their interaction. Besides his great interest in the communication between physics and numerics, he has a growing predilection for designing, constructing, and conducting experiments.

Education

- 2019–2023 Ph.D. research
Department of Maritime and Transport Technology
Delft University of Technology
Delft, the Netherlands
Thesis: Extreme aerated water-wave impacts on
floating bodies
Promoter: prof.dr.ir. B.J. Boersma
Copromoter: dr.ir. P.R. Wellens
- 2016–2018 M.Sc. study *with honors*
Marine Technology
Delft University of Technology
Delft, the Netherlands
- 2013–2016 B.Sc. study *with honors*
Marine Technology
Delft University of Technology
Delft, the Netherlands

Journal articles

This thesis:

1. **M. van der Eijk** and P. R. Wellens. *A compressible two-phase flow model for pressure oscillations in air entrappings following green water impact events on ships*, International Shipbuilding progress 66.4 (2019), pp. 315-343.
2. **M. van der Eijk** and P. R. Wellens. *Experimental and numerical assessment of vertical accelerations during bow re-entry of a RIB in irregular waves*, International Shipbuilding progress 67.2-4 (2020), pp. 173-198.
3. **M. van der Eijk** and P. R. Wellens. *Two-phase free-surface flow interaction with moving bodies using a consistent, momentum preserving method*, Journal of Computational Physics 474 (2023), pp. 111796.
4. **M. van der Eijk** and P. R. Wellens. *Experimental, numerical and analytical evaluation of the buoyant wedge entry problem with reemergence in 2D*, under review Journal of Fluid Mechanics (2023).
5. **M. van der Eijk** and P. R. Wellens. *An efficient pressure-based multiphase finite volume method for interaction between compressible aerated water and moving bodies*, under review Journal of Computational Physics (2023).
6. **M. van der Eijk** and P. R. Wellens. *An efficient 2D bilinear interface reconstruction algorithm and consistent multidimensional unsplit advection scheme for accurate tracking of highly-curved interfacial structures on uniform grids*, under second review Journal of Computational Physics (2023).

Other articles:

6. R. W. Bos, **M. van der Eijk**, J. H. den Besten, P. R. Wellens. *A reduced order model for FSI for wave impacts in LNG sloshing*, International Shipbuilding progress 69.2 (2022), pp. 119-138.

Conferences

1. **M. van der Eijk**, P. R. Wellens, R.W. Bos. *Aerated wave impacts on floating bodies*, The 36th International Workshop on Water Waves on Floating Bodies: IWWWFB36, August 2020, Seoul, South-Korea.
2. **M. van der Eijk** and P. R. Wellens. *Experimental and numerical 2D wedge entry in water with entrained air*, The 38th International Workshop on Water Waves on Floating Bodies: IWWWFB38, April 2022, Giardini Naxos, Italy.
3. **M. van der Eijk** and P. R. Wellens. *Numerical modeling of a high-speed wedge entry in aerated water*, The 8th European Congress on Computational Methods in Applied Sciences and Engineering: ECCOMAS, June 2022, Oslo, Norway.
4. P. R. Wellens and **M. van der Eijk**. *Aerated wave propagation and wave impacts on structures*, The 8th European Congress on Computational Methods in Applied Sciences and Engineering: ECCOMAS, June 2022, Oslo, Norway.